

---

# Structure and Dynamics of the Galactic Bulge and Bar

Matthieu Portail

---



München 2016



---

# Structure and Dynamics of the Galactic Bulge and Bar

Matthieu Portail

---

Dissertation  
an der Fakultät für Physik  
der Ludwig–Maximilians–Universität  
München

vorgelegt von  
Matthieu Portail  
aus Rouen, Frankreich

München, den 6. September 2016

Erstgutachter: Prof. Dr. Ortwin Gerhard

Zweitgutachter: Prof. Dr. Andreas Burkert

Tag der mündlichen Prüfung: 6. Oktober 2016

*Everything will be okay in the end.  
If it's not okay, it's not the end.*

maybe (not) John Lennon



# Contents

<b>Zusammenfassung</b>	<b>xvii</b>
<b>Abstract</b>	<b>xix</b>
<b>1 Introduction</b>	<b>1</b>
1.1 The Milky Way Galaxy . . . . .	1
1.1.1 A little bit of history . . . . .	1
1.1.2 The central Milky Way . . . . .	4
1.1.3 The galactic bulge and bar . . . . .	6
1.1.4 The galactic disk(s) . . . . .	7
1.1.5 The galactic stellar and dark matter halos . . . . .	12
1.1.6 The environment of the Milky Way . . . . .	13
1.2 Galactic archeology: motivation and challenge . . . . .	15
1.2.1 Formation of the Galaxy . . . . .	15
1.2.2 The challenge of geometry . . . . .	15
1.2.3 The age of surveys . . . . .	17
1.3 Dynamical modelling of galaxies . . . . .	19
1.3.1 Collisionless stellar dynamics . . . . .	19
1.3.2 (Semi-) Analytical methods . . . . .	21
1.3.3 Particle/Orbit based methods . . . . .	23
1.4 Goal and outline of the thesis . . . . .	26
<b>2 Made-to-Measure Models of the Galactic Boxy/Peanut Bulge</b>	<b>29</b>
2.1 Introduction . . . . .	30
2.2 Particle models of barred discs . . . . .	31
2.2.1 N-body models in different dark matter haloes . . . . .	31
2.2.2 Geometry and scaling . . . . .	32
2.3 Made-to-measure with MW observables . . . . .	36
2.3.1 Theory of the M2M method . . . . .	36
2.3.2 Density observables . . . . .	37
2.3.3 Kinematic observables . . . . .	39
2.3.4 Dynamical velocity scaling . . . . .	42
2.3.5 Potential and model integration . . . . .	43

2.3.6	NMAGIC parametrization . . . . .	44
2.4	Dynamical models of the MW . . . . .	45
2.4.1	Determination of the stellar mass in the bulge . . . . .	45
2.4.2	Best dynamical models of the Milky Way bulge . . . . .	46
2.4.3	The pattern speed . . . . .	51
2.4.4	Proper motions . . . . .	54
2.5	Mass of the galactic bulge . . . . .	56
2.5.1	Evaluation of the total mass . . . . .	56
2.5.2	Evaluation of systematics . . . . .	56
2.6	Mass-to-light and mass-to-clump ratios . . . . .	61
2.6.1	Population synthesis models . . . . .	61
2.6.2	Mass-to-light ratio . . . . .	63
2.6.3	Mass-to-clump ratio . . . . .	65
2.7	Peanut and X-shape structures of the galactic bulge . . . . .	68
2.7.1	The photometric X-shape . . . . .	68
2.7.2	The mass of the peanut shape . . . . .	68
2.8	Discussion . . . . .	72
2.8.1	Dynamical mass of the bulge . . . . .	72
2.8.2	Stellar and dark matter mass in the bulge . . . . .	72
2.8.3	Pattern speed of the MW bar/bulge . . . . .	73
2.9	Conclusion . . . . .	74
<b>3</b>	<b>Peanuts, Brezels and Bananas</b>	<b>77</b>
3.1	Introduction . . . . .	77
3.2	The orbital structure of B/P bulges in N-body models . . . . .	78
3.2.1	N-body models of B/P bulges . . . . .	78
3.2.2	Orbit classification . . . . .	79
3.2.3	Which orbit classes dominate the X-shape? . . . . .	82
3.3	The orbital structure of the galactic B/P bulge . . . . .	84
3.3.1	Made-to-Measure models of the galactic bulge . . . . .	84
3.3.2	The brezel orbit . . . . .	86
3.3.3	The galactic X-structure . . . . .	87
3.4	Conclusion . . . . .	87
<b>4</b>	<b>Dynamical Modelling of the Galactic Bulge and Bar</b>	<b>89</b>
4.1	Introduction . . . . .	90
4.2	Made-to-Measure modelling of the Galaxy . . . . .	91
4.2.1	M2M modelling . . . . .	91
4.2.2	The problem of the initial conditions . . . . .	92
4.3	Density model of the Galaxy for tailoring initial conditions . . . . .	94
4.3.1	Unified bulge and bar structure as traced by RCGs . . . . .	94
4.3.2	Empirical determination of the mass-to-clump ratio in the bulge . . . . .	96
4.3.3	Stellar disk . . . . .	96



4.3.4	Dark matter halo . . . . .	99
4.4	Tailoring initial models for modelling the Milky Way . . . . .	103
4.4.1	Adiabatic adaptation of the initial conditions . . . . .	103
4.4.2	Integration and potential solver . . . . .	104
4.5	NMAGIC data constraints for the galactic bulge, bar and disk . . . . .	106
4.5.1	Density and kinematics of the inner Galaxy from the ARGOS survey	106
4.5.2	Magnitude distribution of the bulge and bar . . . . .	112
4.5.3	3D density of the bulge and outer disk . . . . .	113
4.5.4	Bulge kinematics from the BRAVA survey . . . . .	114
4.5.5	Bulge proper motions from the OGLE-II survey . . . . .	114
4.6	Dynamical modelling of the bar region . . . . .	116
4.6.1	M2M formalism . . . . .	116
4.6.2	Fitting procedure and parametrization . . . . .	117
4.7	Understanding the bulge dynamics . . . . .	117
4.7.1	Signature of the pattern speed and inner dark matter halo in the bulge kinematics . . . . .	119
4.7.2	Recovering the best dark matter halo . . . . .	119
4.7.3	The missing central mass . . . . .	119
4.8	Key parameters of the Milky Way's effective potential . . . . .	121
4.8.1	Bar pattern speed and corotation . . . . .	122
4.8.2	Central mass distribution . . . . .	125
4.8.3	Best fitting dynamical model of the Galaxy . . . . .	127
4.9	Stellar and dark matter mass distribution in the Milky Way . . . . .	133
4.9.1	Bulge, bar, inner and outer disk . . . . .	133
4.9.2	The dark matter mass distribution in the Milky Way . . . . .	137
4.10	Discussion . . . . .	140
4.10.1	An intermediate bar pattern speed . . . . .	140
4.10.2	The extra central mass . . . . .	141
4.10.3	Comparison with the bulge models of P15 . . . . .	142
4.10.4	Dark matter in the Galaxy . . . . .	142
4.11	Conclusion . . . . .	143
<b>5</b>	<b>Chemodynamical Modelling of the Inner Galaxy</b>	<b>145</b>
5.1	Introduction . . . . .	146
5.2	Made-to-measure chemodynamical modelling . . . . .	149
5.2.1	The Made-to-Measure method . . . . .	149
5.2.2	Modelling the metallicity of stars . . . . .	150
5.2.3	M2M fit of the MDF . . . . .	152
5.3	Dynamical model and data constraints on the MDF . . . . .	153
5.3.1	Dynamical model of the galactic bar region . . . . .	153
5.3.2	ARGOS as a function of distance and metallicity . . . . .	154
5.3.3	APOGEE as a function of metallicity . . . . .	159
5.3.4	Fiducial and variation models . . . . .	160

---

5.4	Spatial distribution of the metallicity in the inner Galaxy . . . . .	168
5.4.1	The 3D distribution of metallicity . . . . .	168
5.4.2	Metallicity gradients in the bar region . . . . .	172
5.5	Kinematic distribution of the metallicity in the Galaxy . . . . .	174
5.5.1	Bar-like kinematics of metal-rich stars . . . . .	174
5.5.2	Kinematics of the metal-poor stars . . . . .	177
5.6	Discussion and conclusion . . . . .	180
<b>6</b>	<b>Outlook &amp; Further Work</b>	<b>185</b>
6.1	Outlook . . . . .	185
6.1.1	The galactic bulge . . . . .	185
6.1.2	The galactic bar . . . . .	189
6.1.3	The dark matter halo . . . . .	190
6.2	Further work . . . . .	191
6.2.1	Spin-off projects on the new galactic potential . . . . .	191
6.2.2	Towards a more complete model . . . . .	192
	<b>Bibliography</b>	<b>195</b>
	<b>Acknowledgements</b>	<b>211</b>

# List of Figures

1.1	The Milky Way in the visible . . . . .	2
1.2	Herschell's map of the Galaxy . . . . .	3
1.3	Artist's impression of the Galaxy based on data from the GLIMPSE survey . . . . .	5
1.4	Formation of a boxy/peanut bulge in N-body simulation from vertical buckling of a stellar bar . . . . .	8
1.5	Model of the galactic bulge and bar structure . . . . .	9
1.6	Complex structure of the galactic disk . . . . .	11
1.7	A slice through the Laniakea Supercluster . . . . .	14
2.1	Circular velocity of the N-body models . . . . .	33
2.2	Projections of the five N-body models M80-M90 . . . . .	35
2.3	Projections of the RCGs bulge density map . . . . .	40
2.4	Effect of the bulge stellar mass on the BRAVA data . . . . .	47
2.5	Kinematic $\chi^2$ as a function of the bulge mass . . . . .	48
2.6	Comparison models/data of the fitted bulge densities . . . . .	49
2.7	Comparison models/data of the bulge kinematics . . . . .	50
2.8	Projections of our best fitting models of the galactic bulge . . . . .	52
2.9	Circular velocity of our best fitting models of the galactic bulge . . . . .	53
2.10	Prediction of the proper motion dispersions in the bulge . . . . .	55
2.11	Mass of the galactic bulge . . . . .	57
2.12	Vertical density profiles in the bulge . . . . .	58
2.13	Effect of modeling assumptions on the bulge total mass . . . . .	60
2.14	Salpeter, Zoccali, Kroupa and Chabrier IMF's . . . . .	62
2.15	Stellar mass-to-light ratio of our best fitting models of the galactic bulge . . . . .	65
2.16	Mass-to-clump ratio of our best fitting models of the galactic bulge . . . . .	67
2.17	The galactic X-shape structure . . . . .	69
2.18	Non-ellipsoidal residual density in the bulge . . . . .	71
3.1	Frequency ratio distribution of bar following orbits in the bulge . . . . .	80
3.2	Side-on projections of the six orbital classes . . . . .	81
3.3	Contribution of the orbital classes to the X-shape of the bulge . . . . .	83
3.4	X-shape overdensity in the bulge . . . . .	85
3.5	Projections of the Brezel orbit . . . . .	86

4.1	Face-on and side-on projections of the initial model M85 . . . . .	93
4.2	$K_s$ -band extinction and completeness corrected magnitude distribution in a beam centered on the NICMOS field . . . . .	97
4.3	Mass density model of the Galaxy as a sum of bulge, bar and disk . . . . .	98
4.4	Rotation curve of the initial density model of the Galaxy . . . . .	100
4.5	Surface density of adiabatically adapted N-body models with different bar pattern speeds . . . . .	105
4.6	Spatial coverage of the datasets used to constrain the models . . . . .	107
4.7	The ARGOS selection function . . . . .	109
4.8	Distribution of observed distances of mock stars drawn from a particle . . . . .	111
4.9	The OGLE selection function . . . . .	115
4.10	Kinematic signature of the pattern speed and dark matter mass in the bulge . . . . .	118
4.11	Effect of the extra central mass on the bulge kinematics . . . . .	120
4.12	The Cheese Plot . . . . .	123
4.13	$\chi^2$ of the BRAVA and ARGOS data as a function of the bar pattern speed . . . . .	124
4.14	$\chi^2$ of the central kinematic data as a function of the additional central mass . . . . .	126
4.15	Comparison of the best model with the BRAVA kinematics . . . . .	127
4.16	Comparison of the best model with the OGLE proper motion dispersions . . . . .	128
4.17	Comparison of the best model with the ARGOS mean velocities as a function of distance . . . . .	130
4.18	Comparison of the best model with the APOGEE kinematics . . . . .	131
4.19	Comparison of the best model with the red clump magnitude distributions in the bar region . . . . .	132
4.20	Stellar surface density map of the best dynamical model of the inner Galaxy . . . . .	134
4.21	Stellar surface density profiles of the best dynamical model of the inner Galaxy . . . . .	135
4.22	Dark matter density profile of the best model . . . . .	138
4.23	Rotation curve of the best model . . . . .	139
5.1	Gaussian components $\alpha - \delta$ vs metallicity bins A-D . . . . .	155
5.2	Spatial coverage in galactic coordinates of the ARGOS and APOGEE fields . . . . .	156
5.3	Distribution of observed distances for mock stars with different metallicities as observed by ARGOS . . . . .	158
5.4	Fraction of each metallicity bin as a function of distance modulus for our fiducial model, compared to the ARGOS data . . . . .	162
5.5	Mean radial velocity as a function of distance modulus for the four metallicity bins, compared to the ARGOS data . . . . .	163
5.6	Radial velocity dispersion as a function of distance modulus for the four metallicity bins, compared to the ARGOS data . . . . .	164
5.7	Comparison between the fraction of stars in the four metallicity bins in the APOGEE data and in the model . . . . .	165
5.8	Comparison between the mean radial velocity of stars in the four metallicity bins in the APOGEE data and in the model . . . . .	166

---

5.9	Comparison between the radial velocity dispersion of stars in the four metallicity bins in the APOGEE data and in the model . . . . .	167
5.10	Face-on and side-on surface densities of the fiducial model in the four metallicity bins obtained after fitting the ARGOS and APOGEE metallicity data	169
5.11	Projections in galactic coordinates of the fiducial model in the four metallicity bins obtained after fitting the ARGOS and APOGEE metallicity data	170
5.12	Azimuthally averaged density of the fiducial model in the four metallicity bins obtained after fitting the ARGOS and APOGEE metallicity data . . .	171
5.13	Maps of the metallicity in the inner Galaxy . . . . .	173
5.14	Kinematic maps of components A and B . . . . .	175
5.15	Fraction of bar-supporting orbits in components A and B . . . . .	176
5.16	Kinematic maps of the components C and D . . . . .	177
5.17	Vertex deviation in Baade's window as a function of metallicity . . . . .	179
6.1	The gas flow in a low bar pattern speed model . . . . .	187
6.2	Maps of microlensing properties towards the bulge . . . . .	188
6.3	RRLyrae stars in the bulge as the inner part of the stellar halo . . . . .	189



# List of Tables

2.1	Main parameters of our five disc-bar-halo models . . . . .	34
2.2	Typical set of NMAGIC parameters . . . . .	45
2.3	Best fitting parameters and $\chi^2$ values . . . . .	51
2.4	Stellar, dark matter and total masses of our best fitting models of the bulge	60
4.1	Parameters of the Galaxy used to tailor initial conditions . . . . .	102
5.1	Parameters of the four components used to introduce the metallicity in the M2M modelling . . . . .	151





# Zusammenfassung

Galaxientstehung ist einer der derzeit aktivsten Forschungsbereiche der Astronomie. In der Milchstraße, unserer Galaxis, lassen sich im Gegensatz zu externen Galaxien die Sterne einzeln beobachten, und sie ist daher ein natürlicher Testfall für moderne Galaxienentwicklungstheorien. Daher werden zur Zeit umfangreiche Beobachtungskampagnen durchgeführt, die uns bisher ungekannte Mengen von Daten zur Analyse verfügbar machen. Jedoch ist es von der Position der Sonne in der Milchstrasse aus eine schwierige Herausforderung, die grosskalige Struktur der Galaxis abzuleiten. Die in dieser Arbeit beschriebenen dynamischen Gleichgewichtsmodelle der Galaxis sind ein grundlegender Beitrag dazu und ein wesentliches Element für die Erklärung der Entwicklungsgeschichte der Milchstraße. Hier werden mittels der flexiblen Made-to-Measure Methode selbstkonsistente Modelle für die Dynamik der Sterne und der Dunklen Materie erzeugt, die eine Vielzahl der aktuellen Datensätze erklären. Dabei wird zunächst der galaktische Bulge nachgebildet, um danach auf größeren Skalen den galaktischen Balken und die innere Scheibe zu modellieren.

Im ersten Schritt ([Kapitel 2](#)) wird eine Reihe von dynamischen Modellen des galaktischen Bulges mit verschiedenen Anteilen Dunkler Materie beschrieben. Diese Modelle werden an die dreidimensionale Sterndichte im Bulge mit ihrer Box/Peanut Gestalt, als auch an die Sternkinematik im Bereich des Bulges angepasst. Dadurch ergibt sich die bisher genaueste Bestimmung der dynamischen Masse des Bulges, zu  $(1.84 \pm 0.07) \times 10^{10} M_{\odot}$  in einem Volumen von  $(\pm 2.2 \times \pm 1.4 \times \pm 1.2)$  kpc entlang der Hauptachse des Bulges. Die Bahnstruktur der Box/Peanut Gestalt wurde mittels dieser Modelle analysiert ([Kapitel 3](#)), wobei eine neue Brezel-ähnliche Bahnfamilie entdeckt wurde, die die Dynamik der Box/Peanut Gestalt des Bulges aufrechterhält. Infolgedessen müssen Box/Peanut Bulges nicht zwingend aus sogenannten Bananen-Bahnen aufgebaut sein, wie es vorher in der Literatur beschrieben wurde.

Außerhalb der inneren 2 kpc geht der galaktische Bulge kontinuierlich in den galaktischen Balken über. Mittels zusätzlicher Daten war es möglich, die vorherigen Bulge Modelle auf den gesamten Balkenbereich zu erweitern ([Kapitel 4](#)). Hierzu wurden hauptsächlich die Red Clump Giant Verteilung aus einer Kombination der VVV, UKIDSS und 2MASS Daten, sowie die Sternkinematik in Abhängigkeit von der Entfernung aus der ARGOS Vermessung berücksichtigt. Aus der Modellierung dieser Daten im Balkenbereich liess sich eine Rotationsfrequenz des Balkens von  $(39.0 \pm 3.5) \text{ km s}^{-1} \text{ kpc}^{-1}$  ableiten. Infolgedessen wurde der Korotationsradius des Balkens zu  $(6.1 \pm 0.5) \text{ kpc}$  ermittelt, sodass der galaktische Balken als typischer schnellrotierender Balken einzustufen ist. Für die Gesamtzahl der Sterne in

der Bulge- und Balken-Struktur wird eine Masse von  $M_{\text{bar/bulge}} = 1.88 \pm 0.12 \times 10^{10} M_{\odot}$  errechnet, deutlich mehr als die Masse der Sterne in der inneren Scheibe,  $M_{\text{inner disk}} = 1.29 \pm 0.12 \times 10^{10} M_{\odot}$ . Durch die ausgedehnteren Daten sowie durch neue Messungen der IMF im Bulge war es möglich, den Anteil der Dunklen Materie im Bulge zu  $17\% \pm 2\%$  zu bestimmen, sowie ein Dichteprofil für die Dunkle Materie abzuleiten, das im Bereich der Sonnenbahn steil ansteigt, aber dann im Bulge in einen flacheren Anstieg übergeht. Schliesslich gelang der dynamische Nachweis einer zusätzlichen zentralen Masse von  $\sim 2 \times 10^9 M_{\odot}$ , die wahrscheinlich zu einer nuklearen Scheibe oder einem scheibenartigen Pseudobulge gehört.

Mit diesem dynamischen Modell stehen sowohl das Gravitationspotential wie auch die Verteilung der Teilchenbahnen zur Verfügung, die als Grundlage für weitergehende Modelle der Galaxis benutzt werden können. Spektroskopische Messungen wie mit APOGEE oder GALAH werden in naher Zukunft Häufigkeiten chemischer Elemente von  $\geq 10^5$  Sternen liefern, mit denen die Entstehungsgeschichte der Galaxis besser verstanden werden kann. Chemodynamische Modelle, d.h. mit chemischen Parametern erweiterte dynamische Modelle, sind entscheidend für die Analyse solcher Daten. Hierzu wurde die Made-to-Measure Methode erweitert, und die ersten Made-to-Measure chemodynamischen Modelle der inneren Galaxis entwickelt ([Kapitel 5](#)). Die neue Methode wurde auf der Basis des dynamischen Modells aus [Kapitel 4](#) angewendet, um die räumlichen und kinematischen Variationen der Metallizität der ARGOS und APOGEE Sterne erfolgreich nachzubilden. Die resultierende Phasenraum-Verteilung verschiedener Metallizitäts-Komponenten in der inneren Galaxis wurden analysiert, und deren Variationen durch ihre Bahnstrukturen erklärt. Dadurch wurde gezeigt, dass chemodynamische Modelle der balkenförmigen inneren Galaxis mittels der Made-to-Measure Methode erstellt werden können. Diese Modelle beschreiben den aktuellen Stand der Galaxis und stellen eine wertvolle Ressource dar, um Galaxienbildungssimulationen zu bewerten.

# Abstract

Understanding galaxy evolution is one of the most active research fields in astronomy today. The Milky Way, our home galaxy can be observed on a star-by-star basis, something impossible in other galaxies and is therefore a natural benchmark for testing in detail galaxy formation theories. Therefore, many recent and ongoing large scale surveys have been carried out, providing an unprecedented collection of data to analyze. It is however challenging from the Sun's perspective to infer the current state of the Galaxy. In the work presented here dynamical equilibrium models of the Galaxy in its current state are built, a key element for later inferring its formation history. The dynamics of stars and dark matter are modeled in a self-consistent way, reproducing as many datasets as possible using the flexible Made-to-Measure method. An inside-out approach is adopted, starting by focusing on the galactic bulge before moving out to the larger scales, the galactic bar and the nearby disk.

First a set of dynamical models of the galactic bulge with different dark matter fractions is made (Chapter 2). Those models are fitted to reproduce both the 3D density of bulge stars, with their boxy/peanut shape, and the radial stellar kinematics in bulge fields measured by the BRAVA spectroscopic survey. Results from the modelling of different stellar and dark matter masses in the bulge lead to the most accurate measurement of the total dynamical mass of the galactic bulge up to date, of  $(1.84 \pm 0.07) \times 10^{10} M_{\odot}$  in a volume of  $(\pm 2.2 \times \pm 1.4 \times \pm 1.2)$  kpc oriented along the bulge's principal axis. The orbital structure of the boxy/peanut shape in these dynamical models is then analyzed (Chapter 3). The boxy/peanut shape is found to be supported by novel brezel-like orbits, from which a strong peanut shape with a relatively short extension can be built, thus showing that boxy/peanut bulges are not necessarily supported by the so-called banana orbits as had been previously claimed in the literature.

Outside the central 2 kpc, the galactic bulge smoothly segues into the long bar. Taking advantage of recent new data, the modelling was extended to the entire long bar region (Chapter 4). Additional data were added to the previous bulge models, mainly the distribution of Red Clump Giants in the bar region from a combination of the VVV, UKIDSS and 2MASS photometric surveys together with stellar kinematics as a function of distance along the line of sight from the ARGOS survey. By modelling the dynamics of the bar region, the pattern speed of the galactic bulge and bar is found to be  $(39.0 \pm 3.5) \text{ km s}^{-1} \text{ kpc}^{-1}$ . This places the bar corotation radius at  $(6.1 \pm 0.5)$  kpc, making the Milky Way bar a typical fast rotator. The stellar mass of the long bar and bulge structure is evaluated

to  $M_{\text{bar/bulge}} = 1.88 \pm 0.12 \times 10^{10} M_{\odot}$ , larger than the mass of disk in the bar region,  $M_{\text{inner disk}} = 1.29 \pm 0.12 \times 10^{10} M_{\odot}$ . Thanks to more extended kinematic datasets and recent measurement of the bulge IMF, the dark matter is found to account for  $17\% \pm 2\%$  of the mass in the bulge, with a density profile that flattens from the solar neighborhood to a shallow cusp or core in the bulge region. Finally, dynamical evidence for an extra central mass of  $\sim 2 \times 10^9 M_{\odot}$  is found, probably in a nuclear disk or disky pseudobulge.

This dynamical model of the bar region provides both the gravitational potential and a consistent library of N-body orbits that can be used as a basis for more advanced modelling of the Galaxy. Recent and future spectroscopic surveys such as APOGEE or GALAH will provide hundreds of thousands of stellar abundances of elements that can allow tracing back the formation history of the Galaxy. Chemodynamical models, a natural extension of the dynamical models to also include chemical information, will be vital to understand these new data. To this end, the Made-to-Measure method was extended to include the metallicity distribution of stars, hence constructing the first Made-to-Measure chemodynamical model (Chapter 5). This method was applied to the ARGOS and APOGEE data to successfully fit with the dynamical model of the galactic bar the spatial and kinematic variations of the metallicity in the inner Galaxy. The resulting phase-space distribution of the different metallicity components in the inner Galaxy is then analyzed. The variations as a function of metallicity observed in the data are described and explained in term of differences in spatial, kinematic and orbital structure. This demonstrates that chemodynamical models of the barred inner Milky Way can be constructed using the Made-to-Measure method. Such models describe the present chemodynamical state of the Galaxy and will in the future be a valuable resource in confronting galactic evolution simulations.

# Chapter 1

## Introduction

In this introduction I first describe the Milky Way from its appearance to the naked eye on the sky to the nature of its different substructures: the Galactic Centre, bulge, bar, disk(s) and halos. I then discuss why understanding the structure and formation history of the Galaxy is a very active scientific field at the moment. I describe the challenges to overcome and the data available to push forward our knowledge of the Milky Way. Next I describe the different techniques used for modelling Galaxies and particularly the Made-to-Measure method, extensively used in this work. I finally describe the outline of this manuscript and state the main results presented in the following chapters.

### 1.1 The Milky Way Galaxy

#### 1.1.1 A little bit of history

Named by the Romans from its appearance as a glowing band on the sky, the Milky Way has been the subject of wonder throughout history. Already back in the fifth century BC, ancient Greek philosophers such as Anaxagoras or Democritus suggested that the Milky Way could be composed of a multitude of distant stars, unresolved by the naked eye. Since the telescope technology was not available at that time this idea remains unproved for more than two millennia. The technical breakthrough in glass manufacturing in the 13th century and the widespread use of glass lenses for spectacles in Europe lead to the creation of new optical designs, including the first optical hand-held telescope device, credited to Hans Lippershey and Jacob Metius. It is finally in the 17th century after further refinement of its telescope that Galileo Galilei obtained the first clear proof that the Milky Way Galaxy is “nothing else but a mass of innumerable stars planted together in clusters” ([Galilei 1610](#)).

Thanks to modern technology, we now have many high resolution images of the Milky Way. Perhaps one of the most beautiful images of our home Galaxy is the composite optical image shown in [Figure 1.1](#) [Credit: ESO/S. Brunier]. It shows the galactic disk as a glowing horizontal band, the galactic bulge as the central prominent feature and the Small and Large Magellanic Clouds, irregular dwarf galaxies orbiting the Milky Way. Dark



Figure 1.1: The Milky Way as seen in the visible wavelength range. This image is a composition of 1200 photographs taken by a regular commercial camera from the Atacama desert in Chile for the southern part and the Canary Island for the northern part. The north galactic pole and galactic east are respectively oriented up and left. Credit: ESO/S. Brunier

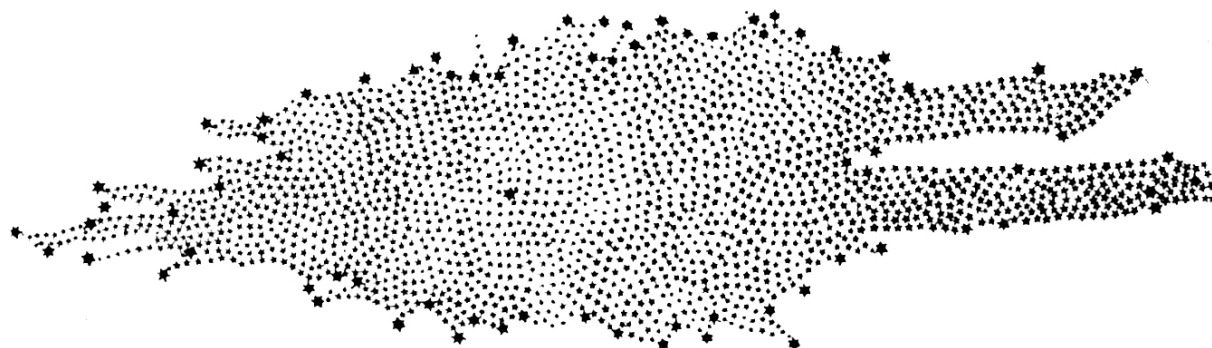


Figure 1.2: Cross-section of the Milky Way as determined by the “star-gages” method of [Herschel \(1785\)](#). The Sun is found to be located close to the center, as indicated by the larger star symbol there.

patches are produced by extinction of the optical light due to the presence of interstellar dust along the line of sight. Since the Sun is located inside it, the Milky Way is the largest object on the sky and is therefore never fully visible from any location on Earth.

The first attempt to map the Milky Way is attributed to William Herschel and his “star-gages” method ([Herschel 1785](#)). Even if the resulting map turned out to be wrong, the method is in itself very interesting. Herschel used his 20-foot telescope and counted stars in about seven hundred sky patches around a great circle of the celestial sphere. Assuming that (i) all stars are distributed uniformly within the Milky Way, (ii) no star is found beyond the boundaries of the Milky Way and (iii) all stars can be resolved by his telescope, the number of stars in a patch of the sky is related to the distance to the boundary of the Milky Way along the corresponding line of sight. The map of the cross-section of the Milky Way as traced by Herschel is reproduced in [Figure 1.2](#) where the Sun is found close to the center. We know now that Herschel’s map is incorrect, due to the violation of the three underlying assumptions. Stars are not uniformly distributed in the Galaxy and can have a very broad distribution of intrinsic luminosities. The interstellar dust greatly extinguishes the light in the visible optical range and hides most of the stars located in the plane. All these factors combined make the conversion of the number count of stars in some field to the stellar density a difficult exercise that is still challenging today.

Interestingly, until the early 1920s it was still not clear whether or not the Milky Way constituted the entire universe. The controversy culminated with the “Great Debate” between Harlow Shapley, defender of the idea that the Milky Way encompasses the entire Universe and Heber Curtis who instead believed that “nebulas” were nothing else as separate “Island Universes” ([Shapley & Curtis 1921](#)), equivalent of what we now call galaxies. The question was finally settled when Edwin Hubble showed that the Andromeda nebula was too distant to belong to the Milky Way ([Hubble 1929](#)).

In the last hundred years, since that time, our knowledge of our home galaxy and its environment has drastically increased and the place of Mankind in the Universe dramati-

cally decreased. The Milky Way is now known to be a fairly regular barred spiral galaxy with loosely wound spiral arms and a central bulge, entering the type SBb-SBc in the Hubble classification. The Sun is one of the hundred billion stars of the Milky Way, itself one of the estimated 170 billion galaxies populating the observable Universe (Gott III et al. 2005). A more recent artist’s impression of the Galaxy as seen from the north galactic pole is reproduced in Figure 1.3. This image is based on data from the GLIMPSE survey but does not perfectly represent the state of our knowledge about the Galaxy. For example, the presence of two distinct bars structure, as depicted in the figure under the denomination of galactic bar and long bar, has been recently disproved (Wegg, Gerhard & Portail 2015). Starting from the very center, let us take an inside-out journey through the Milky Way.

### 1.1.2 The central Milky Way

Locating the center of the Galaxy is made difficult by the large extinction in the galactic plane. Oort & Rougöor (1960) found by combining large scale optical data and radio observations that the radio source SgrA was a good candidate for being the center of the Galaxy. This led the International Astronomical Union to locate the origin of the galactic coordinate system on SgrA. It was shown only later than SgrA is in fact a composite radio source, whose main emission comes from the compact source SgrA\*, slightly offset from the adopted Galactic Centre. SgrA\* is now believed to be associated to a central Super Massive Black Hole (SMBH). Convincing evidence that the Galactic Centre hosts a central SMBH has been obtained by following the motions of stars towards the center over a long time. Monitoring 28 stars located in the innermost arcsecond (called S-stars) with precise astrometry during 16 years, Gillessen et al. (2009) found that their orbits were consistent with the presence of a single point-mass gravitational potential, corresponding to a central object with a mass of  $M_{\bullet} = 4.31 \pm 0.06_{|stat} 0.36_{|RO} \times 10^6 M_{\odot}$ , too dense to allow any other astronomical object than a SMBH. The presence of SMBHs in the center of galaxies is not unusual. Gebhardt et al. (2003) made orbit superposition models for 12 galaxies and found in every case the presence of a SMBH of mass between  $10^6 M_{\odot}$  and a few  $10^9 M_{\odot}$ .

The galactic SMBH is embedded in a more extended near-infrared source called the Nuclear Star Cluster (NSC, Becklin & Neugebauer 1968). Nuclear star clusters are central clusters of stars, bigger than globular clusters with about  $10^6 - 10^7$  stars and effective radii of only about 5 pc (Walcher et al. 2005). They are common in external disk galaxies (Carollo et al. 1997) and are found to obey scaling relations with the mass of the host galaxy and central SMBH. In the Milky Way, the NSC is mostly made of old giant stars forming a flattened axisymmetric structure around SgrA\* that can be observed on a star-by-star basis thanks to its relatively close distance. Fritz et al. (2016) measured proper motions of 10000 stars in the NSC that were used as input data for dynamical modelling of the NSC by Chatzopoulos et al. (2015). When combined with the orbits of S-stars, the dynamical modelling of the NSC provides a very precise determination of the mass of the central SMBH  $M_{\bullet} = 4.23 \pm 0.14 \times 10^6 M_{\odot}$  and the distance to the Galactic Centre  $R_0 = 8.33 \pm 0.11$  kpc.

Infrared data from the Infrared Astronomical Satellite (IRAS) and the Cosmic Back-



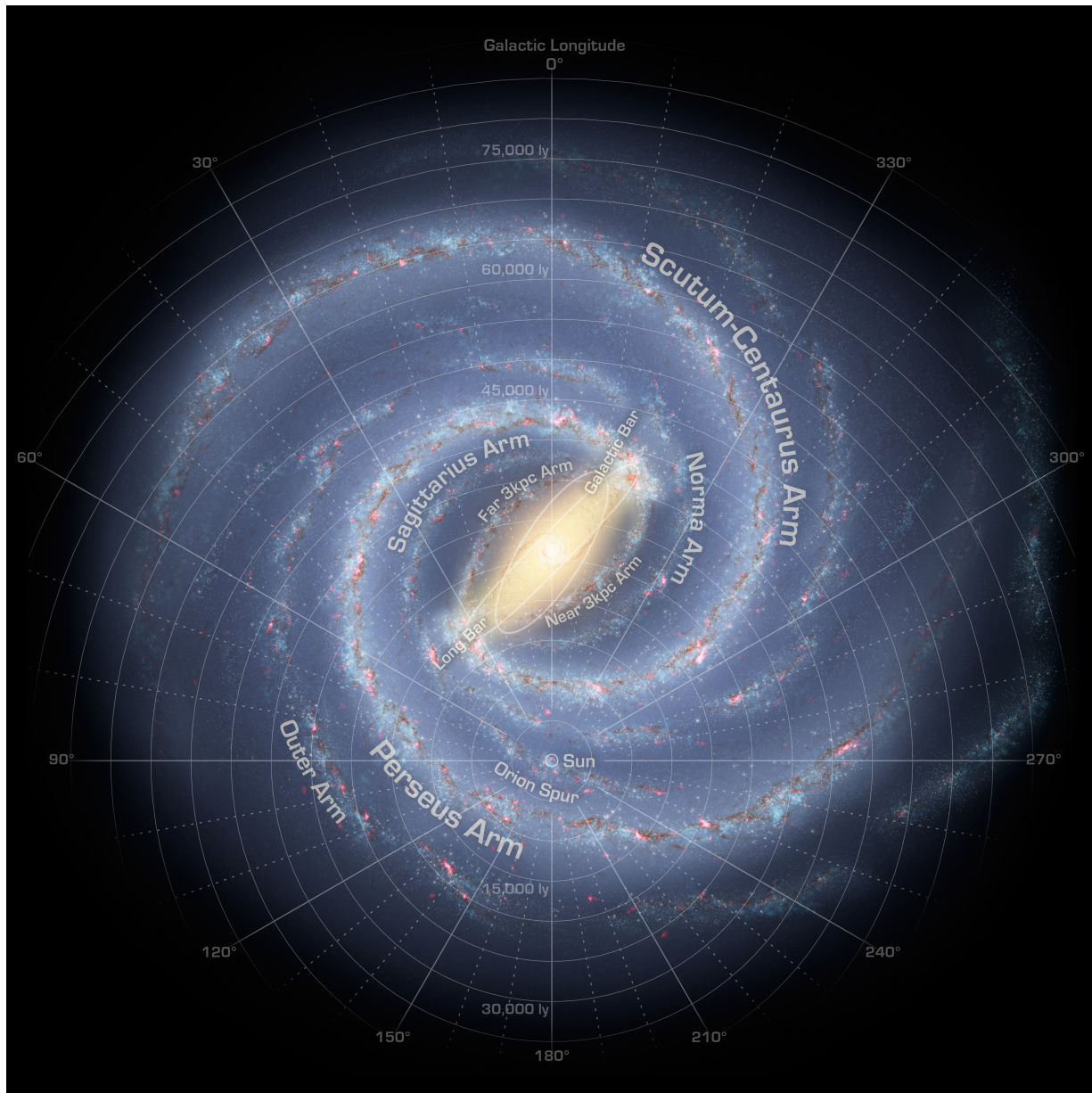


Figure 1.3: Artist's impression of the Galaxy based on data from the GLIMPSE survey. Although well spread this image contains features that are not clearly established, like the central double bar system. Credit: Spitzer Science Center/R. Hurt

ground Explorer (COBE) revealed that the NSC itself is embedded in a larger structure called the Nuclear Stellar Disk (NSD) (Launhardt, Zylka & Mezger 2002). The NSD extends to about 230 pc from the center and is very thin with a vertical exponential scale height of only 45 pc (Nishiyama et al. 2013). SMBH, NSC and NSD form altogether the central component of the Galaxy called the Nuclear Bulge (NB). There is however no consensus yet about the exact mass and shape of the NB. Converting light into mass, Launhardt, Zylka & Mezger (2002) attribute a total stellar mass of  $1.4 \pm 0.6 \times 10^9 M_{\odot}$  to the NB. Independently, Schönrich, Aumer & Sale (2015) found in the APOGEE data (Allende Prieto et al. 2008) the kinematic evidence of a central nuclear disk structure extending to  $\sim 150$  pc with a vertical scale height of 50 pc. They measure a rotation velocity of  $120 \text{ km s}^{-1}$  at 150 pc, in possible tension with the mass of the nuclear bulge from Launhardt, Zylka & Mezger (2002). In addition, Debattista et al. (2015) postulated the presence of a kilo-parsec-scale nuclear central disk in order to explain the high velocity peaks in the line of sight velocity distributions of the APOGEE commissioning data (Nidever et al. 2012). The structure of the central Milky Way is discussed further in Chapter 4 where we find dynamical evidence for a central over-density probably associated to the NB.

### 1.1.3 The galactic bulge and bar

The bulge refers to the central kilo-parsec-scale and vertically extended over-density of the Galaxy. It is very clear to the naked eye from the southern hemisphere even though it is mostly covered by large dust clouds. Central bulges are very common in external galaxies and exist in two flavors: (i) the classical bulges, remnants from mergers during the hierarchical formation of the galaxy, and (ii) the pseudo-bulges, resulting from secular evolution of disk stars (Kormendy & Kennicutt 2004). The galactic bulge has long been thought of as a classical bulge, as supported by its old age (Ortolani et al. 1995) and the presence of a vertical metallicity gradient that was thought at the time to rule out other formation scenarios (Friedli, Benz & Kennicutt 1994).

However, in the last two decades it became clear that a large part of the galactic bulge is in fact a pseudo-bulge that originated from the disk through secular evolution processes. Evidences arose from the detection of non-axisymmetries, found consistently in the HI and CO gas flow (Peters, III 1975; Binney et al. 1991; Englmaier & Gerhard 1999; Fux 1999), in the NIR light distribution (Blitz & Spergel 1991; Weiland et al. 1994; Binney, Gerhard & Spergel 1997) and star counts (Nakada et al. 1991; Stanek et al. 1997; López-Corredoira, Cabrera-Lavers & Gerhard 2005). The bulge was then interpreted as a triaxial and rather short boxy bar structure (Binney et al. 1991; Dwek et al. 1995) extending to 2 – 3 kpc from the center. It is only recently that the picture of the galactic bulge changed with the discovery of the so-called split red clump, independently by Nataf et al. (2010) and McWilliam & Zoccali (2010). By analyzing the density distribution of stars close to the minor axis of the bulge and at latitude around  $-5^{\circ}$  they found that the density distribution in the bulge had a clear double bump feature, with two over densities located in front and behind the Galactic Centre. Such double bump features in the density were already predicted by N-body simulations of cold stellar disks embedded in live dark matter halos

(Combes & Sanders 1981; Raha et al. 1991; Debattista & Sellwood 2000; Athanassoula 2003; Martinez-Valpuesta & Shlosman 2004). In these simulations, the stellar disk that is initially unstable to the disk instability first form a flat rotating bar structure, which then evolves by transferring angular momentum to the dark matter halo. During this evolution the bar grows in length and slows down while remaining vertically thin. The bar can then become vertically unstable and go through the buckling instability, where it extends vertically and form a boxy/peanut (B/P) structure in its inner part, as illustrated in detail in Figure 1.4. B/P bulges are common in external galaxies, as shown by Lütticke, Dettmar & Pohlen (2000) who find that they represent 45% of all bulges in disk galaxies. This high fraction of B/P bulges is not dissimilar to the fraction of bars in disk galaxies, providing an additional piece of evidence that B/P bulges can be explained by a formation scenario based on bars.

Although a B/P bulge was a natural explication for the split red clump in the Galaxy, it was not clear whether or not the N-body simulations provided the complete picture. Simulations predict that the buckling instability thickens only the inner part of the bar, meaning that the outer part of the bar, called flat bar or long bar should also be observed outside the bulge. A long bar component had indeed been observed in the Milky Way by Hammersley et al. (1994) but first studies had found a misalignment between the bulge and the long bar, leading to the hypothesis of a double bar system in the inner Galaxy, shown in the artist's impression of Figure 1.3 (Hammersley et al. 1994; Benjamin et al. 2005; López-Corredoira, Cabrera-Lavers & Gerhard 2005; Cabrera-Lavers et al. 2007; Cabrera-Lavers et al. 2008; but see also Martinez-Valpuesta & Gerhard 2011). It is only last year that Wegg, Gerhard & Portail (2015) showed by combining the VVV, UKIDSS, GLIMPSE and 2MASS catalogs that the galactic bulge smoothly transitions into the long bar, both appearing at a consistent angle. The galactic bulge and the long bar are now believed to form a single bar structure that became vertically thick in its inner part, similarly to the buckled bars of N-body models. Wegg, Gerhard & Portail (2015) found in addition an extra super-thin bar component, confined in the plane with an exponential scale height of only 45 pc.

Figure 1.5 gives an overview of the current picture of the galactic bulge and bar structure. The non-axisymmetry seen in the galactic coordinate projection (top left) originates from the projection on the sky of the bar structure oriented at an angle  $\alpha = 28 - 33^\circ$  with the line of sight towards the Galactic Centre (Wegg, Gerhard & Portail 2015). Seen from the side (bottom left), the inner part of the bar is vertically extended and forms the B/P bulge. Vertical cuts through the galactic projection show a steep increase of the number of stars towards the plane for longitudes between  $15^\circ$  and  $30^\circ$ , indicating the presence of an extra super-thin bar component. The bar is found to extend to  $5 \pm 0.2$  kpc from the Galactic Centre, about a factor of two longer than believed 20 years ago.

#### 1.1.4 The galactic disk(s)

Outside the central 5 kpc bar region, the main galactic component is the galactic disk. By deriving photometric parallaxes of about 12500 stars towards the north galactic pole

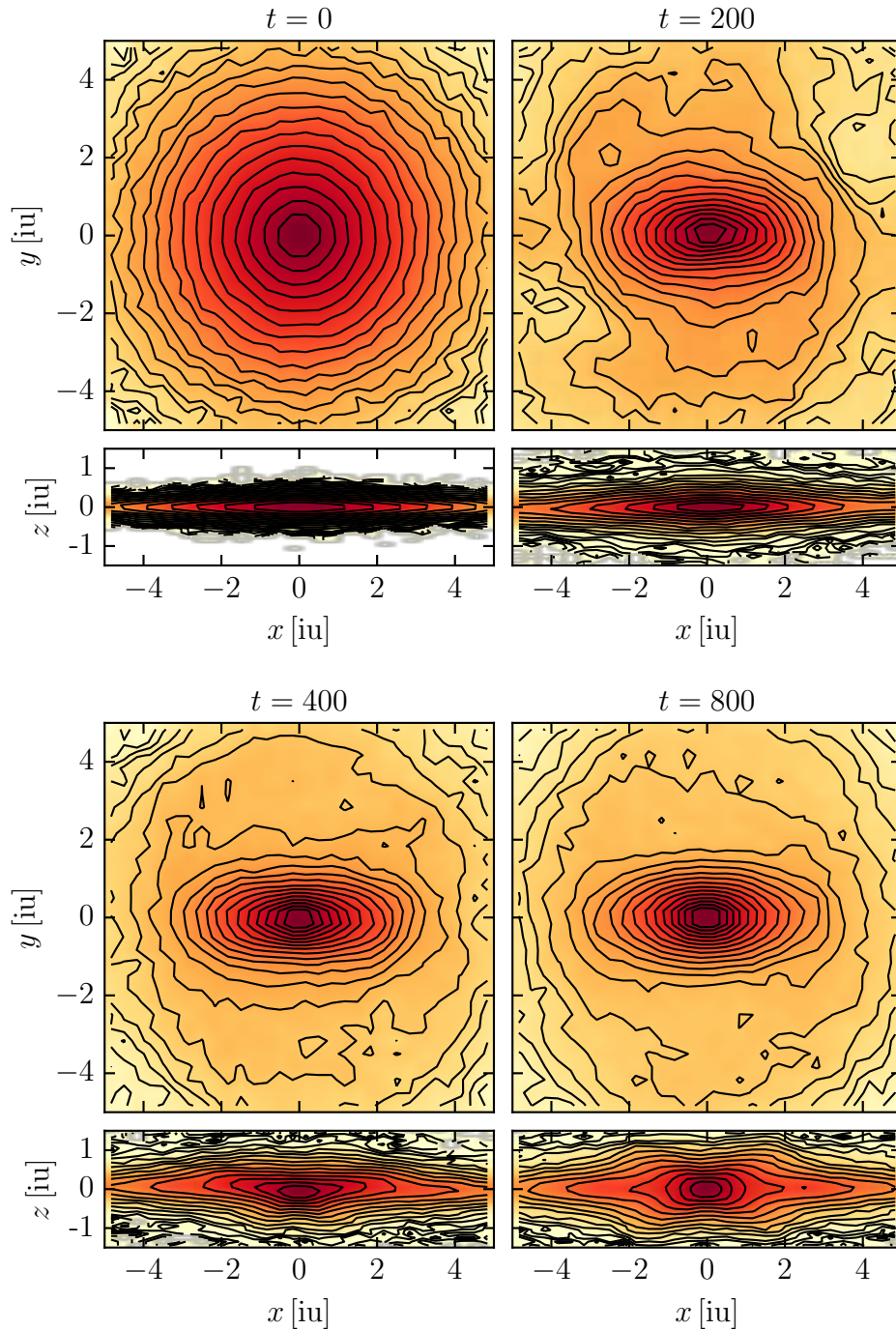


Figure 1.4: Formation of a boxy/peanut bulge in N-body simulation from vertical buckling of a stellar bar. From left to right, an initial axisymmetric stellar disk ( $t = 0$ ) rapidly forms a flat stellar bar ( $t = 200$ ) that undergoes the buckling instability at  $t = 400$ , creating first a vertical asymmetry as shown in the side-on view. At the end of the buckling phase the bar is fully grown and hosts a central boxy/peanut bulge ( $t = 800$ ). Units in this figure are internal model units (iu).

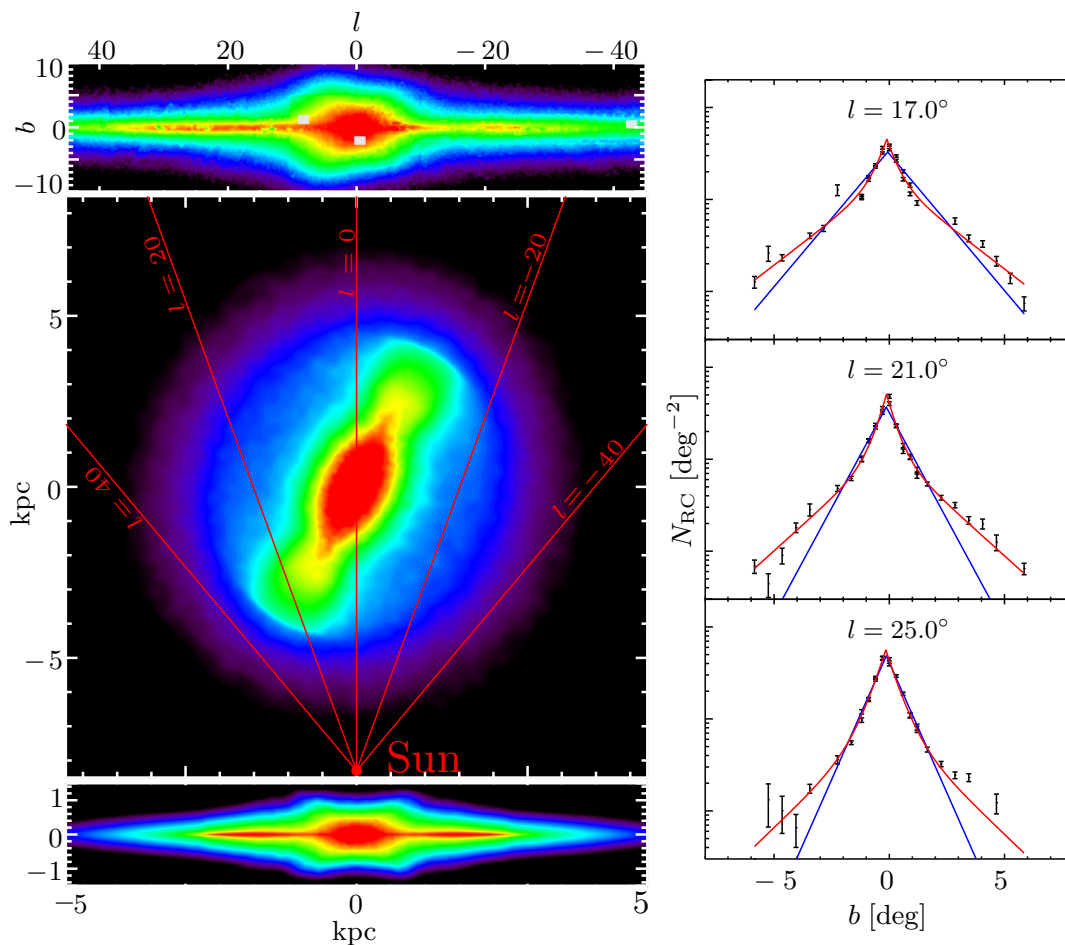


Figure 1.5: Model of the galactic bulge and bar structure as traced by Red Clump Giants, taken from Bland-Hawthorn & Gerhard (2016) as an adaptation of the original work from Wegg, Gerhard & Portail (2015). The left column shows from top to bottom the projection of the model in galactic coordinates (longitude  $l$  and latitude  $b$  coordinates, centered on the line of sight towards the Galactic Centre), followed by the face-on and side-on projections. The right column shows vertical cuts through the projection in galactic coordinates, indicating clearly the super-thin bar component inside one degree from the plane.

Gilmore & Reid (1983) found that the vertical structure of the disk follows a double exponential profile, with a main exponential thin component of scale height  $\sim 300$  pc and an second exponential thicker component of scale height  $\sim 1450$  pc. These two components are now widely accepted as being two separate disks, called the thin and thick disks, as indicated by their distinct chemistry (Bensby 2014) and radial structure (Jurić et al. 2008).

A lot of progress has been made in the last 15 years thanks to large wide-field multiband photometric surveys like the 2MASS (Two Micron All Sky Survey, Majewski et al. 2003) or SDSS (Sloan Digital Sky Survey, York et al. 2000) projects. Jurić et al. (2008) used the multi-band photometry from the SDSS catalogue to compute photometric distances of about 48 million stars located in a cone oriented orthogonally to the galactic plane. They found that the data in the solar neighborhood is well fit by two exponential disks, with a thin disk scale height and scale length of respectively 300 pc and 2.6 kpc, and a thick disk scale height and scale length of respectively 900 pc and 3.6 kpc. At the Sun's location, they also found that the thick disk surface density accounts for 12% of the thin disk surface density, a fraction that decreases inwards due to the larger thick disk scale length.

However, the large variety of tracer populations that can be analyzed leads to a wide range of disk parameters. Bland-Hawthorn & Gerhard (2016) analyzed 130 refereed papers on disk parameters and conclude that the thin disk scale length and scale height are respectively  $2.6 \pm 0.5$  kpc and  $300 \pm 50$  pc. Note that the uncertainty of 0.5 kpc on the thin disk scale length results in a factor of about 2 uncertainty in central surface density when extrapolating the disk inwards to the Galactic Centre. Short disk scale lengths are supported by stellar dynamics (Bovy & Rix 2013) and microlensing data (Wegg, Gerhard & Portail 2016). The structure of the thick disk is even more uncertain. From their literature analysis Bland-Hawthorn & Gerhard (2016) concluded for the thick disk a scale height of  $900 \pm 180$  pc, a local surface density fraction of  $15\% \pm 6\%$  and a scale length ranging from 1.8 to 4.9 kpc.

The scatter of the disk parameters in the literature can be explained in different ways including the presence of substructures (Jurić et al. 2008) or the complex chemistry of the disk. Bovy et al. (2016b) analyzed the structure of Red Clump stars from the APOGEE survey as a function of their  $\alpha$ -enhancement and metallicity. For  $\alpha$ -enhanced stars, they find that their spatial distribution is well reproduced by a single exponential disk with a single scale length of  $2.2 \pm 0.2$  kpc, and so for all metallicities. However low  $\alpha$ -enhanced stars are found to have a more complex structure, where the surface density as a function of radius does not decrease exponentially from the Galactic Centre but instead peaks at some radius depending on the metallicity. This is illustrated in Figure 1.6 by a figure taken from Bovy et al. (2016b). The galactic disk is seen in this work as the sum of torus densities whose radii depend on the stellar population.

Our knowledge of the galactic disks is likely to be greatly improved by upcoming surveys and particularly with the first data release of the *Gaia* mission that will provide accurate distances and photometry for hundreds of millions of stars (see Section 1.2.3).

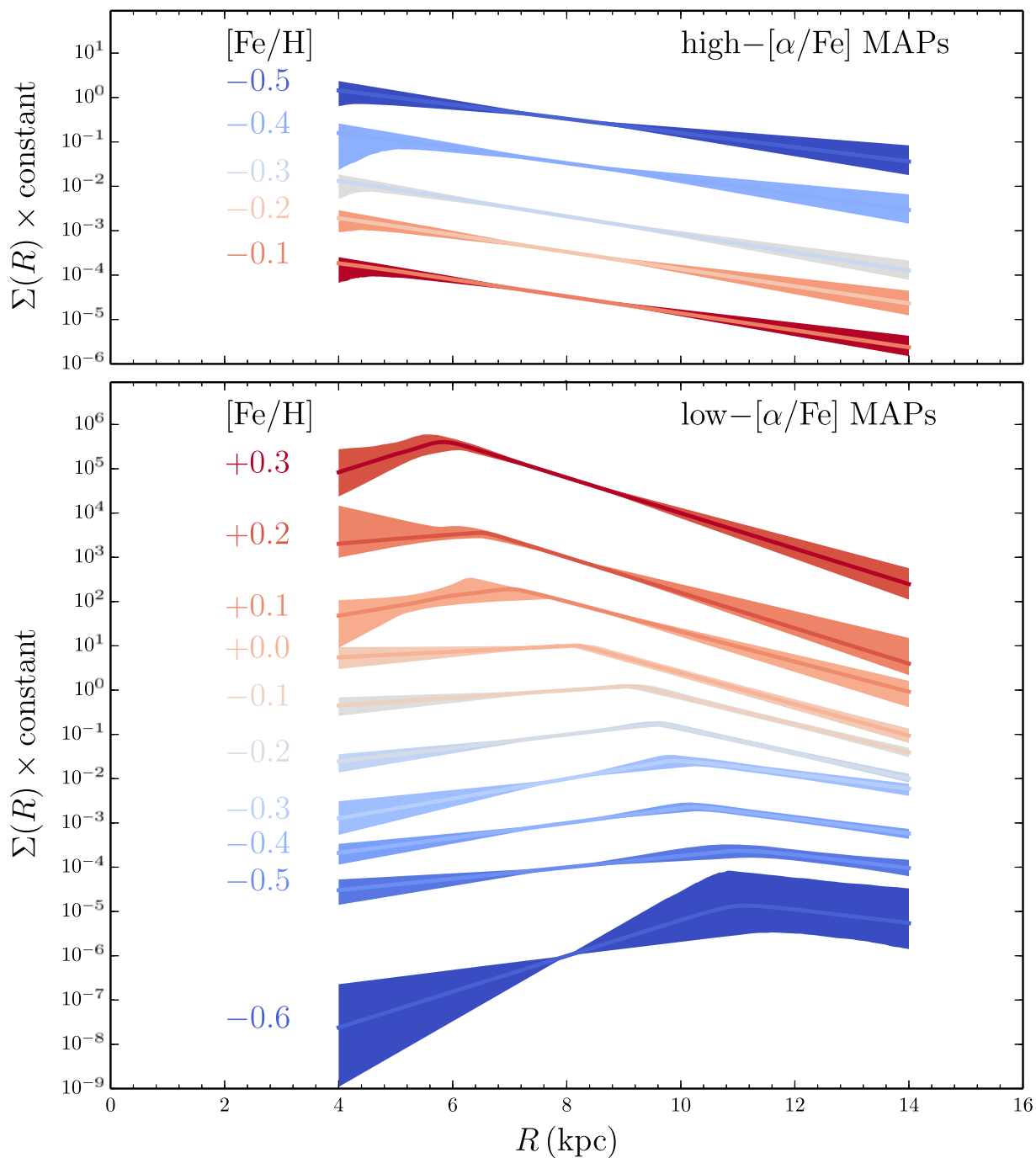


Figure 1.6: The complex structure of the galactic disk, taken from [Bovy et al. \(2016b\)](#) with permission. Although high  $[\alpha/\text{Fe}]$  populations have a consistent exponential surface density profile for different metallicities (upper panel), the low  $[\alpha/\text{Fe}]$  shows a more complex structure (lower panel) depending on metallicity. The galactic disk is then seen as the sum of donut-like densities depending on the traced stellar population.

### 1.1.5 The galactic stellar and dark matter halos

Beyond the galactic disks extend the galactic stellar halo. Stars in the halo are very distinct from stars in the disk: they are more metal-poor, have large random motions, hardly any rotation and are spheroidally distributed. Early work by [Eggen, Lynden-Bell & Sandage \(1962\)](#) proposed that first stars in the halo formed from infalling gas of at the time when the galaxy first collapsed. This view was challenged later by [Searle & Zinn \(1978\)](#) who proposed instead that the halo formed by the infall of independent small fragments, thus explaining the wide range of metal abundances observed at all radii. The discovery of unrelaxed substructures in the halo indicated a subsequent hierarchical formation where the halo grows by accretion of stars tidally disrupted from infalling dwarf galaxies ([Ibata et al. 1997](#); [Schlaufman et al. 2009](#)). This is consistent with cosmological simulations that predict an accretion of about 100 small galaxies for the build-up of the halo ([Bullock & Johnston 2004](#)). Some of those accreted dwarf galaxies are still observable today because of the long relaxation timescale of the order of a Gyr as discussed in the next section.

The stellar halo hosts numerous substructures, consequence of its accretion history, but it is not clear yet how important those substructures are. Using near-main sequence turnoff stars from SDSS data, [Bell et al. \(2008\)](#) find that about 40% of the stellar halo mass is located in substructures while [Deason, Belokurov & Evans \(2011\)](#) find by analyzing horizontal branch stars also from SDSS data that only 5% to 20% of the halo mass is in substructures. Averaging over large scales, [Deason, Belokurov & Evans \(2011\)](#) define the *smooth halo* whose density profile is well described by a double power law or alternatively an Einasto density profile. The break in the halo happens at  $25 \pm 10$  kpc from the center, with an inner and outer slope of  $-2.5 \pm 0.3$  and  $-4.3 \pm 0.6$  kpc ([Bland-Hawthorn & Gerhard 2016](#)). The stellar halo is believed to contain about 1% of the stellar mass in the Galaxy and has therefore a negligible effect on the galactic potential. However since its inner density profile is very steep, it could account for a significant fraction of the metal-poor stars in the bulge ([Pérez-Villegas, Portail & Gerhard 2016](#)).

All the galactic components described previously are by far not sufficient to explain the stellar and gas kinematics in the Galaxy. Hence under Newtonian gravity the Galaxy must be surrounded by a massive dark matter halo, not-directly observed. Locally, the dark matter density can be computed from a measurement of the total surface mass density as provided by dynamical modelling of the vertical kinematics of stars in the solar neighborhood. Alternatively, on larger scales the dark matter distribution can be derived from measurements of the rotation curve of the Milky Way. In both cases the dark matter density is obtained by removing a baryonic component from a dynamical mass measurement, and therefore relies on our knowledge of the distribution of baryons in the Galaxy. A compilation of recent results on the local dark matter density is available in [Read \(2014\)](#). The dark matter contribution to the galactic gravitational potential increases outwards and provides about half the radial acceleration at the Solar radius (see [Chapter 4](#)). Hence the dark matter is sub-dominant in the inner part of the Galaxy. In [Chapter 2](#) and [Chapter 4](#) of this thesis we study in detail the bulge and bar region of the Milky Way and aim at recovering the dark matter mass enclosed in the inner part of the Galaxy.



### 1.1.6 The environment of the Milky Way

The Milky Way is not isolated but instead is surrounded by about 50 satellite dwarf galaxies orbiting in the halo. The two main satellites of the Galaxy are the Small and Large Magellanic Clouds, visible to the naked eye from the southern hemisphere and shown in [Figure 1.1](#) south-west from the bulge. Worth noting is also the Sagittarius dwarf elliptical galaxy, which orbits the Milky Way on a polar orbit. During repeated passages in the deep galactic potential, stars have been tidally stripped from the Sagittarius dwarf galaxy and now form the Sagittarius stream which wraps around the Galaxy ([Lynden-Bell & Lynden-Bell 1995](#); [Newberg et al. 2002](#); [Majewski et al. 2003](#)).

Further away resides the Andromeda system, consisting of many dwarf galaxies orbiting the closest large external galaxy: the Andromeda Galaxy (M31). Andromeda is located at about 780 kpc away from the Sun and forms with the Milky Way a double galaxy system. It is blueshifted so has a significant velocity component towards the Milky Way. Its proper motion has also been measured from HST photometry by [Sohn, Anderson & van der Marel \(2012\)](#) over a baseline of  $\sim 7$  years. [van der Marel et al. \(2012b\)](#) found that all data are consistent with a future head-on collision between the Milky Way and Andromeda, ultimately leading to the merging of the two galaxies in about  $5.7^{+1.6}_{-0.7}$  Gyr from now ([van der Marel et al. 2012a](#)). The Milky Way and Andromeda are the two major galaxies of the so-called Local Group, containing all objects within about 1 Mpc.

The Local Group is itself a member of the next large structure called the Virgo Supercluster, which also hosts other groups and clusters of galaxies like the Virgo Cluster. Using data from the Cosmicflows-2 spectroscopic survey and after removing the Hubble flow, [Tully et al. \(2014\)](#) obtained distances and peculiar velocities of more than 8000 objects extending on larger scales than the Virgo Supercluster. They find in their data the locations of points where the peculiar velocity field of galaxies diverges. The three-dimensional surface tracing these divergence points indicates the boundary of a volume inside which galaxies are attracted towards a common basin. This volume shown in [Figure 1.7](#) is called the Laniakea Supercluster (“immeasurable heaven” in Hawaiian language), with a diameter of about 160 Mpc. Notable additional members of the Laniakea Supercluster are the Hydra cluster, the Norma clusters and the Great Attractor, gravitational focal point within the Laniakea Supercluster.

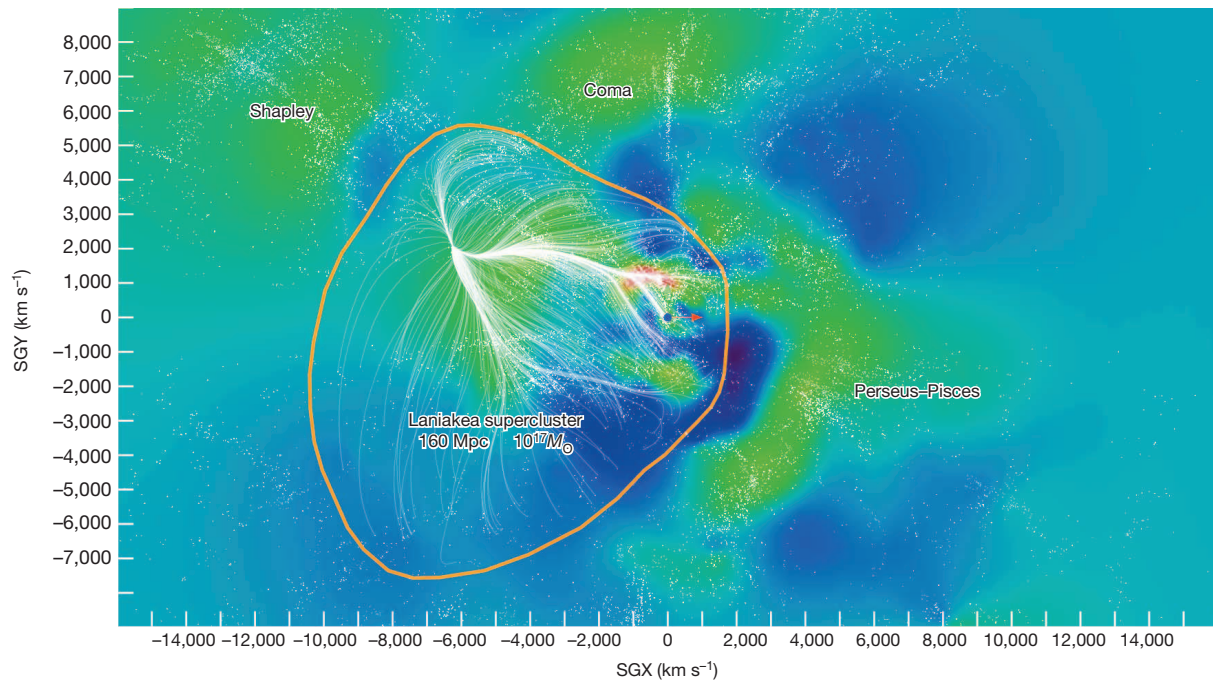


Figure 1.7: A slice through the Laniakea Supercluster in super-galactic coordinates, where the Galaxy is located at the origin. Individual galaxies are shown with white dots and the white lines indicates stream lines of the peculiar velocity field of galaxies. The orange contour shows the boundary of the Laniakea Supercluster, where the peculiar velocity field diverges. This figure is taken from [Tully et al. \(2014\)](#).

## 1.2 Galactic archeology: motivation and challenge

### 1.2.1 Formation of the Galaxy

A currently very active field in astronomy is galactic archeology, focusing on understanding the formation history of the Milky Way from the present distribution of stars. In the  $\Lambda$ -Cold Dark Matter ( $\Lambda$ CDM) context the Galaxy's formation started with the gravitational collapse of dark matter from small overdensities in the early Universe. In  $\Lambda$ CDM simulations such as the *Aquarius* simulation (Navarro et al. 2010), dark halos form from hierarchical assembly, where small halos merge and build larger ones.

In the gravitational potential of the early dark halo, the current theory for the formation of the Milky Way states that the stellar halo and possibly a classical bulge formed first, from either direct collapse of cold gas (Eggen, Lynden-Bell & Sandage 1962) or infall of small fragments (Searle & Zinn 1978). The first stars are however believed to represent only a small fraction of the Galaxy today. Then began a slow accretion process where gas was accreted from the environment across the large scale dark matter filaments. Due to conservation of angular momentum the gas concentrated in a disk and formed new stars that slowly built up the galactic disk. At the same time the Galaxy underwent minor mergers with orbiting dwarf Galaxies, like the merger with the Sagittarius dwarf galaxy that is happening now.

Since the Milky Way is the only disk galaxy that can be observed in great detail and on a star-by-star basis, the idea behind galactic archeology is to use the Milky Way as a benchmark for testing the theory of the formation of disk galaxies in general. Can we explain the present state of the Milky Way within the current theory of hierarchical structure formation in the Universe? How similar is the Milky Way to other barred disk galaxies? How is the dark matter distributed in the Galaxy and how is it affected by evolution of the Galaxy? Answering these questions is now possible thanks to the large amount of data already available but is nevertheless very challenging. Before addressing the question of how the Galaxy formed, it is necessary to build a consensus on the present configuration of the Galaxy.

### 1.2.2 The challenge of geometry

Understanding the present state of the Galaxy is a very challenging task that remains incomplete. From the Sun's perspective, the entire Galaxy is projected as a thin band on the sky, thus making difficult the extraction of structures distributed along the line of sight from observable data. The recovery of the 3D distribution of stars in the Galaxy often requires the measurement of stellar distances, which although a very difficult task can be achieved in two different main ways: the parallax distances and the photometric distances.

Parallax distances rely on the different perspectives from which the observer observes a star as the Earth rotates around the Sun. The change in position on the sky along a year is inversely proportional to the distance to the star. Is it however tiny even for the closest star *Proxima Centauri*, of the order of one arcsecond only. The first large catalogue

of parallax distances was obtained from the *Hipparcos* satellite launched in 1989 (ESA 1997). *Hipparcos* had a median precision in parallax of about 1 mas, which limits the effective volume of the survey to about 1 kpc from the Sun. *Hipparcos* will be superseded by the *Gaia* satellite whose first data release is planned for 2016. *Gaia* will measure precise astrometry and parallax distances to more than a billion objects, with accuracy greatly improved over *Hipparcos*, reaching about  $10\mu$  as for bright stars with  $V \leq 12$ . However since it operate in the visible wavelength range, *Gaia* is not able to pierce through the massive extinction in the galactic plane.

Photometric distances can be obtained by transforming a measurement of the apparent brightness of a star  $m$  into distance modulus  $\mu$  as given by

$$\mu = m - M - A \quad (1.1)$$

where  $M$  is the intrinsic magnitude of the star and  $A$  the extinction between the star and the observer. The difficulty resides in measuring  $M$  and  $A$ . Stars can have a wide variety of absolute magnitudes so that the prior knowledge on  $M$  is usually poor. For example in the visible wavelength band, main sequence stars have absolute magnitudes spanning a range of more than 18 mag. There are however situations in which  $M$  can be measured or statistically constrained. From a measurement of a star's spectrum one can constrain its surface gravity and effective temperature. The comparison with theoretical models of stellar atmospheres allow to infer  $M$  and thus obtain what is often called a spectroscopic distance. Observing a spectrum is an expensive process and unfortunately does not provide particularly accurate distances. In the ARGOS and APOGEE spectroscopic surveys for example,  $M$  can be determined with a typical accuracy of 0.7 mag, corresponding to an error in the inferred distance of about 30%. Another possibility to constrain  $M$  is to use standard candles as target stars. RR Lyrae stars for example are variable stars for which the pulsation period is related to the intrinsic magnitude (Catelan, Pritzl & Smith 2004). Since pulsation periods are relatively easy to measure, RR Lyrae are good targets to obtain stellar distances at relatively low cost. They however sample the metal-poor population only (see Dékány et al. 2013 and Pietrukowicz et al. 2015 for RR Lyrae in the galactic bulge), which in the Milky Way does not trace the bulk of the stellar mass.

In this thesis we will mostly focus on another type of approximate standard candles called the Red Clump Giants (RCGs). RCGs are core Helium burning stars that have a narrow absolute luminosity function. The dispersion of the RCGs' luminosity function is about 0.2 mag (Alves 2000; Bressan et al. 2012) in the  $K_s$  band and therefore allows estimation of photometric distances that are about 10% accurate. Such a standard candle is accurate enough to resolve the variation of the density in the galactic bulge (e.g. Wegg & Gerhard 2013). In addition, theoretical models by Salaris & Girardi (2002) show that RCGs are good tracers of the stellar mass for an old population over a wide range of metallicities (i.e. abundance of elements other than Hydrogen and Helium in the solar atmosphere). Therefore RCGs are a very good target population for studying the structure of the inner Milky Way.

The second ingredient required to estimate distances is the extinction  $A$ . Extinction is caused by absorption and scattering of the light by the interstellar medium distributed

along the line of sight. Extinction in the Galaxy is mostly located in the galactic plane and can reach up to  $A_V = 40$  mag towards the Galactic Centre (Nishiyama et al. 2008). It varies with wavelength and can be lowered by observing in the near infrared. In the  $K_s$  band ( $\sim 2.15 \mu\text{m}$ ) for example the extinction towards the Galactic Centre drops to  $A_{K_s} \sim 2.6$  mag (Fritz et al. 2011). One way to measure extinction is to first measure the reddening of a star (differential extinction between two bands) and then convert this reddening into a single band extinction with an extinction law. Since RCGs also have a narrow distribution of intrinsic colors (standard deviation of about 0.05 mag of the  $J - K_s$  color in Baade's window, from Wegg & Gerhard 2013) their observed color is a direct measure of the reddening. Gonzalez et al. (2012) and Wegg & Gerhard (2013) used this method to build a foreground extinction map of the galactic bulge using RCGs from the VVV survey, with a typical accuracy of 0.03 mag in the  $K_s$  band.

### 1.2.3 The age of surveys

Getting over the challenge of the geometry described above requires accurate data on large scales since the Galaxy covers the entire sky. Fortunately in the past two decades many photometric surveys have been carried out, providing large catalogs of optical and near infrared magnitudes and colors containing billions of stars. A very significant step forward was achieved by the 2MASS which provides accurate photometry in the near-infrared bands  $J$ ,  $H$  and  $K_s$  for more than half a billion stars and galaxies. Since it operates in the near-infrared 2MASS can reach stars located in the bulge and beyond and has been used as input catalogue for many spectroscopic surveys. However the 2MASS catalogue is increasingly incomplete in the galactic plane and towards the Galactic Centre because of extinction and crowding. Other surveys specially designed to penetrate crowded and extinguished regions filled the gap, such as the recent VVV survey (Vista Variables in the Via Lactea, Minniti et al. 2010) in the bulge and the galactic plane at negative longitude, or the UKIDSS survey (United Kingdom Infrared Deep Sky Survey, Lucas et al. 2008) in the galactic plane at positive longitude. In addition the GLIMPSE survey (Galactic Legacy Mid-Plane Survey Extraordinaire, Churchwell et al. 2009; Benjamin et al. 2005) observed the galactic plane from the *Spitzer Space Telescope* in four different bands in the mid-infrared. Number counts of RCGs in the GLIMPSE data show the long bar structure, the tangent point to the Scutum-Centaurus spiral arm, the radial scale length of the disk and the nuclear bulge. Knowledge gained from the GLIMPSE survey is at the origin of the artist's impression of the Galaxy shown in Figure 1.3

In the past decade a significant effort has been made to measure stellar kinematics and chemical compositions in different parts of the Milky Way. By connecting photometry and kinematics through dynamical modelling one can recover key parameters of the Galaxy. For example, using data from the GCS survey (Geneva-Copenhaguen Survey, Nordström et al. 2004) in the solar neighborhood and the RAVE survey (RADial Velocity Experiment, Steinmetz et al. 2006) further away in the nearby disk, Sharma et al. (2014) were able to construct a kinematic model of the Galaxy and recover from it the circular velocity of the Local Standard at Rest (LSR) and the peculiar motion of the Sun in the LSR with

a statistical error of less than  $2 \text{ km s}^{-1}$ . Note however that the measure of the circular velocity of the LSR is affected by systematic uncertainties that are of the order of about  $15 \text{ km s}^{-1}$  (Bland-Hawthorn & Gerhard 2016). With data from the SEGUE survey (Sloan Extension for Galactic Understanding and Exploration, Yanny et al. 2009), Bovy & Rix (2013) were able to put constraints on the structure of the galactic disk and dark matter halo between 4 kpc and 9 kpc from the Galactic Centre. Piffi et al. (2014) modeled the vertical structure of the gravitational potential in the solar neighborhood and by matching the model to RAVE data obtained constraints on the local dark matter density and dark halo shape. RAVE was also used by Antoja et al. (2014) to predict the pattern speed of the galactic bar, interpreting the Hercules stream as a feature caused by the outer Lindblad resonance of the bar.

In the bulge and bar on which this thesis is focused, the three main spectroscopic surveys carried out so far are the BRAVA (Bulge RADial Velocity Assay, Rich et al. 2007), ARGOS (Abundances and Radial velocity Galactic Origins Survey Freeman et al. 2013) and GIBS surveys (Giraffe Inner Bulge Survey, Zoccali et al. 2014). BRAVA and ARGOS are extensively used in this thesis and are described in more detail in Chapter 2 and Chapter 4. The GIBS survey targets RCGs in the bulge identified from the VVV catalogue and provides radial velocities and metallicities for about 5000 stars. GIBS covers fields at galactic latitude  $b = -2^\circ$  and could therefore be used in the future to better constrain the in-plane bulge. Two other large-scale spectroscopic surveys are currently running: the APOGEE survey (Apache Point Observatory Galactic Evolution Experiment, Allende Prieto et al. 2008) and the GES survey (Gaia-ESO, Gilmore et al. 2012). The first phase of the APOGEE survey, observed from the north hemisphere is now complete and observed over  $10^5$  red giant stars across the Galaxy, including the bulge, bar, disk and halo. For each star APOGEE provides radial velocity, stellar parameters and chemical abundances of more than 20 elements. A second phase observed from the south hemisphere is currently running and will target by 2020 about  $3 \times 10^5$  stars. APOGEE is however limited in the bulge and bar by extinction and crowding since its stars are selected from the 2MASS catalogue. GES is a spectroscopic follow-up of the *Gaia* mission that will add radial velocities and stellar parameters to some of the  $10^9$  precise positions and parallax distances measured by *Gaia*. GES will target more than  $10^5$  stars in the Galaxy and will provide a significant insight in the chemistry of the galactic disk. Worth noting is also the OGLE (Optical Gravitational Lensing Experiment, Udalski et al. 1992). OGLE is a photometric survey in the I and V bands, but can still reach bulge stars in low extinction regions. Using the variation of the positions of stars in the sky across the 4 year baseline between 1996 and 2000, Sumi et al. (2004) computed relative proper motions of hundred of millions of stars, hence constraining the stellar kinematics on the plane of the sky.

Although all the datasets presented above have already been individually analyzed, a synthesis effort has to be made to combine these different datasets in a single coherent dynamical model of the Galaxy. The goal of this thesis is to provide part of this synthesis effort, focusing mostly on the galactic bulge, bar and inner disk. To do so we construct dynamical models that are constrained by real data, as described in the next section.

## 1.3 Dynamical modelling of galaxies

### 1.3.1 Collisionless stellar dynamics

Galaxies are mostly empty stellar systems. A typical disk galaxy contains of the order of  $N = 10^{11}$  stars within a radius of 10 kpc, resulting in an average number density of stars of only  $n = 1 \text{ pc}^{-3}$ . A consequence of this fact is that stellar dynamics in galaxies can be considered as *collisionless*, i.e. two-bodies interactions are rare and insignificant enough that stars can be considered to travel through a smooth background gravitational potential. A star traveling at velocity  $v$  relatively to a neighboring star at closest distance  $b$  will experience a typical change in velocity from the two-body interaction of the order of  $\delta v$  given by

$$\delta v \sim \frac{GM}{b^2} \times \frac{2b}{v} \sim \frac{2GM}{bv} \quad (1.2)$$

where  $M$  is the mass of the neighbor star. Strong encounters that lead to a deflection of  $\delta v \sim v$  are extremely rare in disk galaxies, since they require the traveling star to approach its neighbor at a distance of the order of  $b \sim \text{few } 10^{-6} \text{ pc}$ , less than one astronomical unit. Instead, by traveling through the galaxy the star will experience many small deflections  $\delta v$  that statistically cumulate over time and significantly change the orbit of the star. This relaxation process is however very inefficient in galaxies, because its timescale is several orders of magnitude larger than the age of the Universe. This can be shown by integrating all small changes  $\delta v$  experienced by a star traveling through the galaxy (Chandrasekhar 1960). The relaxation time  $T_{\text{relax}}$  is related to the crossing time  $T_{\text{cross}}$  as given by Binney & Tremaine (2008) by

$$T_{\text{relax}} \sim \frac{0.1 N}{\ln N} T_{\text{cross}}. \quad (1.3)$$

For typical disk galaxies with  $N = 10^{11}$  stars and a crossing time of the order of 100 Myr, the relaxation time  $T_{\text{relax}}$  is more than  $10^6$  longer than the age of the Universe. Hence galaxies are ruled by collisionless dynamics. This is not necessarily the case in all stellar systems. Globular clusters for example have a typical crossing time of 1 Myr for about  $N = 10^5$  stars, meaning that their relaxation timescale is of the order of one Gyr only, usually smaller than their age. As a consequence, globular clusters can show some interesting features of collisional dynamics such as mass segregation. Successive encounters of stars with different masses tend to an equipartition of the kinetic energy between the stars, thus reducing the velocity of high mass stars that end up preferentially closer to the center of the cluster than lower mass stars.

The collisionless property is of first importance for modelling galaxies. The relaxation timescale being very long means that stars we observed today have not lost the memory of their initial conditions due to collisional processes. Hence, by measuring the current phase-space density of a Galaxy we can hope to trace back its formation history. In the Milky Way, the *Gaia* mission will provide 6D phase space information of many stars that could allow tracing back the formation history of the galactic stellar halo for example. Note however that the memory of the initial conditions can still be somewhat erased by other

processes than the collisional relaxation, such as variations in the gravitational potential, radial migration or disk instabilities.

A collisionless stellar system can be modeled by a fluid in phase-space whose motion is governed by its smooth gravitational potential. Such a system can then be represented by its phase-space density  $f$ , also called its *distribution function* (DF). Classically,  $f$  is a function of the time  $t$  and the three dimensional spatial position  $\mathbf{x}$  and velocity  $\mathbf{v}$ . Depending on how it is defined  $f$  can represent the stellar mass density in phase-space or the probability to find a star in a small volume  $d\mathbf{x}^3 d\mathbf{v}^3$  around the phase space position  $\mathbf{x}, \mathbf{v}$  at time  $t$ . An observable  $O$  on the model can then be obtained by integrating the distribution function over some kernel  $K_O$  as

$$O = \int_{\mathbf{x}} \int_{\mathbf{v}} \int_t K_O(\mathbf{x}, \mathbf{v}, t) \times f(\mathbf{x}, \mathbf{v}, t) d\mathbf{v}^3. \quad (1.4)$$

For example the 3D stellar mass density at any time  $t$  is simply given by

$$\rho_*(\mathbf{x}, t) = \int_{\mathbf{v}} f(\mathbf{x}, \mathbf{v}, t) d\mathbf{v}^3 \quad (1.5)$$

which through the Poisson equation

$$\nabla^2 \Phi_* = 4\pi G \rho_* \quad (1.6)$$

gives the stellar contribution to the gravitational potential  $\Phi_*$ . Dark matter can then be added into to model by specifying its distribution function in the same way as the stars. The dynamics of the galaxy is then governed by the total gravitational potential, sum of the stellar and dark matter potentials.

Galaxies evolve in time, by accretion, stellar evolution and secular processes. These processes can however have longer timescale than the dynamical (or crossing) timescale of its stars. Hence, for a galaxy in dynamical equilibrium, i.e. that does not evolve significantly over a dynamical timescale, the mass flow in phase-space must obey the continuity equation, so that an increase in density somewhere must be linked to a mass flow towards the considered point. Putting together the conservation of mass of the fluid flow in phase space with the equations of motion in the total gravitational potential  $\Phi$ ,  $f$  can be shown to obey the *Collisionless Boltzmann Equation* (hereafter CBE), given by

$$\frac{df}{dt} = \frac{\partial f}{\partial t} + \mathbf{v} \cdot \nabla f - \nabla \Phi \cdot \frac{\partial f}{\partial \mathbf{v}} = 0 \quad (1.7)$$

Note that the CBE is valid only for collisionless dynamics of a conserved flow in phase space. In real galaxies, finite lifetime of stars, collisional processes or resonances can also contribute to a non-zero right-hand side term of the CBE, thus breaking the conservation of the phase-space flow.

The construction of dynamical equilibrium models of galaxies consist of finding equilibrium solutions or approximate solutions to the CBE that also reproduce a given set of observable data. Finding a solution to the CBE is usually hard since it involves 7 variables in a second order differential equation and can only be done in limited and simplified cases. We describe in the next subsections the different methods that can be used to model galaxies, from more theoretical to more experimental.



### 1.3.2 (Semi-) Analytical methods

#### DF-based modelling

The DF-based modelling aims at finding a distribution function, often assuming a parametric form for it, that solves the CBE while reproducing real data. The idea behind DF-based modelling is to think in term of integrals of motion rather than in term of the phase-space coordinates. An integral of motion  $I$  is a quantity that depends on phase-space coordinates only (no explicit time dependency) and that is conserved along any orbit. Thus the Lagrangian derivative of  $I$  vanishes and  $I$  obeys to

$$\frac{dI}{dt}[\mathbf{x}(t), \mathbf{v}(t)] = \mathbf{v} \cdot \nabla I - \nabla \Phi \cdot \frac{\partial I}{\partial \mathbf{v}} = 0. \quad (1.8)$$

Hence, for a potential with  $n$  integrals of motion, any function  $f(I_1(\mathbf{x}, \mathbf{v}), \dots, I_n(\mathbf{x}, \mathbf{v}))$  of the integrals of motion  $I_n$  verify

$$\frac{df}{dt} = \sum_{i=1}^n \frac{\partial f}{\partial I_i} \frac{dI_i}{dt} = 0 \quad (1.9)$$

and is thus a solution of the CBE. Inversely, by definition a steady-state solution of the CBE is also an integral of motion. This is called the *Jeans theorem* that states that in a given potential, any steady-state solution of the CBE depend on the phase-space coordinates only through the integrals of motion, and reciprocally (Binney & Tremaine 2008).

The DF-based dynamical modelling of galaxies requires finding as many integrals of motion as possible given the symmetries and possible assumptions about the considered system. Then assuming some parametric form of the distribution function in term of the considered integrals of motion and assuming that it does not depend on any other parameters, one can recover the best-fit parameters of the DF by comparing to real data. The problem often resides in finding those integrals of motion. In three dimensional integrable potentials, degenerate cases taken aside, there are only three independent integrals of motion. In an axisymmetric integrable potential, two of the three integrals are the total energy and the component of the angular momentum along the revolution axis, but the third integral is in general unknown. Integrable potential are rare, even mathematically speaking, and so real galaxies are likely to have a non-integrable potential. However in many cases, realistic potentials are near-integrable and near-integrals of motion can be found (see Gerhard 1994 for an extensive discussion in the context of elliptical galaxies).

Although integrals of motion are very hard to find in practice, there is in theory an infinite choice of integrals of motion since Equation 1.9 shows that any function of the integrals of motion only is itself an integral of motion. In integrable potentials, a convenient choice for the integral of motions used as arguments of the DF are the so called actions. The actions are the momenta of a set of canonical coordinates of the phase-space called action-angle coordinates and noted  $(J_i, \Theta_i)_{(1 \leq i \leq 3)}$  in which the  $J_i$  are integrals of motion. By definition the  $J_i$  are integrals of motion, so they stay constant along an orbit, allowing to label an orbit by just the three numbers corresponding to the value of the three actions. It

can be shown using Hamilton's formalism (Binney & Tremaine 2008) that the  $\Theta_i$ , associated variables of the actions are linear functions of the time (modulo  $2\pi$ ). The  $\Theta_i$  represent the phase of a star along its orbit, oscillating periodically. Hence in action-angle modelling an orbit is represented by three constant actions and three angles varying linearly in time, rather than by six complex functions of the time corresponding to the three classical positions and velocities.

DF-based modelling has been applied to spherical or oblate systems (e.g. Dejonghe 1984; Dehnen & Gerhard 1993) but also more recently in the Milky Way for modelling the dynamics of the solar neighborhood (Binney 2010; Piffl et al. 2014) or the nuclear star cluster (Chatzopoulos et al. 2015).

### Jeans equations

Macroscopic properties of stellar systems can sometime be recovered without the need to first obtain the full description of the galaxy by solving the CBE. Jeans modelling is obtained by taking the velocity moments of the CBE and solving for them instead of solving for the full DF. From the zeroth moment of Equation 1.7 we obtain the first Jeans equation given by

$$\frac{\partial \rho_*}{\partial t} + \frac{\partial(\rho_* \bar{v}_i)}{\partial x_i} = 0 \quad (1.10)$$

where

$$\bar{v}_i = \frac{1}{\rho_*} \int v_i d^3 \mathbf{v}, \quad (1.11)$$

for any  $v_i$ , Cartesian component  $i$  of the velocity.

The first velocity moment of Equation 1.7 yields three others Jeans equations for a second index  $j$  given by

$$\frac{\partial(\rho_* \bar{v}_j)}{\partial t} + \rho_* \bar{v}_i \frac{\partial \bar{v}_j}{\partial x_i} = -\rho_* \frac{\partial \Phi}{\partial x_j} - \frac{\partial(\rho_* \sigma_{ij}^2)}{\partial x_i} \quad (1.12)$$

where the velocity dispersion tensor  $\sigma_{ij}$  is given by

$$\sigma_{ij}^2 = \overline{v_i v_j} - \bar{v}_i \bar{v}_j. \quad (1.13)$$

Assuming we know the density  $\rho_*$  and the gravitational potential  $\Phi$ , the 4 Jeans equations stated above are not enough to fully constrain the 9 unknowns variables, i.e. the 3 components of the velocity field and 6 independent components of the dispersion tensor. Some of these quantities can however be directly measured. By integral field spectroscopy we can measure the mean line of sight velocity field and velocity dispersion fields which can be used to directly constrain the models (Emsellem et al. 2004; Cappellari 2008). Provided some additional assumptions on the symmetry of the system and on the dispersion tensor one can close the system of equations and find a solution. In the simple case of a spherical steady-state galaxy for example, the Jeans equations simplify to

$$\frac{d(\rho_* \bar{v}_r^2)}{dr} + 2 \frac{\beta}{r} \rho_* \bar{v}_r^2 = \rho_* \frac{d\Phi}{dr} \quad (1.14)$$

where  $\beta$  is the radial anisotropy parameter. Hence if we know the density and potential, we can relate a measurement of the velocity field to the anisotropy. Inversely an assumption on the anisotropy can be converted into a constraint on the total potential and/or the dark matter distribution.

Jeans modelling has been mostly used to model early-type ellipticals, for spherical galaxies (Binney & Mamon 1982; Mamon et al. 2006) or axisymmetric systems with two-integrals Jeans models (Binney, Davies & Illingworth 1990). Cappellari (2008) proposed the Jeans Anisotropic Modelling (JAM), generalization of the two-integral models for an anisotropic velocity ellipsoid. The JAM method has been applied to the 260 galaxies observed by the ATLAS<sup>3D</sup> survey (Cappellari et al. 2013) but it is not clear yet how physical those models are (Söldner-Rembold et al., in preparation). In the Milky Way, the Jeans equations can be used to understand the axisymmetric drift (Binney & Tremaine 2008) or constrain the vertical structure of the potential in the solar neighborhood (Kuijken & Gilmore 1989; Bovy & Tremaine 2012; Moni Bidin et al. 2014).

### 1.3.3 Particle/Orbit based methods

In a given potential, any linear combination of solutions of the CBE is also a solution of the CBE. Hence an alternative approach to the analytical method described above is to consider many elementary distribution functions  $f_i$  as a basis for approximating  $f$ . Considering a large number of elements  $N \gg 1$ ,  $f$  is approximated as

$$f \simeq \sum_{i=1}^N w_i f_i \quad (1.15)$$

where the  $w_i$  are the weights of the different  $f_i$ .

#### Schwarzschild modelling

The Schwarzschild modelling introduced by Schwarzschild (1979) is an orbit-based method where the galaxy is represented as a sum of many orbits. Assuming a total gravitational potential, the first step of the method consists of constructing an *orbit library* that samples all possible orbits in phase-space. In an integrable potential, any orbit can be fully represented by its integrals of motion  $I_{1,i}, \dots, I_{n,i}$  and thus the Schwarzschild modelling technique writes the elementary  $f_i$  as a discrete sampling of the integral of motion space, as given by

$$f_i(I_1, \dots, I_n) = \delta(I_1 - I_{1,i}) \times \dots \times \delta(I_n - I_{n,i}). \quad (1.16)$$

In non-integrable potentials, or when the integrals of motion have no known analytical expressions, a sampling recipe is required. This is the case in the axisymmetric case where only two of the integrals of motion are known and can be directly sampled: the total energy  $E$  and the angular momentum along the axis of symmetry  $L_z$ . The third integral of motion is then only approximately sampled by integrating test particles in the potential from a fixed value of  $E$  and  $L_z$ . In a second step, the single-orbit DFs  $f_i$  are integrated to predict

model observables that are linearly combined. An optimization process is then charged to find a combination of weights  $w_i$  that maximize some profit function, usually minimizing the  $\chi^2$  between modeled observables and data. Schwarzschild modelling is expensive in memory since it requires the storage of the contribution of all orbits to all observables. This limits in practice the size of the orbits library to the range  $10^4 - 10^5$  orbits.

The problem of orbit sampling mostly restricts the Schwarzschild modelling to axisymmetric (Thomas et al. 2009) and triaxial systems (van den Bosch et al. 2008; Vasiliev 2013; Finozzi et al., in preparation). It has been applied on large elliptical galaxies under the assumption of spherical symmetry or axisymmetry (Richstone 1980; Richstone & Tremaine 1984; Rix et al. 1997; Thomas et al. 2005). The few applications in the Milky Way have been mostly focused on the galactic bar, based on an analytical density model (Zhao 1996; Haefner et al. 2000) or a N-body potential (Wang et al. 2012, 2013).

### N-body modelling

The N-body approach is more straightforward and represents the galaxy as a large set of particles sampling the phase-space. Formally, the  $f_i$  are given by

$$f_i(\mathbf{x}, \mathbf{v}, t) = \delta(\mathbf{x} - \mathbf{x}_i(t)) \times \delta(\mathbf{v} - \mathbf{v}_i(t)) \quad (1.17)$$

where  $\mathbf{x}_i(t)$  and  $\mathbf{v}_i(t)$  are the position and velocity of particle  $i$  at time  $t$  and the weights  $w_i$  of Equation 1.15 are the physical masses of the particles. A potential solver is first required to compute the gravitational field produced by the spatial mass distribution of the full set of particles at their current position. The entire model is then propagated for a small time increment  $\delta t$  integrating Newton's second law of motion, individually for each particle. Repeating this process for many  $\delta t$  allow to study the evolution of the model in time. Note that N-body models only provide approximate solutions of the CBE. Since all the positions of all the particles change between two iterations, so does the gravitational potential, even for a N-body sampling of a steady-state system. As a consequence, particles do not exactly follow orbits. However, the possibility of slow changes in the potential and resonances allow the development of secular evolution processes, such as the formation of B/P bulges already mentioned in Section 1.1.3.

On the bright side, N-body models are fairly simple, widespread and very general. Complicated systems like the Andromeda galaxy with a disk, a classical bulge, a B/P bulge and a dark matter halo can be accurately modeled using pure N-body models (Blaña Díaz et al., in preparation) and several N-body integrators and potential solvers are available e.g in the NEMO stellar dynamics toolbox from Teuben (1995). N-body models are also a unique tool to understand how structures form due to various instabilities that are too complicated to be treated analytically.

On the dark side, it has to be noted first that N-body modelling is not a stand-alone modelling technique, since a N-body run requires an initial N-body model to evolve from. The construction of the N-body initial conditions is usually done by randomly sampling some user-defined mass model and specifying initial velocities to every particle in order to ensure an approximate equilibrium state of the model. This can be done by either sampling

a distribution function (Debattista & Sellwood 1998), solving the Jeans equations (Hernquist 1993) or by trial/error numerical experiments (Rodionov, Athanassoula & Sotnikova 2009; Yurin & Springel 2014). In addition, the user of a N-body models has only a limited amount of control on the end product of a N-body run. Although the integration process is fully deterministic, the model evolution is non-linear. The outcome of two N-body runs starting from initial conditions that have the same macroscopic properties but different microscopic states can lead to evolved models that are macroscopically very different. For example Sellwood & Debattista (2009) showed that the strength of the stellar bar of an evolved N-body model can depend on the seed of the random number generator used to sample the initial conditions. As a consequence, when trying to produce a model that matches some data, the N-body modelling of a galaxy often requires running many models with different initial parameters and then searching inside this large model library which model compares best to the data. Note in addition that a N-body model of a galaxy at a time  $t$  is determined by  $6 \times N$  numbers. At a later time  $t + \Delta t$  all particles have moved and the galaxy is represented by  $6 \times N$  *different* numbers, even though the galaxy remains unchanged in a steady state case.

### Made-to-Measure N-body modelling

In this thesis we use the Made-to-Measure method (M2M) to construct dynamical models of the Galaxy. The M2M method introduced by Syer & Tremaine (1996) is a modelling technique that combines the flexibility of N-body modelling with the orbit superposition of the Schwarzschild method in order to reproduce a given set of data. It relies on an initial self-gravitating N-body model. The particles masses, rigorously representing mass elements located at some point of a time-dependent phase-space, are identified to the weights of the time-averaged orbits that the particles approximately follow when evolving in their own potential. The M2M method consists of slowly adjusting the weights  $w_i$  while integrating the N-body model in order to obtain a self-consistent dynamical model that also reproduces the data. Starting from the initial N-body model, the different model observables are first computed and then compared to the real data. The comparison is quantified by a profit function, usually the opposite of a  $\chi^2$  between model observables and real data. The profit function is maximized by a simple gradient ascent algorithm operating on the particle weights. This gradient ascent on the weights and the propagation of the N-body particles forward in time are performed at the same time, both in small steps. This makes the method is very efficient in memory since it only requires the knowledge of the contribution of all particle to all observables at one time only rather than the knowledge of the time-averaged contributions of all orbits, as in the Schwarzschild modelling. Syer & Tremaine (1996) and De Lorenzi et al. (2007) showed that the method converges to the solution, provided the initial N-body model used as the initial discrete sample of the DF is close enough to the solution. Note that the M2M method acts only on the physical masses of the particles, not directly on their positions or velocities. For variant methods acting on the velocities see Rodionov, Athanassoula & Sotnikova (2009) and Yurin & Springel (2014).

The initial thought behind the M2M method by Syer & Tremaine (1996) was to set up

initial conditions for N-body models. De Lorenzi et al. (2007) adapted the method to match real data by introducing a  $\chi^2$  into the profit function. Several refinements and variations of the method have been studied by Dehnen (2000a), Morganti & Gerhard (2012) and Hunt, Kawata & Martel (2013). Applications prior to this thesis have been carried out in the context of external galaxies (e.g. De Lorenzi et al. 2007, 2009; Das et al. 2011; Morganti et al. 2013) but also in the Milky Way (e.g. Bissantz, Debattista & Gerhard 2004; Long et al. 2013; Hunt & Kawata 2014).

Details about the M2M method are given in Chapter 2 for modelling the galactic bulge, in Chapter 4 for modelling the entire bar region and in Chapter 5 for an extension of the method used to make a chemodynamical model of the bar region. I used the N-particle Made-to-measure AlGorithm mInimizing Chi squared (NMAGIC) implementation, originally written by De Lorenzi et al. (2007) and entirely restructured for the purpose of the thesis.

## 1.4 Goal and outline of the thesis

In this thesis dynamical equilibrium models the inner Milky Way are built that simultaneously reproduce recent photometric and kinematic data. It focuses on constraining the present day state of the Milky Way, a necessary first step towards understanding its formation history.

Chapter 2 describes the construction of a set of N-body models of barred stellar disks in different dark matter halos used as initial conditions for constructing M2M models of the galactic bulge. These five N-body models are then fitted simultaneously to the recent 3D density map of RCGs in the galactic bulge from Wegg & Gerhard (2013) and to the bulge stellar kinematics from the BRAVA survey. I investigate under which conditions the two datasets can be simultaneously reproduced and find a very strong constraint on the total dynamical mass of the bulge (i.e stellar + dark matter), and discuss its consequence on the dark matter fraction in the bulge.

Chapter 3 describes a spin-off project based on the dynamical models of the bulge from Chapter 2. The orbital structure of the bulge models is analyzed, before and after fitting to Milky Way data. In all these models the peanut shape of the bulge is shown to be the superposition of several peanut shapes, all embedded into another and supported by different orbit families. Most of the mass in the peanut shape of these models is supported by a new orbit family called *brezel* orbits. Only a small fraction of the mass populates the famous *banana* orbits, thought before to be the backbone of B/P bulges.

Chapter 4 describes the main effort of this thesis, where the dynamical modelling is extended outside the bulge, to include the long bar and the galactic disk out to 10 kpc. Additional recent datasets are used to constrain the models, including the magnitude distributions of RCGs in bar region from Wegg, Gerhard & Portail (2015) using a combination of the VVV, UKIDSS and 2MASS infrared surveys, together with the stellar kinematics of RCGs as a function of line of sight distance from the ARGOS survey. From this modelling the pattern speed of galactic bulge and bar structure is recovered as well as the

distribution of stellar and dark matter mass in the inner Galaxy. The model thus provides the full effective gravitational potential inside the solar radius, a fundamental element for understanding the orbits of Milky Way stars. Interestingly, matching simultaneously the dynamical mass in the bulge and the rotation curve in the Solar vicinity requires the presence of a central dark matter core for an Einasto density profile.

[Chapter 5](#) extends the dynamical modelling described in [Chapter 4](#). First an extension of the Made-to-Measure method is described that has been designed to incorporate the metallicity of stars into the modelling. A metallicity distribution function is attached to every particle that are altogether fitted in order to reproduce the spatial and kinematic variations of metallicity seen in the ARGOS and APOGEE data. Applying the method to the dynamical model of the bar region results in the first self-consistent and fitted chemodynamical model of the inner Galaxy. The variations as a function of metallicity observed in the ARGOS and APOGEE surveys are then described and explained in term of differences in spatial, kinematic and orbital structure of the different metallicity components.

[Chapter 6](#) concludes the thesis by placing the work described above in a larger context while describing related projects and applications of the dynamical models. Finally, future perspectives are discussed, not only for improving the dynamical models but also for understanding the new data coming in the next decade, that will finally reveal the formation history of our home galaxy.





# Chapter 2

## Made-to-Measure Models of the Galactic Boxy/Peanut Bulge: stellar and total mass in the bulge region

**Original publication:** Matthieu Portail, Christopher Wegg, Ortwin Gerhard and Inma Martinez-Valpuesta, 2015, MNRAS, 448, 713 [↗](#)

### Abstract

We construct dynamical models of the Milky Way’s boxy/peanut (B/P) bulge, using the recently measured 3D density of Red Clump Giants (RCGs) as well as kinematic data from the BRAVA survey. We match these data using the NMAGIC Made-to-Measure method, starting with N-body models for barred discs in different dark matter haloes. We determine the total mass in the bulge volume of the RCGs measurement ( $\pm 2.2 \times \pm 1.4 \times \pm 1.2$  kpc) with unprecedented accuracy and robustness to be  $1.84 \pm 0.07 \times 10^{10} M_{\odot}$ . The stellar mass in this volume varies between  $1.25 - 1.6 \times 10^{10} M_{\odot}$ , depending on the amount of dark matter in the bulge. We evaluate the mass-to-light and mass-to-clump ratios in the bulge and compare them to theoretical predictions from population synthesis models. We find a mass-to-light ratio in the K-band in the range 0.8 – 1.1. The models are consistent with a Kroupa or Chabrier IMF, but a Salpeter IMF is ruled out for stellar ages of 10 Gyr. To match predictions from the Zoccali IMF derived from the bulge stellar luminosity function requires  $\sim 40\%$  or  $\sim 0.7 \times 10^{10} M_{\odot}$  dark matter in the bulge region. The BRAVA data together with the RCGs 3D density imply a low pattern speed for the galactic B/P bulge of  $\Omega_p = 25 - 30 \text{ km s}^{-1} \text{ kpc}^{-1}$ . This would place the Galaxy among the slow rotators ( $\mathcal{R} \geq 1.5$ ). Finally, we show that the Milky Way’s B/P bulge has an off-centred X structure, and that the stellar mass involved in the peanut shape accounts for at least 20% of the stellar mass of the bulge, significantly larger than previously thought.

## 2.1 Introduction

Observations of external disc galaxies have shown that about half of all disc galaxies have strong bars (Eskridge et al. 2000). The Milky Way Galaxy (MW) has been considered for many years as one of them. The galactic bar/bulge causes the non-circular motions in the gas flow seen in H $\alpha$  and CO (Peters, III 1975; Binney et al. 1991; Englmaier & Gerhard 1999; Fux 1999) and is the origin of the asymmetries seen in the near-infrared light distribution (Blitz & Spergel 1991; Weiland et al. 1994; Binney, Gerhard & Spergel 1997) and star counts (Nakada et al. 1991; Stanek et al. 1997; López-Corredoira, Cabrera-Lavers & Gerhard 2005). The galactic bulge (GB) is regarded as the three-dimensional part of the bar seen nearly end-on (Shen et al. 2010; Martínez-Valpuesta & Gerhard 2011) with a semi-major axis of about 2 kpc (Gerhard 2002; Wegg & Gerhard 2013), as is also indicated by the near-cylindrical rotation of the bulge stars (Beaulieu et al. 2000; Kunder et al. 2012; Ness et al. 2013a).

In the last decade, stellar surveys of the GB such as 2MASS (Skrutskie et al. 2006), VVV (Saito et al. 2012), OGLE (Sumi et al. 2004), BRAVA (Rich et al. 2007) and ARGOS (Freeman et al. 2013) have released unprecedented data sets which allow us to study the GB star-by-star. The triaxial bulge of the MW is now believed to be a so called boxy/peanut bulge (B/P bulge) or X-shaped bulge as indicated by its bimodal distribution of Red Clump Giants (RCGs). This was first reported from the 2MASS catalogue by McWilliam & Zoccali (2010) and from the OGLE-III survey by Nataf et al. (2010). Ness et al. (2012) showed that this split red clump is seen for stars with metallicity  $[\text{Fe}/\text{H}] > -0.5$ . The peanut shape was mapped last year in three dimensions by Wegg & Gerhard (2013) using public data from the VVV survey.

Star counts and infrared observations have revealed a long and flat bar component, located mostly in the galactic plane and extending up to  $l \sim 27^\circ$  (Hammersley et al. 2000; Benjamin et al. 2005; Cabrera-Lavers et al. 2007). Curiously, the angle of the bar relative to the line-of-sight to the Galactic Centre (GC) was inferred to be  $\phi = 45^\circ$  in these studies, while the angle of the barred B/P bulge is accurately measured from the RCGs as  $\phi = 27^\circ \pm 2^\circ$  (Wegg & Gerhard 2013). Study of N-body models suggested that the long bar and the B/P bulge data could be explained by a unique B/P bulge and bar structure formed by the buckling instability, if its two-dimensional outer bar component has developed leading ends through interaction with adjacent spiral arm heads (Martínez-Valpuesta & Gerhard 2011).

The buckling instability is a well studied process in N-body simulations (Combes & Sanders 1981; Raha et al. 1991; Martínez-Valpuesta & Shlosman 2004). Cold stellar discs embedded in live dark haloes naturally tend to form a bar which experiences long term secular evolution because of angular momentum transfer from the disc to the halo (Debatista & Sellwood 2000; Athanassoula 2003). During this secular evolution the bar can go through one or more buckling events (Raha et al. 1991; Martínez-Valpuesta, Shlosman & Heller 2006), making it vertically thick and creating the so called boxy/peanut shape, or X-shape in unsharp-masked images.

In this context, the goal of this paper is to combine N-body simulations of evolved

stellar discs with recent MW data to create dynamical models of the galactic bulge and study its total mass, mass-to-light ratio, stellar mass and X-shape structure. To do so we use the 3D density of RCGs from [Wegg & Gerhard \(2013\)](#), hereafter also WG13) as well as kinematic data from the BRAVA survey ([Howard et al. 2008](#); [Kunder et al. 2012](#)) to create particle models using the Made-to-Measure method (M2M). In M2M modelling, the weights of the particles in an N-body system are continuously updated until the observables from the model match a set of target data constraints. The M2M method was introduced by [Syer & Tremaine \(1996\)](#) and recast by [De Lorenzi et al. \(2007\)](#) such that observational errors can be taken into account. We use the NMAGIC code of [De Lorenzi et al. \(2007\)](#) adapted to the Milky Way problem by [Martinez-Valpuesta \(2012\)](#). NMAGIC has been used mostly in extragalactic studies ([De Lorenzi et al. 2009](#); [Das et al. 2011](#); [Morganti et al. 2013](#)). M2M methods were previously used in the Milky Way context by [Bissantz, Debattista & Gerhard \(2004\)](#), [Long et al. \(2013\)](#), also using BRAVA data, and [Hunt & Kawata \(2014\)](#).

This paper is organized as follows. In [Section 2.2](#), we present the set of N-body simulations of barred discs that we use as starting point for our M2M modelling. In [Section 2.3](#), we recount the M2M method and the data sets we use to model the GB. The modelling is detailed in [Section 2.4](#) where we present our best dynamical models and discuss the issue of the pattern speed of the bar. In [Section 2.5](#), we show that we can recover the total mass in the bulge region with great accuracy, thereby relating the stellar mass to the dark matter mass in the bulge. In [Section 2.6](#), we compute the stellar mass-to-light and mass-to-clump ratios of our models and compare them to theoretical predictions from population synthesis models. [Section 2.7](#) quantifies the importance of the X-shape structure in the bulge which accounts for more than 20% of the stellar mass of the bulge. Finally, we discuss our results in [Section 2.8](#) and summarize in [Section 2.9](#).

## 2.2 Particle models of barred discs

### 2.2.1 N-body models in different dark matter haloes

Our M2M modelling of the GB relies on reasonable initial particle models of barred discs. These initial models were created by evolving near-equilibrium stellar discs embedded in live dark matter haloes. Near-equilibrium models are constructed using the program MAGALIE ([Boily, Kroupa & Peñarrubia-Garrido 2001](#)) and evolved with the tree-code GYRFALCON ([Dehnen 2000a](#)), all distributed with the publicly available NEMO toolbox ([Teuben 1995](#)). During the evolution, the disc naturally forms a bar which rapidly buckles out of the galactic plane and creates a B/P bulge ([Combes & Sanders 1981](#); [Raha et al. 1991](#)).

As we want to address the question of the total mass of the GB including the amount of dark matter in the bulge, we generated a set of five disc+halo N-body models using the same disc component and varying the halo properties. The disc is exponential with scale length of 1 internal units (iu), scale height of 0.14 iu, unit total disc mass, and  $Q$  parameters of 1.4 at  $R = 3.07$  iu. Halos have a Hernquist density profile with flattening of

0.8 and a sharp cutoff at 20 iu. All models contain two million particles, one million each for disc and halo. With these settings fixed only two free parameters remain: the halo mass inside the cutoff,  $M_h$ , and the halo break radius of the Hernquist profile,  $a_h$ . They were fixed considering the total rotation curve of a model. Following the language of Sackett (1997), we call the *degree of maximality* of a disc the proportion of the disc contribution to the total velocity curve, at the radius where the disc velocity curve is maximal. Assuming a flat rotation curve at large radii, we build a one parameter family of models parametrized by the degree of maximality of the disc. We make five models of this family, called M80, M82.5, M85, M87.5 and M90 which have different degree of maximality ranging from 80% to 90%. As we show later this allows us to build models of barred galaxy which span all kind of rotators, from slow to fast. The halo parameters used to construct these models are summarized in Table 2.1.

For each model, we select a snapshot of a late evolutionary stage, where the bar is fully grown. The circular velocity curves obtained from the azimuthally averaged potential of this set of models are plotted in Figure 2.1, before any evolution (top) and, for the selected snapshot after bar and B/P bulge formation (bottom). The different colours refer to different models as stated in the legend. In the upper plot, the solid black line is the circular velocity curve of the initial disc component (common for all models) and the vertical dashed line indicates the radius at which the degree of maximality is determined. As expected the bar formation moves material inward which increases the circular velocity in the inner region of the disc.

### 2.2.2 Geometry and scaling

According to the latest studies (Chatzopoulos et al. 2015; Reid et al. 2014), we assume a distance to the Galactic Centre (GC) of  $R_0 = 8.3$  kpc. The bar is placed at an angle of  $\alpha = 27^\circ$  from the Sun-GC line (WG13). All our models are scaled independently based on the length of their long bar. Several studies based on different data sets indicate that the long bar of the MW ends at about  $l = 27^\circ$ . Hammersley et al. (2000) studied star counts of  $K$  giants in several in-plane fields and places the end of the long bar at  $l \sim 27^\circ$  while Cabrera-Lavers et al. (2007, 2008) found respectively values of  $27^\circ$  and  $28^\circ$ , based on RCGs counts from the 2MASS catalogue and from UKIDSS data. Benjamin et al. (2005) also found indication of a long bar for  $l < 30^\circ$  using star counts from the GLIMPSE catalogue. All these different estimates agree well with each other and give therefore a consistent length scale. With  $R_0 = 8.3$  kpc, a bar angle of  $27^\circ$  and the end of the bar at  $l = 27^\circ$ , the half length of the bar is  $R_{\text{bar}} = 4.66$  kpc. The different parameters quoted above constitute our fiducial set of parameters. We checked that our main results are not significantly affected by assuming a bar angle of  $32^\circ$  instead of  $27^\circ$  or a shorter bar half-length of  $R_{\text{bar}} = 3.8$  kpc (see Section 2.5.2), or by using  $R_0 = 8$  kpc instead of 8.3 kpc.

We used ellipse fitting of the face-on projection of our models to compute their bar lengths, and scaled them to 4.66 kpc. The velocity scaling is kept free and will be determined dynamically from the data during the modelling process, as explained in Section 2.3.4.

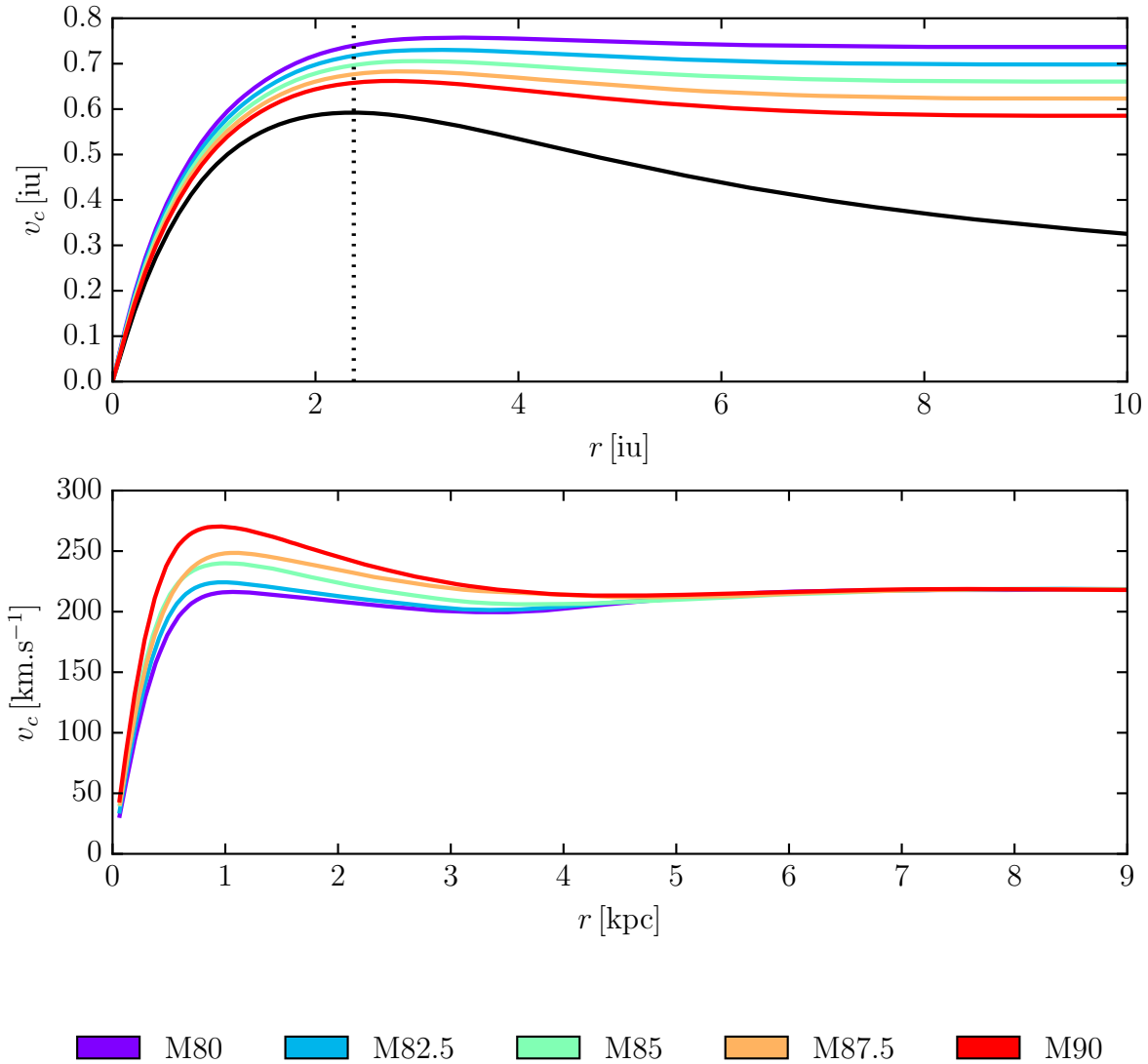


Figure 2.1: *Top* : Circular velocity curves of our five disc-halo models before evolution, in model units. The black line shows the circular velocity curve of the disc only, kept the same for all models. The dashed vertical line indicates the radius where the maximality of the disc is computed. *Bottom* : Azimuthally averaged circular velocity curves after the bar and B/P bulge formation, also in model units.

Table 2.1: Main parameters of our five disc-bar-halo models. The two first rows show the initial halo parameters: the halo mass inside cutoff  $M_h$  in units of the disc mass  $M_d$  and the Hernquist break radius  $a_h$ . The next rows give parameters after bar and bulge formation and scaling to physical units (see Section 2.2.2): the corotation radius  $R_{\text{cr}}$  of the bar, the ratio of the corotation radius over bar half-length  $\mathcal{R}$  and the dark matter fraction in the bulge  $M_{\text{DM}}/M_{\text{tot}}$ .

	M80	M82.5	M85	M87.5	M90
$M_h/M_d$	9.42	8.51	7.68	6.94	6.27
$a_h$ [iu]	17.62	19.44	22.05	26.16	33.68
$R_{\text{cr}}$ [kpc]	8.4	7.6	6.7	5.6	5.0
$\mathcal{R} = R_{\text{cr}}/R_{\text{bar}}$	1.80	1.64	1.44	1.21	1.08
$M_{\text{DM}}/M_{\text{tot}}$	44.2%	40.8%	34.5%	28.6%	25.2%

In order to avoid referring to scale dependent quantities we will refer to the rotational velocity of the bar using the dimensionless number  $\mathcal{R} = R_{\text{cr}}/R_{\text{bar}}$ , the ratio between the corotation radius and the half-length of the bar. Bars with  $\mathcal{R} \geq 1.4$  are called slow rotators, while those with  $\mathcal{R} \leq 1.4$  are fast rotators (Debattista & Sellwood 2000). Because the bar cannot extend beyond corotation (Contopoulos 1980),  $\mathcal{R}$  has to be larger than one. Our models span  $\mathcal{R}$  values quite uniformly from 1.8 to nearly 1.1, which corresponds to the full range of reasonable values for barred galaxies (Elmegreen 1996). Statistics for external galaxies from Rautiainen, Salo & Laurikainen (2008) show that nearly all galaxies of Hubble types S0, SBa or SBb are consistent with being fast rotators while for SBc galaxies (like the MW), bars can be either fast or slow. The sampling of  $\mathcal{R}$  values we obtain is a consequence of the different haloes we used. The halo absorbs angular momentum during the bar formation and therefore the more maximal the initial disc, the less halo material there is to absorb angular momentum and so the faster the bar. One should keep in mind that for our set of models, the halo mass in the inner parts and the  $\mathcal{R}$  value are not independent parameters. The different model and bar parameters are given in Table 2.1.

Throughout this paper the  $(x, y, z)$  frame refers to the Galactocentric inertial frame where  $z$  is the vertical axis pointing to the Galactic North and  $y$  the Sun-GC axis. The bar rotates at pattern speed  $\Omega_p$  in this inertial frame and we shall refer to the rotating frame of the bar as  $(x', y', z')$ , with  $x'$ ,  $y'$  and  $z'$  respectively the major, intermediate and vertical axis of the bar. Figure 2.2 shows the face-on and side-on projections of our models with these geometry and scaling.

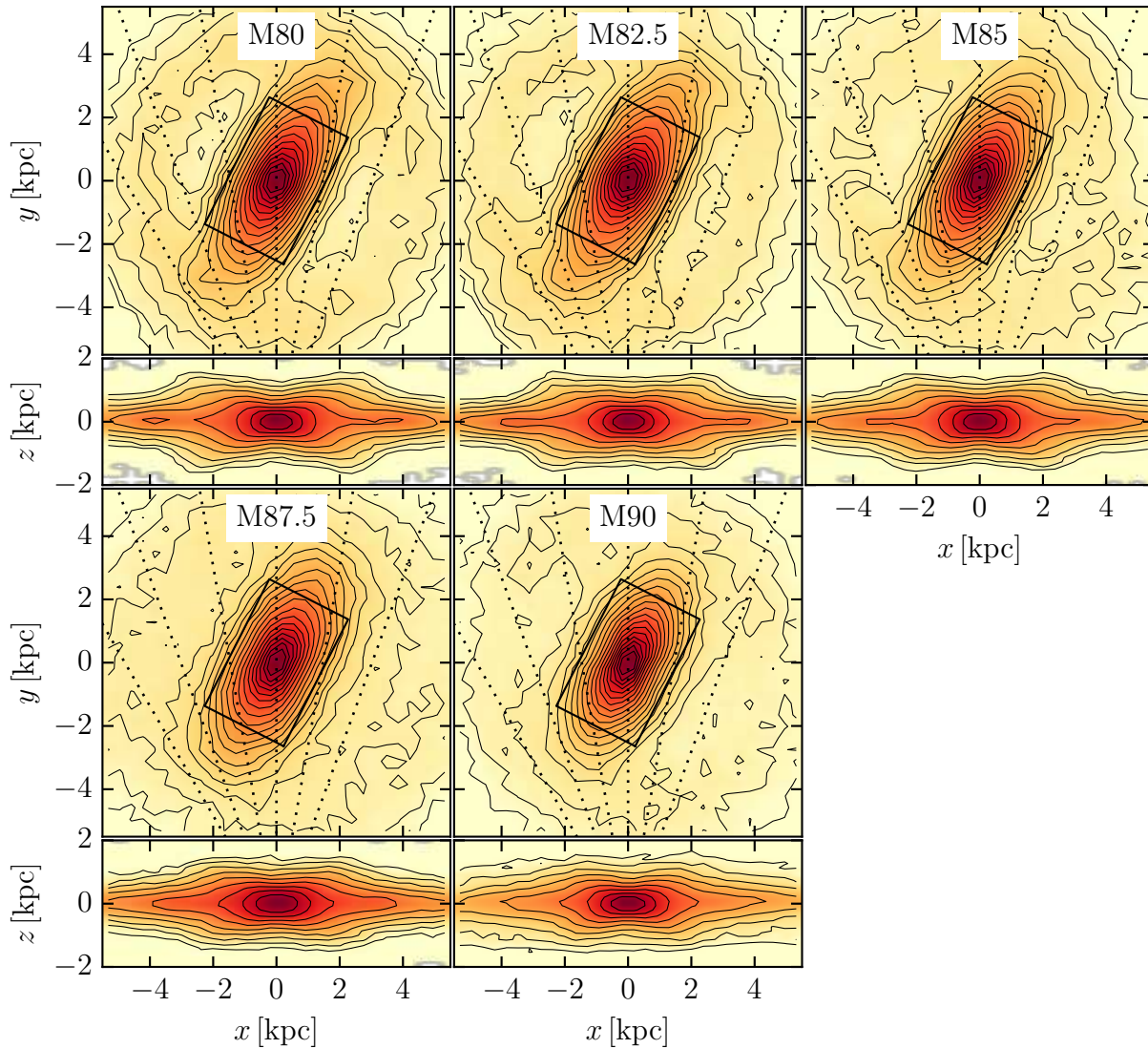


Figure 2.2: Face-on and side-on views of our five initial models of barred discs with B/P bulges. The Sun is located 8.3 kpc from the Galactic Centre and the bar is at an angle of  $27^\circ$  from the Sun-GC line. The dotted lines on the face-on view indicate sight lines spaced every  $10^\circ$  in galactic longitude. The bold rectangle indicates the boundary of the box where the density is given by [Wegg & Gerhard \(2013\)](#), see [Section 2.3.2](#).

## 2.3 Made-to-measure with MW observables

As an alternative to distribution function-based methods (Dejonghe 1984; Binney 2010), moment-based methods (Binney, Davies & Illingworth 1990; Cappellari et al. 2009) or orbit-based methods (Schwarzschild 1979; Thomas et al. 2009), Syer & Tremaine (1996) proposed a particle-based algorithm to study stellar dynamical equilibria, known as the Made-to-Measure (M2M) method. This algorithm consists of adapting the particles weights of an initial particle model of the system of interest such as to reproduce a given set of observables. De Lorenzi et al. (2007, hereafter DL07) improved the original method by Syer & Tremaine (1996) to take into account observational errors, and implemented it as the NMAGIC code. NMAGIC has been used in numerous studies, mostly in the context of elliptical galaxies (e.g. De Lorenzi et al. 2009; Das et al. 2011; Morganti et al. 2013) and has been adapted to barred galaxies by Martinez-Valpuesta (2012). In the context of the Milky Way, the M2M method has previously been used by Bissantz, Debattista & Gerhard (2004), Long et al. (2013) and Hunt & Kawata (2014).

### 2.3.1 Theory of the M2M method

Let us consider a system characterized by its DF  $f(\mathbf{z})$  defined on the phase space of the system. Any observable  $y_j$  of this system will be written as

$$y_j = \int K_j(\mathbf{z}) f(\mathbf{z}) d^6 z, \quad (2.1)$$

where  $K_j$  is the kernel of the observable and  $\mathbf{z}$  the phase space vector. If we represent the system by a set of  $N$  particles, with particle weights  $w_i(t)$ , the observable will be written as

$$y_j(t) = \sum_{i=1}^N K_j(\mathbf{z}_i(t)) w_i(t), \quad (2.2)$$

where  $\mathbf{z}_i(t)$  is the phase-space coordinate of particle  $i$  at time  $t$ . The  $w_i$  are proportional to the physical weights of the particles but one can also see them as density-elements of the phase-space.

Let us now consider different data sets, indexed by the subscript  $k$ , that one wants to fit. The difference between the model and the observational target is quantified using the residuals  $\Delta_j^k(t)$  defined as

$$\Delta_j^k(t) = \frac{y_j^k(t) - Y_j^k}{\sigma(Y_j^k)}, \quad (2.3)$$

where  $Y_j^k$  denotes an observable of data set  $k$ ,  $\sigma(Y_j^k)$  its associated error, and  $y_j^k(t)$  the corresponding model observable.



The M2M method will adapt the weights of the particles in order to maximize the profit function  $F$  defined by

$$F = \mu S - \frac{1}{2} \chi_{\text{tot}}^2, \quad (2.4)$$

where

$$S = - \sum_i w_i \log \left( \frac{w_i}{\widehat{w}_i} \right) \quad (2.5)$$

and

$$\chi_{\text{tot}}^2 = \sum_{k,j} \lambda_k (\Delta_j^k)^2. \quad (2.6)$$

$S$  corresponds to an entropy term used to regularize the particle weights in order to ensure that they do not deviate too much from a set of predefined priors  $\widehat{w}_i$ . The  $\lambda_k$  are numerical weights of the different data sets, as formally introduced by Long & Mao (2010). The determination of these factors is discussed in Section 2.3.6.

The heart of the M2M method is the following weight evolution equation:

$$\frac{dw_i}{dt} = \varepsilon w_i(t) \left[ \frac{\partial F}{\partial w_i} \right] \quad (2.7)$$

$$= \varepsilon w_i(t) \left[ \mu \frac{\partial S}{\partial w_i} - \sum_k \lambda_k \sum_j \frac{K_j(\mathbf{z}_i(t))}{\sigma(Y_j^k)} \Delta_j^k(t) \right] \quad (2.8)$$

where the bracket term is the so-called force-of-change. Note that the passage from Equation 2.7 to Equation 2.8 is made under the assumption that the kernels  $K_j^k$  do not depend on the weights of the particles. We will make this assumption as it allowed Syer & Tremaine (1996) and DL07 to prove the convergence of the particle weights for small linear deviations from the solution. No additional term is used in Equation 2.8, in particular we do not re-normalize the weights of the particles. This is done on purpose to allow fitting different masses of the bulge as shown in Section 2.4.

In order to reduce the shot noise of the particle model we follow Syer & Tremaine (1996) and DL07 and artificially increase the effective number of particles using temporal smoothing, replacing  $y_j(t)$  in Equation 2.3 by

$$\tilde{y}_j(t) = \int y_j(t - \tau) e^{-\alpha\tau} d\tau. \quad (2.9)$$

## 2.3.2 Density observables

### 3D density of Red Clump Giants

Using the Red Clump Giants (RCGs) from the VVV survey, WG13 measured the three-dimensional density distribution of the inner part of the galactic bar/bulge. They evaluate line-of-sight density distributions of the RCGs by deconvolution of extinction and completeness corrected  $K_s$  band magnitude distributions for different VVV fields. To do so,

they fit a background to each  $K_s$  band magnitude distribution and identify the RCGs as the excess over this background. Assuming an 8-fold mirror symmetry, they constructed a 3D density map of the RCGs in the inner  $\pm 2.2 \times \pm 1.4 \times \pm 1.2$  kpc along the  $(x', y', z')$  axes of the galactic bar/bulge, and checked that the data show only small deviations from 8-fold symmetry (their 15). Their work relies on several assumptions that they carefully investigated for systematic variations of their fiducial parameters. They finally provide us with one fiducial and five variant density maps of RCGs in the bulge. We use the range of these variant maps as a systematic error on the density measurements. The typical magnitude of these errors is about 10%.

We assume here that RCGs are good tracers of the stellar mass in the bulge, i.e. that the ratio of number of RCGs per unit of stellar mass stays constant in the bulge. This assumption is supported by the theoretical work of [Salaris & Girardi \(2002\)](#) where they showed that for an old star population of about 10 Gyr one would expect the number of RCGs to vary by less than 10% for metallicity in the range  $-1.5 \leq [M/H] \leq 0.2$ . As the bulge appears uniformly old with no significant metallicity component extending beyond the range  $-1.5 \leq [M/H] \leq 0.2$  ([Zoccali et al. 2003](#)), we can consider RCGs as good tracers of the stellar mass and therefore use the map of WG13 as a constraint on the shape of the stellar mass density in our models. Note that the map gives only the shape of the density and not its absolute value because the number of RCGs per unit of stellar mass is a priori unknown.

Unfortunately high extinction and crowding prevented WG13 to reliably measure the RCGs density within 150 pc of the galactic plane, and also cause some uncertainty immediately above this 150 pc strip. Using directly the original map with this missing strip would be inappropriate since we want to model different bulge masses by changing the scaling of the density constraint. An incomplete map would let the midplane free and lead to unrealistic models, with for example a light in-plane component and a massive out-of-plane component. Hence we model the density in the missing  $\pm 150$  pc strip by extrapolation of each vertical density profile of the original 3D map.

We found that the vertical density profiles in both the data of WG13 and the initial particle models are well represented by a  $\text{sech}^2$  function. Our fiducial extrapolation is thus based on the best  $\text{sech}^2$  fit of each vertical profile. We account for the uncertainty due to the choice of the extrapolation law by considering a different one in [Section 2.5.2](#), showing that the total bulge mass is insensitive to this choice.

The fiducial extrapolated density map of RCGs in the  $\pm 2.2 \times \pm 1.4 \times \pm 1.2$  kpc box is plotted in projection in [Figure 2.3](#). The side-on view shows a very strong peanut-shape.

## Implementation in NMAGIC

The 3D density map was evaluated on a regular Cartesian grid of (30, 28, 32) cells along the  $(x', y', z')$  axis, covering a box of the inner  $\pm 2.2 \times \pm 1.4 \times \pm 1.2$  kpc, as in WG13. We will refer to this region as the “bulge-in-box” or the abbreviation b-b. From WG13 we know the total number of RCGs in the b-b, but the corresponding stellar mass must still be determined from dynamical modelling. We parametrize the total stellar mass of the b-b

using a dimensionless factor,  $\mathcal{F}$ , defined as the ratio of the target stellar mass of the b-b divided by its value in the initial model. The target density observables  $Y_j^d$ , corresponding to the target stellar mass in cells  $j$ , in internal units, are then given by

$$Y_j^d = \mathcal{F} \left( \sum_{i \in \text{b-b}} w_i(t=0) \right) \frac{n_{\text{RCGs}}(j) \Delta^3 x}{\int_{\text{b-b}} n_{\text{RCGs}} d^3 x} \quad (2.10)$$

where the sum is over all initial particle weights in the b-b,  $n_{\text{RCGs}}$  is the number density of RCGs, and  $\Delta^3 x$  the volume of the cells. For a given scaling from model internal units to physical units, a change in the value of  $\mathcal{F}$  is equivalent to a change in the target stellar mass of the b-b. For a given  $\mathcal{F}$ , NMAGIC takes care of increasing or decreasing the weights of the particles to reach the target observables  $Y_j^d$ , thereby modelling different-mass bulges.

The model density observables in the cells of the b-b are then computed from [Equation 2.2](#) using the following kernel

$$K_j^d(\mathbf{z}_i) = \begin{cases} 1 & \text{if } i \in \text{cell } j, \\ 0 & \text{otherwise.} \end{cases} \quad (2.11)$$

### 2.3.3 Kinematic observables

#### BRAVA data

We kinematically constrain our models using data from the Bulge RAdial Velocity Assay (BRAVA) ([Rich et al. 2007](#); [Howard et al. 2008](#); [Kunder et al. 2012](#)). The BRAVA survey is a large spectroscopic survey of M giant stars selected from the 2MASS catalogue. According to [Howard et al. \(2008\)](#), the light of these M giants traces the  $2 \mu\text{m}$  light of the GB and therefore M giants are a good proxy to study the overall kinematics of the GB. The BRAVA survey provides us with galactocentric rest-frame mean radial velocity and velocity dispersion in more than 80 fields through the bulge, mostly between  $l = -10^\circ$  to  $l = 10^\circ$ . On starting this project the ARGOS data ([Ness et al. 2013a](#)) were not yet available so we restricted ourselves to the BRAVA data. The ARGOS data have a more complicated selection function and will be included in a later paper.

Before constraining a model it is important to study in detail how the BRAVA stars were selected in order to reproduce any selection bias. The BRAVA stars were selected from their location on a  $K$  versus  $J - K$  colour-magnitude diagram aiming to select only bulge members with no metallicity bias. [Howard et al. \(2008\)](#) deployed a lot of effort to ensure no metallicity bias but the bulge membership criteria based on magnitude cuts adjusted by eye are more questionable. We used the GALAXIA model ([Sharma et al. 2011](#)) to evaluate the possible foreground contamination using the same selection criteria. We found that contamination was negligible toward the centre but appears to rise with increasing galactic longitude, reaching 20% of the sample at  $l \sim 15^\circ$ . We found no significant variation with latitude in the latitude range of the BRAVA fields. We decided not to simulate this contamination, given the fact that the foreground discs in our models are not made to

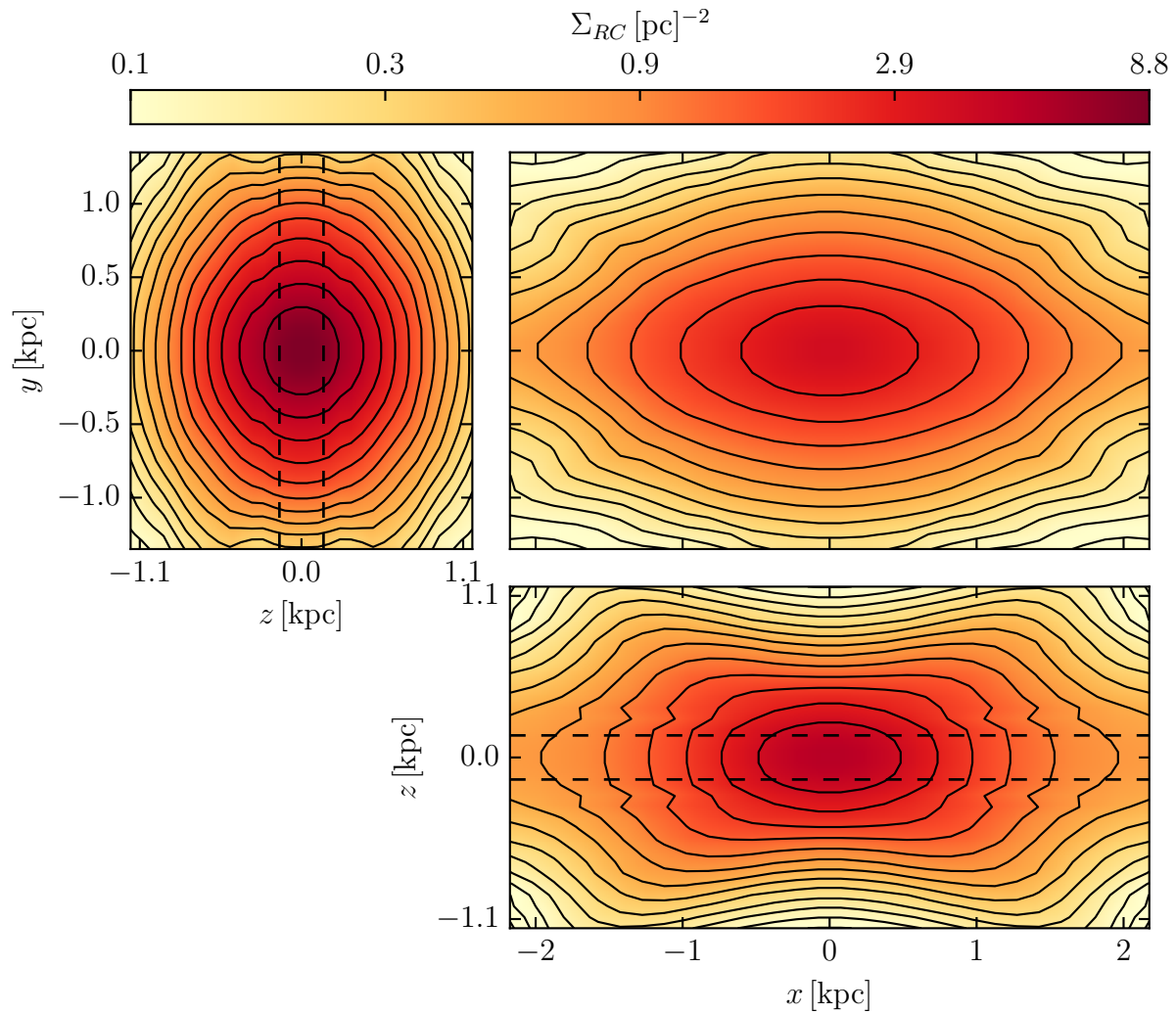


Figure 2.3: End-on (top left), face-on (top right) and side-on (bottom right) projection of the extrapolated 3D RCGs density map originally from [Wegg & Gerhard \(2013\)](#). The dashed lines in the end-on and side-on view show the  $\pm 150$  pc region where the density map was extrapolated.

match the disc of the Milky Way. Instead, we simply exclude from our analysis all the fields outside the inner  $\pm 10^\circ$  in longitude, where contamination is probably significant. The magnitude cuts also introduce a slight bias towards the near side of the bulge. Faint M giants are more numerous than bright ones so have a larger probability to be part of the sample on the near side than on the far side of the GB. We model this effect below.

### Implementation on NMAGIC

As stated in [Section 2.3.1](#), the linear convergence of the M2M method is assured if our observables are of the form given by [Equation 2.2](#), where the kernels do not depend on the weights of the particles. Therefore as our observables, instead of using the mean radial velocity and velocity dispersion we use the first and second mass weighted radial velocity moments, indexed as  $v_{r1}$  and  $v_{r2}$ . The observables are then of the form of [Equation 2.2](#) with the following kernels:

$$K_j^{v_{r1}}(\mathbf{z}_i) = \delta_j^{v_{r1}}(\mathbf{z}_i) v_i^r \quad (2.12)$$

$$K_j^{v_{r2}}(\mathbf{z}_i) = \delta_j^{v_{r2}}(\mathbf{z}_i) (v_i^r)^2 \quad (2.13)$$

where  $v_i^r$  is the radial velocity of the particle  $i$  and  $\delta_j^{v_{r1}, v_{r2}}$  are the field selection functions. In order to remove foreground contamination we consider only particles whose  $y$  coordinate (along the GC-Sun axis) is in absolute value lower than 3.5 kpc. This corresponds to the selection criterion used in the ARGOS survey ([Ness et al. 2013a](#)) and its use here is supported by the fact that ARGOS data and BRAVA data agree with each other. We checked that the exact form of this selection function does not change significantly the kinematic observables in the inner  $10^\circ$ .

In order to map the bias toward the near side we use the approximate luminosity function of giant stars in the bulge  $\Phi(M_K) \propto 10^{0.28 M_K}$  from [WG13](#) where  $M_K$  is the absolute magnitude in the  $K$  band. In each field, stars of the BRAVA sample are uniformly selected between two magnitude cuts from their apparent magnitude  $m_K = M_K + 5 \log(r/10 \text{ pc}) + A_K$  where  $r$  is the distance to the Sun and  $A_K$  is the extinction. If we consider the extinction as a foreground extinction, this uniform selection in  $m_K$  is equivalent to a non-uniform selection in  $r$  along the line of sight with weighting  $10^{-0.28 \times 5 \log(r)} = r^{-1.4}$ . This  $r^{-1.4}$  weighting lowers the natural  $r^2$  weighting due to the cone opening of the line-of-sight. We therefore adopt the following selection function:

$$\delta_j^{v_{r1,2}}(\mathbf{z}_i) = \begin{cases} r_i^{-1.4} & \text{if } i \in \text{field } j \text{ and } |y_i| < 3.5 \text{ kpc,} \\ 0 & \text{otherwise.} \end{cases} \quad (2.14)$$

In order to compare the model observables to the target data, we have to weigh the target data by the expected mass in each field. As the stellar mass in each field is unknown, we use the model mass, and update this weighting several times during the fit (see [Section 2.3.6](#)).

### Proper motions

In addition to the BRAVA data, we use proper motion data from [Rattenbury et al. \(2007a\)](#). These authors computed proper motion dispersions,  $\sigma_{l,b}$ , in the  $l$  and  $b$  directions for a large number of bulge RCGs in 45 bulge fields from proper motion measurements for stars in the OGLE-II survey. We use these proper motions as a check of our modelling, comparing the data to our model predictions, without fitting them. [Rattenbury et al. \(2007a\)](#) selected bulge RCGs from their colours and magnitudes, and excluded all stars with total proper motion larger than  $10 \text{ mas yr}^{-1}$ . The bulge membership of model particles is evaluated using the same criterion as for the BRAVA observables, i.e.  $|y| \leq 3.5 \text{ kpc}$ . Similarly to the BRAVA observables, our proper motion observables are the first and second velocity moments in the  $l$  and  $b$  direction, indexed by  $v_{l1,2}$  and  $v_{b1,2}$ . The kernels of the first and second velocity moments in the  $l$  and  $b$  directions are similar to those of [Equation 2.12](#) and [Equation 2.13](#), replacing  $v_i^r$  by the velocity of particle  $i$  in the  $l$  and  $b$  direction, expressed in  $\text{mas yr}^{-1}$ .

Our selection function when evaluating the model proper motion observables is then given by:

$$\delta_j^{\mathbf{v}_{l1,2}, \mathbf{v}_{b1,2}}(\mathbf{z}_i) = \begin{cases} 1 & \text{if } i \in \text{field } j, |y_i| < 3.5 \text{ kpc} \\ & \text{and } \sqrt{v_l^2 + v_b^2} \leq 10 \text{ mas yr}^{-1} \\ 0 & \text{otherwise} \end{cases} \quad (2.15)$$

### 2.3.4 Dynamical velocity scaling

Our models are evolved in a system of internal units where the length unit, velocity unit and gravitational constant are set to unity. When comparing model to data we scale the models to physical units using the length of the bar (see [Section 2.2.2](#)), the gravitational constant and a velocity scaling. This velocity scaling is first fixed to some reference value using the circular velocity at the radius of the Sun from [Bovy et al. \(2012\)](#) ( $218 \text{ km s}^{-1}$ ). Keeping the velocity scaling fixed to this value would be inappropriate, however: our models are constrained in the inner part by the BRAVA data and the 3D density but no effort has been made to make the model rotation curves match the MW rotation curve at larger radii. Therefore the velocity scaling given by the circular velocity at the radius of the Sun is not relevant in the bulge. Hence we determine the velocity scaling directly from the BRAVA data using a variant of the method presented by [De Lorenzi et al. \(2008\)](#). In [Equation 2.12](#) and [Equation 2.13](#) we replace the radial velocity of a particle  $v_i^r$  by  $\gamma v_i^r$ , where  $v_i^r$  is now the radial velocity of particle  $i$  expressed in physical units using the reference velocity scaling, and  $\gamma$  is a numerical factor initially set to one. Through [Equation 2.2](#) and [Equation 2.3](#) the total  $\chi^2$  ([Equation 2.6](#)) and the profit function  $F$  ([Equation 2.4](#)) now depend on  $\gamma$ . To find the maximum of  $F$  with respect to  $\gamma$ , we use the following evolution equation for  $\gamma$ , similar to the force-of-change equation:

$$\frac{d\gamma}{dt} = -\eta\gamma \frac{\partial \chi^2}{\partial \gamma} \quad (2.16)$$

where  $\eta$  sets the magnitude of the force-of-change applying on  $\gamma$ . The velocity scaling plays a role for the kinematic observables only, so the derivative of  $\chi^2$  is given by

$$\frac{\partial \chi^2}{\partial \gamma} = 2 \sum_j \lambda_{v_{r1}} \Delta_j^{v_{r1}} \frac{\partial \Delta_j^{v_{r1}}}{\partial \gamma} + \lambda_{v_{r2}} \Delta_j^{v_{r2}} \frac{\partial \Delta_j^{v_{r2}}}{\partial \gamma} \quad (2.17)$$

where the derivatives of the  $\Delta_j^{v_{r1,2}}$  are given by the following equations:

$$\frac{\partial \Delta_j^{v_{r1}}}{\partial \gamma} = \frac{y_j^{v_{r1}}}{\gamma \sigma(Y_j^{v_{r1}})} \quad (2.18)$$

$$\frac{\partial \Delta_j^{v_{r2}}}{\partial \gamma} = \frac{2 y_j^{v_{r2}}}{\gamma \sigma(Y_j^{v_{r2}})} \quad (2.19)$$

The value of  $\eta$  should be large enough to ensure the convergence of  $\gamma$  during the fit, but the time-scale for its evolution must be longer than the temporal smoothing time-scale. We fixed  $\eta$  to 0.4 from estimating the magnitude of the right hand side of [Equation 2.16](#). In all our fits,  $\gamma$  converges to some final value which we use to convert internal units to physical units. All velocities and proper motions are scaled by  $\gamma$  with respect to their value with the reference scaling and all masses are scaled by  $\gamma^2$ .

### 2.3.5 Potential and model integration

Stellar and dark matter particles are all integrated in their combined potential that comes initially from our models of barred discs evolved in dark matter haloes (see [Section 2.2](#)). Only stellar particles are used as M2M particles, whose masses are both used as gravitational masses and as M2M weights. During the NMAGIC fits, the gravitational potential changes as the particle weights in the bulge adapt to match the target density (including the  $\mathcal{F}$  factor) and the kinematic constraints. To take this into account, the potential of the stellar and halo particles is recomputed from time to time during the fit. This ensures that the new weights of the disc particles can influence the kinematics of the model and that the final converged model evolves in its own gravity. In between potential updates, the particles are integrated in a frozen rotating potential. The potential always rotates at the constant pattern speed  $\Omega_p$  of the initial model, in internal units, and the centre of mass as well as the rotation axis of the potential are kept fixed during the complete NMAGIC fit. Each potential update corresponds to an update of the orbit library.

In all our fits the potential is recomputed 10 times during the weight evolution, which we found is sufficient to ensure the self-gravity of the converged model as well as smooth updates of the orbit library. The potential is computed using the 3D polar grid code from [Sellwood & Valluri \(1997\)](#). The particles are integrated with a drift-kick-drift adaptive leap-frog algorithm. The integration scheme is such that over a typical fit integration time in a fixed potential, the Jacobi energy is conserved to a level of  $10^{-3}$  or better.

### 2.3.6 NMAGIC parametrization

#### Fitting procedure

A typical NMAGIC fit consists of the three following phases. First we evolve the particles  $T_{\text{smooth}}$  iterations during which we compute the model observables in order to initialize the temporally smoothed observables. Then we integrate the model for  $T_{\text{M2M}}$  iterations, changing the weights of the particles according to Equation 2.8 while updating the potential regularly. All observables are matched to the data at the same time. After a last potential update we finally relax the model for  $T_{\text{relax}}$  iterations without changing the particle weights. This last phase is important to avoid over-fitting the data and obtain realistic models. The usually slight  $\chi^2$  increase during this relaxation reveals how much the model was forced to fit the data by Equation 2.8. At the end of the run, we also checked the convergence of the particle weights, using the convergence criterion detailed in Long & Mao (2010). A particle weight is considered to have converged if its maximum relative deviation from its mean value over some period of time is smaller than some threshold. Assuming a period of time corresponding to four circular orbits at 2 kpc and a threshold of 10%, about 97% of the particles weights converge in a typical NMAGIC fit.

#### Parameter values and time-scales

The parameter values we use are shown in Table 2.2. The iteration step of the M2M procedure  $dt$  is fixed to one thousandth of the time needed to complete a circular orbit of radius 2 kpc. All models are integrated for a constant number of  $dt$  so the number of bar rotations during the weight adaptation phase varies from model to model, ranging between 25 for model M80 and 35 for model M90. This corresponds to a physical integration time between 6 and 7 Gyr, once scaled to physical units using the velocity scaling determined dynamically by NMAGIC.  $1/(\alpha * dt)$  is the time-scale of the temporal smoothing expressed in terms of number of M2M iterations, and  $\varepsilon/w_0$  is the magnitude of the force-of-change in Equation 2.8, where  $w_0$  is the initial weight of a stellar particle.

#### $\lambda_k$ parameters and regularization

The different set of observables, here RCGs 3D density and BRAVA data are weighted by the  $\lambda_k$  parameters in the profit function. The force-of-change (Equation 2.8) already takes into account observational errors so in theory these  $\lambda_k$  should all be set to 1, in order to really minimize the total  $\chi^2$ . In practice, experiments showed that with all  $\lambda_k = 1$  the model ignores completely the kinematic constraints. This is mostly caused by the very large number of density constraints (26880) with respect to kinematic constraints (164). As we do want to fit the BRAVA data, we increase the weighting of BRAVA constraints with respect to the RCGs density using  $\lambda_{v,r1}/\lambda_d = \lambda_{v,r2}/\lambda_d = 25$ , even if then we no longer strictly minimize the total  $\chi^2$ . These  $\lambda_k$  were determined using the distribution of the force-of-change contribution of each set of observables, such that the mean force-of-change due to the density observables should be equal to the mean force-of-change due to the



Table 2.2: Typical set of NMAGIC parameters.  $T_{\text{smooth}}$ ,  $T_{\text{M2M}}$  and  $T_{\text{relax}}$  are the number of iterations for the 3 phases of a NMAGIC fit.  $T_{\Phi}$  and  $T_{\text{mass}}$  are the number of iterations between two potential updates and updates of the mass weighting for the kinematic observables.  $1/(\alpha * dt)$  is the time-scale of the temporal smoothing in number of iterations.  $\varepsilon/w_0$  is the magnitude of the force of change and  $w_0$  is the initial weight of the stellar particles. The  $\lambda$  parameters are described in [Section 2.3.6](#).

$T_{\text{smooth}}$ [it]	$T_{\text{M2M}}$ [it]	$T_{\text{relax}}$ [it]	$T_{\Phi}$ [it]	$T_{\text{mass}}$ [it]
$10^4$	$10^5$	$2 \times 10^4$	$10^4$	$10^4$
$1/(\alpha * dt)$ [it]	$\varepsilon/w_0$ [iu <sup>-1</sup> ]	$\lambda_d$	$\lambda_{v_{r1}, v_{r2}}$	
$2.5 \times 10^3$	0.04	1	25	

BRAVA observables. This causes the BRAVA data to be reasonably fitted without being over-fitted. A strong over-fitting would lead to a significant increase of  $\chi^2$  during the relaxation step at the end of the fit.

We found that our models were smooth enough without using any entropy smoothing. This is a consequence of the very dense constraint from the 3D density data. Hence we chose to set  $\mu = 0$  in [Equation 2.8](#) for all our models.

## 2.4 Dynamical models of the MW

In this section we fit our initial models to the BRAVA data and the 3D RCGs density using NMAGIC. The models differ by their dark matter fraction in the inner part and by their dimensionless corotation radius  $\mathcal{R}$  (see [Section 2.2.2](#)). In [Section 2.4.1](#), we determine the best bulge stellar mass  $\mathcal{F}$  for each model, using the full NMAGIC modelling procedure described above, and in [Section 2.4.2](#), we compare all models with their respective best  $\mathcal{F}$ . In [Section 2.4.3](#), we constrain the pattern speed of the MW bar from this modelling, and in [Section 2.4.4](#) we compare the models with available proper motion data.

### 2.4.1 Determination of the stellar mass in the bulge

In [Section 2.3.2](#) we parametrized the target density observables using a free numerical factor  $\mathcal{F}$ . The value of  $\mathcal{F}$  directly sets the stellar mass of the bulge in internal units for each model. We find that  $\mathcal{F}$  has a strong influence on the velocity dispersions but only a very slight influence on the mean velocities. Empirically, the shape of the mean velocity profile in our models is fixed by the density distribution. The velocity amplitude in internal units is then fixed by the pattern speed (8 of [Debattista, Gerhard & Sevenster 2002](#)). The larger kinetic energy in models with larger bulge mass  $\mathcal{F}$  can therefore only be put into the velocity dispersion. This is shown in [Figure 2.4](#) where the kinematic observables of model

M85 are plotted along with the BRAVA data. In this figure the different coloured lines show the kinematic profiles obtained after fit of the density normalized with different values of  $\mathcal{F}$ . The upper (lower) plots show mean radial velocity (velocity dispersion) profiles for three different latitudes as well as along the minor axis. For the comparison, the model observables in [Figure 2.4](#) have all been plotted for the same scaling constant so as to match only the mean velocity data. As  $\mathcal{F}$  has nearly no influence on the velocity, this better highlights the effect of  $\mathcal{F}$  on the dispersion.

[Figure 2.4](#) illustrates how more massive bulges lead to higher radial velocity dispersions. By finding the value of  $\mathcal{F}$  which gives the best agreement with the data, we can recover the stellar mass of the b-b for each model. [Figure 2.5](#) shows the  $\chi^2$  per data point of the velocity and velocity dispersion for all models plotted in [Figure 2.4](#), versus  $\mathcal{F}$ . As expected, a clear minimum is present in the dispersion plot and provides us with a best value of  $\mathcal{F}$  for each model. Best values of  $\mathcal{F}$  are given for all models in the first column of [Table 2.3](#). With the optimal velocity scaling determined in these NMAGIC fits, these  $\mathcal{F}$  values can be converted into physical values of stellar mass in the b-b. We find values of  $1.25 \times 10^{10} M_\odot$  for model M80 to  $1.6 \times 10^{10} M_\odot$  for model M90; see also [Section 2.5](#).

$\mathcal{F}$  was sampled on a regular grid with spacing 0.1 and is therefore determined with an accuracy of 0.05. Due to the rescaling during the NMAGIC fits, an uncertainty of 0.05 in  $\mathcal{F}$  typically corresponds to a change of less than  $0.025 \times 10^{10} M_\odot$  in the final stellar mass and less than  $0.01 \times 10^{10} M_\odot$  in total mass (stellar and dark matter in the b-b).

### 2.4.2 Best dynamical models of the Milky Way bulge

Now we compare our five best dynamical models M80-M90 with different dark matter haloes, obtained after NMAGIC fit to the data for their respective best value of  $\mathcal{F}$ . For all models the density and its peanut shape is well fitted as shown in [Figure 2.6](#). This figure compares the contours of the three principle axis projections of the density in the bulge after fitting with the target RCGs density. Each colour line represents one of our best mass models and the black line is the projection of the target density.

The radial velocity and dispersion profiles of the same best  $\mathcal{F}$  models are plotted in [Figure 2.7](#). Except for small differences in the shapes of the dispersion curves, they all look very similar and provide a good fit to the data. This similarity is explained by the fact that the shape of the velocity profile is mostly fixed by the shape of the density and its magnitude is adapted to the data by the floating velocity scaling. The magnitude of the velocity dispersion profiles can then be adapted independently by the  $\mathcal{F}$  parameter.

More quantitatively, the  $\chi^2$  per data point is shown in [Table 2.3](#) separately for the density, the total kinematics, the velocity only and the velocity dispersion only. Values in this table are not weighted by the corresponding  $\lambda_k$  parameters. The total  $\lambda_k$ -weighted chi square  $\chi_{\text{tot}}^2/n_{\text{tot}} = \sum \lambda_k \chi_k^2 / \sum \lambda_k n_k$  actually minimized by NMAGIC is given in the last column of [Table 2.3](#).

All our models provide good fits of the RCGs density with a final  $\chi_{\text{d}}^2/n_{\text{d}}$  from 0.23 to 0.42. As the errors in the density are systematic, one should not over-interpret these  $\chi^2$  values. The kinematics are also well fitted for all models with the model dispersions

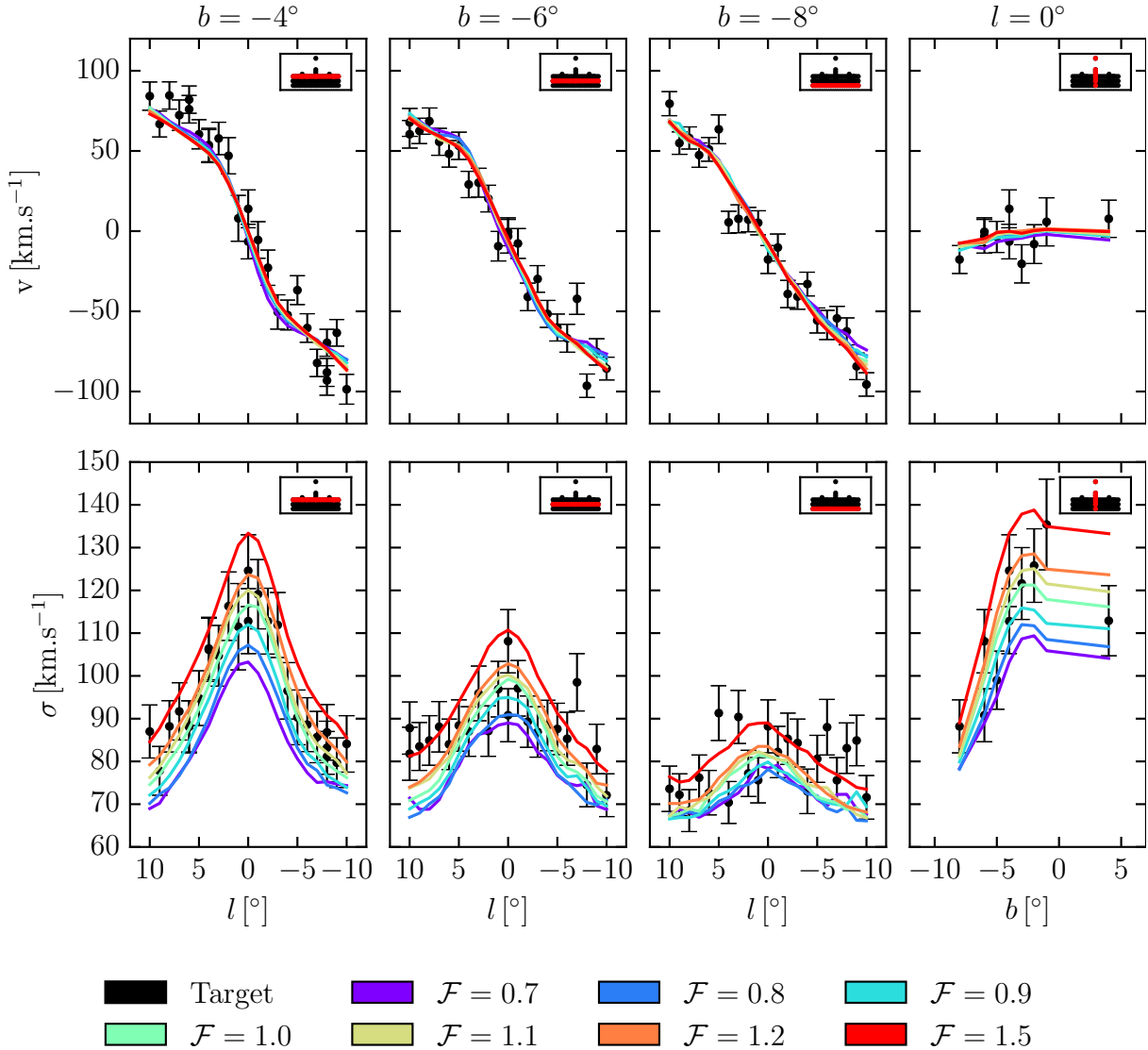


Figure 2.4: Comparison of the BRAVA data to the fitted model M85, for different values of the stellar mass parameter  $\mathcal{F}$ . The upper (lower) plots show the BRAVA mean radial velocity (velocity dispersion) profiles for  $b = -4^\circ$ ,  $b = -6^\circ$ ,  $b = -8^\circ$  and along the minor axis  $l = 0^\circ$ . The different colours indicate different values of  $\mathcal{F}$  as stated in the legend. The influence of  $\mathcal{F}$  on the kinematics is clearly visible in the dispersion plots. The small inserts on the top right of each plot show the BRAVA fields in galactic coordinates and highlight the fields shown in the corresponding plot.

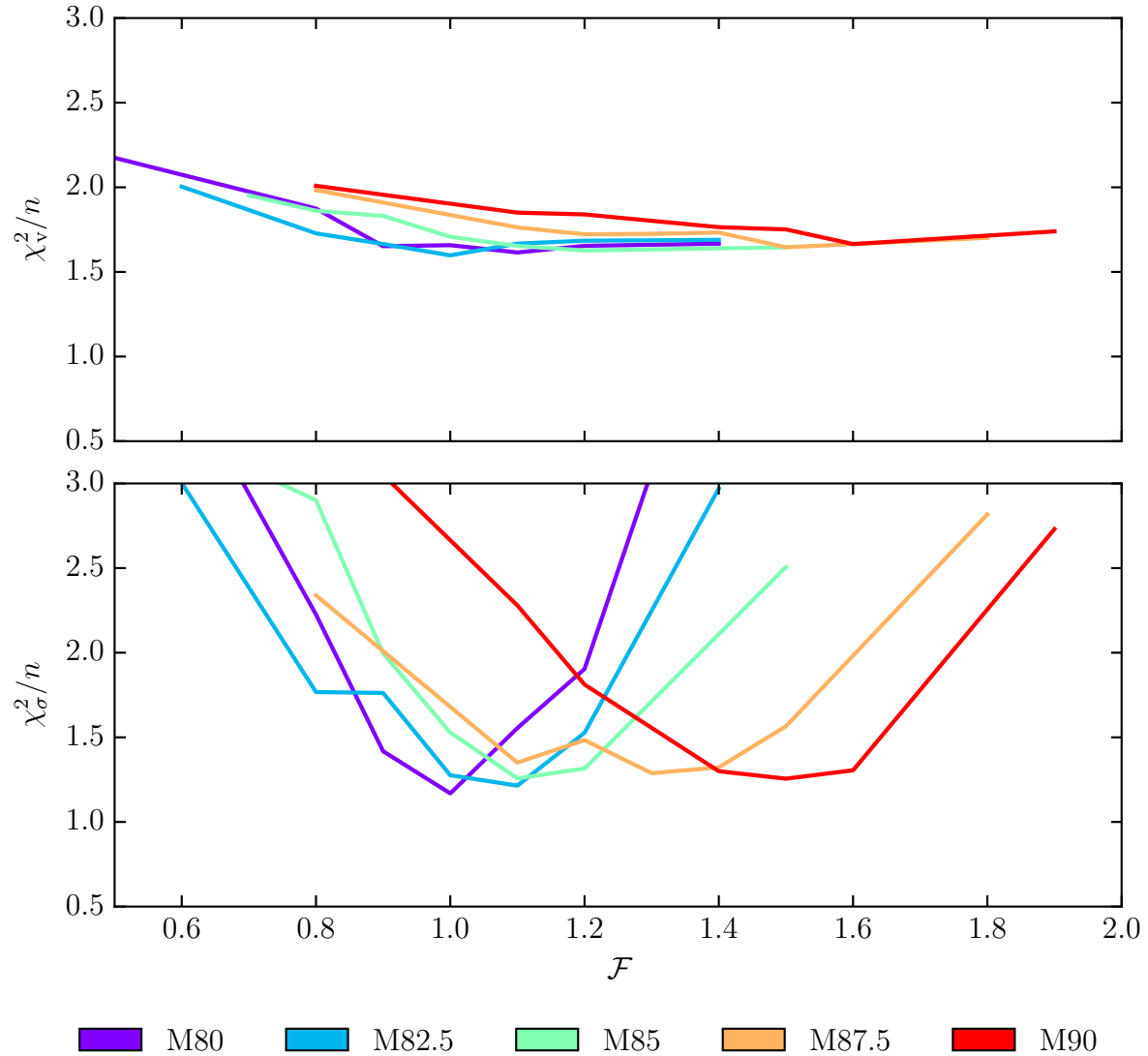


Figure 2.5:  $\chi^2$  per data point of the velocity observables (*upper plot*) and velocity dispersion observables (*lower plot*) as a function of the bulge mass factor  $\mathcal{F}$ . Each colour represents a different initial model from Section 2.2 as shown in the legend. In all cases, a best value of  $\mathcal{F}$  is clearly visible from the velocity dispersion  $\chi^2$ -curves.

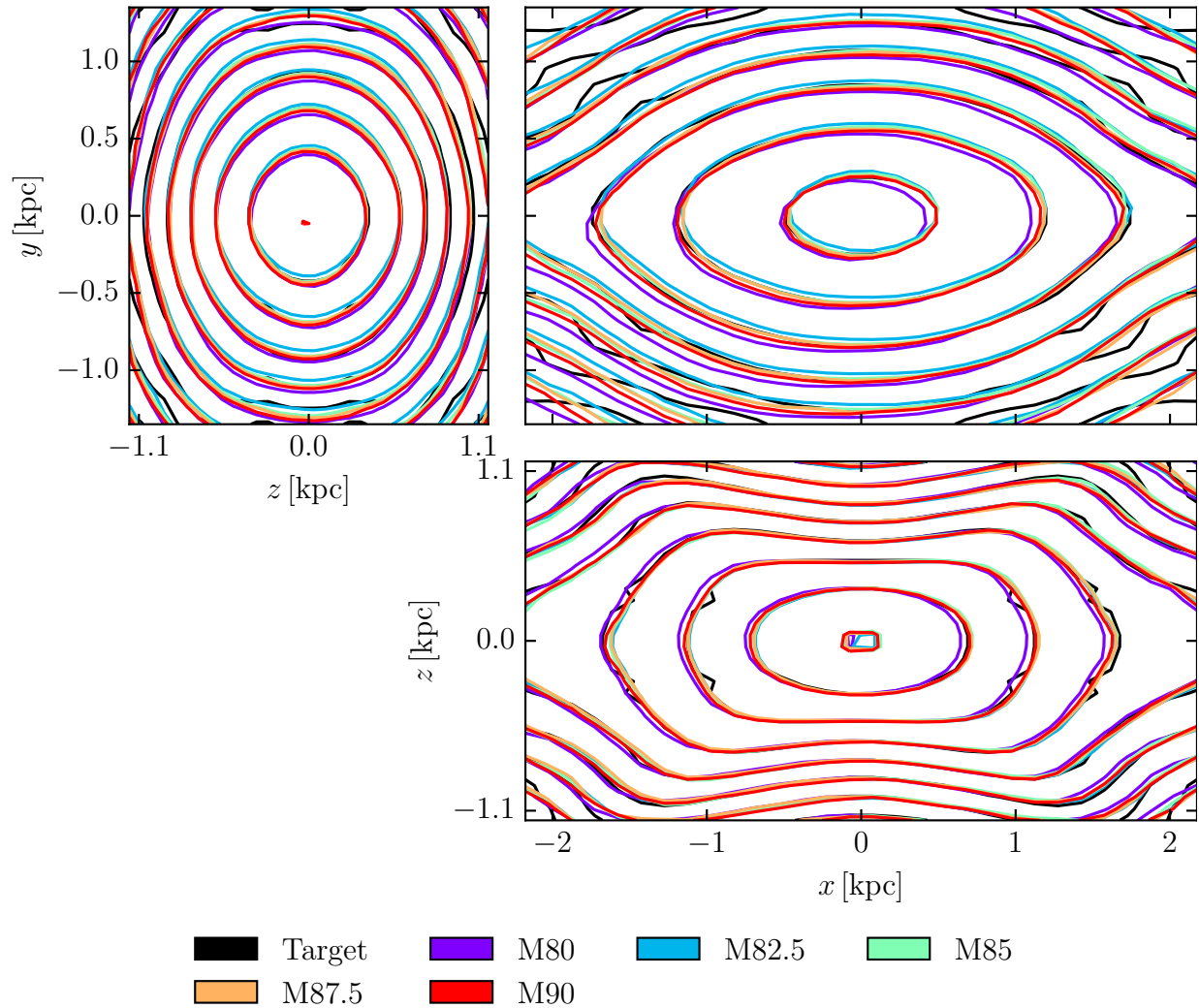


Figure 2.6: Contour plot of the projected 3D density in the bulge of our best dynamical mass models compared to the measured RCGs density from [Wegg & Gerhard \(2013\)](#). The projections are the same as in [Figure 2.3](#) and the contours are spaced by a third of a magnitude. In all cases the density is well fitted.

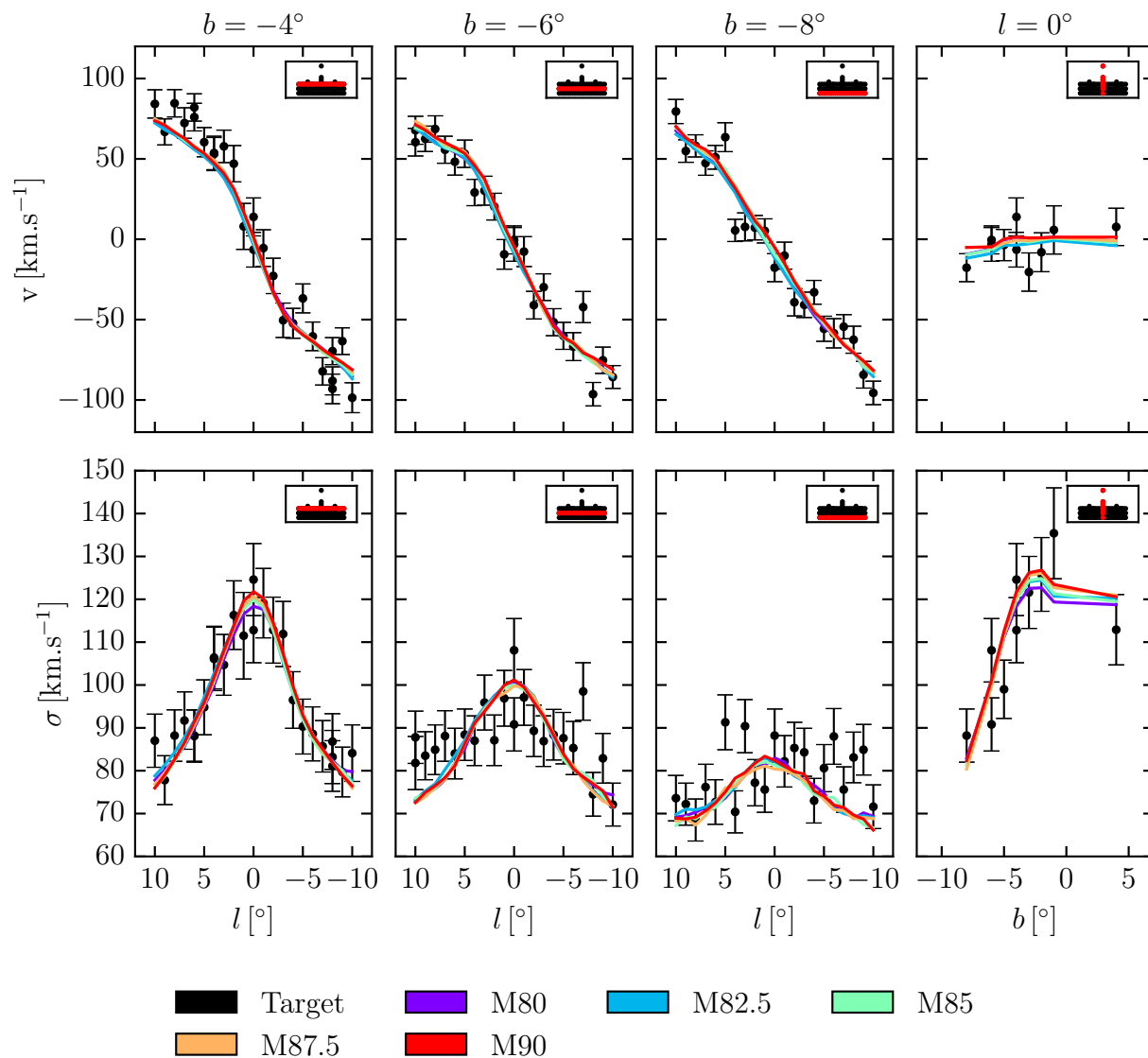


Figure 2.7: Velocity and velocity dispersion profiles for our five best dynamical models of the Milky Way with different dark matter haloes. The plotting conventions are the same as in Figure 2.4 except that here the colours indicate different models as stated in the legend.

Table 2.3: Best values of  $\mathcal{F}$  and  $\chi^2$  per data point of the density observables ( $\chi_d^2/n_d$ ), total kinematic observables ( $\chi_k^2/n_k$ ), velocity only ( $\chi_v^2/n_v$ ) and dispersion only ( $\chi_\sigma^2/n_\sigma$ ) for our five best dynamical mass models. The last column shows the reduced  $\lambda_k$  weighted  $\chi^2$  actually minimized by NMAGIC.

Model	$\mathcal{F}$	$\chi_d^2/n_d$	$\chi_k^2/n_k$	$\chi_v^2/n_v$	$\chi_\sigma^2/n_\sigma$	$\chi_{\text{tot}}^2/n_{\text{tot}}$
M80	1.0	0.42	1.45	1.67	1.24	0.56
M82.5	1.1	0.32	1.46	1.68	1.24	0.47
M85	1.1	0.24	1.46	1.65	1.27	0.40
M87.5	1.3	0.23	1.52	1.73	1.31	0.40
M90	1.5	0.30	1.52	1.75	1.29	0.46

marginally steeper than the data for large  $|l|$  and  $|b|$ , and  $\chi_k^2/n_k$  ranging from 1.45 for model M80 to 1.52 for model M90. This kinematic  $\chi^2$  is significantly better than that obtained by Long et al. (2013). Given the scatter visible in the kinematic data, these models are good candidates to represent the MW bulge even if the kinematic  $\chi_k^2$  is about 1.5.

Because the different models all give a reasonable fit, we do not rule out some of them based on simple  $\chi^2$  considerations. One has to be careful when drawing conclusions comparing  $\chi^2$  values on typical M2M problems. Indeed, as shown by Morganti et al. (2013) the common practice to use  $\Delta\chi^2 = \chi^2 - \chi_{\text{min}}^2$  and  $\chi^2$  statistics to evaluate confidence levels on  $\chi_{\text{min}}^2$  is not appropriate for their M2M results. The  $\Delta\chi^2$  analysis requires a positive number of degrees of freedom, while it is usually negative in M2M problems because the particles are vastly more numerous than the data constraints. Hence, the  $\chi^2/n$  given in Table 2.3 are only an indication of the distance between model and data. These values are also strongly influenced by a few data points which appear to be possible outliers. This is the case for example in the fields at  $(l, b) = (-7^\circ, -6^\circ); (-5^\circ, -4^\circ); (-4^\circ, -8^\circ)$ . Removing these possible outliers reduces the absolute value of the kinematic  $\chi_k^2/n_k$  by about 0.2. It does not however change our best value of  $\mathcal{F}$ .

The face-on and side-on projections of our final best mass models are plotted Figure 2.8. Even though not enforced by NMAGIC, the long bar component is still there in the fitted models. Its presence indicates that the gravitational potential updates performed during the fit were smooth enough to keep long bar particles on bar orbits.

### 2.4.3 The pattern speed

The pattern speeds of our models are converted to physical units using the velocity scaling determined by NMAGIC in order to fit the BRAVA data. For models M80, M82.5, M85, M87.5 and M90 we get the values  $\Omega_p [\text{km s}^{-1} \text{kpc}^{-1}] = 24.7, 25.7, 27.7, 29.0, 28.8$ . This shows that the pattern speed of the MW bar and bulge in absolute units, as determined by the combination of the RCGs density and the BRAVA data, is between 25 and  $30 \text{ km s}^{-1} \text{kpc}^{-1}$ . This is slightly lower than the value of  $\Omega_p \sim 30 - 40 \text{ km s}^{-1} \text{kpc}^{-1}$

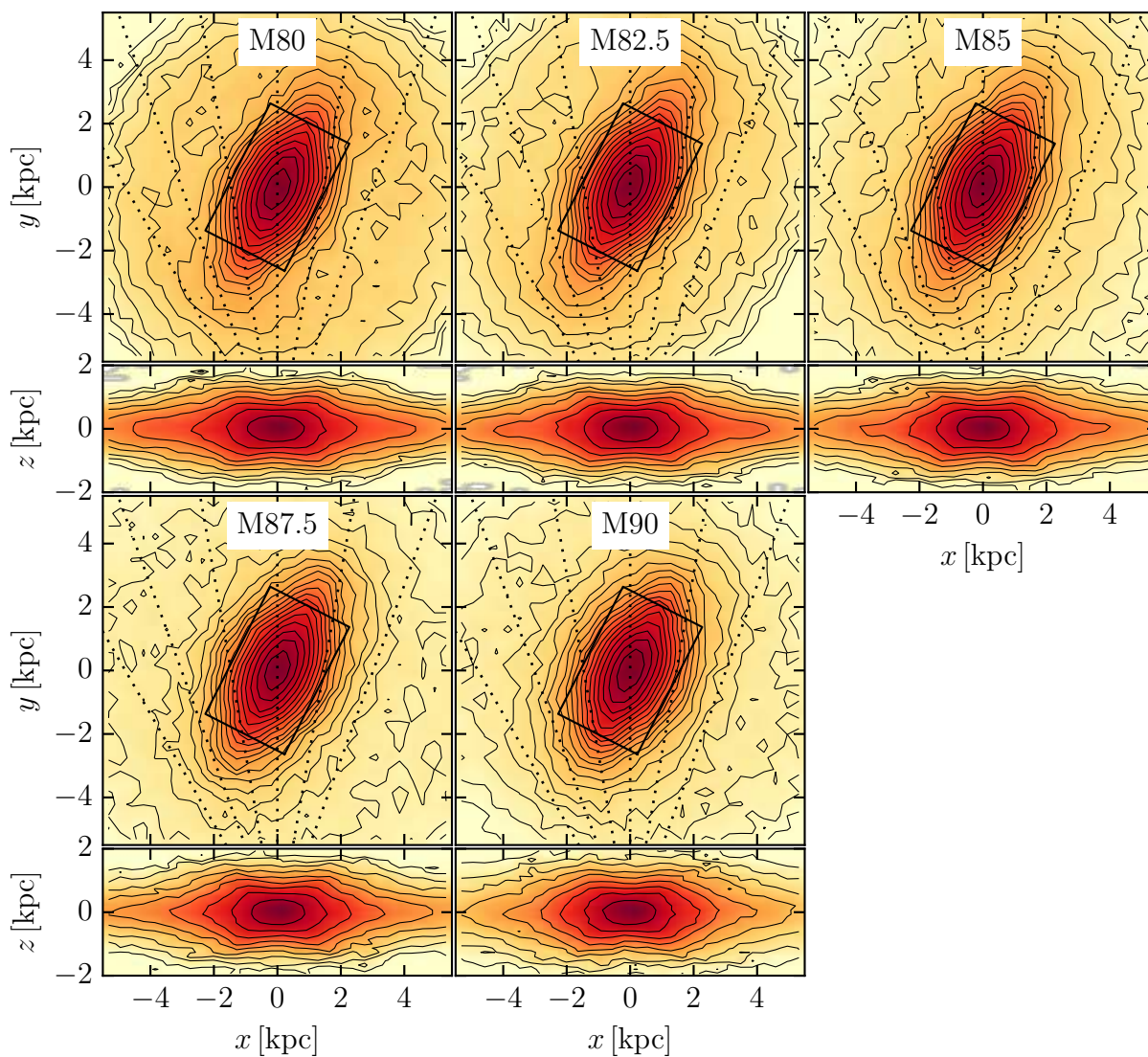


Figure 2.8: Face-on and side-on views of our best dynamical mass models after NMAGIC fit. Plotting conventions are the same as in Figure 2.2.



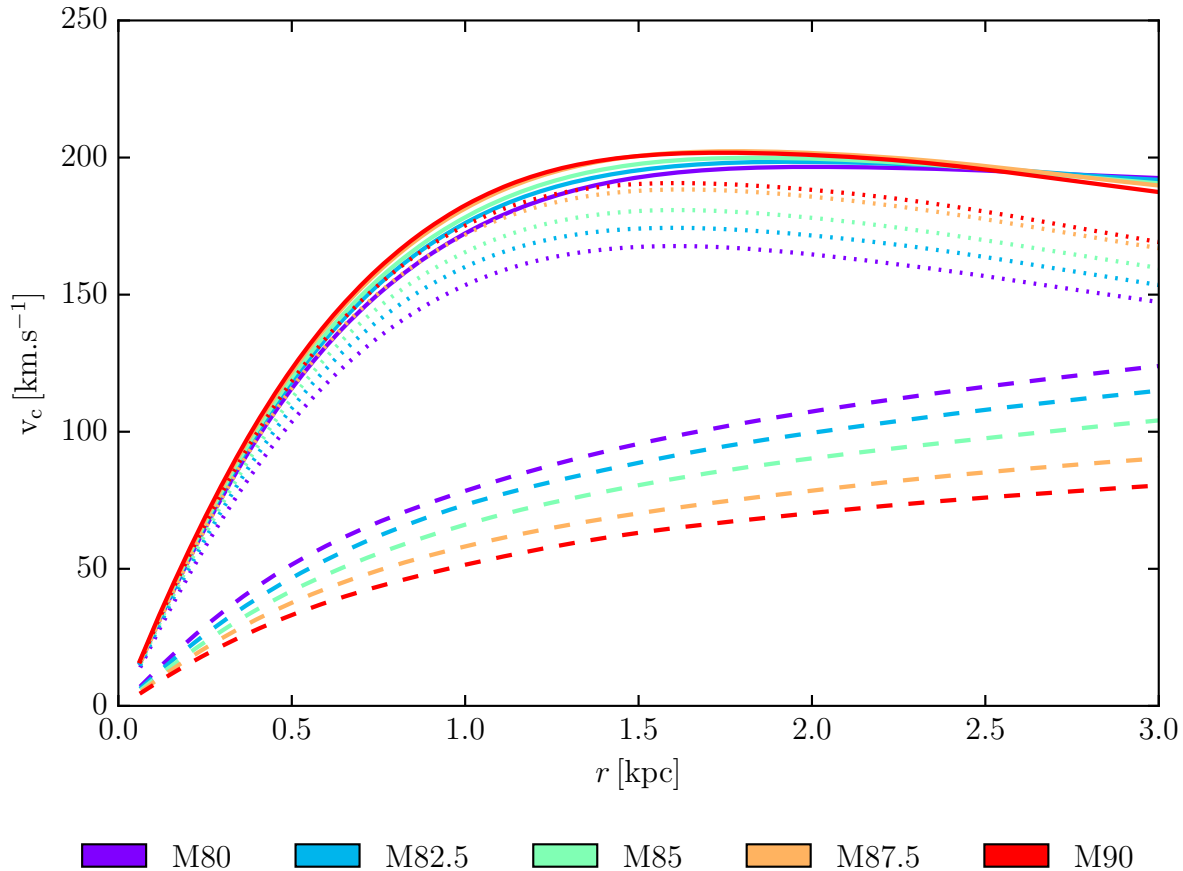


Figure 2.9: Circular velocity curves obtained from the azimuthally averaged potential of our best dynamical mass models after NMAGIC fit. The solid lines display the total rotation curves while dashed and dotted lines display the halo and disc contributions, respectively.

determined by [Long et al. \(2013\)](#), also from the BRAVA data. The comparison with other determinations in the literature is discussed in [Section 2.8.3](#).

Our initial models were constructed with different dark matter haloes, and the bars formed in these models had different corotation radii and  $\mathcal{R}$  values  $\mathcal{R} = 1.1 - 1.8$  based on their individual rotation curves ([Figure 2.1](#)). After the rescaling during the NMAGIC fit, the rotation curves of all models are essentially identical in the inner 3 kpc, such that these models all provide equally good fits to the RCGs density and BRAVA data. This is displayed in [Figure 2.9](#) which shows the azimuthally averaged rotation curves of our best mass models, together with their disc and halo contributions. The models' scaled outer rotation curves are different, however, consistent with the different  $\mathcal{R}$  values. This is not expected to influence the bulge dynamics, because very few stars from 4 kpc and beyond will reach the BRAVA bulge fields along their orbits.

Because no effort has been made to match the rotation curve of the MW at large radii, the models'  $\mathcal{R}$  ratio does not correspond to that of the MW. There are several ways in which the outer rotation curve of the MW could have changed after the bar and bulge

formed, e.g., by later growth of the disc. Therefore, in order to estimate the corotation radius and  $\mathcal{R}$  of the Galaxy corresponding to  $\Omega_p \sim 25 - 30 \text{ km s}^{-1} \text{ kpc}^{-1}$  we need to use additional data. Assuming the composite rotation curve of Sofue, Honma & Omodaka (2009) rescaled to  $(R_0, V_0) = (8.3 \text{ kpc}, 218 \text{ km s}^{-1})$ , this range of pattern speed would result in a corotation radius between 7.2 and 8.4 kpc, which implies  $\mathcal{R}$  between 1.5 and 1.8. The MW would then belong to the so-called slow rotators. This result is discussed in more detail in Section 2.8.3.

#### 2.4.4 Proper motions

As an independent check we predict proper motion dispersions  $\sigma_{l,b}$  in the  $l$  and  $b$  direction for our best dynamical models as explained in Section 2.3.3, and compare them to the data from Rattenbury et al. (2007a). A comparison model/data is shown in Figure 2.10 for  $\sigma_l$  (left-hand plot) and  $\sigma_b$  (right-hand plot). The different colours refer to the five best dynamical models, and the shaded regions display different levels of relative error of the model with respect to the data. Data error bars are not plotted: errors given by Rattenbury et al. (2007a) are only statistical errors at the level of 1% or better. However, reproducing their derivation of  $\sigma_{l,b}$  from the original motions of individual stars in a couple of fields, it seems to us that systematic errors dominate. These systematic effects are due to the selection thresholds and have a typical magnitude of 10%, which is indicated in Figure 2.10 by the white band.

Our models provide good proper motion predictions in the  $l$  direction, being mostly inside the 10% limit. Proper motions in the  $b$  direction are slightly worse, with model values mostly 10% to 20% lower than the data. This hints at additional systematic errors, either in the models or in the data.  $\sigma_b$  is directly related to the vertical derivative of the potential and therefore to the mass concentration toward the midplane. This is apparent in Figure 2.10 where models with a more massive stellar bulge component have larger  $\sigma_b$ . There is only limited scope for increasing  $\sigma_b$  in the models as will be discussed in Section 2.8.2. Rattenbury et al. (2007a) noted that deviations of proper motion dispersions between adjacent fields could be as high as  $0.2 \text{ mas yr}^{-1}$  and concluded that some small systematic effect could indeed be present in the data. All together our models predict reasonable proper motion dispersions, indicating that the dynamics of the GB is quite constrained by the combination of the BRAVA data and the RCGs density.

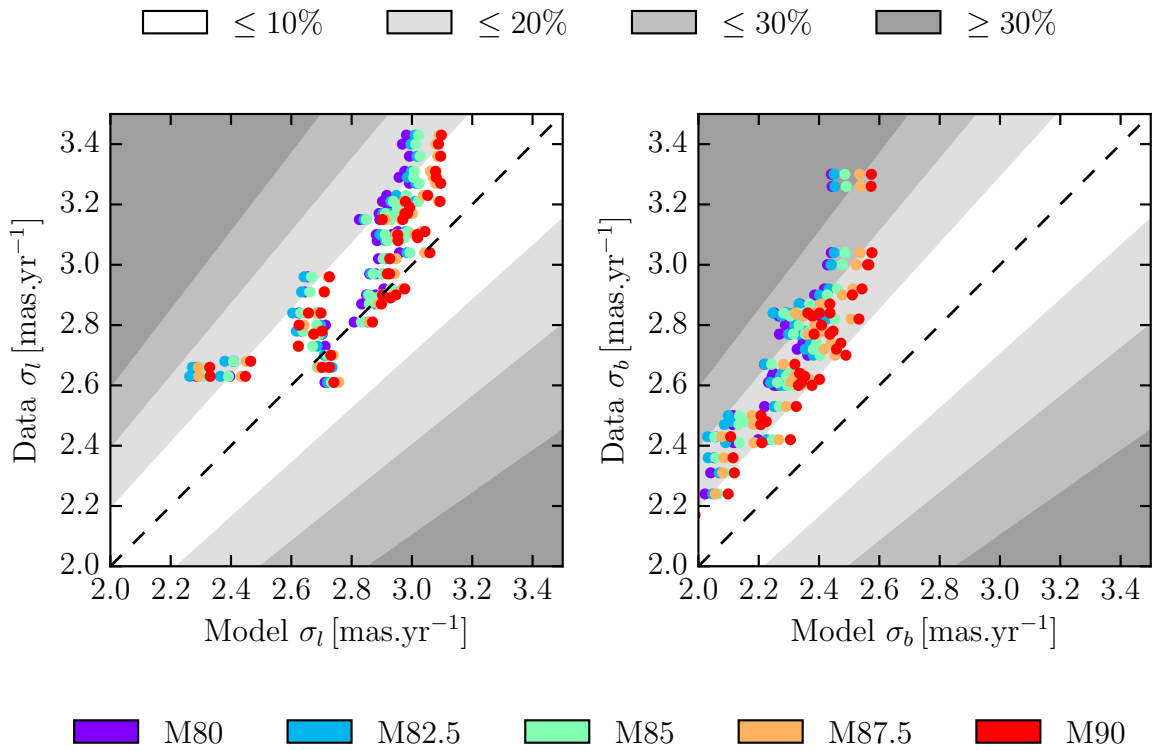


Figure 2.10: Comparison between model and data for proper motion dispersions in the  $l$  direction (left-hand plot) and in the  $b$  direction (right-hand plot) for all bulge fields from [Rattenbury et al. \(2007a\)](#). The different colours refer to the models as stated in the legend. The shaded regions indicate the relative error of model predictions with respect to the data, from  $\leq 10\%$  in white to  $\leq 20\%$ ,  $\leq 30\%$  and  $\geq 30\%$  in dark grey.

## 2.5 Mass of the galactic bulge

### 2.5.1 Evaluation of the total mass

The stellar mass in the bulge-in-box (b-b, the inner  $\pm 2.2 \times \pm 1.4 \times \pm 1.2$  kpc of the GB) is determined by the value of  $\mathcal{F}$  derived in the previous section together with the velocity scaling found by NMAGIC during the fit. The stellar mass recovered this way differs from model to model, ranging from about  $1.25 \times 10^{10} M_{\odot}$  for model M80 to  $1.6 \times 10^{10} M_{\odot}$  for model M90. This is expected given the fact that our models have different dark matter masses. More massive haloes (like M80) can build the BRAVA dispersion with relatively low stellar mass while low mass haloes need more stellar mass. All our models are good fits to the data, so purely from the BRAVA data we cannot infer the stellar mass of the bulge accurately. However, our modelling gives us a very good estimate of the *total* mass of the bulge-in-box. [Figure 2.11](#) shows the stellar mass (blue points) and total mass (red points) of the b-b for all models. We can see that our estimates of the total mass are quite constant along our range of model haloes. Altogether we evaluate the total mass of the b-b to be  $1.84 \pm 0.07 \times 10^{10} M_{\odot}$ . The errors quoted here are combined statistical and systematic whose determination is discussed below.

To estimate statistical errors, we use a  $\Delta\chi^2$  analysis, based on two approaches. First, we regard the velocity dispersion profiles for a given model with different  $\mathcal{F}$  parameters as a one-parameter family of curves matched to the 82 BRAVA velocity dispersions, in which case the appropriate  $\Delta\chi^2 = 1$ . This leads to an average uncertainty for the models of  $\Delta\mathcal{F} = 0.04$ ,  $\Delta M_s = 0.025 \times 10^{10} M_{\odot}$ ,  $\Delta M_{\text{tot}} = 0.028 \times 10^{10} M_{\odot}$ . Secondly, we consider the kinematic  $\chi_k^2/n_k$ -values of the best-fitting models from [Table 2.3](#) for the different dark matter haloes as the combination of a systematic variation modelled as linear, plus a fluctuating component which has a root mean square of  $\text{rms}(\chi_k^2) = 0.0119 \times 164 = 1.95$ . We take this as an approximation of the scatter in  $\chi_k^2$  at minimum, which according to the simulations of [Morganti et al. \(2013\)](#) can be taken as a proxy for the  $\Delta\chi^2$  to be used for estimating the accuracy with which the mass can be determined from the data using NMAGIC modelling. Applying this to the combined  $\chi_k^2$  curve derived from [Figure 2.5](#) results in estimated uncertainties of  $\Delta\mathcal{F} = 0.05$ ,  $\Delta M_s = 0.033 \times 10^{10} M_{\odot}$ ,  $\Delta M_{\text{tot}} = 0.036 \times 10^{10} M_{\odot}$ . Based on both methods, we estimate the statistical uncertainty in the stellar and total mass measurement for the b-b as  $\Delta M_s = 0.03 \times 10^{10} M_{\odot}$ ,  $\Delta M_{\text{tot}} = 0.03 \times 10^{10} M_{\odot}$ .

### 2.5.2 Evaluation of systematics

Our modelling relies on some assumptions whose influence on the derived bulge mass we now investigate. Here we describe variations of our four main assumptions: the midplane extrapolation, the length scaling, the snapshot selection and the bar angle. We show that the effect of these assumptions on the estimate of the mass of the bulge is small. These test variations are then used to set the error on the mass measurement previously quoted.

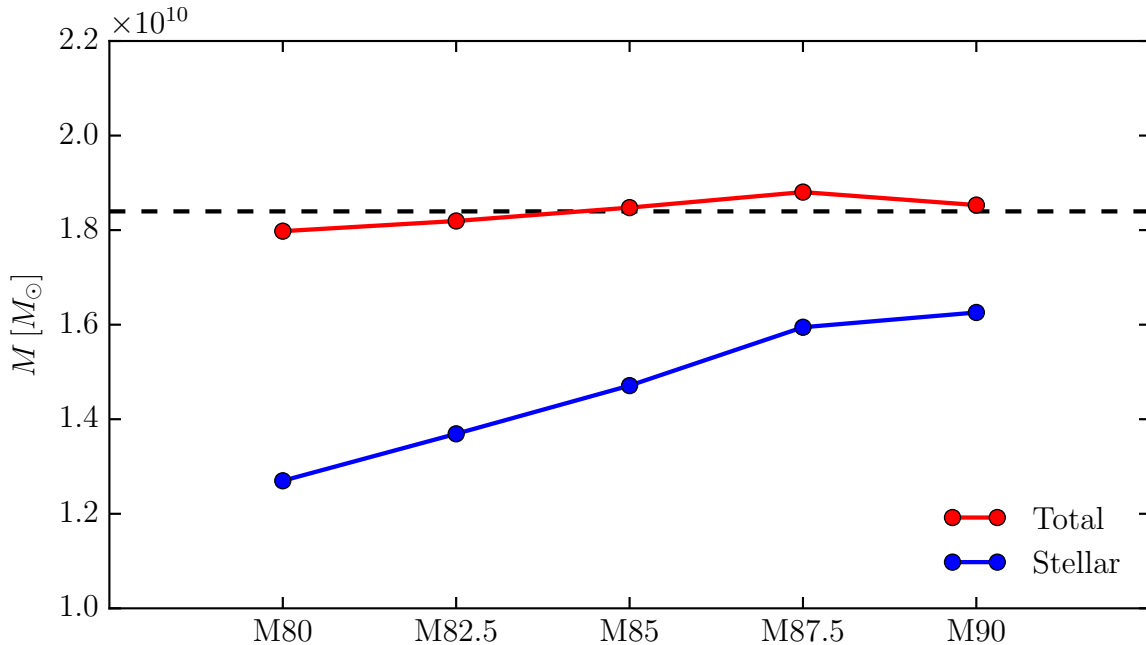


Figure 2.11: Mass of the bulge-in-box for our five best mass models in different dark matter haloes. The blue curve refers to the stellar mass while the red curve refers to the total mass.

### Midplane extrapolation

In order to quantify the uncertainty introduced by the assumed shape of the extrapolation in the midplane (see Section 2.3.2), we do the same study as detailed in Section 2.4 with a variant extrapolation, more concentrated in the midplane.

In the fiducial case, we use the best  $\text{sech}^2$  fit to fill in the midplane. For our variant, we perform an exponential extrapolation down to the midplane, with scale height  $h$  varying as a function of the in plane coordinates  $(x', y')$  (see Section 2.2.2). We assume that  $h(x', y')$  is proportional to the scale height of the best  $\text{sech}^2$  fit at large  $z$ , normalized with numerical value fixed such that  $h(0, 0)$  is equal to  $1^\circ \sim 140$  pc. The implied additional RCGs in the midplane strip increase the total number of RCGs in the b-b by 10% with respect to our fiducial extrapolation. We consider this extrapolation as giving extreme but still reasonable stellar concentration towards the midplane.

The vertical density profiles along the major axis of this variant extrapolation are plotted along with our fiducial ones in Figure 2.12. In this figure, the different colours indicate the absolute value of the position along the  $x'$  axis, from red at the centre to blue at the edges of the 3D map.

### Length scaling

In the fiducial case we scale our model using the length of the long bar, assuming that this long bar ends at  $l = 27^\circ$ . Even though this assumption seems well founded, such a long

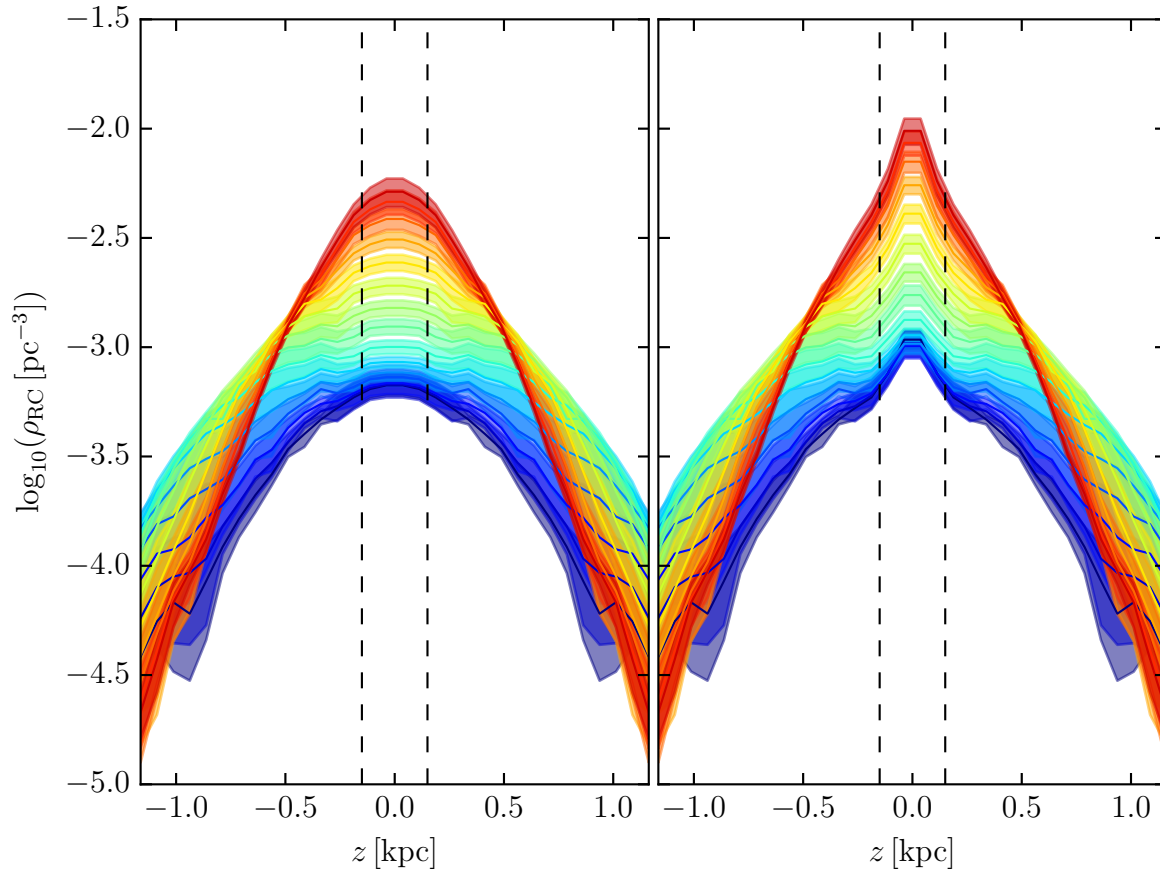


Figure 2.12: Vertical density profiles along the major axis of the bar for the fiducial extrapolation of the density to the midplane (left plot) and the variant extrapolation (right plot). The different colours indicate the coordinate along the major axis, from red in the centre to blue at the edge of the map at 2.2 kpc. The colour shaded region depicts the errors in the density from [Wegg & Gerhard \(2013\)](#) and the dashed lines show the  $\pm 150$  pc region where the original density map from [Wegg & Gerhard \(2013\)](#) has been extrapolated.

bar is in clear tension with previous claims that the pattern speed of the Milky Way bar could be as high as  $60 \text{ km s}^{-1} \text{ kpc}^{-1}$  (see [Section 2.8.3](#)). Ongoing work by Wegg et al. (in preparation) shows that the long bar can be reliably traced up to at least  $l = 20^\circ$ . Hence we repeat our experiments by scaling our models on a long bar which would end at  $l = 20^\circ$  instead of  $27^\circ$ . With the assumed bar angle and distance to the GC the semi-major axis of such a bar would be 3.8 kpc long.

### Snapshot selection

Our fiducial study is based on initial models which are late evolutionary snapshots of pure disc+halo simulations. Throughout its evolution the bar gives away angular momentum, slows down and builds a strong B/P bulge. As our target density has a very strong peanut shape, late evolutionary stages are a priori more suitable starting points for our modelling. However, when looking at the ratio of the size of the peanut shape to the length of the bar, we found that early evolutionary snapshots better match our target ratio. Consequently we repeat the same modelling analysis using earlier snapshots, taken just after the buckling is complete.

### Bar angle

The angle between the major axis of the barred bulge and the Sun-GC line has in the past generally been found in the range  $20 - 30^\circ$  ([Stanek et al. 1997](#); [Bissantz & Gerhard 2002](#); [Rattenbury et al. 2007b](#); [Nataf et al. 2013](#)). In this study we assumed an angle of  $27^\circ$  which is what WG13 measured with an accuracy of  $\pm 2^\circ$  when making their 3D density map of RCGs in the bulge. Even though this result seems robust we quantify the effect of a different bar angle by experimenting with a bar angle of  $32^\circ$  ( $2.5\sigma$ ).

### A very robust estimate of the total mass

[Figure 2.13](#) shows the total mass  $M_{\text{tot}}$  as a function of the model for our fiducial case as well as for each variant detailed above. The average total mass in the fiducial case gives an estimate of the total mass of the bulge of  $1.84 \times 10^{10} M_\odot$ , shown by the dashed line in [Figure 2.11](#). Systematic variations of our four main assumptions have only small effects on the derived value of the total mass as shown in [Figure 2.13](#). As stated in [Section 2.4.1](#) the uncertainty of the total mass determination due to the discrete sampling of  $\mathcal{F}$  is less than  $0.01 \times 10^{10} M_\odot$ . The estimated statistical error is  $\Delta_{\text{stat}} M_{\text{tot}} = \pm 0.03 \times 10^{10} M_\odot$ . Systematics dominate and are evaluated by simply taking the range of all mass measurements, as showed by the grey band in [Figure 2.11](#), corresponding to  $\Delta_{\text{sys}} M_{\text{tot}} = {}^{+0.07}_{-0.04} \times 10^{10} M_\odot \simeq \pm 0.06 \times 10^{10} M_\odot$ . Adding the statistical and systematic error in quadrature, we conclude that the total mass of the bulge-in-box is  $1.84 \pm 0.07 \times 10^{10} M_\odot$ . Numerical values of stellar, dark matter and total mass in the b-b for the different models are given in [Table 2.4](#).

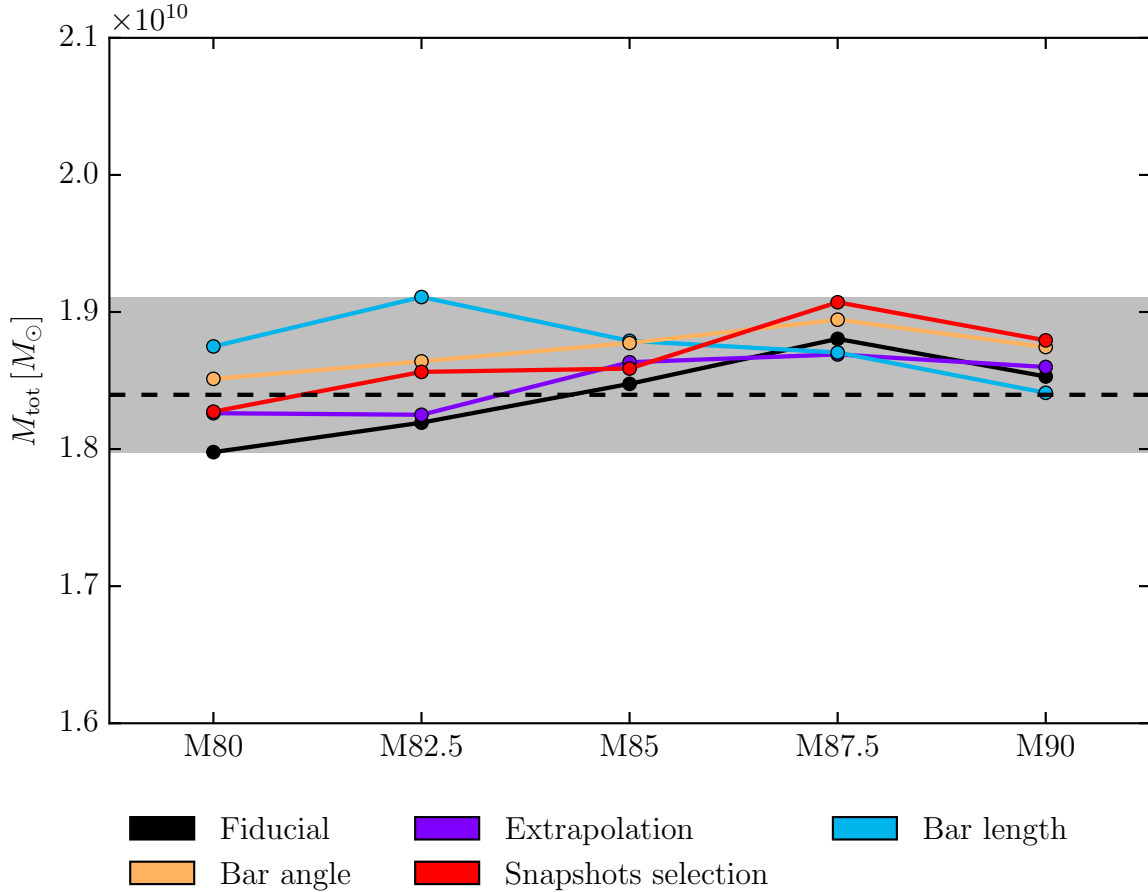


Figure 2.13: Total mass (stellar + dark matter) of the bulge-in-box for the five models. The black points show our fiducial results already plotted in Figure 2.11. The coloured dots show masses obtained when varying some of the model assumptions as stated in the legend. Only small deviations from our fiducial case are found. The dashed line displays the mean value obtained in the fiducial case while the grey band spans the range of all results.

Table 2.4: Stellar mass  $M_s$ , dark matter mass  $M_{\text{DM}}$  and total mass  $M_{\text{tot}}$  for all models in the bulge-in-box, in units of  $10^{10} M_{\odot}$ . The first row refers to our fiducial models while the lower four rows refer to the different systematic variations of the model assumptions detailed in Section 2.5.2.

	M80			M82.5			M85			M87.5			M90		
	$M_s$	$M_{\text{DM}}$	$M_{\text{tot}}$	$M_s$	$M_{\text{DM}}$	$M_{\text{tot}}$	$M_s$	$M_{\text{DM}}$	$M_{\text{tot}}$	$M_s$	$M_{\text{DM}}$	$M_{\text{tot}}$	$M_s$	$M_{\text{DM}}$	$M_{\text{tot}}$
Fiducial	1.27	0.53	1.80	1.37	0.45	1.82	1.47	0.38	1.85	1.59	0.29	1.88	1.63	0.23	1.85
Extrapolation	1.29	0.54	1.83	1.36	0.47	1.83	1.49	0.37	1.86	1.58	0.29	1.87	1.63	0.23	1.86
Bar length	1.32	0.55	1.87	1.41	0.50	1.91	1.50	0.38	1.88	1.57	0.30	1.87	1.60	0.24	1.84
Bar angle	1.30	0.55	1.85	1.38	0.48	1.86	1.50	0.38	1.88	1.60	0.29	1.89	1.64	0.23	1.87
Snapshots selection	1.41	0.42	1.83	1.48	0.37	1.86	1.56	0.30	1.86	1.69	0.22	1.91	1.70	0.17	1.88



## 2.6 Mass-to-light and mass-to-clump ratios

A good estimate of the total mass together with a constraint on the stellar mass would give useful insight into the dark matter mass in the bulge. In this section we constrain the stellar mass in the b-b through the stellar mass-to-light ratio  $\Upsilon_K$  and what we call the stellar “mass-to-clump” ratio, i.e. the amount of stellar mass per number of Red Clump and Red Giant Branch Bump stars. We first construct predictions from population synthesis models and compare our best mass dynamical models to these predictions. In this way we can relate the stellar Initial Mass Function (IMF) to the dark matter mass of the GB.

### 2.6.1 Population synthesis models

We predict the stellar mass-to-light and mass-to-clump ratios from modelling the evolution of the bulge stellar population. This modelling relies on the three different ingredients.

1. An Initial Mass Function (IMF):

We use four IMFs which span the range of reasonable IMFs for the galactic bulge. Our two extremes are the bottom-heavy Salpeter IMF (Salpeter 1955) for masses between  $10^{-1} M_\odot$  and  $10^2 M_\odot$ , and the Zoccali IMF (Zoccali et al. 2000, third entry of their table 3), the latter being derived specifically from measurements towards the galactic bulge. In between we use the Kroupa (Kroupa 2001) and the Chabrier IMF (Chabrier 2003), which are quite similar. These four IMFs normalized to  $1 M_\odot$  are displayed in Figure 2.14. Following Kroupa (2001) we plotted the logarithmic form of the IMF  $\xi_L(\log_{10}(M)) = M \ln(10) \frac{dN}{dM}$ , where  $\xi_L(\log_{10}(M)) d\log_{10}(M)$  corresponds to the fraction of stars with mass between  $\log_{10}(M)$  and  $\log_{10}(M) + d\log_{10}(M)$  and  $M$  is expressed in  $M_\odot$ .

2. A set of isochrones:

We choose the solar metallicity and  $\alpha$ -enhanced BASTI isochrones (Pietrinferni et al. 2004) and assume a single age population of 10 Gyr. As shown later the choice of the age has a small effect and is therefore not critical.

3. A way to treat stellar remnants:

Stars that evolve beyond their isochrones have to be turned properly into white dwarfs, neutron stars or black holes. We use the choices described in Maraston (1998).

Using these three ingredients, we first construct a luminosity function  $\Phi(M_K)$  in units of  $\text{mag}^{-1} M_\odot^{-1}$  by evolving  $1 M_\odot$  through the set of isochrones for a given age, according to the considered IMF mass distribution. After renormalization of the luminosity function to

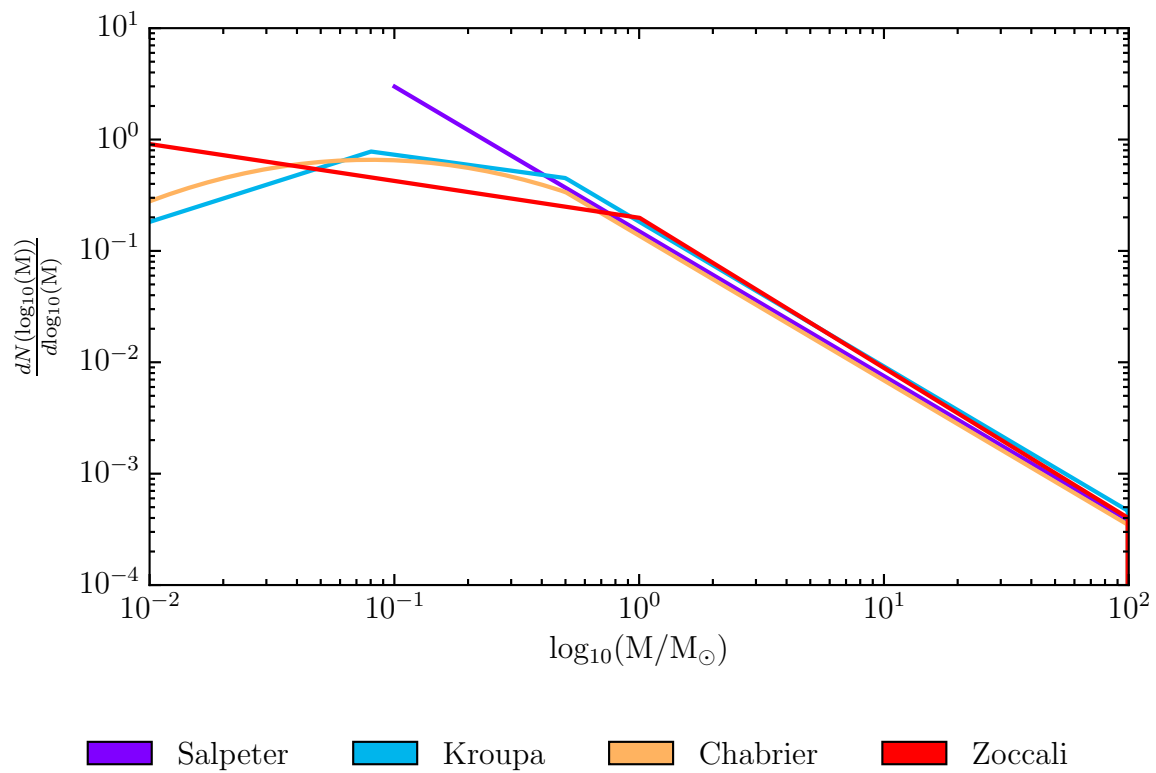


Figure 2.14: Plot of the logarithmic form of the different IMF used in this study (Salpeter 1955; Zoccali et al. 2000; Kroupa 2001; Chabrier 2003).

a remaining mass of  $1 M_{\odot}$  (evolved stellar population + stellar remnants), the synthesized stellar mass-to-light ratio in the K-band  $\Upsilon_K$  is given by

$$\Upsilon_K = \left( \int \Phi(M_K) 10^{-0.4(M_K - M_{K_{\odot}})} dM_K \right)^{-1}. \quad (2.20)$$

We checked our mass-to-light ratio predictions by reproducing the work of [Maraston \(1998\)](#) and [Percival et al. \(2009\)](#) and found a very good agreement with both of them for the old population considered here.

In order to compute the stellar mass-to-clump ratio we use the same technique as in WG13. We fit an exponential background plus two Gaussians to the previously derived luminosity function. The two Gaussians represent the RCGs and the Red Giant Branch Bump (RGBB), as in WG13. This mass-to-clump ratio includes RGBB stars as well for two reasons. First because for some ages, the RCGs and RGBB have the same luminosity and are therefore indistinguishable. Secondly because WG13 made their map by fitting these two Gaussians under the assumption that the RGBB represents 20% of the Red Clump. Hence the total number of RCGs and RGBB stars is a priori better constrained than the number of RCGs only. As the luminosity function was renormalized to a remaining mass of  $1 M_{\odot}$ , the number of stars contained in the two fitted Gaussians directly leads to the mass-to-clump ratio, denoted as  $M/n_{\text{RC+RGBB}}$ .

## 2.6.2 Mass-to-light ratio

The COBE/DIRBE instrument provides us with  $K$ -band measurements in many bulges fields. Here we use the data from [Drimmel & Spergel \(2001\)](#) who removed point sources by applying a median filter to the original “Zodi-Subtracted Mission Average” map ([Kelsall et al. 1998](#)). In order to correct for galactic extinction, we use the extinction map presented in WG13, also derived from  $K$ -band data. This map covers the inner  $l \in [-10^{\circ}, 5^{\circ}]$ ,  $b \in [-10^{\circ}, 10^{\circ}]$  of the bulge and has a resolution of  $1'$  which is much finer than the  $42' \times 42'$  COBE/DIRBE field size. We correct the COBE/DIRBE data by using the mean extinction on each COBE/DIRBE pointing. We ignore the fields in the inner  $|b| < 2^{\circ}$  because the extinction is too high to make a reliable correction. We apply a disc contamination correction to the remaining data points as follows. The average disc contamination as a function of latitude is evaluated using the surface brightness profile in two  $0.5^{\circ}$  wide strips along the  $b$  direction, located at  $l = \pm 15^{\circ}$ . At these large longitudes the galactic bulge is no longer important and the flat long bar does not contribute significantly to the surface brightness for  $|b| \geq 2^{\circ}$ . Hence the average surface brightness profile of the strips is mostly due to the disc component. By assuming that this disc vertical surface brightness profile stays constant at all longitudes inside  $|l| < 15^{\circ}$  we can estimate and then remove the disc contamination from the COBE data. Finally this provides us with about 2800 extinction and foreground corrected surface brightness measurements towards the galactic bulge which can be compared to our models.

To compute the surface brightness of our particle models we convert scaled stellar particle weights  $w_i$  into  $K$ -band luminosity  $L_i = w_i \Upsilon_K^{-1}$ , assuming a constant but still

unknown stellar mass to-light ratio  $\Upsilon_K$  in the bulge.  $\Upsilon_K$  will be determined by matching our model surface brightness to the COBE/DIRBE  $K$ -band data. The extinction-free model surface brightness in some field  $\Sigma_j(l, b)$  as one would see from the Sun's location is given by

$$\Sigma_j(l, b) = \frac{1}{\Delta\Omega_j} \sum_i \frac{w_i \cdot \Upsilon_K^{-1}}{r_i^2} \delta_j(r_i) \quad (2.21)$$

where  $\Delta\Omega_j$  is the solid angle of the considered field,  $r_i$  is the distance of the particle  $i$  from the Sun in kpc, and  $\delta_j(r_i)$  is a suitable selection function that we describe below in Equation 2.22. Our models have been matched to the MW inside the b-b but no attempts have been made to match the model discs to the MW disc. In order to reduce the uncertainty due to the disc contribution we evaluate for each COBE field the fraction of model light which comes from particles located in the b-b. We remove from the analysis all fields where this fraction is lower than 90%, i.e. all fields where not directly constrained particles contribute more than 10% of the model surface brightness. Given that a single particle can theoretically dominate the surface brightness by being arbitrarily close to the Sun's location, we also remove nearby disc particles from the analysis in the remaining fields by taking the following selection function:

$$\delta_j(r_i) = \begin{cases} 1 & \text{if } i \in \text{field } j \text{ and } r_i \geq 3 \text{ kpc} \\ 0 & \text{otherwise} \end{cases} \quad (2.22)$$

We then apply the same foreground contamination correction to the model surface brightness as for the data, using the two strips at  $l = \pm 15^\circ$ . We checked that our results do not depend on the exact form of the selection function, indicating that the foreground contamination has been properly removed.

Finally, we compute the mass-to-light ratio as stated in Equation 2.21 independently for all remaining COBE fields and average the results. The statistical error in the mean mass-to-light ratio is very low due to the large number of COBE fields so that systematics dominate. We evaluate systematic effects by repeating this analysis for the four variants described in Section 2.5.2 of the considered model. The full range of values is then taken as the systematic error.

Figure 2.15 shows the mean value of  $\Upsilon_K$  and its associated systematic error for the five best dynamical models with different dark matter haloes. These mass-to-light ratios are compared to the predictions from different IMFs shown as the coloured lines, for a single 10 Gyr age population. The coloured strips span the range of values for ages between 9 and 11 Gyr. With the total mass and integrated light fixed, the models with low dark matter mass (M90 for example) have higher stellar mass-to-light ratios. We see that most of our models are in agreement with predictions from a Kroupa or Chabrier IMF which are somewhat similar, the Kroupa IMF predicting slightly higher mass-to-light ratios than the Chabrier IMF. Only the most dark matter dominated model M80 approximately matches the predictions from the Zoccali IMF, which is a priori the best candidate IMF because it was measured directly from the stellar luminosity function of the bulge. In order to agree with the Zoccali IMF about 40% dark matter mass is required in the b-b.

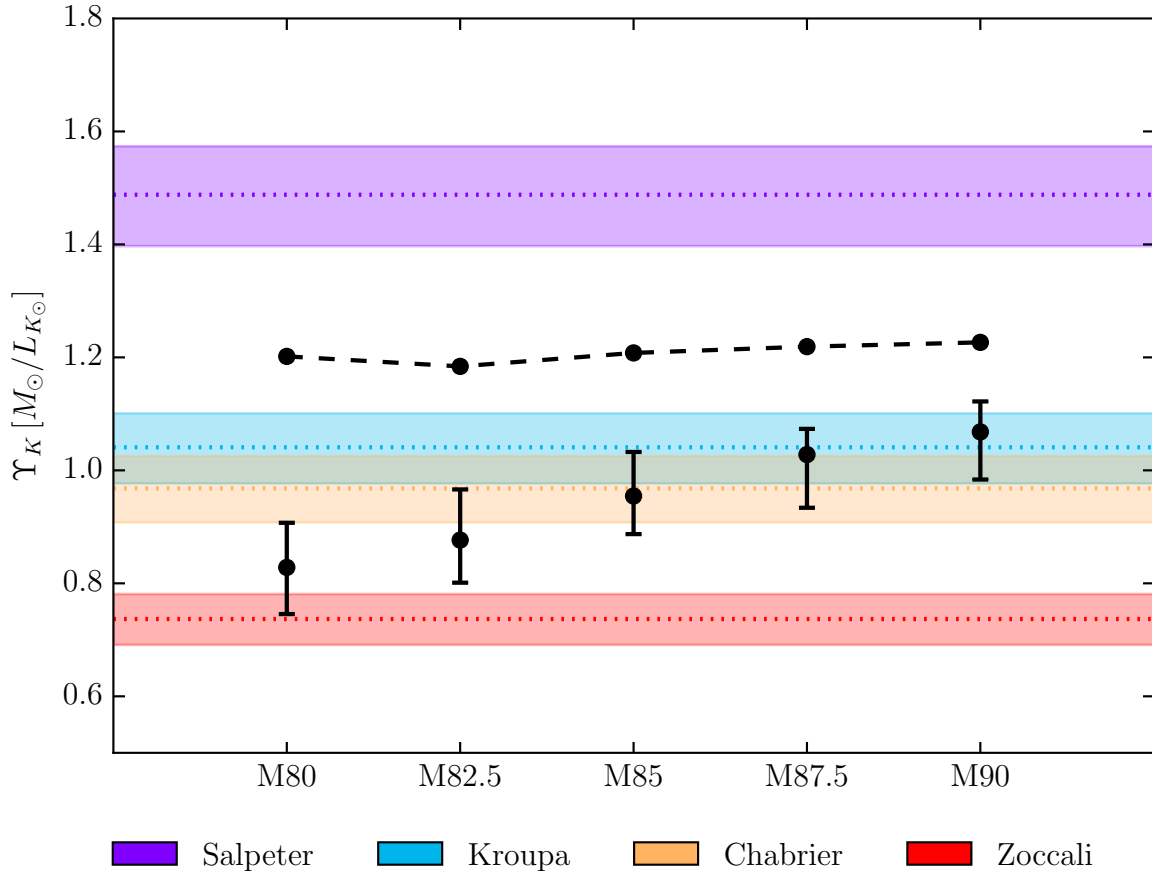


Figure 2.15: Stellar mass-to-light ratio in the  $K$  band for our five best dynamical models of the bulge in different dark matter haloes. The model errors shown are dominated by systematic effects. The different coloured lines indicate predictions from different IMFs as stated in the legend. The black dashed line is an estimate of the highest allowed mass-to-light ratio obtained by turning all dark matter of the b-b into luminous matter. This allows us to rule out the Salpeter IMF for the galactic bulge with age 10 Gyr.

In addition, the dynamical models rule out a Salpeter IMF for a bulge population with age 10 Gyr. The dashed line in Figure 2.15 represent the highest possible stellar mass-to-light ratio which would be obtained if all the dark matter in the bulge was turned into stars with the same density distribution as the stellar component of the bulge in our fiducial models. For all our models, the mass-to-light predictions for a Salpeter IMF for a 10 Gyr galactic bulge are higher than this extreme mass-to-light ratio by at least three times the model error, showing that it is too bottom-heavy.

### 2.6.3 Mass-to-clump ratio

The mass-to-clump ratio is also a useful quantity to relate stellar mass and stellar population. With RCGs being approximate standard candles with standard colours, issues like

foreground contamination and dust extinction are easier to solve when computing a mass-to-clump ratio than a mass-to-light ratio. The number of RCGs in the b-b was computed directly from our fiducial extrapolation of the density map of WG13. Using the variant extrapolation presented in Section 2.5.2 would increase this number by only 10%. In order to include the RGBB in this calculation, we add the 20% fraction assumed in the derivation of the 3D map by WG13. The computation of  $M/n_{\text{RC+RGBB}}$  is then straightforward from the stellar mass determination of Section 2.5.1. Results are shown in Figure 2.16 for all dark matter models. The errors plotted in Figure 2.16 are systematic, determined from the four variant assumptions described in Section 2.5.2. Again the different colour strips indicate predictions of different IMFs for ages between 9 and 11 Gyr.

Qualitatively we reach from the mass-to-clump ratio similar conclusion as from the mass-to-light ratio, indicating the need of a large dark matter fraction in the bulge in order to match the prediction from the Zoccali IMF. However quantitatively we have some tension between mass-to-light and mass-to-clump ratios, where for a given IMF the mass-to-clump ratio seems to be about 20% too large with respect to the predicted value from the theoretical models. The two views can be reconciled if some physical process prevents about 20% of the Giants to ignite their Helium core and become RCG. We speculate that such a process could be the stripping of the star envelope resulting from the interaction with a companion star in a binary system and leading to the formation of a low mass white dwarf as suggested by Marsh (1995). The issue of the mass-to-clump ratio in the bulge is discussed further in Chapter 4.

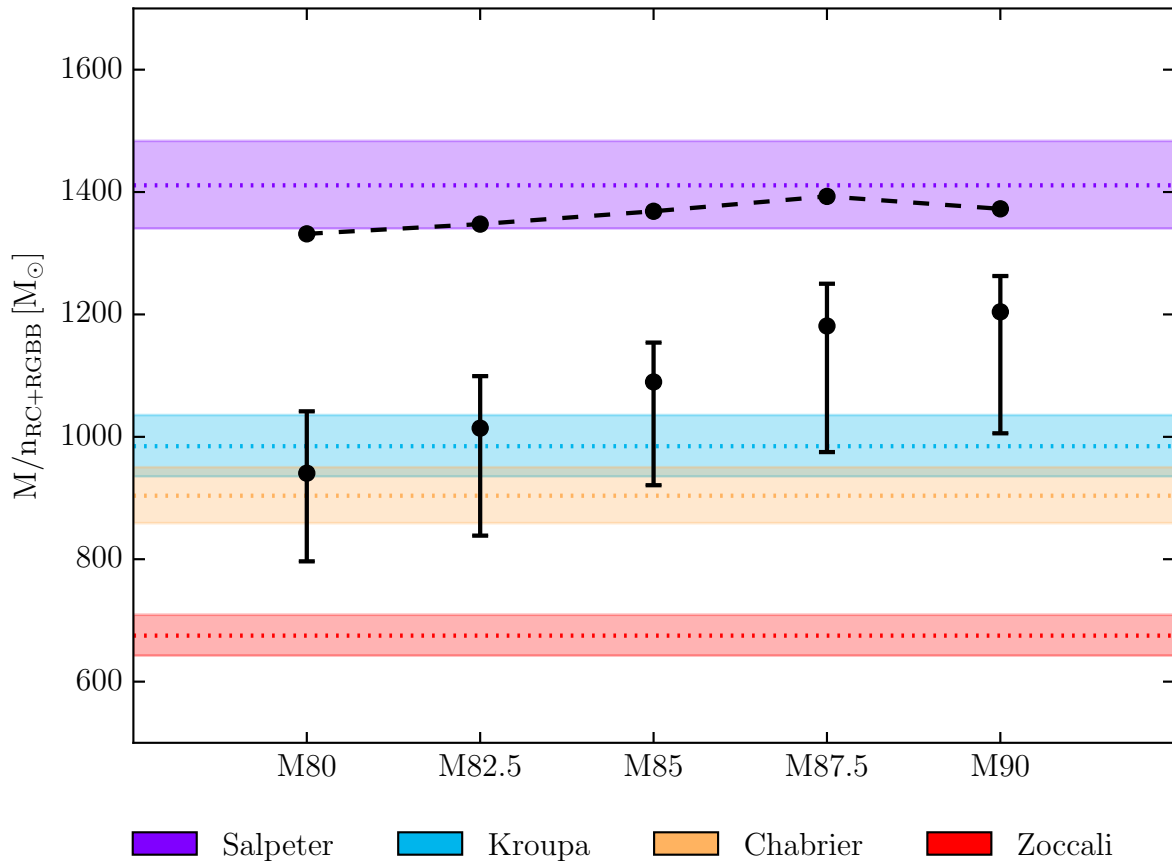


Figure 2.16: Mass-to-clump ratio,  $M/n_{RC+RGBB}$  for our five best dynamical models of the bulge in different dark matter haloes. The coloured lines indicate predictions from different IMFs as stated in the legend. The black dashed line is an estimate of the highest allowed mass-to-clump ratio obtained by turning all dark matter of the b-b into luminous matter.

## 2.7 Peanut and X-shape structures of the galactic bulge

In this section we study the structural properties of the GB further, based on the 3D density map of RCGs from WG13. We first illustrate and discuss its X-shape in a similar way as usually done for external galaxies. We then use a 3D photometric diagnostic to quantify the fraction of stellar mass involved in the peanut shape of the GB.

### 2.7.1 The photometric X-shape

Observations of external galaxies have revealed that boxy/peanut bulges exist with a variety of shapes. In order to highlight the internal structure of external edge-on B/P bulges, a common practice is to use unsharp masking techniques as described by Bureau et al. (2006). They applied a median filter to images of 30 edge-on spirals and removed the smoothed images from the original ones. This reveals what is called the X-shape. Bureau et al. (2006) proposed a classification of external B/P bulges based on the properties of this X-shape. Where would the galactic bulge appear in such a classification? To answer this question, we apply a median filter with kernel size 500 pc to the side-on projection of the 3D density of RCGs from WG13 and remove it from the original projection. The positive residuals revealing the X-shape of the GB are shown in Figure 2.17 with contours spaced by a third of a magnitude.

Figure 2.17 shows that the galactic bulge has an off-centred X-shape structure, its two arms crossing the major axis about 500 pc away from the centre. This feature is identified in 50% of external edge-on B/P bulges (Bureau et al. 2006).

### 2.7.2 The mass of the peanut shape

Consistent with the strong X-shape, the Milky Way bulge in the side-on map from WG13 shows a very prominent peanut shape. An interesting issue is the amount of stellar mass involved in this feature. This was already addressed by Li & Shen (2012) who applied a technique somewhat similar to unsharp masking to the side-on projection of the model of Shen et al. (2010). They fitted ellipses to the isophotes of the side-on projection, modelled the light projected by these elliptical isophotes and removed the modelled light from the original image. Doing so revealed a centred X-structure in the model accounting for about 7% of the bulge stellar mass. Because their model had been shown to give a good representation of the BRAVA kinematic data, they then concluded that the stellar mass involved in the peanut shape of the GB was similarly about 7%.

Since we now have a direct measurement of the 3D density of RCGs in the bulge, we can perform a similar photometric analysis directly on the 3D density map. Consider the density profile  $\rho(0, 0, z)$  along the minor axis of the bar. For each particular value of  $z$ , we evaluate the 3D isodensity surface with density  $\rho(0, 0, z)$ . Then we look for the most voluminous ellipsoid we can find which fits *inside* this particular 3D isodensity surface. This search is done under the constraint that the ellipsoid is centred on the centre of the bulge, the principal axes are aligned with the principal axes of the bulge, the semi-principal



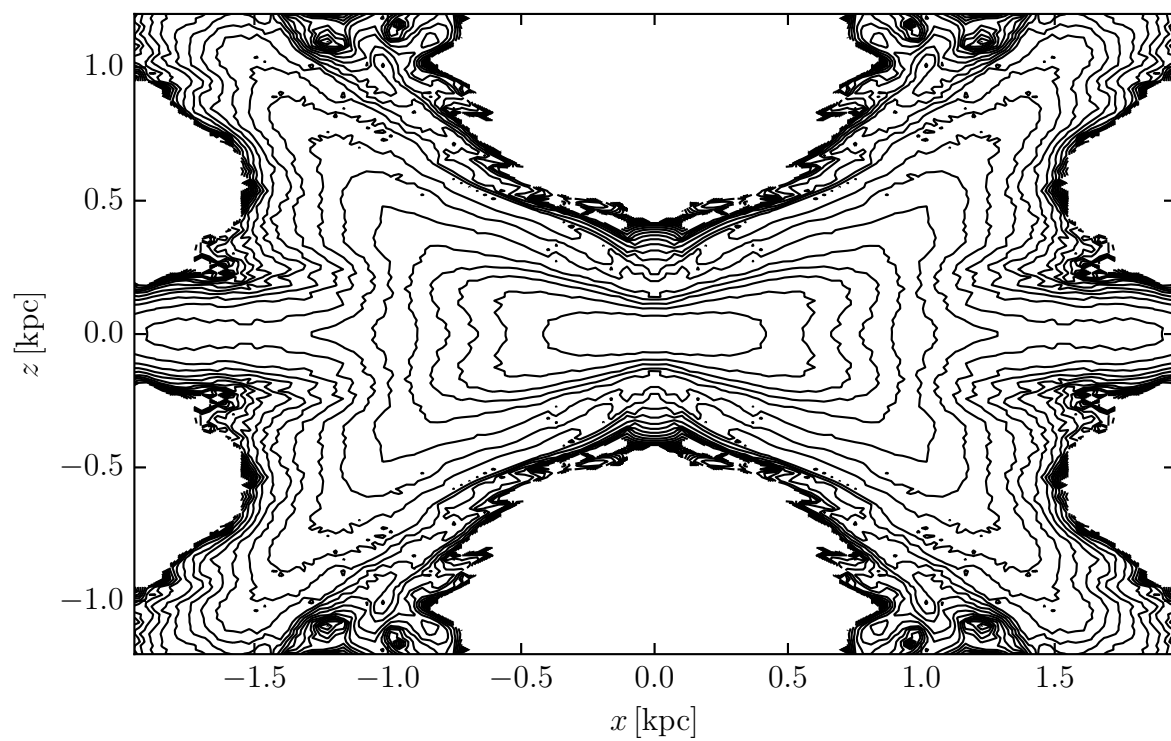


Figure 2.17: X-shape structure of the galactic bulge obtained by unsharp masking as described in Bureau et al. (2006). The galactic bulge has a so-called off-centred X-shape.

length along the vertical axis is fixed to  $|z|$ , and the ellipsoid stays inside the isodensity surface considered. By doing so for all  $z$  we construct a family of ellipsoidal isodensity surfaces. We compute the 3D density arising from this ellipsoidal isodensity family and remove it from the original 3D map. The residuals correspond to the “non-ellipsoidal” part of the bulge density. As all our ellipsoids are truly inside their corresponding isodensity surfaces of the original map, we are assured that the residual map is positive at all points.

To reduce the effect of measurement errors in the original map of WG13, we actually do this analysis using model M80, which through NMAGIC fitting of the density gives a smoother density map which is everywhere within the errors of the original map. We note that the results do not depend on which initial model is used for the density fit.

The residual map is plotted in projection in [Figure 2.18](#). The four lobes responsible for the peanut shape of the bulge are clearly visible in the side-on view for  $|z| > 300$  pc. For  $|z| < 300$  pc the peanut is not prominent enough with respect to its surroundings to make the density shape deviate from ellipsoidal shape. The stellar mass involved in this residual peanut shape is about 24% of the total stellar mass of the bulge. This figure probably underestimates the real amount of mass involved in the peanut structure as one expects the orbits responsible for this structure to also visit the strip inside  $|z| < 300$  pc and therefore to contribute to the ellipsoidal density that was removed here.

We can estimate an error on the 24% by applying the same procedure to each of the modelled five variant maps of WG13. We find that the non-ellipsoidal residuals account for  $24_{-4}^{+5}\%$  of the stellar mass of the bulge. By applying our diagnostic in a two dimensional version to the side-on projection of the density, we find that the 2D residuals sum to only  $11_{-1}^{+1}\%$  of the stellar mass of the bulge, showing that 2D determinations tend to underestimate the mass in the peanut structure.

Our peanut mass fraction of  $24_{-4}^{+5}\%$  results from an observational definition of the peanut shape: a deviation from ellipsoidal density shape. A more physical definition of the peanut structure would be to identify the different orbits responsible for its shape in side-on projection. We are currently working on such an orbit-based characterization of the peanut shape which will be presented in a companion paper.

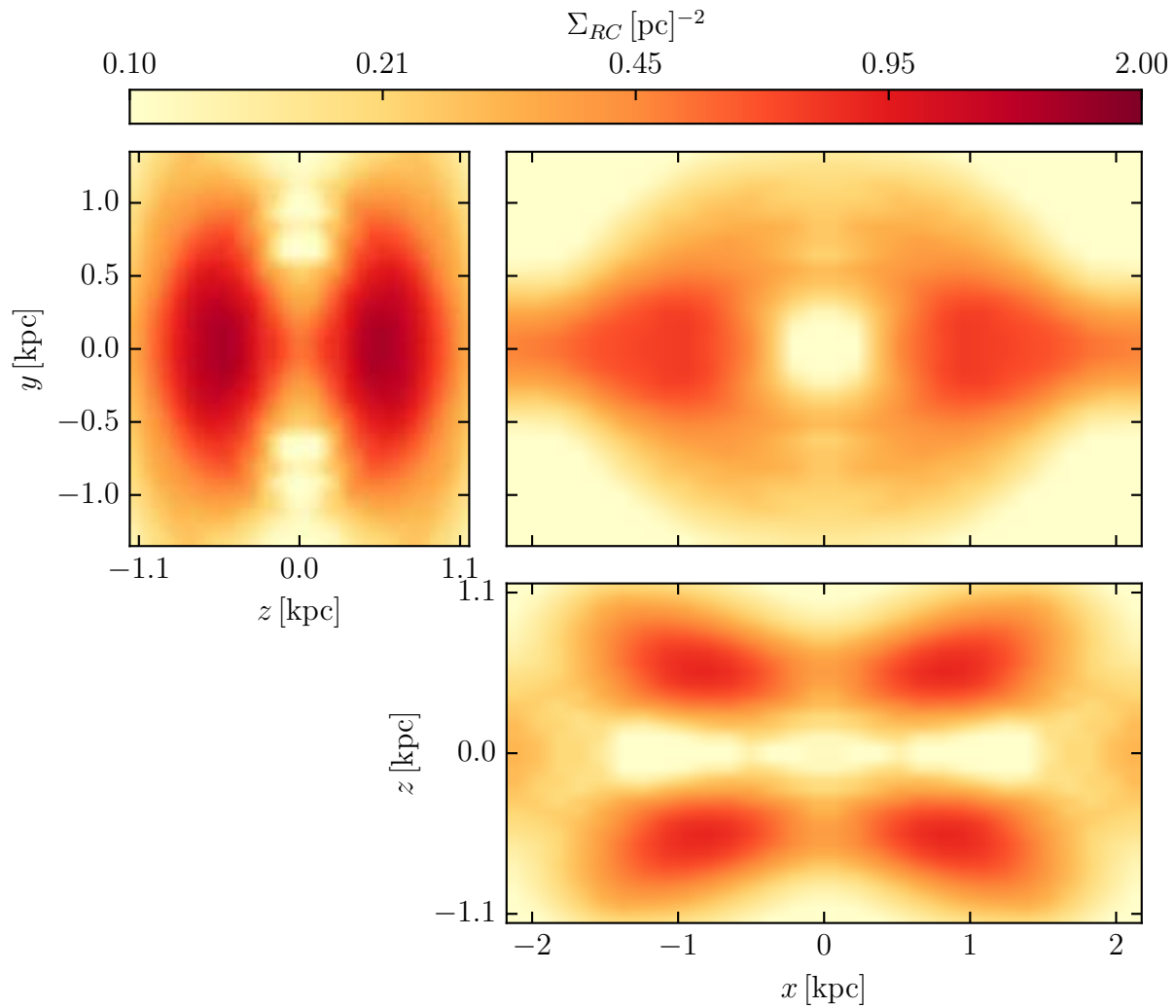


Figure 2.18: “Non-ellipsoidal” residual density of RCGs in the density map of [Wegg & Gerhard \(2013\)](#). The residual density accounts for 24% of the RCGs in the bulge. Plotting conventions are the same as in [Figure 2.3](#).

## 2.8 Discussion

### 2.8.1 Dynamical mass of the bulge

The galactic B/P bulge transits into a longer two-dimensional bar; therefore in this paper we use a simple definition for determining the dynamical mass of the bulge. We use the three-dimensional box  $\pm 2.2 \times \pm 1.4 \times \pm 1.2$  kpc as our bulge volume in which the RCGs density was determined by [Wegg & Gerhard \(2013\)](#) and which contains most of the three-dimensional bulge part of the bar. The total mass of this bulge-in-box (b-b) is accurately determined by the dynamical models,  $M_{\text{tot}} = 1.84 \pm 0.07 \times 10^{10} M_{\odot}$ . This value is essentially independent of the dark matter mass fraction in the bulge throughout our models, and the estimated error includes both statistical and systematic uncertainties; the systematic part is determined from varying the modelling assumptions around our fiducial model.

Dynamical models have previously been used to estimate the mass of the bulge. Using the Schwarzschild method, [Zhao \(1994\)](#) built a self-consistent model of the bar/bulge and found a total bulge mass of  $2 \times 10^{10} M_{\odot}$  while [Kent \(1992\)](#) found a mass of  $1.8 \times 10^{10} M_{\odot}$  by modelling an oblate isotropic rotator with a constant mass-to-light ratio. By studying gas dynamics in the potential of the model from [Bissantz & Gerhard \(2002\)](#) obtained by deprojecting the COBE luminosity distribution, [Bissantz, Englmaier & Gerhard \(2003\)](#) determined the circular velocity at 2.2 kpc to be  $190 \text{ km s}^{-1}$ . Once converted to mass under the assumption of spherical symmetry, this leads to a total bulge mass of about  $1.85 \times 10^{10} M_{\odot}$ . All these results compare well with our estimate of the mass of  $1.84 \pm 0.07 \times 10^{10} M_{\odot}$ , especially when considering the difficulty of a precise definition of the bulge.

An independent way to obtain a dynamical mass is from the virial theorem. Such studies lead to quite different values depending on the assumed pattern speed and bar angle, from  $1.6 \times 10^{10} M_{\odot}$  ([Han & Gould 1995](#)), up to  $2.8 \times 10^{10} M_{\odot}$  ([Blum 1995](#)) obtained for a high pattern speed ( $81 \text{ km s}^{-1} \text{ kpc}^{-1}$ ). The use of the virial theorem has two weaknesses. First, it relies on an estimation of the total kinetic energy, which cannot be measured accurately from line-of-sight data only. Secondly, it assumes that the bulge on its own is a system in equilibrium, whereas it is in fact part of a bar embedded in a disc.

Traditionally, the contribution of dark matter to the mass in the bulge region has been considered unimportant. In this case, a bulge mass can be estimated simply from the stars. For example, [Dwek et al. \(1995\)](#) estimated the stellar mass of the bulge at  $1.3 \times 10^{10} M_{\odot}$  from the COBE luminosity and a Salpeter IMF. However, neglecting dark matter in the bulge is not a good approximation as we have seen in [Section 2.5](#).

### 2.8.2 Stellar and dark matter mass in the bulge

Because the total mass of the bulge-in-box (b-b) is well determined, knowing the stellar mass independently would give insight into the amount of dark matter in the central part of the Galaxy. As shown in [Section 2.6](#), the stellar mass can be constrained by comparing mass-to-light and mass-to-clump ratio measurements with stellar population

synthesis predictions. However, for this the choice of the IMF is crucial: candidate IMFs disagree within a factor of two in their prediction of the stellar mass-to-light ratio, so a reliable measurement of the IMF in the GB is needed. Currently, the Zoccali IMF (Zoccali et al. 2000) measured from the bulge star luminosity function in a field located near  $(l, b) = (0^\circ, -6^\circ)$  is the favoured IMF for the GB. For this case, the predicted mass-to-light ratio from isochrones (Section 2.6.1) gives a stellar mass for the b-b of  $1.12 \times 10^{10} M_\odot$ . From our modelling, both the mass-to-light and the mass-to-clump ratio independently agree that models with fairly high dark matter mass fraction are required to provide the remaining part of the dynamical mass in the b-b. These models predict a dark matter mass in the b-b of  $M_{DM} \sim 0.7 \times 10^{10} M_\odot$ , accounting for about 40% of the total mass of the b-b.

Further insight on the dark matter part of the b-b mass can be obtained from proper motions. In particular, the proper motion dispersions in the  $b$  direction directly constrain the derivative of the potential along the vertical direction, and therefore the total mass concentration towards the plane. We showed in Section 2.4.4 that our proper motion predictions  $\sigma_b$  are 10% to 20% lower than the data. Increasing the stellar mass concentration towards the plane as in Section 2.5.2 can indeed increase  $\sigma_b$ , but only at percent level which is not significant enough. It is also possible that a systematic effect is present in the data, e.g., due to extinction or incompleteness of the sample. Before we can use the proper motion data to measure the mass concentration and dark matter content of the GB, these possible systematic effects in the data need to be better understood. A more detailed study of the proper motion constraints is part of our ongoing work to make a more complete model of the galactic bulge and long bar.

### 2.8.3 Pattern speed of the MW bar/bulge

Our dynamical models, based on the RCGs density from Wegg & Gerhard (2013) together with the BRAVA kinematic data for the bulge stars, imply a pattern speed of the MW bar-bulge of  $25 - 30 \text{ km s}^{-1} \text{ kpc}^{-1}$  (see Section 2.4.3). This result remains unchanged when varying the modelling assumptions, for example when we consider a shorter bar, as detailed in Section 2.5.2. Comparing with the composite rotation curve from Sofue, Honma & Omodaka (2009), this would place the corotation value of the bar just inside the solar circle, and give a ratio of corotation over bar half length between 1.5 and 1.8. The MW would then belong to the so-called slow rotators. Slow rotators are quite rare for external galaxies in general (Aguerri, Beckman & Prieto 1998), but fairly common among SBc galaxies (Rautiainen, Salo & Laurikainen 2008).

There have been a quite a number of pattern speed measurements in the MW by other techniques. The bulk of the measurements indicate a fast bar, but some studies suggest a lower pattern speed (see Gerhard (2011) for a review). Direct measurement by Debattista, Gerhard & Sevenster (2002) using a variant of the Tremaine & Weinberg method (Tremaine & Weinberg 1984) leads to the high value of  $\Omega_p = 59 \pm 5 \text{ km s}^{-1} \text{ kpc}^{-1}$  but depends strongly on the radial velocity of the local standard of rest towards the GC.

Numerous indirect measurements of the bar pattern speed have been obtained by

matching some of the observed features in the position-velocity diagrams for HI and CO to gas-dynamical model predictions. Most of these studies argue for a high pattern speed, such as Englmaier & Gerhard (1999) who found  $\sim 60 \text{ km s}^{-1} \text{ kpc}^{-1}$ , Fux (1999) who obtained  $\sim 50 \text{ km s}^{-1} \text{ kpc}^{-1}$ , and Bissantz, Englmaier & Gerhard (2003) with  $55 - 65 \text{ km s}^{-1} \text{ kpc}^{-1}$ . However, Weiner & Sellwood (1999) and Rodriguez-Fernandez & Combes (2008) obtained lower values of respectively  $42 \text{ km s}^{-1} \text{ kpc}^{-1}$  and  $30 - 40 \text{ km s}^{-1} \text{ kpc}^{-1}$ .

High pattern speeds were also obtained by explaining the stellar kinematics of nearby disc stars with the dynamical effects of the Outer Lindblad Resonance (OLR) of the bar. By interpreting the bimodality of the velocity distribution in the solar neighbourhood in this way, Dehnen (2000a) found  $\Omega_p = 53 \pm 3 \text{ km s}^{-1} \text{ kpc}^{-1}$ . Antoja et al. (2014) presented an analytical model of the effect of the OLR in the velocity distributions of stars at different radii and showed that they could reproduce measurements of the Hercules stream for a bar pattern speed of  $\Omega_p = 54 \pm 0.5 \text{ km s}^{-1} \text{ kpc}^{-1}$ .

The low pattern speed value found from the RCGs and BRAVA data is consistent with Rodriguez-Fernandez & Combes (2008) and Long et al. (2013) but not with the majority of these measurements. We note that models based on variants of the RCGs density map as well as models constrained by a model B/P bulge density independent of the RCGs measurement (Martinez-Valpuesta 2012) give similarly low values. The BRAVA kinematics are in agreement with the ARGOS kinematics (Ness et al. 2013a) despite the quite different selection functions of both surveys. In our modelling, the details of the selection function assumed for the BRAVA data were not important. Therefore our value measured from modelling the bulge kinematics appears robust.

The highest pattern speeds reported in the literature are also in conflict with other data. Using the composite rotation curve from Sofue, Honma & Omodaka (2009), a pattern speed of  $\Omega_p = 55 \text{ km s}^{-1} \text{ kpc}^{-1}$  would place corotation at 3.7 kpc. Because the long bar cannot extend beyond corotation (Contopoulos 1980), this is incompatible with the apparent end of the long bar at  $l = 27^\circ$  (Hammersley et al. 2000; Cabrera-Lavers et al. 2008). Even if we relax the hypothesis that the long bar ends at  $l = 27^\circ$ , recent star counts from the UKIDSS survey (Wegg et al. in preparation) show that it can be reliably traceable at least out to  $l = 20^\circ$ . This gives a lower bound of the half-length of the bar of 3.8 kpc, still in tension with a pattern speed of  $55 \text{ km s}^{-1} \text{ kpc}^{-1}$ .

We conclude that despite of the many effort made by different groups, the question of the pattern speed of the galactic bar remains an unsolved issue. One way to settle this question by dynamical modelling would be to include data that more accurately constrain the long bar component, which is one of our future goals.

## 2.9 Conclusion

In this work we have presented a set of self-consistent dynamical models of the galactic bulge with different dark matter haloes, which match recent data on the spatial distribution and kinematics of bulge stars. We started with a family of N-body models of barred discs with B/P bulges, evolved from near-equilibrium stellar discs embedded in live dark matter

haloes. We then fitted these models to the recent 3D density measurements of Red Clump Giants in the bulge from [Wegg & Gerhard \(2013\)](#), as well as to the BRAVA kinematic data of [Kunder et al. \(2012\)](#) in multiple bulge fields, using the NMAGIC Made-to-Measure method.

From this modelling, we obtain an accurate and robust estimate of the total mass (stellar and dark matter) of the bulge in the RCGs box, of  $M_{\text{tot}} = 1.84 \pm 0.07 \times 10^{10} M_{\odot}$ . We also find a low pattern speed of about  $25 - 30 \text{ km s}^{-1} \text{ kpc}^{-1}$ , which with the measured rotation curve places the Milky Way among the slow rotators ( $\mathcal{R} \geq 1.5$ ). We compute the mass-to-light and mass-to-clump ratios and compare them with theoretical predictions from population synthesis models using different IMFs. We show that the Salpeter IMF ([Salpeter 1955](#)) is ruled out for a 10 Gyr old bulge population. We find that a relatively high dark matter mass fraction in the bulge is needed in order to match predictions from the IMF inferred from the stellar luminosity function in the upper bulge ([Zoccali et al. 2000](#)),  $\sim 40\%$  or  $M_{\text{DM}} \sim 0.7 \times 10^{10} M_{\odot}$ . In addition we study the X-shape of the galactic bulge and find an off-centred X-shape, common in external B/P bulges ([Bureau et al. 2006](#)). By a three-dimensional analysis of the isodensity surfaces of the RCGs density we find that the peanut-shaped deviations from ellipsoidal shape account for  $24_{-4}^{+5}\%$  of the bulge stellar mass, significantly larger than the previous estimate of 7% of [Li & Shen \(2012\)](#).

## Acknowledgements

We gratefully acknowledge the work of Flavio De Lorenzi in writing the initial version of NMAGIC, Matías Blaña for his help and advice in setting up our initial N-body models, and Jerry Sellwood and Monica Valluri for making their potential solver available. We thank the anonymous referee for a careful reading of the paper.





# Chapter 3

## Peanuts, Brezels and Bananas: food for thought on the orbital structure of the galactic bulge

**Original publication:** Matthieu Portail, Christopher Wegg and Ortwin Gerhard, 2015, MNRASL, 450, L66 [↗](#)

### Abstract

Recent observations have discovered the presence of a boxy/peanut or X-shape structure in the galactic bulge. Such boxy/peanut structures are common in external disc galaxies, and are well-known in N-body simulations where they form following the buckling instability of a bar. From studies of analytical potentials and N-body models it has been claimed in the past that boxy/peanut bulges are supported by “bananas”, or  $x_1v_1$  orbits. We present here a set of N-body models where instead the peanut bulge is mainly supported by brezel-like orbits, allowing strong peanuts to form with short extent relative to the bar length. This shows that stars in the X-shape do not necessarily stream along banana orbits which follow the arms of the X-shape. The brezel orbits are also found to be the main orbital component supporting the peanut shape in our recent Made-to-Measure dynamical models of the galactic bulge. We also show that in these models the fraction of stellar orbits that contribute to the X-structure account for 40 – 45% of the stellar mass.

### 3.1 Introduction

There has been much recent interest in the dynamical structure of the galactic bulge, following the discovery of the bimodal distribution of red clump giants (RCGs) magnitudes in upper bulge fields (the split red clump; [McWilliam & Zoccali 2010](#); [Nataf et al. 2010](#); [Ness et al. 2012](#)). Analyzing 50 million RCGs from the VVV survey, [Wegg & Gerhard \(2013\)](#) were able to measure directly the 3D density distribution of the dominant bulge

stellar population, finding a very pronounced boxy/peanut (B/P) bulge structure extending about 2 kpc along its major axis. B/P bulges are found in about half of the external edge-on disc galaxies (Lütticke, Dettmar & Pohlen 2000) and are the focus of several recent and on-going studies (Williams et al. 2011; Fabricius et al. 2012; Walcher et al. 2014; Seidel et al. 2015). B/P bulges are common in N-body simulations of barred discs where instability of the bar leads to one or more buckling events, creating a prominent peanut shape in the inner part of the bar (Combes & Sanders 1981; Raha et al. 1991; Martinez-Valpuesta, Shlosman & Heller 2006).

The orbital structure of bars was first studied in two dimensions (for a review see Contopoulos & Grosbøl 1989), showing that bars are largely made out of regular orbit families trapped around stable periodic orbits. Later, studies of the 3D orbital structure were carried out, focusing mostly on the stable periodic orbit families. The third dimension introduces instability in the dynamics and leads to bifurcations of stable periodic planar orbits. Pioneering work by Pfenniger & Friedli (1991) found that the main orbit family of planar bars (the  $x_1$  orbits) becomes vertically unstable in certain regions and bifurcates to several 3D orbital families including the  $x_1v_1$  family.  $x_1v_1$  orbits are also called banana orbits because of their banana shape when seen side-on. These banana orbits have since been considered as the backbone of B/P bulges (eg. Pfenniger & Friedli 1991; Martinez-Valpuesta, Shlosman & Heller 2006), even though other higher order resonant orbit families could also build a peanut shape bulge (Patsis et al. 2002).

In this letter we show that the banana orbits are not necessarily the main building block of B/P bulges, challenging the picture of stars streaming along the arms of the X-shape. We describe a new family of brezel-like orbits with which a peanut bulge can form at smaller radii relative to the bar than is possible with banana orbits. We find that this orbit family dominates the peanut shape of the galactic bulge in both our N-body models (Section 3.2) and our Made-to-Measure models (Section 3.3) for the galactic bulge from Portail et al. (2015). We also present an orbit-based characterization of the X-shape structure of the galactic bulge and show that in our models, the galactic X-shape structure accounts for 40 – 45% of the stellar mass of the bulge.

## 3.2 The orbital structure of B/P bulges in N-body models

### 3.2.1 N-body models of B/P bulges

We analyze N-body models of barred discs evolved from a near equilibrium stellar disc embedded in different live dark matter halos. During this evolution the disc naturally forms a bar which rapidly buckles out of the galactic plane and creates a B/P bulge (Combes & Sanders 1981; Raha et al. 1991). In this work we use the initial N-body models M80, M85 and M90 already presented in Portail et al. (2015). These three models differ by their dark matter fraction in the bulge, ranging from 30% for model M80 to 12% for model M90. Using the definition of Debattista & Sellwood (2000) where  $\mathcal{R}$  is the ratio between

corotation radius and half-length of the bar, they span the complete range of reasonable values for the  $\mathcal{R}$  parameter (Elmegreen 1996), from a slow bar for M80 ( $\mathcal{R} = 1.8$ ) to a fast bar for M90 ( $\mathcal{R} = 1.08$ ).

We assume a distance to the Galactic Centre of  $R_0 = 8.3$  kpc (Reid et al. 2014; Chatzopoulos et al. 2015) and place the bar at an angle of  $27^\circ$  with respect to the line-of-sight towards the Galactic Centre (Wegg & Gerhard 2013). We scale the models to the Milky Way by placing the end of their long bar component at  $l = 27^\circ$  as seen from the Sun’s location (Hammersley et al. 2000; Cabrera-Lavers et al. 2007), resulting in a bar half length of 4.6 kpc. In the following we use the  $(x, y, z)$  coordinates in the rotating frame of the bar where  $x$  is along the major axis of the bar and  $z$  is the axis orthogonal to the galactic plane.

### 3.2.2 Orbit classification

Most studies of the orbital structure of B/P bulges focus on studying families of periodic orbits in rotating potentials, either analytical (e.g. Skokos, Patsis & Athanassoula 2002) or N-body (Pfenniger & Friedli 1991, but see also Harsoula & Kalapotharakos (2009)). In this paper, we study the orbits of the particles in the N-body potential frozen well after the formation and buckling of the bar, which is then assumed to rotate at a constant pattern speed. We integrate the orbits using a drift-kick-drift adaptive leap-frog algorithm and use frequency analysis to classify those that build the B/P bulge. We consider all stellar particles in a box of  $\pm 4$  kpc  $\times$   $\pm 1.5$  kpc  $\times$   $\pm 1.5$  kpc in the bar frame ( $\sim 7 \times 10^5$  particles) and integrate the orbits for 50 dynamical times, where the dynamical time is defined as the time necessary to complete a circular orbit at 2 kpc. We record 100 positions of the selected particles per dynamical time and construct this way a time series for the particle coordinates. For each particle we compute the Fast Fourier Transform of its coordinate time series and identify the main frequency of each coordinate as the frequency corresponding to the highest spectral peak. We do this for the Cartesian coordinates  $x$  and  $z$  in the bar frame as well as the cylindrical radius  $r$  and consider the ratios of the main frequencies  $f_r/f_x$  and  $f_z/f_x$ .

In our models we find two main groups of particles: bar particles and disc particles. Bar particles are identified by their frequency ratio  $f_r/f_x \in 2 \pm 0.1$ . They have an elongated shape along the bar major or intermediate axis. Disc particles are defined through  $f_r/f_x \notin 2 \pm 0.1$ . They do not support the bar shape and do not show any prominent peanut shape. As we focus on the peanut shape of the bar, we exclude the disc particles from further analysis.

In order to identify the orbital components of the peanut structure we focus on the frequency ratio of the side-on coordinates,  $f_z/f_x$ . The top plot of Figure 3.1 shows the distributions of the frequency ratio  $f_z/f_x$  for our three N-body models. As  $f_z/f_x$  is almost entirely contained between 1.5 and 2.0, we make a low resolution orbit classification by splitting the particles into 6 classes A to F, corresponding to equally spaced bins in  $f_z/f_x$  centred on 1.5, 1.6, 1.7, 1.8, 1.9 and 2.0. The colored dots in Figure 3.1 indicate the fraction of stellar mass belonging to each orbital class in the three models.

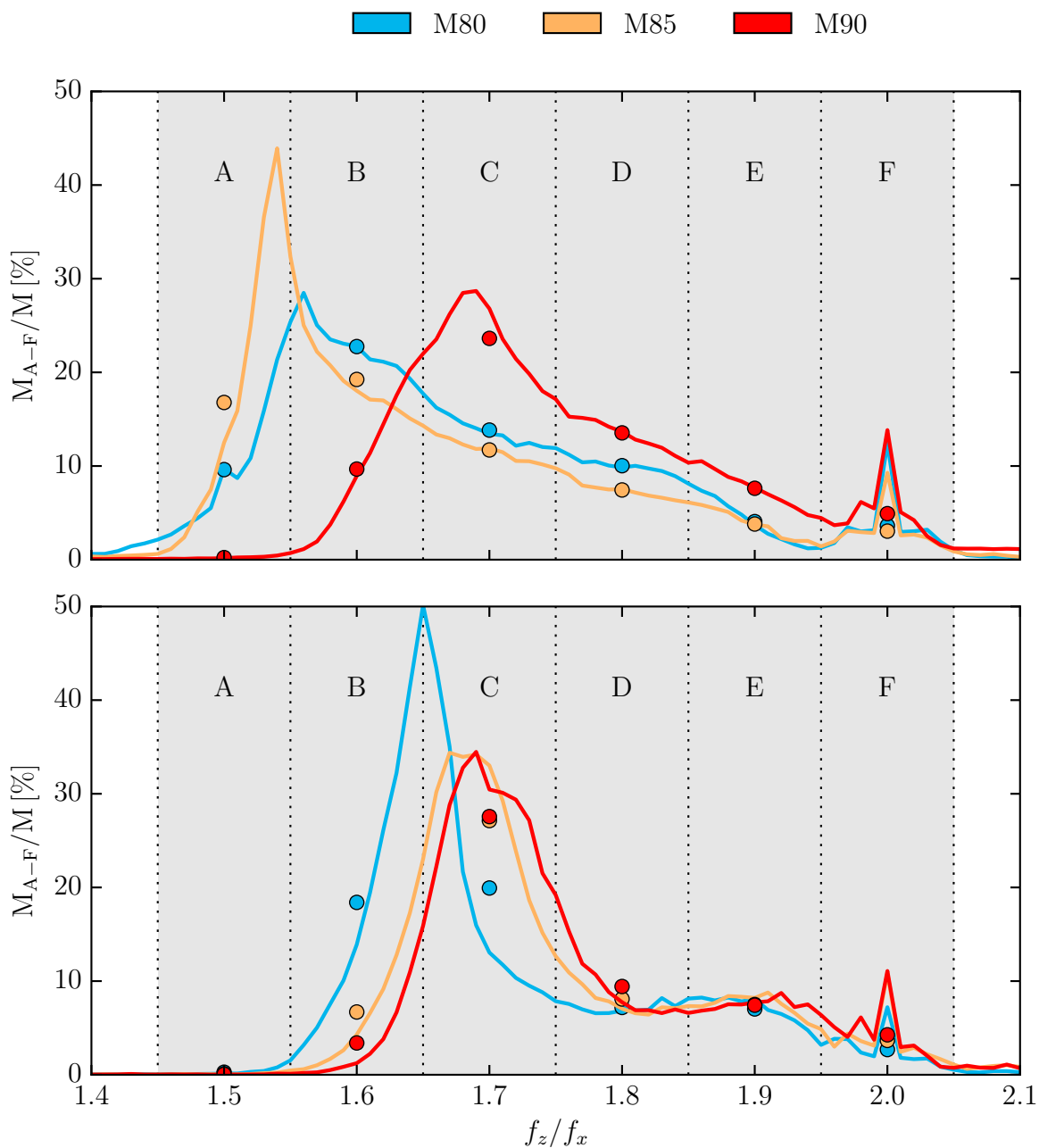


Figure 3.1: Fraction of the selected stellar particles belonging to orbital classes A-F defined through their frequency ratio  $f_z/f_x$  as shown in the figure. Top: for the three N-body models (see Section 3.2); bottom: for the models fitted to the Milky Way bulge (see Section 3.3). The colored dots indicate the fraction of mass in the orbital classes while the solid lines show the continuous distribution of the frequency ratio  $f_z/f_x$ . The banana orbits are located in the peak at  $f_z/f_x = 2$ .

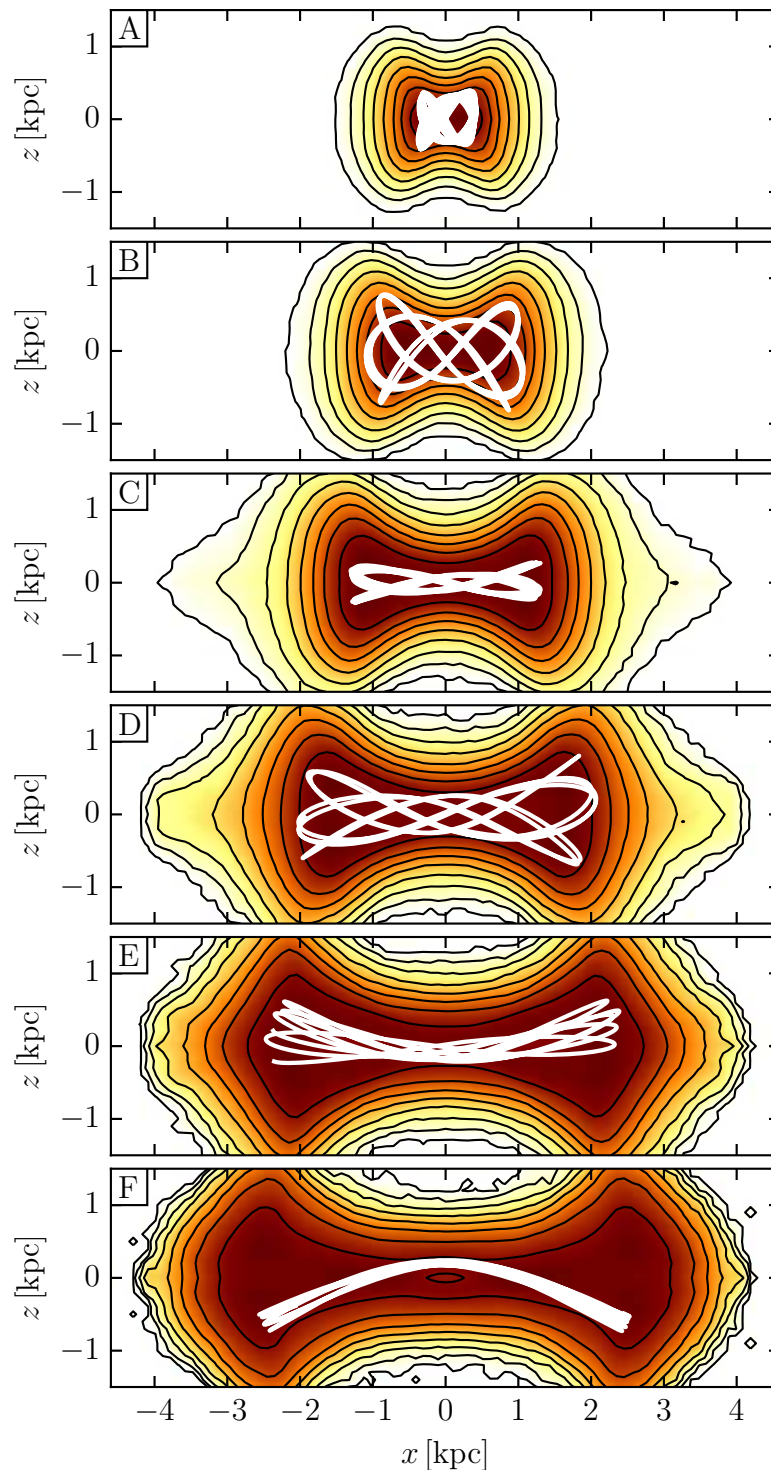


Figure 3.2: Side-on projections of the six orbital classes identified by frequency analysis of model M85. The white curves show the side-on trajectories of typical sample orbits belonging to each class. The banana orbits identified by Pfenniger & Friedli (1991) are in class F.

Figure 3.2 shows the side-on projections of these 6 orbital classes identified in model M85. All these classes display a strong peanut shape on the side-on projection. We find that orbits with larger frequency ratio  $f_z/f_x$  have larger radial extent. The total B/P structure of the model is then the sum of all these embedded peanut shapes. All orbits in any one class are very similar to each other and the white curves in Figure 3.2 show the side-on trajectory of a typical sample orbit of each class.

### 3.2.3 Which orbit classes dominate the X-shape?

The orbital structure of 3D bars has been studied both in analytical potentials by Con-topoulos & Barbanis (1994) and Skokos, Patsis & Athanassoula (2002), and in self gravitating N-body models by Combes et al. (1990) and Pfenniger & Friedli (1991). These authors found that the dominant  $x_1$  orbit family of 2D bars may become vertically unstable when introducing the third dimension. Instability of planar  $x_1$  orbits results in the birth of many different 3D periodic orbits families, called the  $x_1$  tree. The simplest member of the  $x_1$  tree is the  $x_1v_1$  family, also called “banana” orbits by Pfenniger & Friedli (1991) because of the shape of their side-on trajectories. Banana orbits have been found in many N-body or analytical models and have since been considered as the main building block of B/P bulge (Combes et al. 1990; Pfenniger & Friedli 1991; Patsis, Skokos & Athanassoula 2002; Martinez-Valpuesta, Shlosman & Heller 2006; Quillen et al. 2013). They appear at the vertical 2 : 1 resonance (i.e. 2 vertical oscillations per revolution), causing the peak at  $f_z/f_x = 2$  in Figure 3.1, and are therefore the main contribution to our orbital class F. Higher order members of the  $x_1$  tree can also play a role in 3D bars and eventually contribute to the peanut shape, as noted by Skokos, Patsis & Athanassoula (2002) and Patsis, Skokos & Athanassoula (2002). However these orbits arise at larger energies, which means even larger radial extent.

Identifying the building blocks of the B/P feature from our N-body models is not a trivial task. B/P bulges are composite structures where different orbits existing at different energies and radii overlap and all together create the B/P feature. In our models, all orbital classes shown in Figure 3.2 are at some radius the main component of the 3D part of the bar. In order to clarify this, we make the distinction between B/P shape and X-shape. B/P shape refers to the shape of the isophotes in the side-on projection, while X-shape refers to the typical X-feature that is revealed when applying unsharp-masking techniques to the side-on projection of the B/P feature. Determining the X-shape is a common practice to study external galaxies and can be performed in several ways, using a median filter as in Bureau et al. (2006) or removing a fit of the image, as in Li & Shen (2012).

Figure 3.3 shows in black contours the B/P shape of the N-body model M85 and its X-shape obtained after removing the median filtered image. In this figure, the colors indicate which orbital class contributes the highest surface density at each point of the side-on view of the bar. The B/P feature, which is the sum of the different orbital classes shown in Figure 3.2, appears mostly boxy with no well defined length. On the contrary the X-shape is clear and contained inside 2 kpc. Only classes A, B, C and D contribute significantly to the X-shape in this model. The banana orbits, the lowest energy member of the  $x_1$  tree,

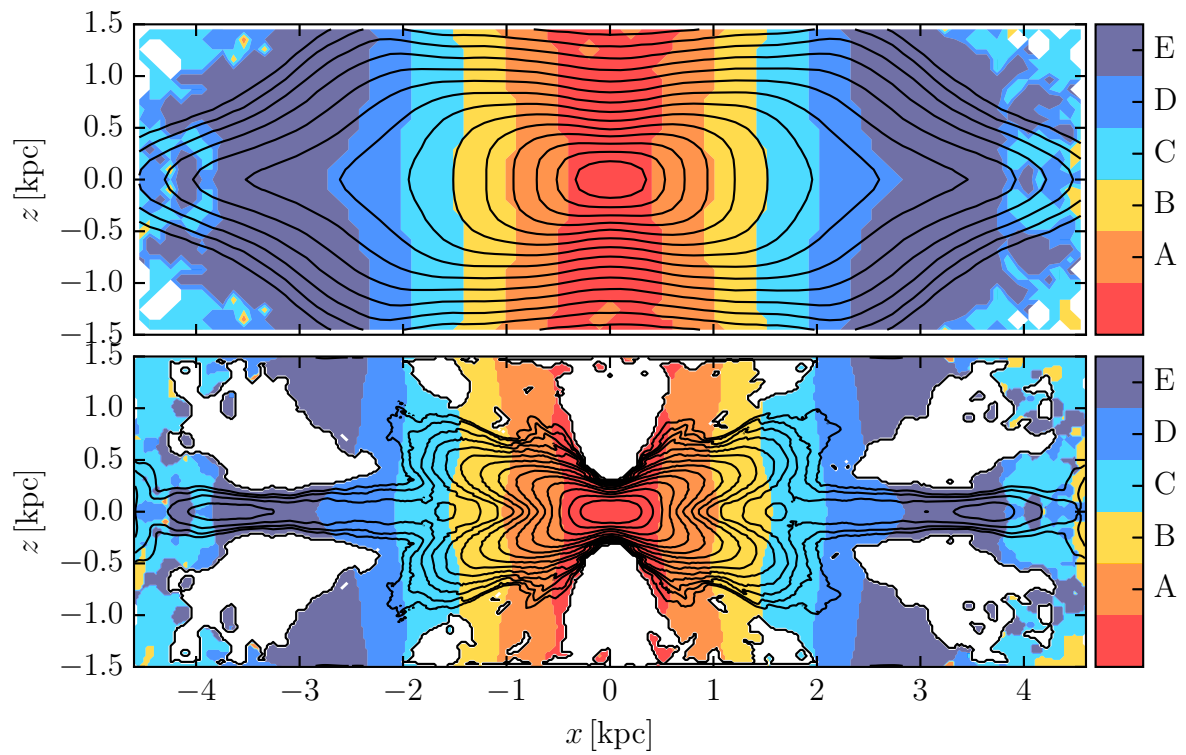


Figure 3.3: Peanut shape (top) and X-shape produced by unsharp-masking (bottom), for model M85. The colors indicate the orbital class which contribute the highest surface density at each point of the side-on view.

dominate the light only at radii larger than 2.5 kpc and contain only a small fraction of the stellar mass in the bulge as shown in [Figure 3.1](#). Therefore, in this N-body model, the picture that the X-shape is the result of stars trapped around banana orbits streaming along the arms of an X is incorrect. The X-shape in this model consist mostly of similar non resonant orbits whose parent orbits we call *brezel* orbits, which build an X-shape at shorter radii. Brezel orbits are described in [Section 3.3.2](#) in the context of the galactic bulge.

### 3.3 The orbital structure of the galactic B/P bulge

#### 3.3.1 Made-to-Measure models of the galactic bulge

In [Portail et al. \(2015\)](#) we constructed a set of dynamical models of the galactic bulge, with different dark matter halos. We used the Made-to-Measure method ([Syer & Tremaine 1996](#); [De Lorenzi et al. 2007](#)) to adapt the particle weights of the N-body models M80, M85 and M90 just described, to force them to reproduce the stellar density and kinematic measurements of the galactic bulge. We constrained the stellar density using the 3D density map of RCGs in the bulge from [Wegg & Gerhard \(2013\)](#), which trace the dominant fraction of the stellar mass. This map was derived by deconvolution of extinction and completeness corrected line-of-sight magnitude distributions from the VVV survey ([Saito et al. 2012](#)) and covers a box of  $\pm 2.2 \text{ kpc} \times \pm 1.4 \text{ kpc} \times \pm 1.2 \text{ kpc}$ . As kinematic constraints we used the radial velocity and dispersion measurements from the BRAVA survey ([Kunder et al. 2012](#)). After the Made-to-Measure fit, the resulting three models match the data very well and are equally good candidates to represent the dynamics of the galactic bulge, differing from each other by their dark matter fraction in the bulge.

The top plot of [Figure 3.4](#) shows the side-on projection of the RCGs density map of [Wegg & Gerhard \(2013\)](#) extrapolated in the midplane by [Portail et al. \(2015\)](#). The peanut shape is strong and mostly contained inside 1.5 kpc from the centre along the major axis of the bar. It can be highlighted in a more physical way than usually done with unsharp masking. For this we follow [Portail et al. \(2015\)](#) and compute the elliptical component  $\Sigma_e$  of the side-on projection of the map  $\Sigma$ , by fitting a family of ellipses to  $\Sigma$  with the constraint that the residuals  $\Sigma - \Sigma_e$  are everywhere positive. The non-elliptical residual fraction  $(\Sigma - \Sigma_e)/\Sigma$  is plotted on the bottom panel of [Figure 3.4](#). It shows a large deviation from elliptical shape at radii as short as 1.5 kpc, about one third of the bar length. In these models, the banana orbits do not achieve significant height at radii around one third of the bar length. The lower plot of [Figure 3.1](#) shows the orbital compositions of our three models after fitting to the Milky Way data. The comparison with the upper plot shows that the Made-to-Measure procedure (i.e. the data) moved most of the mass to the orbital classes B and especially C. These classes display a strong peanut at radii around a third of the bar length, as shown in [Figure 3.2](#).

Thus, the relation between the X-shape and the orbital structure is not straightforward. X-shapes in external galaxies are often off-centered, with the two arms of the X not crossing



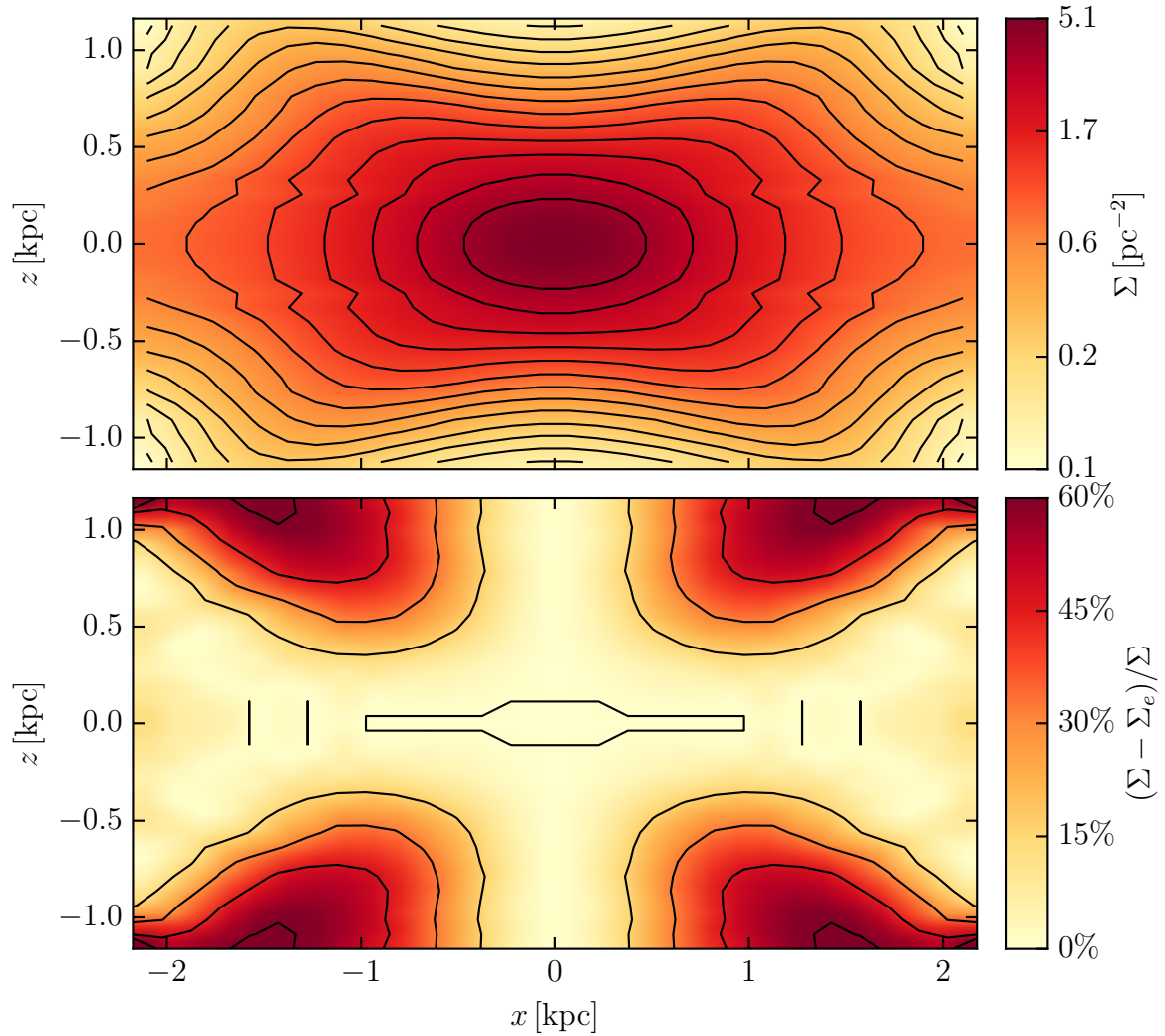


Figure 3.4: *Top:* Side-on projection of the extrapolated 3D red clump giants number density map originally from Wegg & Gerhard (2013). *Bottom:* Non-elliptical residual fraction of the side-on projection.

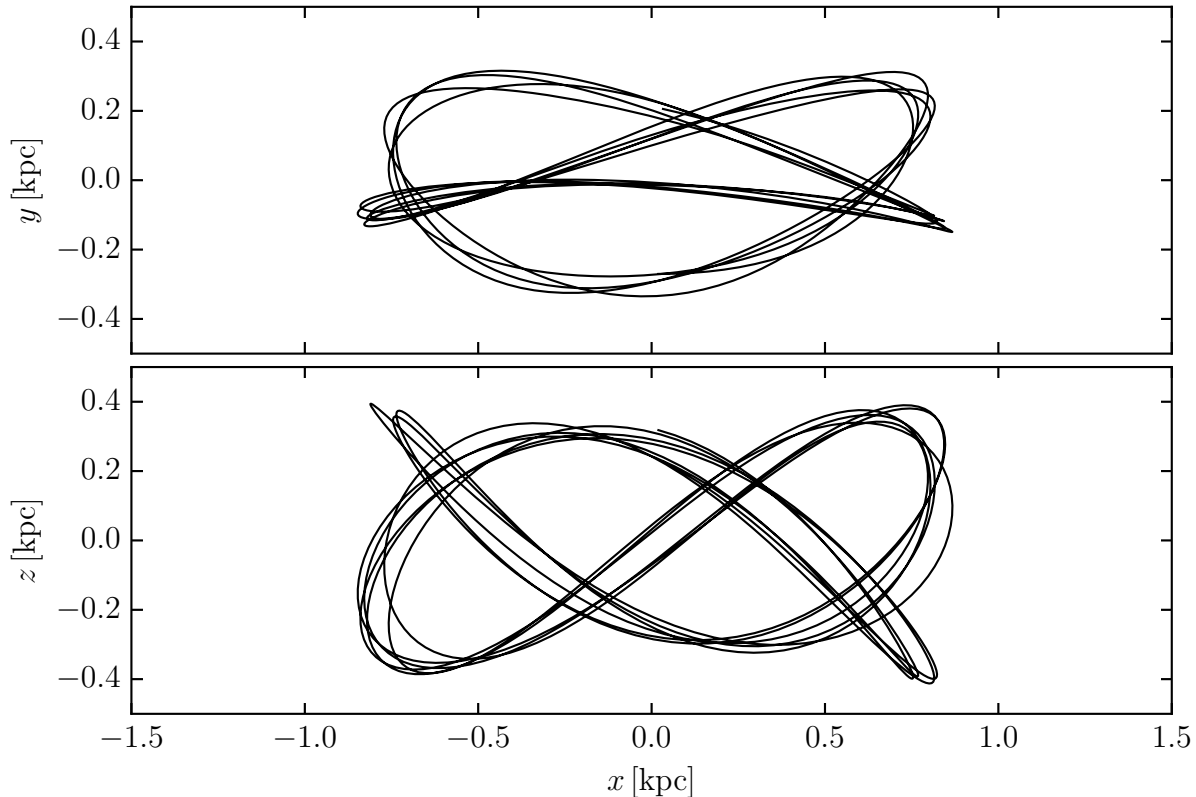


Figure 3.5: Brezel orbit viewed face-on (top) and side-on (bottom).

at the center as shown by Bureau et al. (2006). These authors suggested that off-centered X-shapes could be associated with banana orbits given their morphological similarity. The X-shapes of our Made-to-Measure models of the MW bulge are also off-centered (as shown in Fig. 17 of Portail et al. 2015), even though the banana orbits represent only a small fraction of the orbital structure in these models.

### 3.3.2 The brezel orbit

After fitting of the BRAVA data and RCGs density, most of the stellar mass of bar particles are on orbits of class C. These orbits were already present in the initial models but in lower proportion. This class is mostly made of non-resonant orbits which show morphological similarities with one particular orbit family. Figure 3.5 shows the face-on (top) and side-on (bottom) view of such an orbit that we call brezel orbit.<sup>1</sup> This orbit has a mirror-symmetric counterpart with respect to the  $y = 0$  plane. It has  $f_z/f_x \simeq 5/3$  but needs 10 oscillations in  $z$  and 6 oscillations in  $x$  in order to close. A possible origin for the brezel orbit would be the  $5 : 3$  vertical resonance of the so called  $x_1 \text{ mul}_2$  planar orbit, in the notation of Skokos,

<sup>1</sup>Note that our brezel orbit is topologically different from the “prezel boxlet” orbit, found at the 4:3 resonance in triaxial non-rotating potentials (Miralda-Escude & Schwarzschild 1989; Merritt & Fridman 1996).

Patsis & Athanassoula (2002) (i.e. the usual 2D  $x_1$  orbit but considered to close after two rotations instead of one). Their face-on shapes are also similar to the rm21 and rm22 identified by Patsis & Katsanikas (2014) (see their Fig. 2), arising from a radial bifurcation of the  $x_1\text{mul}_2$ . A detailed study of the  $x_1\text{mul}_2$  tree is needed to study this further.

### 3.3.3 The galactic X-structure

What is the stellar mass fraction associated with the X-shape in the galactic bulge? In models where there is no correspondence between the X-shape and a particular orbit family, this question cannot be answered easily. In these models, the X-shape only reveals the excess of light over some smooth background in the side-on projection, but is no longer directly related to any physical substructure of the bulge. Therefore, using our orbit classification, we define the *X-structure* as the physical stellar component which is built by all bar orbits ( $f_r/f_x \in 2 \pm 0.1$ ) that contribute significantly to the non-elliptical fraction identified in Figure 3.4; specifically, by all bar orbits that visit regions of the side-on view where the non-elliptical fraction is larger than 10%. With this definition, the peanut shape of Figure 3.4 can be seen as the sum of three components: the surrounding disc, made of orbits that do not follow the bar; the main bar, made of orbits that follow the bar but do not contribute significantly to  $\Sigma - \Sigma_e$ ; and the X-structure, contributing to most of the deviation of  $\Sigma$  from elliptical density.

With this definition, the fraction of the stellar mass in the X-structure contained in a box of  $\pm 4\text{kpc} \times \pm 1.5\text{kpc} \times \pm 1.5\text{kpc}$ , is 44%, 43% and 42%, respectively, for the fitted models M80, M85 and M90. Restricting this computation to the box of  $\pm 2.2\text{kpc} \times \pm 1.4\text{kpc} \times \pm 1.2\text{kpc}$  where Wegg & Gerhard (2013) measured the RCGs density, gives very similar numbers, 45%, 44% and 43%, respectively. This large fraction is in agreement with the lower bound estimated in Portail et al. (2015). It is mostly due to the morphology of class B and C orbits, which provide the peanut shape as well as a significant part of the in-plane density.

## 3.4 Conclusion

We have analyzed the orbits of three B/P bulges in N-body models of bars evolved in different dark matter halos. We find that the B/P bulges of these models are complex structures made of the superposition of several peanut shapes produced by different orbits, that are embedded at different radii. Contrary to what is usually stated in the literature, these B/P bulges are not mainly made out of “banana” or  $x_1v_1$  orbits and their X-shape is not the result of stars streaming along these orbits as they follow the arms of the X-shape. Instead, in these models a strong peanut shape bulge is built from a family of brezel-like orbits, with a typical extent of about one third of the bar length.

In our Made-to-Measure models fitted to Milky Way observables, i.e., to the red clump giants 3D density map from Wegg & Gerhard (2013) and the BRAVA kinematics data (Kunder et al. 2012), we find that the brezel orbit family is the backbone of the orbits

populating the galactic boxy/peanut feature. Using our orbital classification we propose a definition of the physical structure associated with the galactic X-shape and we estimate that the fraction of stellar orbits that contribute to it account for 40 – 45% of the stellar mass of the bulge.

## Acknowledgement

We thank Panos Patsis for helpful discussions on orbits, stability and chaos as well as Matías Blaña for his help in setting up our N-body models of barred discs.

# Chapter 4

## Dynamical Modelling of the Galactic Bulge and Bar: pattern speed, stellar, and dark matter mass distributions

**Original publication:** Matthieu Portail, Ortwin Gerhard, Christopher Wegg and Melissa Ness, submitted to MNRAS [↗](#)

### Abstract

We construct a large set of dynamical models of the galactic bulge, bar and inner disk using the Made-to-Measure method. Our models are constrained to match the red clump giant density from a combination of the VVV, UKIDSS and 2MASS infrared surveys together with stellar kinematics in the bulge from the BRAVA and OGLE surveys, and in the entire bar region from the ARGOS survey. We are able to recover the bar pattern speed and the stellar and dark matter mass distributions in the bar region, thus recovering the entire galactic effective potential. We find a bar pattern speed of  $39.0 \pm 3.5 \text{ km s}^{-1} \text{ kpc}^{-1}$ , placing the bar corotation radius at  $6.1 \pm 0.5 \text{ kpc}$  and making the Milky Way bar a typical fast rotator. We evaluate the stellar mass of the long bar and bulge structure to be  $M_{\text{bar/bulge}} = 1.88 \pm 0.12 \times 10^{10} M_{\odot}$ , larger than the mass of disk in the bar region,  $M_{\text{inner disk}} = 1.29 \pm 0.12 \times 10^{10} M_{\odot}$ . The total dynamical mass in the bulge volume is  $1.85 \pm 0.05 \times 10^{10} M_{\odot}$ . Thanks to more extended kinematic datasets and recent measurement of the bulge IMF we obtain a low dark matter fraction in the bulge of  $17\% \pm 2\%$ . We find a dark matter density profile which flattens to a shallow cusp or core in the bulge region. Finally, we find dynamical evidence for an extra central mass of  $\sim 2 \times 10^9 M_{\odot}$ , probably in a nuclear disk or diskly pseudobulge.

## 4.1 Introduction

Although it is well established that the Milky Way hosts a central barred bulge which causes non-axisymmetric gas flow (Peters, III 1975; Binney et al. 1991) and asymmetries in the near infrared light (Blitz & Spergel 1991; Weiland et al. 1994) and star counts (Nakada et al. 1991; Stanek et al. 1997); our understanding of this structure has dramatically improved in the last decade. The discovery of the so-called split red clump in the galactic bulge (Nataf et al. 2010; McWilliam & Zoccali 2010) and the later 3D mapping of the bulge density by Wegg & Gerhard (2013) showed the galactic bulge has a boxy/peanut (B/P) shape, similarly to bulges formed in N-body models by buckling of a vertically unstable stellar bar (Combes et al. 1990; Martinez-Valpuesta, Shlosman & Heller 2006).

The existence of the bar outside of the bulge initially revealed by Hammersley et al. (1994) has been subject to controversy as to whether it is a separate structure from the bulge. First studies indicated a misalignment between the bulge and the bar, leading to the hypothesis of a double bar system in the inner Milky Way (Benjamin et al. (2005); López-Corredoira, Cabrera-Lavers & Gerhard (2005); Cabrera-Lavers et al. (2008); but see also Martinez-Valpuesta & Gerhard (2011)). Recently Wegg, Gerhard & Portail (2015, hereafter W15) demonstrated by combining the VVV, UKIDSS, GLIMPSE and 2MASS catalogs that the galactic bulge smoothly segues into the long bar. Both components appear at a similar angle, showing that the galactic bulge and the long bar in the Milky Way are consistent with being a single structure that became vertically thick in its inner part, similarly to the buckled bars of N-body models.

In Portail et al. (2015, hereafter P15) we constructed dynamical models of the galactic bulge by combining the 3D density of Red Clump Giants (RCGs) in the bulge from Wegg & Gerhard (2013) with bulge kinematics from the BRAVA survey (Rich et al. 2007; Kunder et al. 2012) using the Made-to-Measure method. In this paper we extend the Made-to-Measure modelling to the entire bar region by taking advantage of the recent measurement of W15 on the bar outside the bulge together with stellar kinematics in the bar region from the ARGOS survey (Freeman et al. 2013; Ness et al. 2013a). The goal is to combine stellar density and kinematics under the constraint of dynamical equilibrium in order to recover the effective potential in the bar region, i.e. the stellar and dark matter mass distribution together with the bar pattern speed.

Extending the modelling from the bulge to the entire bar region is not a straightforward task. The galactic long bar extends about 5 kpc from the Galactic Centre as shown by W15 and thus reaches radii where the outer disk contribution to the potential is important. Hence modelling the bar region also requires modelling the disk potential into which the bar is embedded. In addition, the dark matter contribution to the radial force increases with galactocentric radius reaching about 50% at the solar radius (Read 2014). As a consequence the global mass distribution of Galaxy has to be taken into account in order to produce a good model of the galactic bar region. The building of good initial conditions for the Made-to-Measure modelling is particularly challenging.

The paper is organized as follows. In Section 4.2 we briefly describe the Made-to-Measure method and the problem posed by the initial conditions. In Section 4.3 we con-

struct a static density model of the inner 10 kpc for the Galaxy by combining the current knowledge of the bulge, bar, disk and dark matter density. This density model is used in [Section 4.4](#) to tailor a set of N-body models with different bar pattern speeds that already broadly match the Milky-Way mass distribution. In [Section 4.5](#) we discuss the different datasets used in this study to constrain the models and summarize the modelling procedure in [Section 4.6](#). In [Section 4.7](#) we show the effect of the main modelling parameters on the bulge dynamics, and in [Section 4.8](#) we analyze a large number of models, recover the bar pattern speed of the Milky Way and identify our best model. In [Section 4.9](#) we summarize our constraints on the stellar and dark matter mass distribution that arises from our models, and discuss our results in the light of other works in [Section 4.10](#). We finally conclude in [Section 4.11](#). The impatient reader can read first [Sections 4.8](#) and [4.9](#) where we use our modelling to recover the effective potential in the Galaxy. Our best model is the first non-parametric model of the entire bar region and we plan to make it available upon request once the paper is accepted.

## 4.2 Made-to-Measure modelling of the Galaxy

### 4.2.1 M2M modelling

Stellar dynamical equilibria for galaxies can be studied with moment-based methods ([Binney, Davies & Illingworth 1990](#); [Cappellari et al. 2009](#)), classical distribution function-based methods ([Dejonghe 1984](#); [Qian et al. 1995](#)), actions-based methods ([Binney 2010](#); [Sanders & Binney 2013](#)), orbit-based methods ([Schwarzschild 1979](#); [Thomas et al. 2009](#)) or with the Made-to-Measure method ([Syer & Tremaine 1996](#); [De Lorenzi et al. 2007](#)). In these Made-to-Measure models (M2M) an initial self-gravitating N-body model is used to provide a discrete sample of a distribution function reasonably close to the system of interest. This N-body model is then slowly adapted by modifying the weights of the N-body particles such as to make the model reproduce a given set of constraints. The N-body weights can hence be seen simultaneously as mass elements (N-body point of view), or as weights for the orbits traced by the particles (Schwarzschild’s method point of view). The method was extended to allow the fitting of observational data and implemented as the NMAGIC code by [De Lorenzi et al. \(2007\)](#). The M2M method has been used in both extragalactic (e.g. [De Lorenzi et al. 2008, 2009](#); [Das et al. 2011](#); [Morganti et al. 2013](#); [Zhu et al. 2014](#)) and Galactic context (e.g. [Bissantz, Debattista & Gerhard 2004](#); [Long et al. 2013](#); [Hunt & Kawata 2014](#); P15). We heavily modified the NMAGIC code for the purpose of modelling barred disk galaxies.

Formally, the M2M method works as follow. Any observable  $y$  of a system can be written in term of the distribution function  $f(\mathbf{z})$  of the system by

$$y = \int K(\mathbf{z})f(\mathbf{z}) d^6\mathbf{z} \quad (4.1)$$

where  $K$  is the kernel corresponding to the observable and  $\mathbf{z}$  the phase space vector. In the M2M method  $f(\mathbf{z})$  is discretely sampled via a set of  $N$  particles with particle weights

$w_i(t)$ . Equation 4.1 is then evaluated by

$$y(t) = \sum_{i=1}^N K(\mathbf{z}_i(t)) w_i(t) \quad (4.2)$$

where  $\mathbf{z}_i(t)$  is the phase-space coordinate of particle  $i$  at time  $t$ .

The M2M method consists of adjusting the particle weights  $w_i$  in order to maximize a given profit function  $F$ . This is achieved by a simple gradient descent in which the particle weights are evolved with time according to

$$\frac{dw_i}{dt} = \varepsilon w_i \frac{\partial F}{\partial w_i} \quad (4.3)$$

and  $\varepsilon$  is a numerical factor that sets the typical timescale of the weight evolution. The profit function  $F$  usually consist of a chi-square term, that drives the model towards the data, and an entropy term to regularize the particle model. We describe the M2M formalism in more detail in Section 4.6.1.

Note that the M2M method only weights particles and does not have the ability to create new N-body orbits. It is thus a very efficient modelling technique provided all the N-body orbits required to fit the data are already present in the initial model. Building good initial conditions, including its dark matter component, is a major issue when modelling the inner 10 kpc of the Milky Way.

### 4.2.2 The problem of the initial conditions

To model the galactic bar we need an initial N-body model of a barred stellar disk that provides a first-guess discrete sampling of the final model. The classical way to build such initial conditions is to evolve a near-equilibrium N-body stellar disk in a live dark matter halo. During the evolution the disk becomes unstable and forms a bar, that later forms a B/P bulge through the buckling instability mechanism (Combes et al. 1990; Martinez-Valpuesta, Shlosman & Heller 2006). This process has been used widely in order to build models that can then be compared to data (Martinez-Valpuesta, Shlosman & Heller 2006; Athanassoula 2007; Shen et al. 2010) but suffers from three major limitations:

- (i) The evolution process is non-linear and very sensitive to initial conditions. As noted by (Sellwood & Debattista 2009) large changes in the evolved bar model can result from simply changing the seed of the random number generator used in building the initial conditions.
- (ii) The bar properties such as pattern speed, bar length and bar strength cannot be easily controlled a priori.
- (iii) The bar tend to be 3-5 disk scale lengths long as already noted by Debattista & Sellwood (2000) and Athanassoula (2002). This is much larger than what would be required to model the Milky Way where this ratio lies is within  $1.9 \pm 0.4$  (Bland-Hawthorn & Gerhard 2016).



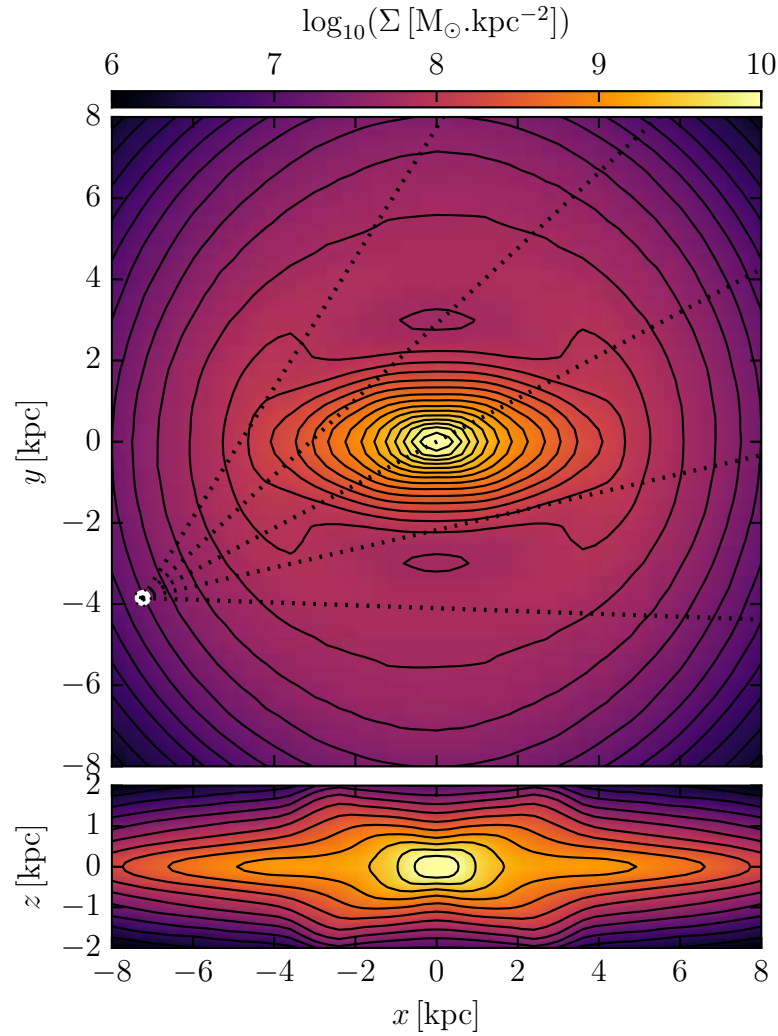


Figure 4.1: Face-on (upper) and side-on (lower) projections of the initial model M85 from [Portail et al. \(2015\)](#). The bar is 5 kpc long and at an angle of  $\alpha = 28^{\circ}$  from the Sun-GC line of sight. The dotted lines originating from the Sun (dot symbol) indicates sight lines with galactic longitudes  $l = -30^{\circ}, -15^{\circ}, 0^{\circ}, +15^{\circ},$  and  $+30^{\circ}$ .

An example of such a buckled bar N-body model is the model M85 of P15 shown in [Figure 4.1](#). When scaled to a bar half-length of 5 kpc, M85 has a very short disk scale length of only  $\sim 1.2$  kpc, resulting in a very low contribution of the outer disk to the potential at the end of the bar region together with a lack of mass on long bar orbits. M85 was good enough to model only the bulge in P15 but does not suit our purpose here to model the inner 10 kpc of the Galaxy. To get around the three limitations of pure N-body evolution shown above we use a variant the M2M method to tailor initial conditions in a two step process: In [Section 4.3](#) we first create a mass density model of the Milky Way by adding together our best-guess densities for the bulge, bar, disk and dark halo. This density is then imprinted on M85 using a variant of the M2M method in [Section 4.4](#), for different bar pattern speeds. At the end of this process we obtain a family of N-body models with different bar pattern speeds that have broadly the right mass distribution and provide suitable initial conditions for modeling the inner 10 kpc of the Milky Way by fitting real data.

### 4.3 Density model of the Galaxy for tailoring initial conditions

In this section we construct a mass density model of the inner 10 kpc of the Galaxy by combining the 3D densities of the B/P bulge, bar, outer disk and dark matter halo. This density model is only used to tailor our initial conditions for the actual M2M modelling which is performed in [Section 4.6](#). Throughout the paper we place the Sun in the galactic plane at a distance  $R_0 = 8.2$  kpc ([Bland-Hawthorn & Gerhard 2016](#)) from the Galactic Centre. The bar is oriented at an angle of  $\alpha = 28^\circ$  with the Sun-GC line of sight, consistent with the measurement of  $27^\circ \pm 2^\circ$  from the bulge RCGs ([Wegg & Gerhard 2013](#)) and the range  $28^\circ - 33^\circ$  measured by W15 from the long bar RCGs. Following [Bland-Hawthorn & Gerhard \(2016\)](#) we assume that the Local Standard at Rest (LSR) is on a circular orbit at  $V(R_0) = 238 \text{ km s}^{-1}$ , and a peculiar motion of the Sun in the LSR of  $(U, V, W) = (11.1, 12.24, 7.25) \text{ km s}^{-1}$  ([Schönrich, Binney & Dehnen 2010](#)). This set of assumption predicts a solar tangential velocity of  $250 \text{ km s}^{-1}$ , in good agreement with several recent measurements of  $248 \pm 6 \text{ km s}^{-1}$  ([Schönrich 2012](#), from SEGUE data),  $242_{-3}^{+10} \text{ km s}^{-1}$  ([Bovy et al. 2012](#), from APOGEE data),  $244 \pm 5 \text{ km s}^{-1}$  ([Sharma et al. 2014](#), from RAVE data) and  $251 \pm 5 \text{ km s}^{-1}$  ([Reid et al. 2014](#), from maser velocities). All parameters of the density model are summarized in [Table 4.1](#).

#### 4.3.1 Unified bulge and bar structure as traced by RCGs

Recently, [Wegg & Gerhard \(2013\)](#) constructed the first non-parametric measurement of the 3D density of RCGs in the bulge. They took advantage of the narrow luminosity function of RCGs to directly deconvolve the extinction and completeness corrected magnitude distributions of bulge stars from the VVV survey and obtain line of sight densities of RCGs. Combining the different lines of sight and assuming 8-fold symmetry they produced a 3D

density map of RCGs in a box of  $(\pm 2.2 \times \pm 1.4 \times \pm 1.2)$  kpc around the principal axes of the bulge. This map together with the BRAVA kinematics was later used in P15 to construct a family of dynamical models of the galactic bulge. As bulge component we adopt here the 3D density of the fitted model M85 of P15 that reproduces the original RCG density very well, with the advantage of being smooth and complete in the plane where the direct measurement of the density was not possible because of extinction and crowding.

Outside the bulge W15 combined the VVV, UKIDSS and 2MASS surveys and showed that the bulge smoothly segues from its vertically extended B/P shape to the flat long bar. The bulge and long bar are shown in this later work to be consistent with forming a single structure, oriented at  $\alpha = 28^\circ$  from the Sun-GC line of sight. They estimated the long bar half-length to be 5 kpc and found evidence for an extra super-thin bar component existing predominantly near the bar end. They finally fit a parametric model of the long bar density that once added to the fitted bulge model M85 of P15 and convolved with the bulge luminosity function fits well the magnitude distribution of stars across the entire bulge and bar region. Consequently we complement the bulge model described above using their best fit parametric densities of the thin long bar and super-thin components. Note that due to their analysis method, the long bar density of W15 does not include the inner disk, smooth background of stars filling the bar region. We add the inner disk density in Section 4.3.3.

Both the bulge and long bar density were measured using RCGs as tracers. Theoretical models by Salaris & Girardi (2002) show that for a 10 Gyr old stellar population, RCGs trace the stellar mass within 10% for metallicities in the range  $-1.5 \leq [\text{Fe}/\text{H}] \leq 0.2$ . In the particular case of the galactic bulge and bar, Ness et al. (2013a) find from the ARGOS sample that 95% of the stars enter this metallicity range. The age of the bulge is still under debate with contradictory evidences: photometric studies of the color-magnitude diagram (Zoccali et al. 2003; Clarkson et al. 2008; Calamida et al. 2015) find that the bulge is older than 10 Gyr while spectroscopic age measurements of microlensed dwarfs find evidence for 4 – 5 Gyr old population among stars with  $[\text{Fe}/\text{H}] \geq -0.1$  (Bensby et al. 2011, 2013). We assume here that the bulge and bar are 10 Gyr old, implying that the RCGs density of the bulge and long bar considered above are proportional to the stellar density with expected variations of less than 10%. We call the proportionality factor between stellar mass density and RCG density *mass-to-clump ratio*<sup>1</sup>, denoted  $M/n_{\text{RCG}}$  by analogy to the mass to-light-ratio. We make the fiducial assumption that the bulge and the thin long bar have the same mass-to-clump ratio, as expected if they both formed at the same time. The origin of the super-thin bar is still unclear as stated by W15 but its stellar population is expected to be younger given its extremely short scale height (45 pc), and therefore it is likely to have a lower mass-to-clump ratio than the bulge. Assuming a constant star formation rate and a Kroupa IMF as in W15, the mass-to-clump ratio of the superthin bar is a factor 1.6 times smaller than that of a 10 Gyr old bulge.

---

<sup>1</sup>Note that, as in P15 our definition of the mass-to-clump also includes the red giant branch bump stars, as the number of RCGs + red giant branch bump stars is better defined than the number of RCGs only (see Wegg & Gerhard 2013).

### 4.3.2 Empirical determination of the mass-to-clump ratio in the bulge

The mass-to-clump ratio can be predicted by stellar population synthesis models using an Initial Mass Functions (IMFs), a stellar age distribution and a metallicity distribution as in P15. The most recent measurement of the galactic bulge IMF is from Calamida et al. (2015) who used ultra-deep HST photometry to recover the IMF in the mass range  $0.15 \leq M/M_{\odot} \leq 1$ . They find an IMF in good agreement with the Kroupa IMF (Kroupa 2001), for which we computed in P15 a mass-to-clump ratio of  $M/n_{\text{RCG}} = 984$  for a 10 Gyr old population.

An alternative and more direct approach is to combine stellar mass measurements in some bulge field with the observed number of RCGs in that field, in analogy to the method of Valenti et al. (2015). This approach is advantageous since it does not rely on stellar populations models or parametrization of the IMF. Zoccali et al. (2000) used HST photometry in the NICMOS field and after cleaning for disk contamination they find a stellar mass in that field of  $M_{\text{NICMOS}} = 570 M_{\odot}$  (see the revision of the mass in the NICMOS field in Valenti et al. 2015). The NICMOS field has an area of only 408 square arcseconds and does not contains many giant stars. To improve the statistics on the number of RCGs we follow Valenti et al. (2015) and consider a larger  $15'$  beam centered on the NICMOS field and rescale the mass and number of RCGs by the ratio of the area of the two fields. We use the completeness and extinction corrected VVV catalogue of Wegg & Gerhard (2013) and identify RCGs statistically as the excess above the smooth background of stars in the extinction corrected magnitude distribution. Figure 4.2 show the magnitude distributions of VVV stars in our larger field centered on the positions of the NICMOS fields with the identified RCGs above the background of stars.

With this approach we find a mass-to-clump ratio of  $M/n_{\text{RCG}} = 1015$ . We estimate the error on this figure of about 10%, mostly due to systematic effect arising in defining the smooth background of stars onto which the RCGs sits (see Wegg & Gerhard 2013). This direct measurement is in good agreement with the predicted value of 984 for a Kroupa or Calamida IMF. In all the following we adopt the fiducial value of  $M/n_{\text{RCG}} = 1000$  for the main stellar population in the bulge and bar together with a lower value of  $M/n_{\text{RCG}} = 600$  for the superthin bar component. We show in Section 4.8 the effect of a 10% smaller or larger mass-to-clump ratio.

### 4.3.3 Stellar disk

Our prime interest in modelling the disk is to obtain a reasonable disk contribution to the potential in the bar region and disk foreground contamination when observing the bulge and bar. Outside the bar region ( $R \geq 5.5 \text{ kpc}$ ) we adopt an axisymmetric stellar disk structure with scale length  $h_{R,*}$  and exponential scale height  $h_{Z,*}$ . From papers based on infrared data Bland-Hawthorn & Gerhard (2016) concluded that  $h_{R,*} = 2.6 \pm 0.5 \text{ kpc}$  with the shorter disk scale lengths in the range  $2.1 - 2.6 \text{ kpc}$  usually favored by dynamical studies of stellar kinematics or microlensing optical depth towards the bulge (Wegg, Gerhard &

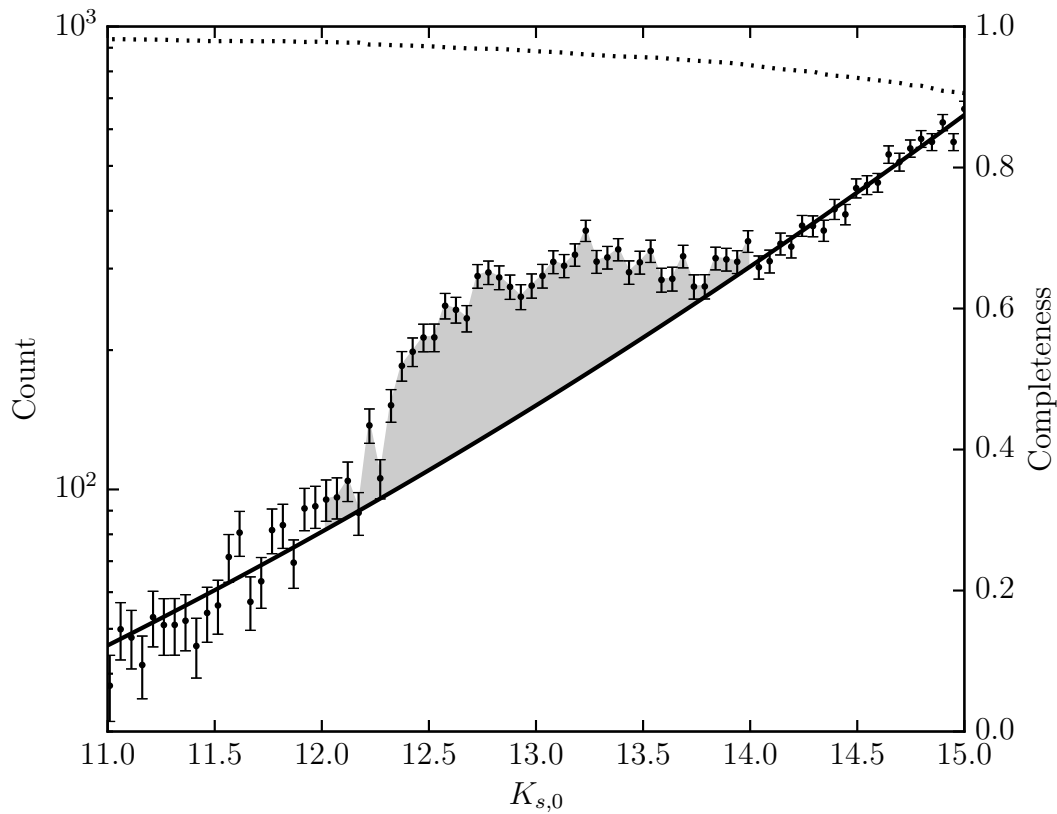


Figure 4.2:  $K_s$ -band extinction and completeness corrected magnitude distribution from the VVV catalogue of [Wegg, Gerhard & Portail \(2015\)](#) in a beam centered on the NICMOS field of radius  $15'$ . RCGs are identified as the excess above the background of stars. The dotted line indicate the completeness of the original VVV catalogue as a function of magnitude.

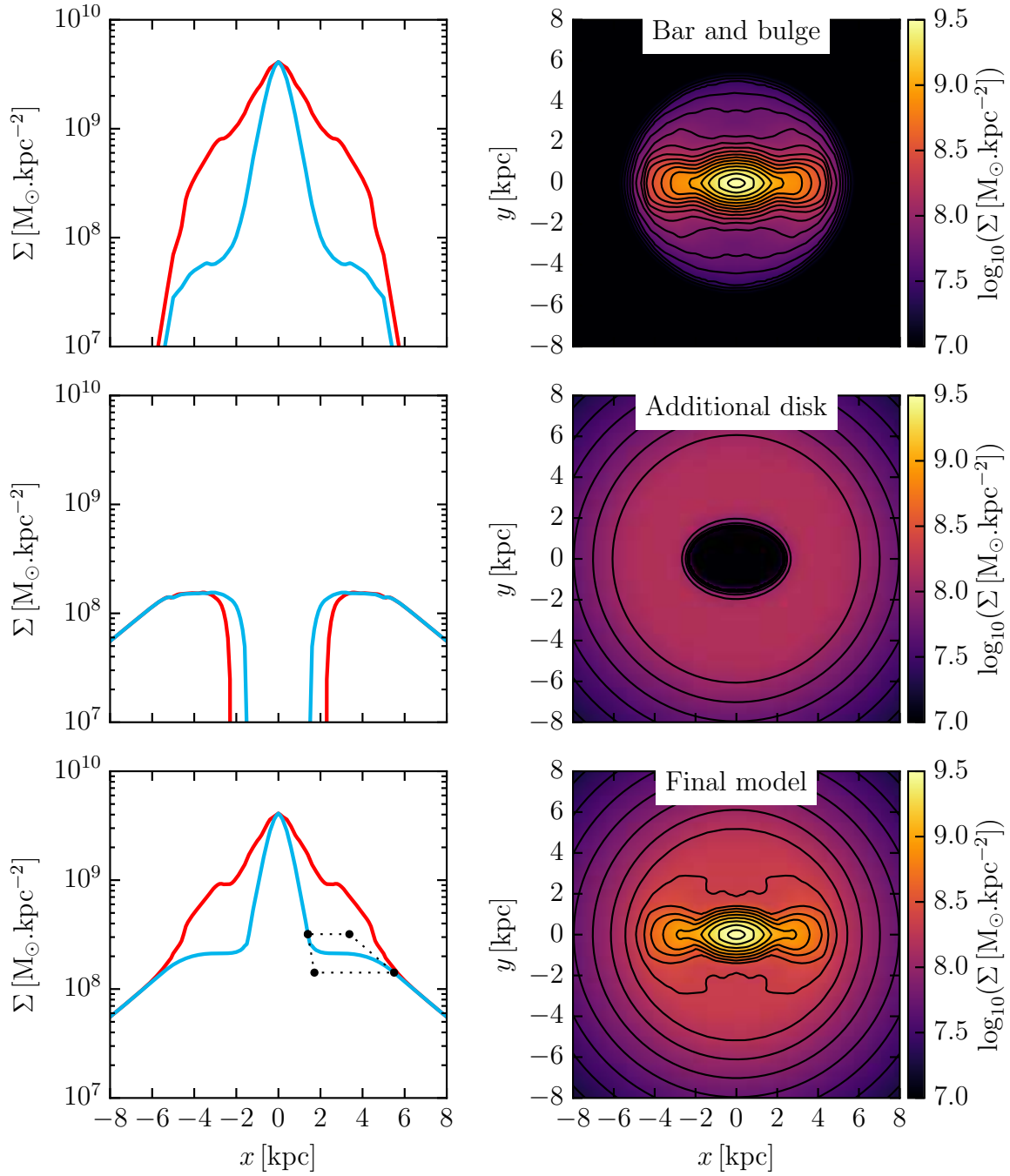


Figure 4.3: From top to bottom, surface density of the bulge and bar component, additional disk and total density model. Left column: surface density profiles along the bar major axis (red) and the bar intermediate axis (blue). The dashed region shows the convex hull of the Bézier curve controls points used for the interpolation of the intermediate axis surface density profile between 5.5 kpc and 1.4 kpc. Right column: Face-on surface density of the model components.

Portail 2016). We adopt here a fiducial scale length of  $h_{R,*} = 2.4$  kpc and scale height of  $h_{Z,*} = 300$  pc (Jurić et al. 2008) and test in Section 4.9 the effect of a shorter scale length of 2.15 kpc (Bovy & Rix 2013) and 2.6 kpc (Jurić et al. 2008).

Following Bovy & Rix (2013) we add the interstellar medium contribution to the potential by modelling it as an additional thin disk with scale length  $h_{R,\text{ism}} = 2 \times h_{R,*}$  and scale height  $h_{R,\text{ism}} = 130$  pc. The disks are normalized to a baryonic local surface density inside 1.1 kpc above and below the plane of  $\Sigma_{1.1}(R_0) = 51 \text{ M}_\odot \cdot \text{pc}^{-2}$  among which  $38 \text{ M}_\odot \cdot \text{pc}^{-2}$  are stars and  $13 \text{ M}_\odot \cdot \text{pc}^{-2}$  are interstellar medium (Bovy & Rix 2013).

Inside the bar region, very little is known about the structure of the disk component that surrounds the bar and bulge. We can fortunately constrain this inner disk by combining our knowledge of the bulge and of the disk at the boundary of the bar region (i.e. 5.5 kpc). In the bulge region, approximated as the interior of an ellipse reaching 2.2 kpc along the bar major axis and 1.4 kpc along the intermediate axis, the "bulge" model already represents the entire stellar density. Hence the total surface density along the intermediate axis has to smoothly transition between its value at 5.5 kpc to the bulge value at 1.4 kpc. We construct the inner disk in the bar region by first interpolating the total surface density along the intermediate axis between 5.5 kpc and 1.4 kpc using the logarithm of a quadratic Bézier curve interpolation, whose control points are defined to ensure continuity of the derivative. The disk surface density is then constructed assuming a linear decrease of the ellipticity of the disk isocontours between the bulge and the boundary of the bar region. This procedure is shown in Figure 4.3 where the bar and bulge model (top) and its additional disk component (center) sum up to a total density that smoothly joins the bulge to the disk at the end of the bar region (bottom). Although several assumptions enter in joining the bulge, bar and disk as described above it results in a reasonable global density model for the Milky Way that suits well our purpose of tailoring the initial conditions for the M2M modelling as already stated at the beginning of this section.

#### 4.3.4 Dark matter halo

By adding up the bulge, bar and disk as described above we obtain a 3D density model of the baryonic mass in the Milky Way. Figure 4.4 shows the rotation curve  $V_c(r)$  of these baryonic mass models together with the composite rotation curve from Sofue, Honma & Omodaka (2009) rescaled to a distance to the GC and a local circular velocity of  $(R_0, V_0) = (8.2 \text{ kpc}, 238 \text{ km s}^{-1})$  as described in Section 4.2.2. This baryonic model is insufficient to match the rotation curve of the Milky Way and we therefore require dark matter within the framework of Newtonian dynamics. Recent studies of dark matter simulations such as Navarro et al. (2010) showed that the innermost regions of dark matter halos were better represented by the Einasto density profile (Einasto 1965) than by the NFW profile. Inspired by this, we adopt the three parameter Einasto density profile given by

$$\rho_{\text{DM}}(m) = \rho_0 \exp \left\{ - \left( \frac{2}{\alpha} \right) \left[ \left( \frac{m}{m_0} \right)^\alpha - 1 \right] \right\} \quad (4.4)$$

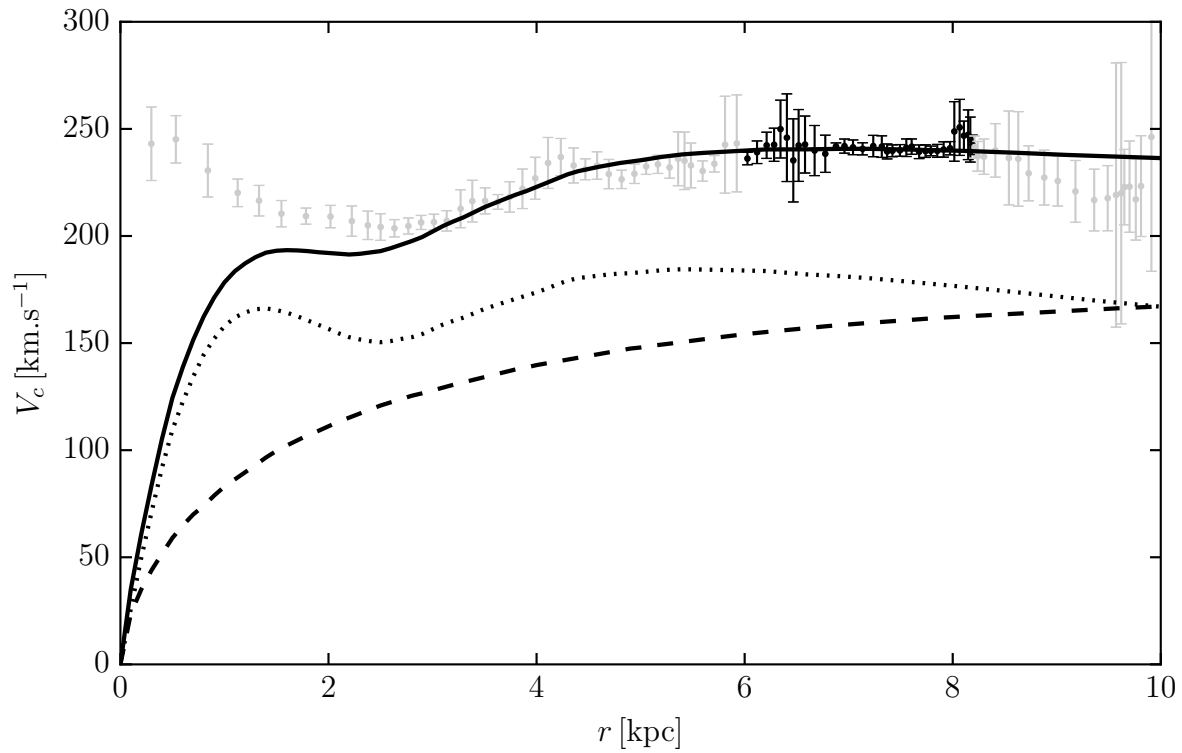


Figure 4.4: Rotation curve of the initial density model of the Galaxy compared to the composite rotation curve of Sofue, Honma & Omodaka (2009). Solid, dotted and dashed lines show respectively the total, baryonic and dark matter rotation curves of our model. Data points used for fitting the dark matter halo as described in the text are shown in black.



where  $m = \sqrt{x^2 + y^2 + (z/q)^2}$  is the elliptical radius for an assumed vertical flattening of  $q = 0.8$  (Piffl et al. 2014). We can constrain the halo parameters using the rotation curve but caution has to be taken inside the bar region. The data from Sofue, Honma & Omodaka (2009) shown in Figure 4.4 is a combination of different datasets and rely mostly on the tangent-point method from terminal velocity measurement of CO and H<sub>I</sub> gas inside the solar circle. Because of the influence of the bar on the gas flows, the tangent point method is likely to be flawed inside the bar region (Englmaier & Gerhard 1999; Chemin, Renaud & Soubiran 2015) so we exclude datapoints inside 6 kpc from the GC. We also exclude all datapoints outside the solar circle, as the rescaling to our assumptions for  $(R_0, V_0)$  would require to take into account the nature of the different datasets entering the work of Sofue, Honma & Omodaka (2009). The rotation curve between 6 kpc and  $R_0$  provide a good constraint on the average value and slope of the dark matter circular velocity at the solar position, but is not sufficient to constrain the dark matter in the inner region. The determination of the dark matter contribution in the inner Galaxy requires proper dynamical modelling and is addressed in detail in Section 4.7.1. At this stage we assume a dark matter mass inside 2 kpc of  $5 \times 10^9 M_\odot$ , resulting in the rotation curve shown in Figure 4.4, consistent with our bulge models in P15. In Section 4.7.2 we relax the constraint on the dark matter mass inside 2 kpc during the modelling process and adapt it directly to match the bulge kinematics.

A summary of the diverse parameters of our fiducial model for tailoring the initial conditions is given in Table 4.1.

Table 4.1: Parameters of the Galaxy used to tailor initial conditions.

	Parameter	Fiducial value	Reference	Section
Geometry	Distance to GC $R_0$	8.2 kpc	Bland-Hawthorn & Gerhard (2016)	Section 4.3
	Bar angle	28°	average between Wegg & Gerhard (2013) and W15	Section 4.3
Bulge	3D density	Fitted M85	P15	Section 4.3.1
	Mass-to-clump ratio $M/n_{\text{RCG}}$	1000	direct measurement, Kroupa + Calamida IMF	Section 4.3.2
Bar	Thin component	Analytical density	W15	Section 4.3.1
	Superthin component	Analytical density	W15	Section 4.3.1
	$M/n_{\text{RCG}}$ of thin bar	same as bulge	–	Section 4.3.1
	$M/n_{\text{RCG}}$ of superthin bar	600	stellar populations models	Section 4.3.1
Stellar disk	scale length $h_{R,*}$	2.4 kpc, middle of range 2.15 – 2.6 kpc	Bland-Hawthorn & Gerhard (2016)	Section 4.3.3
	scale height $h_{Z,*}$	300 pc	Jurić et al. (2008)	Section 4.3.3
	local surface density $\Sigma_{1.1,*}(R_0)$	$38 M_{\odot} \cdot \text{pc}^{-2}$	Bovy & Rix (2013)	Section 4.3.3
ISM disk	scale length $h_{R,\text{ism}}$	$2 \times h_{R,*}$	Bovy & Rix (2013)	Section 4.3.3
	scale height $h_{Z,\text{ism}}$	130 pc	Bovy & Rix (2013)	Section 4.3.3
	local surface density $\Sigma_{1.1,\text{ism}}(R_0)$	$13 M_{\odot} \cdot \text{pc}^{-2}$	Bovy & Rix (2013)	Section 4.3.3
Dark matter halo	profile	best fitting Einasto	–	Section 4.3.4
	flattening	0.8	Piffl et al. (2014)	Section 4.3.4
	outer constraints	$V_c(6 \text{ kpc} \leq r \leq R_0 \text{ kpc})$	Sofue, Honma & Omodaka (2009)	Section 4.3.4
	inner constraint	$M(< 2 \text{ kpc}) = 0.5 \times 10^{10} M_{\odot}$	P15	Section 4.3.4
Dynamical parameters	LSR circular velocity $V_0$	$238 \text{ km s}^{-1}$	Schönrich (2012), Reid et al. (2014)	Section 4.3.4
	Solar motion in the LSR ( $U, V, W$ )	(11.1, 12.24, 7.25) $\text{km s}^{-1}$	Schönrich, Binney & Dehnen (2010)	Section 4.3
	Bar pattern speed $\Omega_b$	Systematic search in the range $25 - 50 \text{ km s}^{-1} \text{ kpc}^{-1}$	–	Section 4.3

## 4.4 Tailoring initial models for modelling the Milky Way

In this section we use a variant of the M2M method to create a family of Milky Way models with a specified mass distribution and different bar pattern speeds. We adiabatically adapt M85 to the density model of the Galaxy described above and change slowly the bar pattern speed, hence gaining full control on the effective potential of the model.

### 4.4.1 Adiabatic adaptation of the initial conditions

We first evaluate the initial stellar and dark matter mass distribution of M85 on respectively a Cartesian grid of  $\pm 12 \text{ kpc} \times \pm 12 \text{ kpc} \times \pm 2 \text{ kpc}$  and a radial grid extending to 40 kpc with flattening  $q = 0.8$ . We then integrate our fiducial stellar and dark matter density target from [Section 4.3](#) in the grid cells and define 25 intermediate targets, log-spaced between the initial model and the target mass distribution. We modify the bar pattern speed by defining 25 intermediate corotation radii, linearly spaced between the initial model corotation and the target corotation.

The adiabatic adaptation of M85 to the target model then consist of 25 iterations of the following procedure:

- (i) Perform a M2M fit of the stellar and dark matter mass distributions to the current target mass distribution while evolving the model in the current rotating potential at constant pattern speed. We run this M2M fit for one time unit, corresponding to the period of one circular orbit at 4 kpc.
- (ii) Update the potential to the new particles masses and adapt the pattern speed at which the potential rotates to place the corotation at the next intermediate target value.
- (iii) Multiply all particle velocities by a factor  $\sqrt{\mathbf{r} \cdot \nabla \Phi_{\text{new}} / \sqrt{\mathbf{r} \cdot \nabla \Phi_{\text{old}}}}$  where  $\mathbf{r}$  is the particle position and  $\Phi_{\text{old}}$  and  $\Phi_{\text{new}}$  are the potential respectively before and after the potential update. This step is necessary as the circular velocity in the new potential is different from that of the original model.

Each M2M fit to an intermediate target mass distribution is performed using [Equation 4.3](#) with the following profit function

$$F = -\frac{1}{2} \sum_{k,j} (\Delta_j)^2 \quad (4.5)$$

where  $\Delta_j$  is the difference between the model mass and the target mass in cell  $j$ . Since model observables can be noisy in regions of space where the particle density is low, we use temporal smoothing by replacing the instantaneous model observable  $y(t)$  at time  $t$  by

its temporally smoothed value  $\tilde{y}(t)$  defined as

$$\tilde{y}(t) = \int y(t - \tau) e^{-\alpha\tau} d\tau . \quad (4.6)$$

where  $1/\alpha$  is the temporal smoothing timescale.

We then continue the M2M fit to the final target mass distribution and corotation radius for another 25 time units. The M2M fit can lead to a broad distribution of weights that has the undesired effect of lowering the model resolution and potentially introducing clumps in the potential due to very massive particles. We added to NMAGIC the particle resampling algorithm described in [Dehnen \(2009\)](#). This algorithm consist of creating a new particle model with equal weights particles by resampling the original set of particles with a probability proportional to their weights. When multiple selection of a given particle occurs, we evolve the parent particle for one orbital time (estimated as  $T \sim 2\pi\sqrt{\frac{r}{f_r}}$  where  $r$  and  $f_r$  are the radius and radial acceleration of the particle) and select multiple particles along the trajectory in phase-space sampled by the parent particle.

Following this procedure we create a set of N-body models that broadly matches the static density model of [Section 4.3](#) with bar pattern speeds in the range  $25\text{--}50 \text{ km s}^{-1} \text{ kpc}^{-1}$ . [Figure 4.5](#) shows the surface densities of three N-body models with pattern speeds of 25, 35 and  $45 \text{ km s}^{-1} \text{ kpc}^{-1}$ . As expected, different pattern speeds lead to slightly different bar shapes but the global mass distribution of the target density is anyway well reproduced in these adiabatically adapted N-body models.

#### 4.4.2 Integration and potential solver

The particle model is integrated using a drift-kick-drift adaptive leap-frog algorithm in the full gravitational potential rotating at a constant patten speed. The gravitational potential is computed directly from the particle mass distributions using the hybrid grids method described in appendix of [Sellwood \(2003\)](#). This hybrid method combines a grid based potential solver on a flat cylindrical grid to evaluate the disk potential with a spherical harmonics potential solver on a spherical grid to evaluate the potential of the dark matter halo. For the cylindrical potential solver we use the 3D polar grid code from [Sellwood & Valluri \(1997\)](#), in a cylindrical grid extending to 12 kpc in radius and  $\pm 2$  kpc in the vertical direction. As a spherical solver we use the spherical harmonics solver of [De Lorenzi et al. \(2007\)](#) up to order 8 on a spherical grid extending to 40 kpc.

In addition to the hybrid grid method, we modified the 3D polar Grid Code in order to allow the resolution of strong vertical gradients. In the original code from [Sellwood & Valluri \(1997\)](#), the particle mass distribution is softened using a spherical cubic spline density kernel where the softening scale should not be smaller that the planar scale of the grid cells in order to give accurate results. To keep the number of planar cells under control and still resolve strong vertical gradient we replace the spherical softening by an oblate softening with vertical axis ratios of 0.2. In the end we define the grid parameters in order to obtain a planar resolution of 100 pc and a vertical resolution of  $\sim 20$  pc.

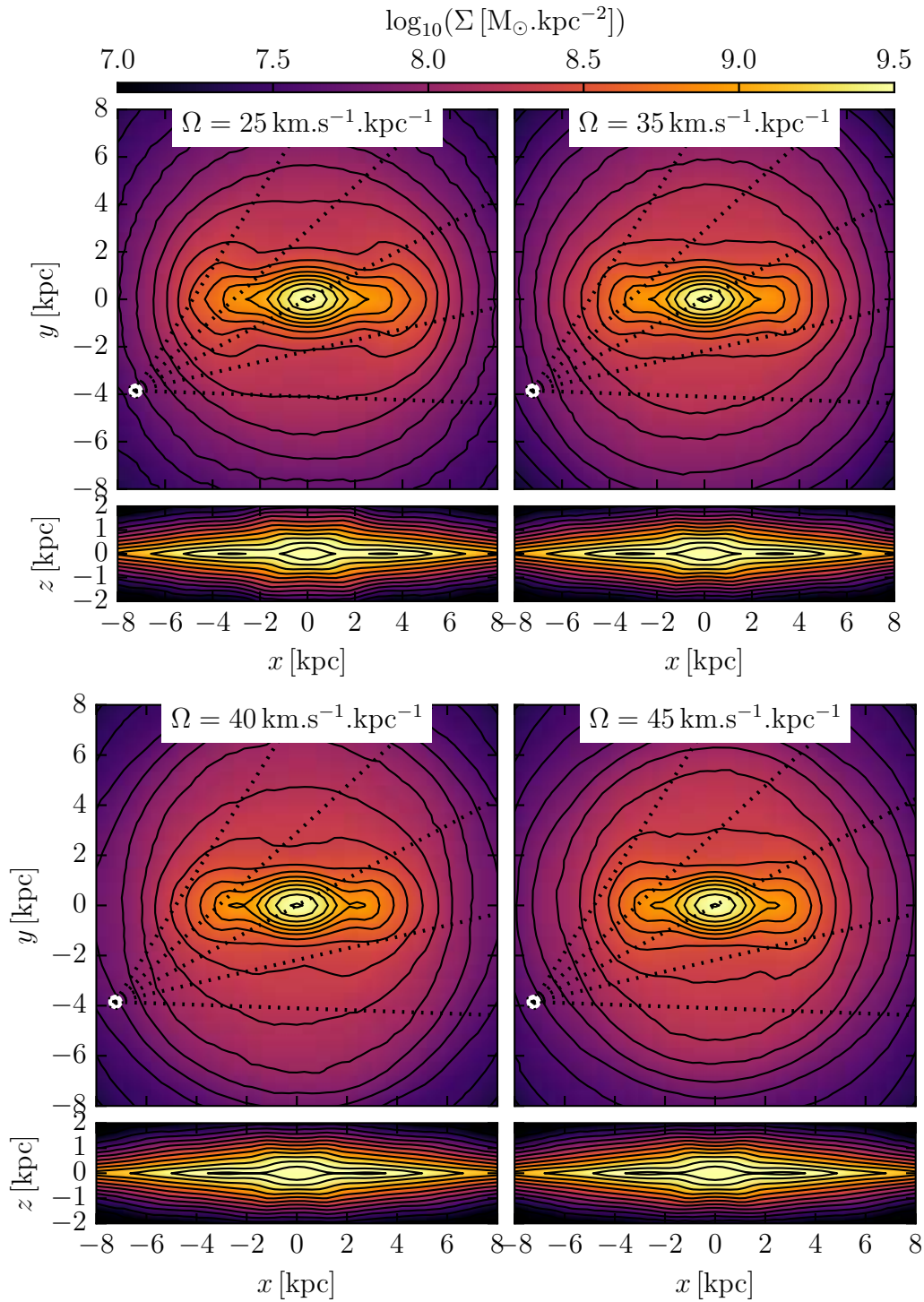


Figure 4.5: Face-on (top row) and side-on (bottom row) surface density of three N-body models adiabatically adapted to the Milky-Way density model of Section 4.3 for patterns speed of 25, 35 and 45  $\text{km s}^{-1}$ .

## 4.5 NMAGIC data constraints for the galactic bulge, bar and disk

In the previous section we built a set of initial N-body models with different pattern speeds that already broadly matches the Milky-Way bulge, bar, and disk density. In this section we describe the different data sets to which we fit our N-body models in [Section 4.6](#). For each dataset  $k$  and observable  $j$  we describe the NMAGIC kernels  $K_j^k$  to be used in [Equation 4.2](#) for applying observational selection bias to the particles when observing the N-body models. An overview of the spatial coverage of the different datasets described in this section is plotted on [Figure 4.6](#).

### 4.5.1 Density and kinematics of the inner Galaxy from the ARGOS survey

The Abundance and Radial velocity Galactic Origin Survey (ARGOS) is a large spectroscopic survey of about 28000 stars of the galactic bulge and inner disc. It was designed to sample RCGs all the way from the near disk ( $\sim 4.5$  kpc from the Sun) to the far side of the Galactic Centre ( $\sim 13$  kpc from the Sun). From the medium resolution spectra [Ness et al. \(2013a\)](#) estimated various stellar parameters including radial velocity, stellar temperature and surface gravity. These parameters together with the intrinsically narrow luminosity function of RCGs allow the determination of relatively accurate distances. Hence, the ARGOS survey provides structural information about the inner disk, bulge and bar together with the radial velocity field in a wide spatial range extending up to  $|l| = 20^\circ$ . In [Section 4.5.1](#) we briefly review the selection strategy of the ARGOS survey and compute its selection function. In [Section 4.5.1](#) we determine distances for all ARGOS stars and compute the mean velocity and velocity dispersion in several distance modulus bins in each field. Finally in [Section 4.5.1](#) we describe the NMAGIC observable kernels that map the survey selection strategy.

#### The ARGOS selection function

The ARGOS stars were selected from the 2MASS point source catalogue ([Skrutskie et al. 2006](#)), according to a selection procedure fully described in [Freeman et al. \(2013\)](#). When computing the ARGOS selection function the three following points need to be considered.

1. About 1000 stars are selected for each field. The sampling of a large distance range from  $\sim 4.5$  kpc to  $\sim 13$  kpc is achieved by selecting randomly  $\sim 330$  stars in three magnitude bins defined in the  $I$ -band ( $I \sim 13 - 14$ ,  $14 - 15$  and  $15 - 16$ ).
2. The 2MASS stars from which the ARGOS stars are selected in (i) do not correspond to the full point-source 2MASS catalogue but only to a high-quality subsample of it. This subsample is defined by a blue color cut  $(J - K_s)_0 \geq 0.38$  to remove foreground

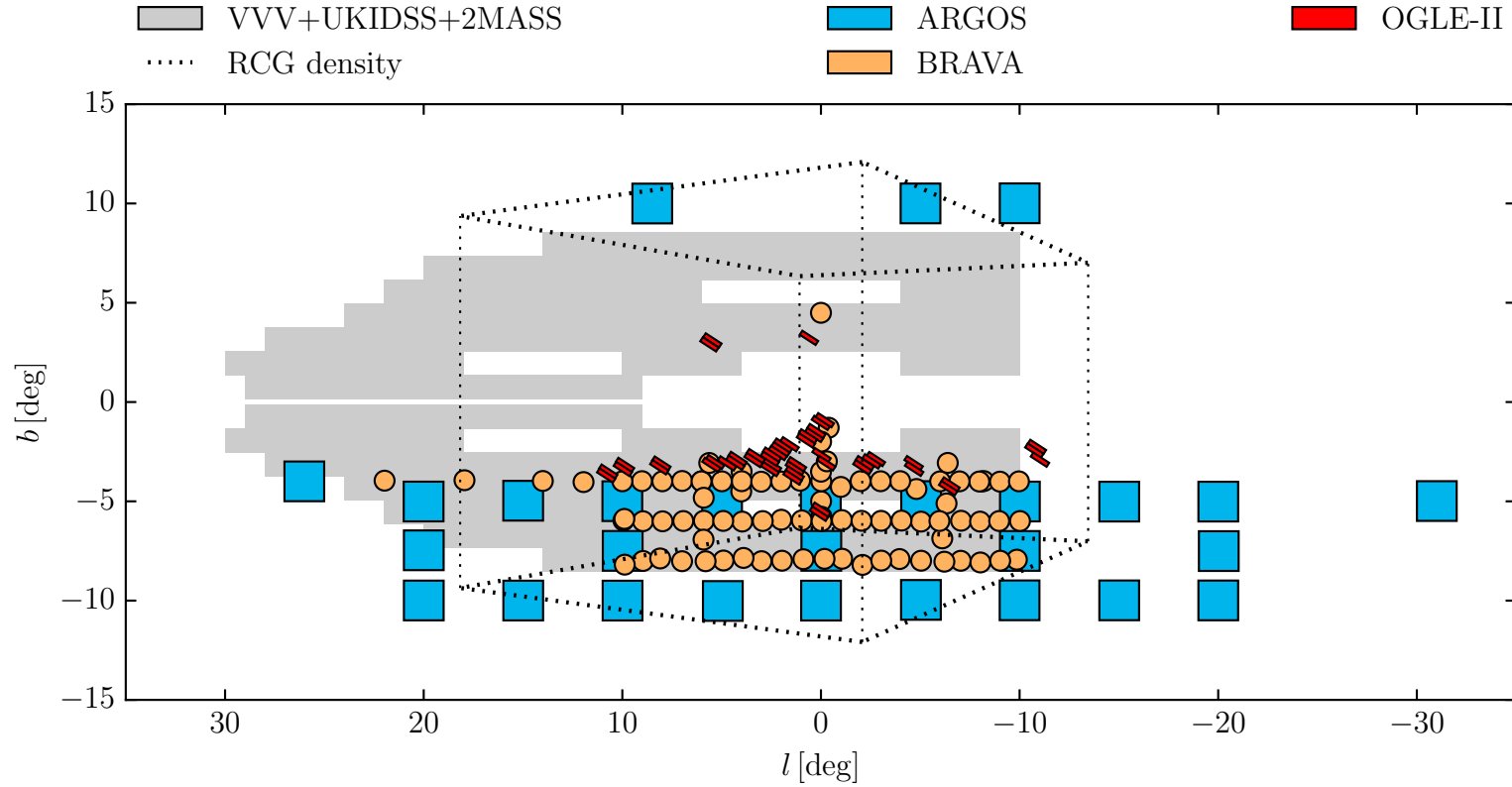


Figure 4.6: Spatial coverage in galactic coordinates of the different datasets used to constrain the models: ARGOS kinematics (Section 4.5.1), VVV + UKIDSS 2MASS star counts (Section 4.5.2), bulge density (Section 4.5.3), BRAVA kinematics (Section 4.5.4) and OGLE proper motions (Section 4.5.5).

disk contamination, two magnitude cuts  $11.5 \leq K_s \leq 14$ , and additional criteria to exclude stars with large photometric errors, contamination, blends and low photometric quality. The subsample is biased towards the bright stars for which high quality imaging is easier to achieve.

3. The 2MASS catalogue is rapidly incomplete in crowded fields. This affects mostly the three fields at  $(l, b) = (0^\circ, -5^\circ)$  and  $(\pm 5^\circ, -5^\circ)$  where 2MASS is only  $\sim 45\%$  complete at  $K_s \sim 14$ .

We evaluate the incompleteness of the 2MASS survey by comparing with the deeper VVV survey where available (Saito et al. 2012), completeness corrected by Wegg & Gerhard (2013). In all the ARGOS fields at the edges of the VVV coverage, 2MASS and VVV do not deviate significantly from each other over the magnitude range  $11.5 \leq K_s \leq 14$ . Given that the effect of crowding decreases with increasing  $|l|$  and  $|b|$ , we consider that 2MASS is complete in all the ARGOS fields out of the VVV coverage area.

Extinction is evaluated on a star-by-star basis using the Rayleigh-Jeans Color Excess method (Majewski, Zasowski & Nidever 2011; W15) given by:

$$A_{K_s} = \frac{A_{K_s}}{E(J-K_s)} [(J-K_s) - (J-K_s)_{\text{RCG}}] \quad (4.7)$$

where  $(J-K_s)_{\text{RCG}}$  is the colors of RCGs and  $\frac{A_{K_s}}{E(J-K_s)}$  is a constant that depends on the extinction law. For consistency with Wegg & Gerhard (2013) we adopt  $(J-K_s)_{\text{RCG}} = 0.674$  (Gonzalez et al. 2011b) and  $\frac{A_{K_s}}{E(J-K_s)} = 0.528$  (Nishiyama et al. 2006).

To take points (ii) and (iii) into account we construct the selection function  $C(K_{s0})$  that gives the probability for a star of extinction corrected magnitude  $K_{s0}$  to belong to the high-quality photometric 2MASS subsample from which the ARGOS stars were selected. This is evaluated empirically as shown in Figure 4.7. We finally define  $C(K_{s0})$  as the fraction of stars with magnitude  $K_{s0}$  from the completeness corrected 2MASS catalogue that are also in the high-quality 2MASS subsample.

To correct for the selection bias (i) we assign a weight  $w_k$  to each of the ARGOS stars, corresponding to the fraction of selected stars with the number of stars present in the considered  $I$ -band bin from the 2MASS subsample of good photometric quality.

Figure 4.7 illustrates this selection procedure for the field at  $(l, b) = (0^\circ, -5^\circ)$ , the field most affected by selection effects.

### Density and kinematics as a function of distance

Assuming that all ARGOS stars are RCGs and using the star-by-star extinction of Equation 4.7 we estimate the distance moduli  $\mu_{K_s}$  of all ARGOS stars as

$$\mu_{K_s} = K_s - A_{K_s} - M_{K_s, \text{RCG}} \quad (4.8)$$



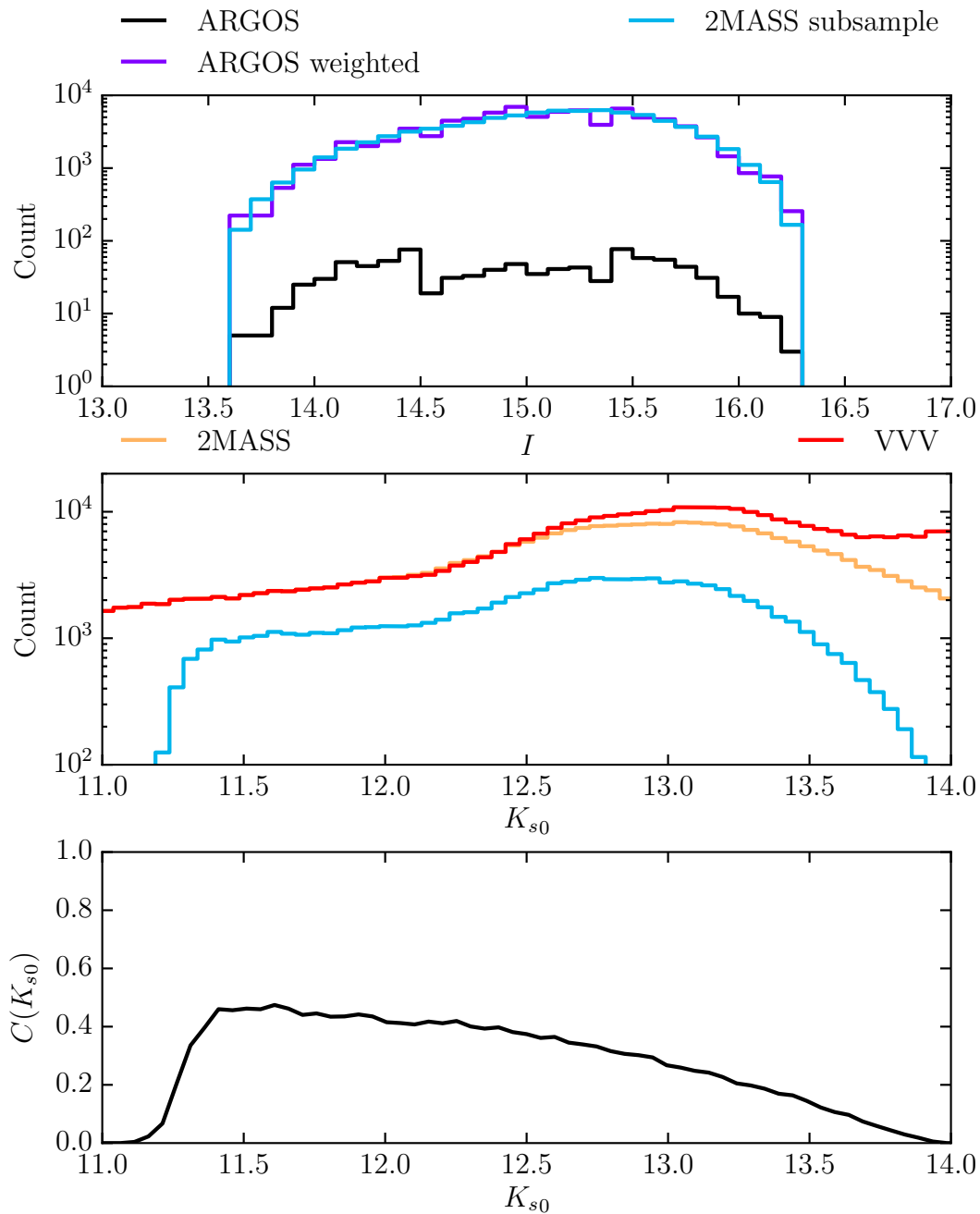


Figure 4.7: Illustration of the ARGOS selection procedure for the most problematic field at  $(l, b) = (0^\circ, -5^\circ)$ . The top panel shows the  $I$ -band magnitude distribution for the ARGOS stars (black) and the 2MASS data subsample of good photometric quality (blue), in good agreement with the weighted ARGOS stars (purple). The middle panel shows the extinction corrected magnitude distributions of the 2MASS catalogue (yellow), the completeness corrected VVV data (red) and the 2MASS subsample of good photometric quality considered by the ARGOS team (blue). The bottom panel shows the final selection function  $C(K_{s0})$  for this field.

where we adopt an absolute magnitude of RCGs of  $M_{K_s, \text{RCG}} = -1.72$  for consistency with Wegg & Gerhard (2013).

Stars in the ARGOS sample are either real RCGs, for which distances are accurately determined by Equation 4.8, or red giants that happen to be at the right distance to appear with similar color and magnitude as the real RCGs. For these giants the distance estimate given by Equation 4.8 can be wrong by several magnitudes. To minimize their effect we follow Ness et al. (2013a) and evaluate the absolute magnitude  $M_{K_s}$  of every star using the surface gravity  $\log g$  measurement obtained from fitting the spectra together with the PARSEC isochrones (Bressan et al. 2012; Chen et al. 2014; Tang et al. 2014) and assuming a 10 Gyr old population, a Kroupa IMF and the overall metallicity distribution of all the ARGOS stars. We then statistically remove non-RCG stars by replacing the weights  $w_k$  of all ARGOS stars with  $w_k \times \omega(M_{K_s})$  where  $\omega$  is a weighting function depending on the inferred absolute magnitude. The uncertainty in  $\log g$  is  $\sim 0.3$  mag, which is equivalent to an uncertainty in  $M_{K_s}$  of 0.7 mag. Original work from the ARGOS team chose for  $\omega$  a top-hat function around  $M_{K_s, \text{RCG}}$ , identifying in this way what they call the "probable RCGs". In order to take advantage of the full sample of stars we adopt instead the weighting  $\omega(M_{K_s}) = G_{[M_{K_s, \text{RCG}}, 0.7]}(M_{K_s})$  where  $G_{[\mu, \sigma]}$  is the Gaussian function of mean  $\mu$  and standard deviation  $\sigma$ .

Finally we bin the distance modulus space in bins of 0.25 mag and compute for each field the number of stars  $n_{j,m}$ , the mean radial velocity  $v_{j,m}$  and radial velocity dispersion  $\sigma_{j,m}$  of the stars in field  $j$  and distance modulus bin  $m$ , taking into account each star weight  $w_k$ . Errors in those quantities are computed by 1000 bootstrap resamplings.

### NMAGIC observable for the ARGOS data

In order to map the observational criteria to observing an N-body model we first need to study the stellar population that falls into the ARGOS sample in more detail. Using the PARSEC isochrones for a 10 Gyr old population with a Kroupa IMF and the overall metallicity distribution of all the ARGOS stars we predict the luminosity function  $\Phi$  of the stars that matches the ARGOS color and magnitude cuts. The RCGs then appear as a sharp peak over a large background of red giants, located at  $M_{K_s, \text{RCG}} = -1.47$ , slightly fainter than the assumed value of  $M_{K_s, \text{RCG}} = -1.72$  used by Wegg & Gerhard (2013) for measuring the 3D density of the galactic bulge. For internal consistency between our datasets we shift the isochrone luminosity function to agree with the maximum of the RCG peak at  $M_{K_s, \text{RCG}} = -1.72$ .

Let us now observe an N-body model by effectively turning the particles into stars and applying the selection procedure of the ARGOS survey. We consider a particle at distance modulus  $\mu_i$  and note  $f_i(\mu_{K_s})$  the distribution of observed distances of mock stars drawn from  $\Phi(K_s)$  at the position of the considered particle when assuming that they are all RCGs. A mock star with an absolute magnitude  $M_{K_s}$  will be inferred to lie at a distance

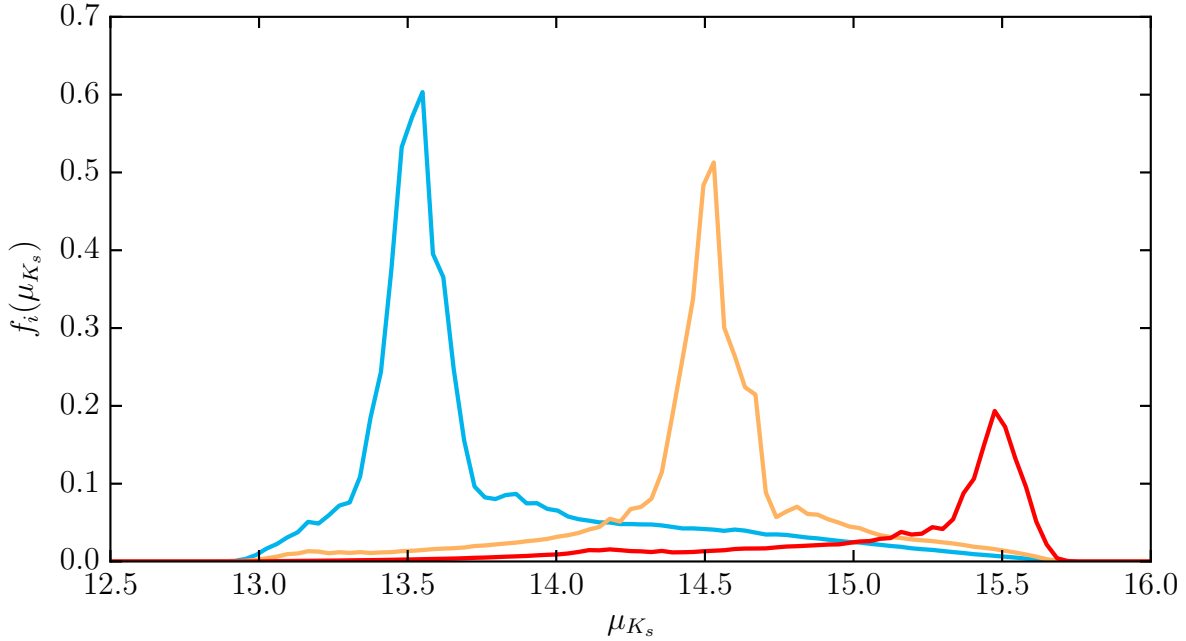


Figure 4.8: Distribution of observed distances  $f_i(\mu_{K_s})$  of mock stars drawn from a particle at distance modulus  $\mu_i = 13.5$  (blue),  $\mu_i = 14.5$  (yellow) and  $\mu_i = 15.5$  (red), in the field at  $l, b = 10^\circ, -5^\circ$ . The background of Giants present in the luminosity function is attenuated here by the weighting  $\bar{w}(\mu_{K_s} - \mu_i + M_{K_s, \text{RCG}})$  together with the incompleteness of the 2MASS subsample for faint magnitudes.

$\mu_{K_s} = M_{K_s} + \mu_i - M_{K_s, \text{RCG}}$ .  $f_i(\mu_{K_s})$  can be written as

$$f_i(\mu_{K_s}) = \Phi(\mu_{K_s} - \mu_i + M_{K_s, \text{RCG}}) \times \bar{w}(\mu_{K_s} - \mu_i + M_{K_s, \text{RCG}}) \times C(\mu_{K_s} + M_{K_s, \text{RCG}}) \quad (4.9)$$

where  $C(K_{s0})$  is the selection function computed in [Section 4.5.1](#). The mean weight  $\bar{w}(M_{K_s})$ , average of the weights obtained after statistical removal of non-RCGs from a mock measurement of  $M_{K_s}$  with accuracy 0.7 mag is given by

$$\bar{w}(M_{K_s}) = \int \omega(M) \times G_{[M_{K_s}, 0.7]}(M) dM. \quad (4.10)$$

The distribution of distances  $f_i(\mu_{K_s})$  resulting of [Equation 4.9](#) is shown in [Figure 4.8](#) for three particles at  $\mu_i = 13.5$ ,  $\mu_i = 14.5$  and  $\mu_i = 15.5$ . The distribution is narrow in all cases, showing that the ARGOS survey provide accurate distances. The spreading in distances due to the background of Giants is minimized thanks to the selection bias toward nearby stars and also the extra information provided by the measurement of  $\log g$ .

As NMAGIC observables we adopt the number count and first and second mass weighted velocity moments. The corresponding kernels for a field  $j$  and distance modulus  $m$  to be

used in Equation 4.2 are given by

$$K_{j,m}^{\text{ARGOS},0} = \delta_{j,m}^{\text{ARGOS}}(\mathbf{z}_i) \quad (4.11)$$

$$K_{j,m}^{\text{ARGOS},1} = \delta_{j,m}^{\text{ARGOS}}(\mathbf{z}_i) \times \frac{v_i}{W_{j,m}^{\text{ARGOS}}} \quad (4.12)$$

and

$$K_{j,m}^{\text{ARGOS},2} = \delta_{j,m}^{\text{ARGOS}}(\mathbf{z}_i) \times \frac{v_i^2}{W_{j,m}^{\text{ARGOS}}} \quad (4.13)$$

where  $v_i$  is the radial velocity of particle  $i$ ,  $W_{j,m}^{\text{ARGOS}}$  is given by

$$W_{j,m}^{\text{ARGOS}} = \sum_i w_i \delta_{j,m}^{\text{ARGOS}}(\mathbf{z}_i) \quad (4.14)$$

and  $\delta_{j,m}^{\text{ARGOS}}$  by

$$\delta_{j,m}^{\text{ARGOS}}(\mathbf{z}_i) = \begin{cases} \int_{\mu(m)}^{\mu(m+1)} f_i(\mu) d\mu & \text{if } i \in \text{field } j, \\ 0 & \text{otherwise} \end{cases} \quad (4.15)$$

with  $\mu(m)$  and  $\mu(m+1)$  the boundaries of the distance modulus bin  $m$ .

### 4.5.2 Magnitude distribution of the bulge and bar

In the region delimited by  $|l| \leq 40^\circ$  and  $|b| \leq 9^\circ$  we use the combined catalogue of the VVV, UKIDSS and 2MASS surveys from W15. For each line of-sight this catalogue consist of histograms of distance moduli of stars  $\mu_{K_s}$  defined as in Equation 4.8. Each of these histograms show an exponential background distribution of stars plus an overdensity of stars due to the RCGs located in the bulge or bar, as shown in Figure 4.2 for one bulge field. Information on the density is very hard to extract from the exponential background distribution of stars as it arises from the convolution of the line of sight density with the luminosity function of giant and dwarf stars that is very broad, poorly known and likely to vary from field to field and along the line-of-sight. Hence we restrict our use of the histograms to the fields that show a significant excess of stars above the exponential background. To do so we follow W15 and first fit a Gaussian plus an exponential to the distribution of distance moduli, separately in each fields. We remove from further considerations all lines of sight where either the RCGs bump is not detected to at least three sigma or the exponential background slope is too small, indicating incompleteness (see W15). The spatial coverage of the remaining fields is plotted in Figure 4.6.

The kernels of our model observables in a field  $j$  and distance modulus bin  $m$  bounded by  $\mu(m)$  and  $\mu(m+1)$  are given by

$$K_{j,m}^{\text{hist}}(\mathbf{z}_i) = \begin{cases} \frac{1}{M/n_{\text{RCG}}} \times \int_{\mu(m)}^{\mu(m+1)} \Phi(\mu - \mu_i) d\mu & \text{if } i \in \text{field } j, \\ 0 & \text{otherwise} \end{cases} \quad (4.16)$$

where  $M/n_{\text{RCG}}$  is the mass-to-clump ratio described in Section 4.3.2 and  $\Phi$  the luminosity function for RCGs only, expressed in distance modulus (see equation 17 in W15). The exponential background of stars, absent from the model observables need to be introduced before comparing model to data. To do so we follow Wegg, Gerhard & Portail (2015) and first fit an exponential distribution  $y_j^e$  to the difference between the model observable  $y_j^{\text{hist}}$  and full data histogram  $Y_j^{\text{hist}}$ . This exponential background of stars is then included in the data-model comparison by replacing  $y_j^{\text{hist}}$  to  $y_j^{\text{hist}} + y_j^e$  in Equation 4.24.

For all fields with  $|b| \geq 1.35^\circ$  we assume a 10 Gyr old stellar population with a Kroupa IMF and the metallicity distribution of Zoccali et al. (2000) in Baade’s window and compute  $\Phi$  from the PARSEC isochrones. After removing the exponential background we scale  $\Phi$  to our fiducial mass-to-clump ratio of 1000 (see Section 4.3.2).

For  $|b| < 1.35^\circ$  as already discussed in Section 4.3.1, W15 found evidence for a superthin bar component, present mostly near the bar end. This super thin bar is likely to be formed by younger stars as indicated by its extremely small scale height of only 45 pc. Detailed modelling of the superthin component is beyond the scope of this paper, but as our goal is to constrain the gravitational potential, its mass has to be included in the modelling. We follow W15 and assume a constant star formation rate for the superthin component to compute its luminosity function. The superthin bar population has a mass-to-clump ratio of 600, lower than the old bar population. For fields with  $|b| \leq 1.35^\circ$  we use a superposition of the thin bar and superthin bar populations, using the ratio of the densities given by the parametric models of W15.

For efficiency we combine the original data of W15 in cells of  $2^\circ \times 1.2^\circ$  in galactic coordinates for  $|b| \geq 1.35^\circ$  and cells of  $2^\circ \times 0.6^\circ$  for  $|b| < 1.35^\circ$  and symmetrize with respect to the  $b = 0^\circ$ .

### 4.5.3 3D density of the bulge and outer disk

In the bulge we constrain the stellar density using the 3D density of RCGs measured by Wegg & Gerhard (2013), scaled to stellar mass density using our fiducial mass-to-clump ratio. The map covers a box of  $(\pm 2.2 \times \pm 1.4 \times \pm 1.2)$  kpc along the bulge principal axes but is incomplete within  $\pm 150$  pc above and below the galactic plane because of large extinction and crowding. To fill in this gap we use our fiducial extrapolation of the density from P15, obtained by fitting a  $\text{sech}^2$  profile to each vertical slice through the bulge. This extrapolation provides us with the full 3D density of what we call the *smooth bulge*. In Section 4.7.3 we consider an extra in-plane disk component and show that indeed an in-plane over density is required to match our bulge kinematic data. We finally integrate the RCGs map on a grid of  $(30 \times 28 \times 32)$  cells and the corresponding observable kernels  $K_j^{\text{RCG}}$  are given by

$$K_j^{\text{RCG}}(\mathbf{z}_i) = \begin{cases} M/n_{\text{RCG}}^{-1} & \text{if } i \in \text{cell } j, \\ 0 & \text{otherwise.} \end{cases} \quad (4.17)$$

Outside the bar region, for cylindrical radius larger than 5 kpc, we use the 3D density of the disk of Section 4.3.3 evaluated on a large 3D density grid using a mass-in-cell kernel

similarly to Equation 4.17.

#### 4.5.4 Bulge kinematics from the BRAVA survey

The BRAVA survey is a large spectroscopic survey of about 10000 M giants stars, mostly toward the bulge (Rich et al. 2007; Howard et al. 2008; Kunder et al. 2012). We use only the fields with  $|l| \leq 10^\circ$  as we found in P15 that the disk contamination could become significant outside the bulge. The selected BRAVA fields provide 82 measurements of the mean radial velocity and velocity dispersion through the bulge.

As NMAGIC observables we use here the first and second weighted velocity moments whose kernels are given by:

$$K_j^{\text{BRAVA},1}(\mathbf{z}_i) = \delta_j^{\text{BRAVA}}(\mathbf{z}_i) \times \frac{v_i}{W_j^{\text{BRAVA}}} \quad (4.18)$$

and

$$K_j^{\text{BRAVA},2}(\mathbf{z}_i) = \delta_j^{\text{BRAVA}}(\mathbf{z}_i) \times \frac{v_i^2}{W_j^{\text{BRAVA}}} \quad (4.19)$$

where  $v_i$  is the radial velocity of particle  $i$  and  $\delta_j^{\text{BRAVA}}$  is the selection function of the BRAVA survey and  $W_j^{\text{BRAVA}}$  is given by

$$W_j^{\text{BRAVA}} = \sum_i w_i \delta_j^{\text{BRAVA}}(\mathbf{z}_i). \quad (4.20)$$

As shown in P15 the BRAVA survey is biased toward nearby stars and the selection function is given by:

$$\delta_j^{\text{BRAVA}}(\mathbf{z}_i) = \begin{cases} r_i^{-1.4} & \text{if } i \in \text{field } j \text{ with } |y_i| < 3.5 \text{ kpc,} \\ 0 & \text{otherwise.} \end{cases} \quad (4.21)$$

#### 4.5.5 Bulge proper motions from the OGLE-II survey

As additional bulge kinematics we use the proper motion dispersions of RCG in the bulge from the OGLE-II survey as computed by Rattenbury et al. (2007a) from the proper motion catalogue of Sumi et al. (2004). RCGs are selected in an ellipse of the dereddened  $I_0$  vs  $(V - I)_0$  color magnitude diagram centered on the expected locus of the red clump at  $I_0 = 14.6$  and  $(V - I)_0 = 1.0$ . Stars with proper motion error larger than  $1 \text{ mas yr}^{-1}$  in either the  $l$  or the  $b$  direction were excluded from the sample, as well as stars with total proper motion larger than  $10 \text{ mas yr}^{-1}$  which are likely to belong to the foreground disk. We compute the selection function by using again the PARSEC isochrones for a 10 Gyr population, a Kroupa IMF and the metallicity distribution of ARGOS stars in the bulge. The cut in proper motion error introduces a bias toward nearby stars as the error is more likely to be large for faint stars. To model this effect we first compute in each field  $j$  the fraction of stars that pass the error cut threshold as a function of their extinction

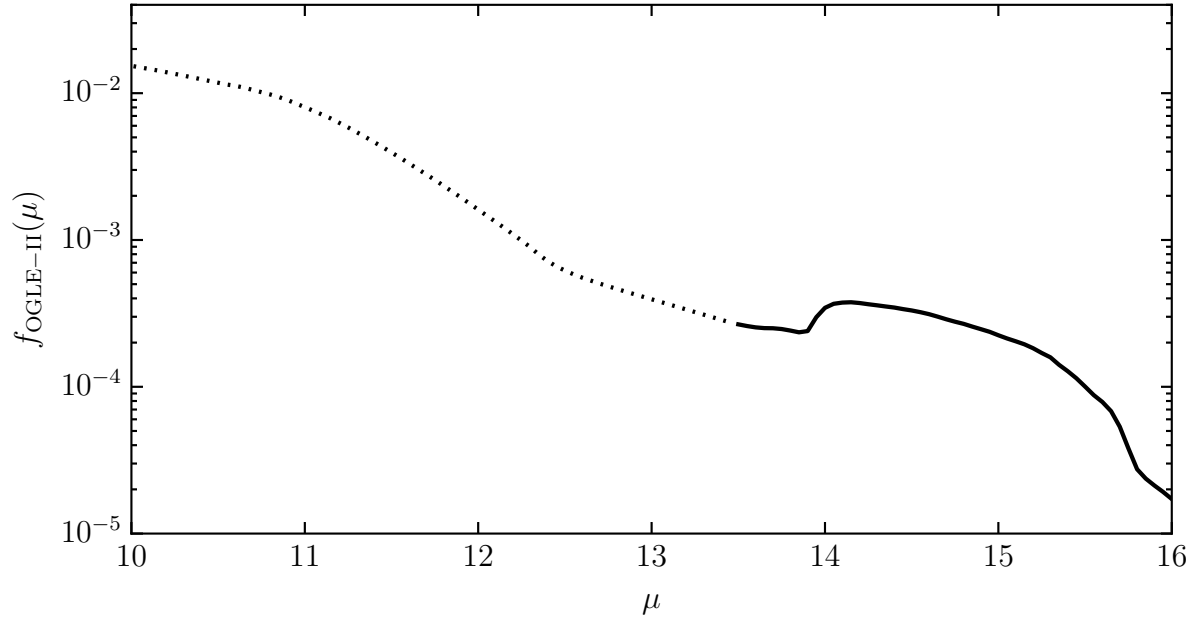


Figure 4.9: Selection function of the OGLE survey as a function of distance modulus for the field at  $(l, b) = (1.0^\circ, -3.7^\circ)$ . The solid line indicates the selection function in the range of distances considered in this work. The large contribution of nearby stars indicated by the dashed line is ignored.

corrected  $I_0$  magnitude, denoted by  $C_{\sigma_{\mu,j}}(I_0)$ . Then from the isochrones we compute for each distance  $\mu$  the distribution of  $I_0$  magnitudes  $C_j(\mu, I_0)$  of stars that end up inside the ellipse selection region of the  $I_0$  vs.  $(V - I)_0$  diagram. The final selection function  $f^{\text{OGLE}}(\mu)$  is then given by

$$f^{\text{OGLE}}(\mu) = \int C_j(\mu, I_0) \times C_{\sigma_{\mu,j}}(I_0) dI_0 \quad (4.22)$$

and is shown in [Figure 4.9](#) for the field at  $(l, b) = (1.0^\circ, -3.7^\circ)$ . The large theoretical contribution of low distance modulus is due to faint main sequences stars in the disk that are close enough to fall into the ellipse selection of the CMD. As the stellar population of the nearby disk is very different from the old bulge population, the selection function should not be trusted at small distances. We adopt a simple distance cut and discard contribution from any particle at distances less than 5 kpc. Disk contamination is also likely to be removed in the data thanks to the cut in total proper motion.

Observables kernels are defined similarly to [Equations 4.18](#) and [Equations 4.19](#) by replacing the radial velocity by the proper motion in the heliocentric frame, with the selection function  $\delta_j^{\text{OGLE}}$  given by:

$$\delta_j^{\text{OGLE}}(\mathbf{z}_i) = \begin{cases} f^{\text{OGLE}}(\mu_i) & \text{if } i \in \text{field } j \text{ with } r_i > 5 \text{ kpc} \\ & \text{and } \sqrt{\mu_{l_i}^{*2} + \mu_{b_i}^{*2}} < 10 \text{ mas yr}^{-1}, \\ 0 & \text{otherwise.} \end{cases} \quad (4.23)$$

The errors in proper motion dispersion quoted by [Rattenbury et al. \(2007a\)](#) are statistical errors, very small due to the large number of observed stars. However [Rattenbury et al. \(2007a\)](#) noted that adjacent fields could show variations in proper motion dispersion of up to  $0.2 \text{ mas yr}^{-1}$ . To take those systematics into account we replace the error bars by adding in quadrature to statistical error a systematic error of  $0.1 \text{ mas yr}^{-1}$ . In this paper we use the OGLE proper motion only to compare with model predictions but we do not fit them.

## 4.6 Dynamical modelling of the bar region

In this section we use the M2M method to fit the N-body models constructed in [Section 4.4](#) to the data described in [Section 4.5](#).

### 4.6.1 M2M formalism

Indexing again an observable by  $j$  and a dataset by  $k$ , the difference between the model observable  $y_j^k(t)$  and the real data  $Y_j^k$  is evaluated through the residual  $\Delta_j^k(t)$  defined as

$$\Delta_j^k(t) = \frac{y_j^k(t) - Y_j^k}{\sigma(Y_j^k)} \quad (4.24)$$

where  $\sigma(Y_j^k)$  is the error on  $Y_j^k(t)$ .

Following [De Lorenzi et al. \(2007\)](#) we match our data adopting the profit function

$$F = -\frac{1}{2} \sum_{k,j} \lambda_k (\Delta_j^k)^2 + \mu S. \quad (4.25)$$

The first term in [Equation 4.25](#) is a weighted chi-square term where the  $\lambda_k$  are numerical weights for the different datasets (see [Long & Mao 2010](#)). The second term is an entropy term, forcing the particle weight distribution to remain narrow around some pre-determined prior values, improving hence the convergence of the individual particle weights. We use the pseudo-entropy  $S$  of [Morganti & Gerhard \(2012\)](#) given by

$$S = - \sum_{i=1}^N w_i \left[ \log \left( \frac{w_i}{\hat{w}_i} \right) - 1 \right] \quad (4.26)$$

where  $\hat{w}_i$  are prior weights, chosen to be the mean stellar weight and mean dark matter weight for respectively the stellar and dark matter particles.

Using the observable kernels  $K_j^k$  described in [Section 4.5](#), [Equation 4.3](#) becomes

$$\frac{dw_i}{dt} = -\varepsilon w_i \left[ \mu \log \left( \frac{w_i}{\hat{w}_i} \right) + \sum_k \lambda_k \sum_j \left( K_j(\mathbf{z}_i) + w_i \frac{\partial K_j(\mathbf{z}_i)}{\partial w_i} \right) \frac{\Delta_j^k(t)}{\sigma(Y_j^k)} \right]. \quad (4.27)$$



When the observable kernels do not depend on the weights, [Syer & Tremaine \(1996\)](#) and [De Lorenzi et al. \(2007\)](#) showed that the observables converge exponentially on a timescale  $O(\varepsilon^{-1})$  provided the initial model is sufficiently close to the solution. We find in practice that weight dependent kernels, as chosen for the ARGOS and BRAVA surveys can be introduced without affecting the convergence provided (i) the derivative of the kernel with respect to the weight is taken into account in [Equation 4.27](#) (ii) some other observables constrain the absolute value of the weights on the spatial domain where the weight dependent kernel is non-null. We numerically evaluate the convergence of the weights by following the method of [Long & Mao \(2010\)](#) considering that a given particle weight has converged if its maximum relative deviation from its mean value on the previous orbit is smaller than 10%.

### 4.6.2 Fitting procedure and parametrization

After the adiabatic evolution of the initial model a typical NMAGIC fit consist of three phases:

1. Temporal smoothing: evolve and observe the model for a time  $T_{\text{smooth}}$  to initialize the observables.
2. M2M fit: evolve the model and modify the particle weights according to [Equation 4.27](#) for a time  $T_{\text{M2M}}$ .
3. Relaxation: evolve and observe the model for a time  $T_{\text{relax}}$  to test the stability of the fit.

We use 4, 40 and 16 internal time units for respectively  $T_{\text{smooth}}$ ,  $T_{\text{M2M}}$  and  $T_{\text{relax}}$ , with one internal unit of time corresponding to the period of one circular orbit at 4 kpc (i.e. about 125 Myr). We adopt a smoothing timescale of  $1/\alpha = 1$  model time units.

For the force-of-change parameter  $\varepsilon$  we adopt a value of  $\varepsilon = 10^{-1} \times w_0$  where  $w_0$  is the mean particle mass. We adopt  $\lambda_{\text{density}} = 1$  for all density observables and  $\lambda_{\text{kinematics}} = 10$  for all kinematic observables, giving each dataset in [Equation 4.25](#) a similar contribution to the bracket term of [Equation 4.27](#). The priors of the entropy term of [Equation 4.26](#) are fixed to the mean particle weight and the magnitude of the entropy is fixed to  $\mu = 10^4$ . This value allows more than 97% of the particle to converge while resulting in a weight distribution that extends only to  $\pm 1$  dex from the priors.

## 4.7 Understanding the bulge dynamics

In this section we show how the bar pattern speed, dark matter density and in-plane stellar bulge density influence the bulge kinematics and how we can recover and constrain the effective potential by fitting our models to the data described in [Section 4.5](#).

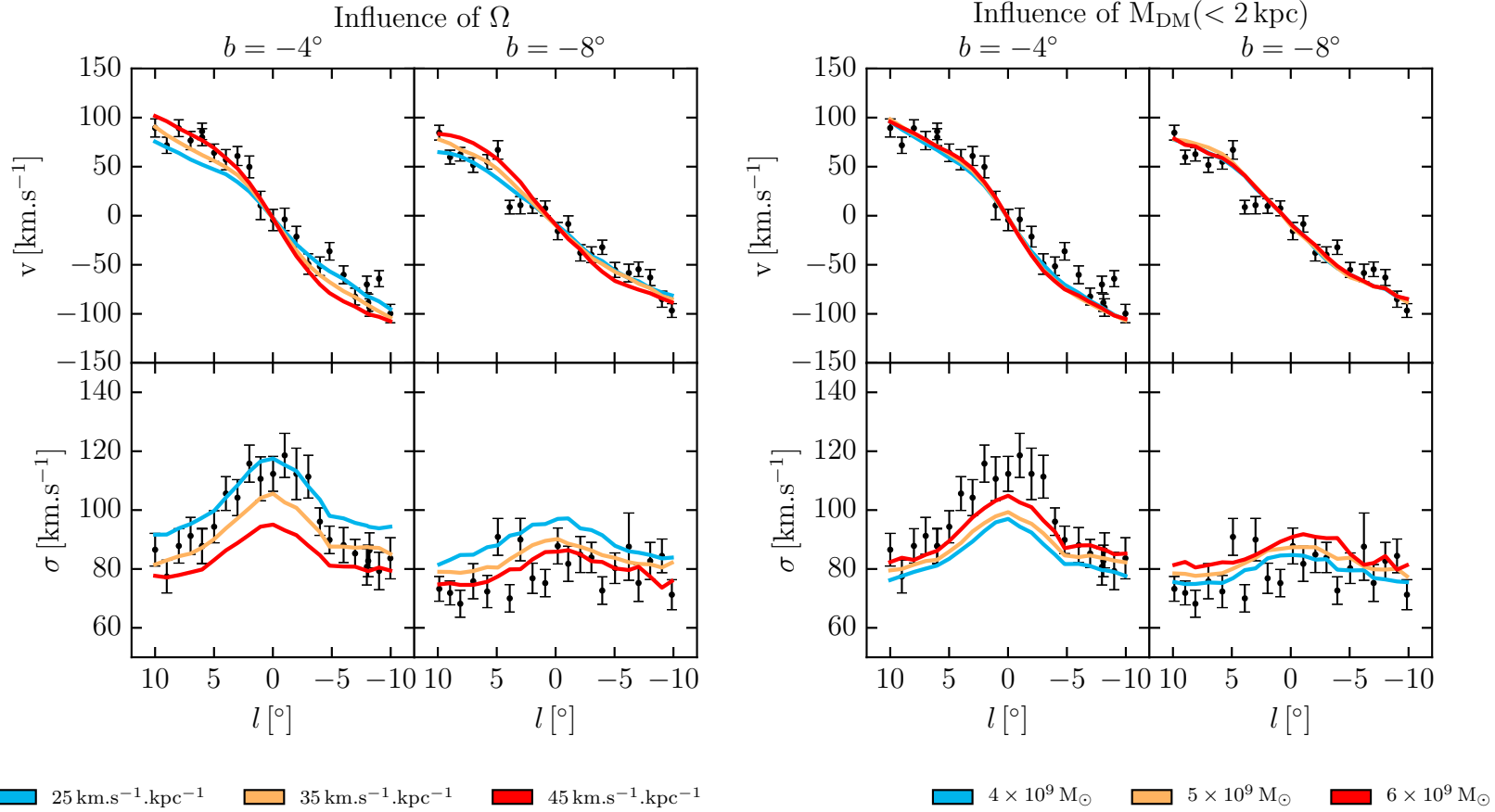


Figure 4.10: Kinematic signature of the pattern speed and dark matter mass in the bulge. The first column shows the influence of the pattern speed on the BRAVA kinematics for a constant stellar and dark matter mass distribution. The three models plotted here are for pattern speeds of  $25 \text{ km s}^{-1} \text{ kpc}^{-1}$  (blue),  $35 \text{ km s}^{-1} \text{ kpc}^{-1}$  (yellow) and  $45 \text{ km s}^{-1} \text{ kpc}^{-1}$  (red) for a constant bulge dark matter mass of  $M_{\text{DM}}(< 2 \text{ kpc}) = 5 \times 10^9 M_{\odot}$ . The pattern speed has a strong influence on both the mean velocity and the velocity dispersion in the bulge. The second column shows the influence of the dark matter mass in the bulge for  $4 \times 10^9 M_{\odot}$  (blue),  $5 \times 10^9 M_{\odot}$  (yellow) and  $6 \times 10^9 M_{\odot}$  (red) and a constant pattern speed of  $40 \text{ km s}^{-1} \text{ kpc}^{-1}$ . The dark matter in the bulge has a negligible influence of the mean BRAVA velocity and can thus be recovered from the velocity dispersion once the pattern speed is fixed.

### 4.7.1 Signature of the pattern speed and inner dark matter halo in the bulge kinematics

The first column of [Figure 4.10](#) show the BRAVA kinematics for three models with different pattern speed between  $25$  and  $45 \text{ km s}^{-1} \text{ kpc}^{-1}$ , fitted to our bulge and long bar data in the same dark matter halo. The effect of the bar pattern speed is clearly visible both in the mean velocity and velocity dispersion. Increasing pattern speed leads to an increase in mean velocity but a decrease in the velocity dispersion. The virial theorem provides intuitive explanation of this: for a given mass distribution and hence a given potential energy, a larger pattern speed places more kinetic energy in pattern rotation, leaving less energy available to build up random motions. The second panel of [Figure 4.10](#) shows the BRAVA kinematics for three models with the same pattern speed and stellar mass density but different dark matter masses in the bulge. As already found in P15 large masses increase the dispersion but leave the mean velocity essentially unchanged. Hence for a given pattern speed and stellar density model we can recover the dark matter mass in the bulge from the BRAVA velocity dispersions.

### 4.7.2 Recovering the best dark matter halo

In [Section 4.3.4](#) we constructed a first-guess dark matter density in the Galaxy by fitting an Einasto profile to the rotation curve between  $6 \text{ kpc}$  and  $R_0$  under the constraint of an assumed dark matter mass inside  $2 \text{ kpc}$ ,  $M_{\text{DM}}(< 2 \text{ kpc})$ . Now from our dynamical modelling we can adapt the value of  $M_{\text{DM}}(< 2 \text{ kpc})$  to what would be required in order to best match the BRAVA velocity dispersions. This is done iteratively during the NMAGIC fit: every eight time units we evaluate the value of a factor denoted  $\mathcal{F}$  to be applied on the model velocity dispersions in the BRAVA fields in order to best fit the data. We then increase  $M(< 2 \text{ kpc})$  by  $1.0 \times 10^{10} M_{\odot} \times (\mathcal{F}^2 - 1)$  and redefine the dark matter density in the entire galaxy by fitting again the Einasto density to the rotation curve data and the new value for  $M_{\text{DM}}(< 2 \text{ kpc})$ . At the end of the fit, we check that  $M(< 2 \text{ kpc})$  has converged to the best agreement possible with the BRAVA dispersion for the considered pattern speed and stellar mass distribution. We assume that the halo is an oblate spheroid with a vertical flattening of  $0.8$  throughout the Galaxy. There is not enough power in our data to see a significant effect of the dark matter shape that is not degenerate with the dark matter profile and therefore more complicated 3D shapes of the dark matter density are not justified. In practice we expand the target halo density in spherical harmonics up to order eight and fit the dark matter particles to the expansion with the M2M method using the spherical harmonics kernels extensively described in previous uses of NMAGIC (see [De Lorenzi et al. 2007](#) and subsequent work for more detail).

### 4.7.3 The missing central mass

Using the modelling procedure defined above and the best dark matter halo that matches the overall BRAVA dispersion, we find evidence for a lack of central mass concentration in

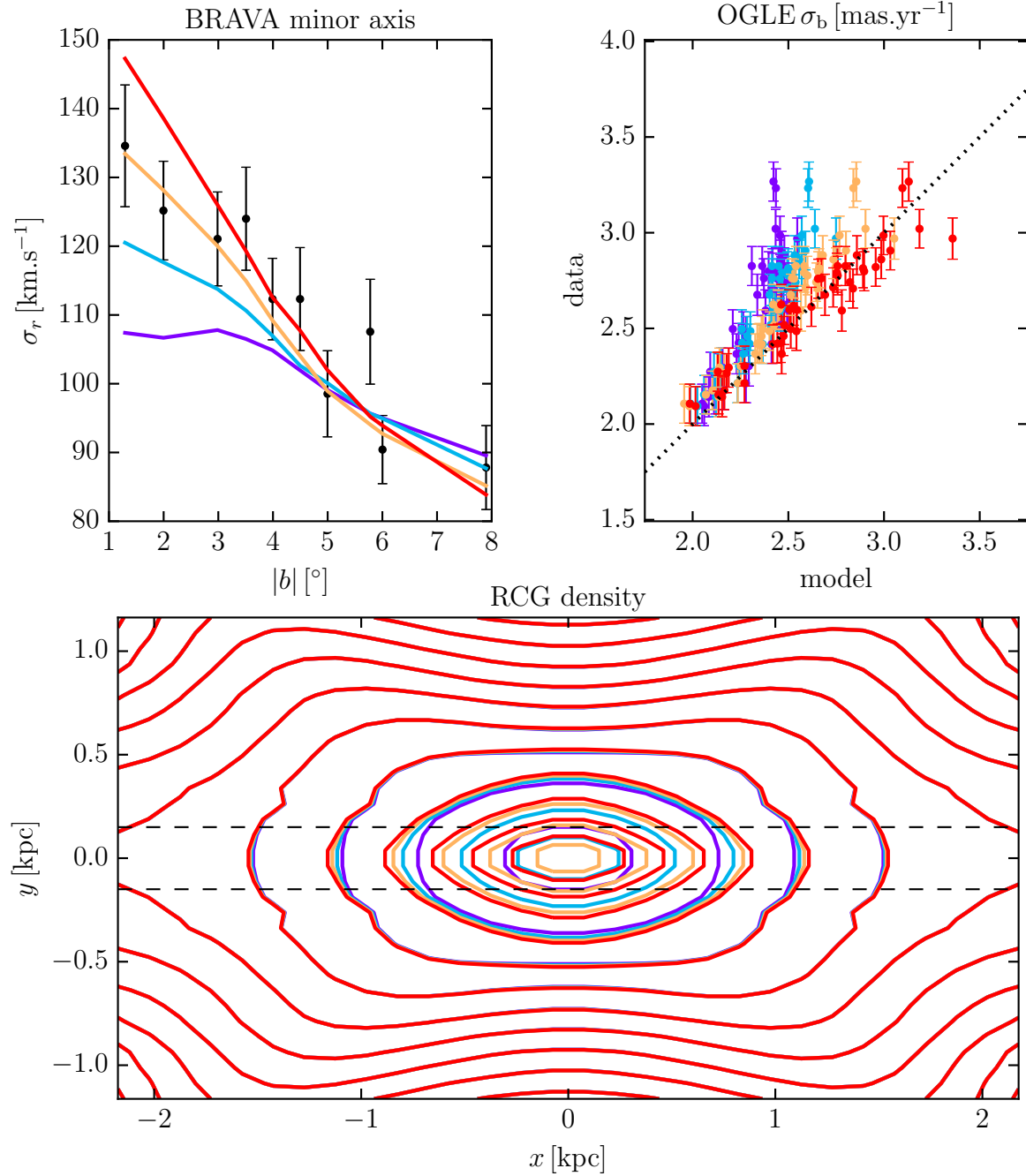


Figure 4.11: Illustration of the effect of the extra central mass on the BRAVA dispersions along the minor axis (upper left) and on the proper motion dispersion in the  $b$  direction (upper right) for four models with no extra central mass (purple) or an extra central bar mass of  $1 \times 10^9 M_\odot$  (blue),  $2 \times 10^9 M_\odot$  (yellow) and  $3 \times 10^9 M_\odot$  (red). The lower plot show the side on projection of the peanut shape assuming that the extra mass is stellar. Most of the extra mass is located in the missing  $\pm 150$  pc strip and therefore does not violate the measurement of the peanut shape from RCGs.

the models. In [Figure 4.11](#) the purple line and points show the model predictions of the BRAVA dispersions along the minor axis and the OGLE proper motion dispersions along the  $b$  direction for our fiducial bulge density and a pattern speed of  $40 \text{ km s}^{-1} \text{ kpc}^{-1}$ . The underestimation of the central dispersion is very clear and very little freedom is available either in the mass-to-clump ratio or in the pattern speed to correct for this. As NMAGIC adjusts the orbital structure in order to best match the kinematics, the only way remaining to increase the central dispersion is to deepen the gravitational potential by adding an extra central mass component. Motivated by the massive nuclear disk found by [Launhardt, Zylka & Meizer \(2002\)](#) and considering the fact that the vertical structure of the bulge density could be steeper than our fiducial  $\text{sech}^2$  extrapolation we model the missing mass by assuming that it is distributed as an elongated exponential disk following the bar, whose density is given by

$$\rho_c \propto \exp\left(-\frac{\sqrt{x^2 + (y/0.5)^2}}{h_r}\right) \times \exp\left(-\frac{|z|}{h_z}\right) \quad (4.28)$$

where  $x$ ,  $y$ , and  $z$  are coordinates along the principal axes of the bar in kpc. When  $h_r$  and  $h_z$  are too small, the large central concentration leads to the death of the peanut shape as already noted by [Athanassoula, Lambert & Dehnen \(2005\)](#). When  $h_r$  and  $h_z$  are too large the central concentration is not sufficient to provide the central potential we need to match our kinematic data. After experimenting with several combinations of  $h_r$  and  $h_z$  we adopt the values of 250 pc and 50 pc respectively.

The other three lines in [Figure 4.11](#) show the predictions of models containing an extra bar-like component with the density of [Equation 4.28](#) normalized to masses of  $M_c = 1, 2$  and  $3 \times 10^9 M_\odot$ . We see that we need an additional mass of about  $2 \times 10^9 M_\odot$  in order to reproduce both the BRAVA minor axis dispersions and the OGLE proper motions. In the lower plot of [Figure 4.11](#) we show the side-on projection of the RCG density in the bulge assuming that this extra mass is stellar and traced by red clump stars. With our parametrization most of the extra central component is located in the inner midplane  $\pm 150$  pc strip where the RCG density has not been directly measured. The interpretation of this extra mass is discussed in more detail in [Section 4.10.2](#).

## 4.8 Key parameters of the Milky Way’s effective potential

In this section we explore systematically the key parameters of the Milky Way’s effective potential. We focus on the three parameters that have the largest impact on our datasets: (i) the bar pattern speed  $\Omega_b$ , (ii) the mass-to-clump ratio  $M/n_{\text{RCG}}$  and (iii) the extra central mass noted  $M_c$ . We explore 9 values of  $\Omega_b$  between  $25 \text{ km s}^{-1} \text{ kpc}^{-1}$  and  $50 \text{ km s}^{-1} \text{ kpc}^{-1}$  in steps of  $2.5 \text{ km s}^{-1} \text{ kpc}^{-1}$ , 3 values for  $M/n_{\text{RCG}}$ , 1000 (our fiducial) and 900 and 1100 corresponding to the range of values consistent with the bulge stellar population (see [Section 4.3.2](#)), and 5 values for  $M_c$  between  $1 \times 10^9 M_\odot$  and  $3 \times 10^9 M_\odot$  in steps of  $0.5 \times$

$10^9 M_\odot$ . This results in a 3D grid of 135 NMAGIC runs for which we will evaluate how well they reproduce each individual dataset.

In [Figure 4.12](#) we give an overview of our 135 simulations. In this figure the area of the different wedges for each model show how well that simulation performs in reproducing the various dataset, larger area meaning better agreement. The area of each wedge is proportional to  $1 - \tilde{\chi}^2$  where  $\tilde{\chi}^2$  is the  $\chi^2$  rescaled so that the best simulation has  $\tilde{\chi}^2$  of 0 and the median simulation has  $\tilde{\chi}^2$  of 1, separately for each observable. Some interesting features are directly visible in [Figure 4.12](#). From the ARGOS and BRAVA kinematics we see that the mass-to-clump ratio has some degeneracy with both the pattern speed and the central mass: low mass-to-clump ratio tend to prefer lower pattern speed and higher central mass. The model at  $(M/n_{\text{RCG}}, M_c, \Omega_b) = (1000, 2 \times 10^9 M_\odot, 40 \text{ km s}^{-1} \text{ kpc}^{-1})$  as indicated by the black square in [Figure 4.12](#) is able to reproduce well all datasets simultaneously and therefore constitutes our best model.

In order to recover the range of  $M/n_{\text{RCG}}$ ,  $M_c$  and  $\Omega_b$  around the best model that is allowed by the data we would ideally construct a global likelihood for all our datasets together and search for the 3D region of the grid that contains the 68% most likely models. However, this approach is not applicable here for two reasons:

1. Comparing different datasets in a purely statistical way is dubious when datasets with different systematics are involved. We are more interested in reproducing all datasets fairly well at once than in maximizing the formal total likelihood, which may be dominated by one particular aspect or by systematics.
2. The evaluation of the range of models consistent with some data within some confidence limit is not a straightforward task in M2M modelling. [Morganti et al. \(2013\)](#) showed that the magnitude of the  $\Delta\chi^2$  that allows a fair estimation of the range of models that is compatible with the data can be much larger than that expected, due to modelling noise.

Instead we adopt a more phenomenological approach where we use our knowledge of the bar dynamics gained from the experiments of [Section 4.7](#) to explore the 3D grid of models in more detail. In [Section 4.8.1](#) we study the mass-to-clump/pattern speed degeneracy and quantify the uncertainty in the recovered bar pattern speed. In [Section 4.8.2](#) we study the mass-to-clump/central mass degeneracy and identify two boundary models at each end of the three dimensional degeneracy valley between mass-to-clump, central mass and pattern speed. Those two boundary models are used later in [Section 4.9](#) to quantify uncertainties in the recovery of the stellar and dark matter distributions. We finally show how our best model compares to the different datasets in [Section 4.8.3](#).

### 4.8.1 Bar pattern speed and corotation

We showed in [Section 4.7.1](#) that the pattern speed had a clear signature in the mean radial velocity observables. Hence we focus on the mean velocity of both the BRAVA and ARGOS surveys and show in [Figure 4.13](#) the  $\chi^2$  per datapoint as a function of the pattern speed

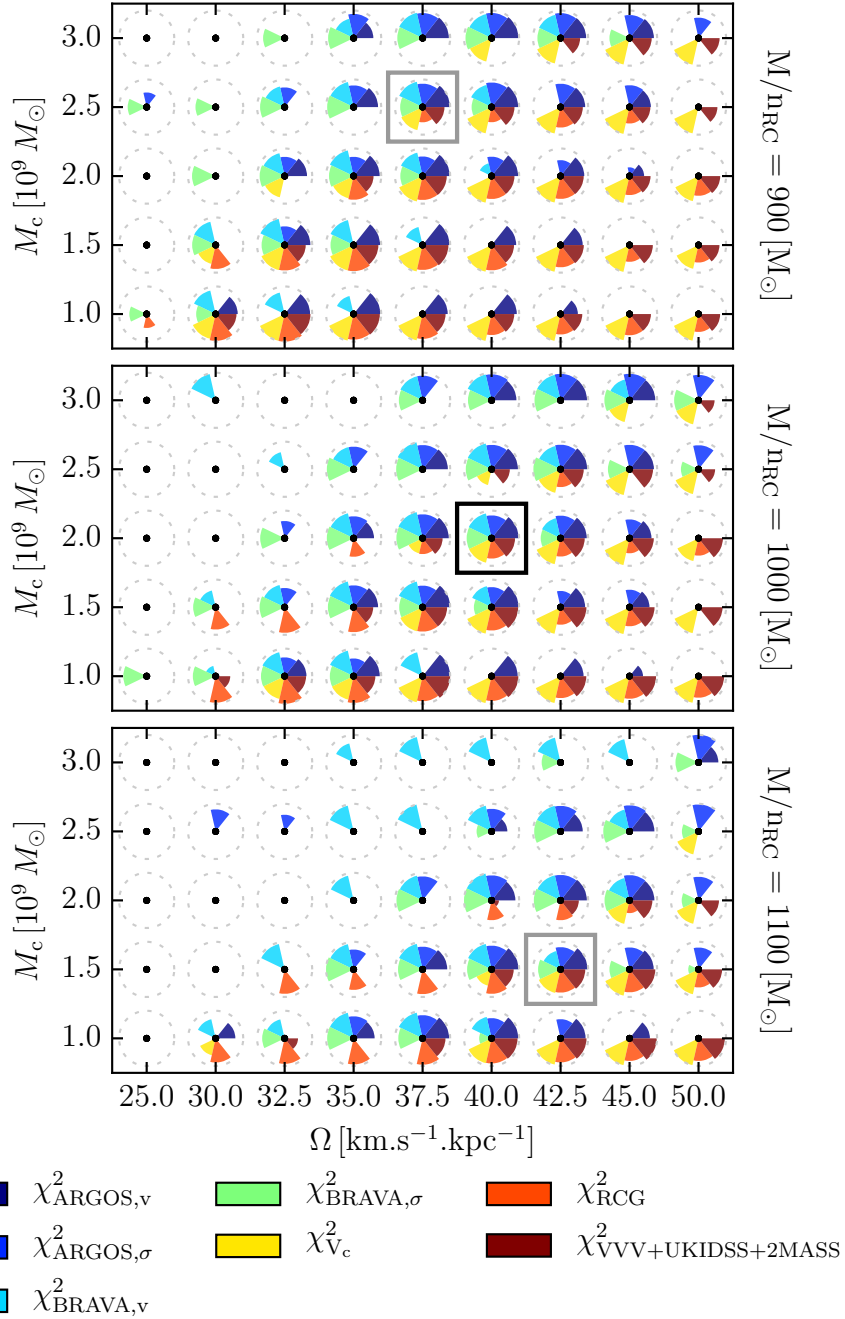


Figure 4.12: The Cheese Plot: Overview of the systematic search of the 3D parameter space ( $M/n_{\text{RCG}}, M_c, \Omega_b$ ). Each panel shows a slice in the 3D parameter space for a mass-to clump ratio of 900 (top), 1000 (middle) and 1100 (bottom). Each black dot correspond to one simulation and the area of each color wedges is a measure of how well a simulation reproduces the different datasets. We identify our best model at  $(M/n_{\text{RCG}}, M_c, \Omega_b) = (1000, 2 \times 10^9 M_\odot, 40 \text{ km s}^{-1} \text{ kpc}^{-1})$  as shown by the solid black square. The two models in grey squares are our two boundary models identified in Section 4.8.2.

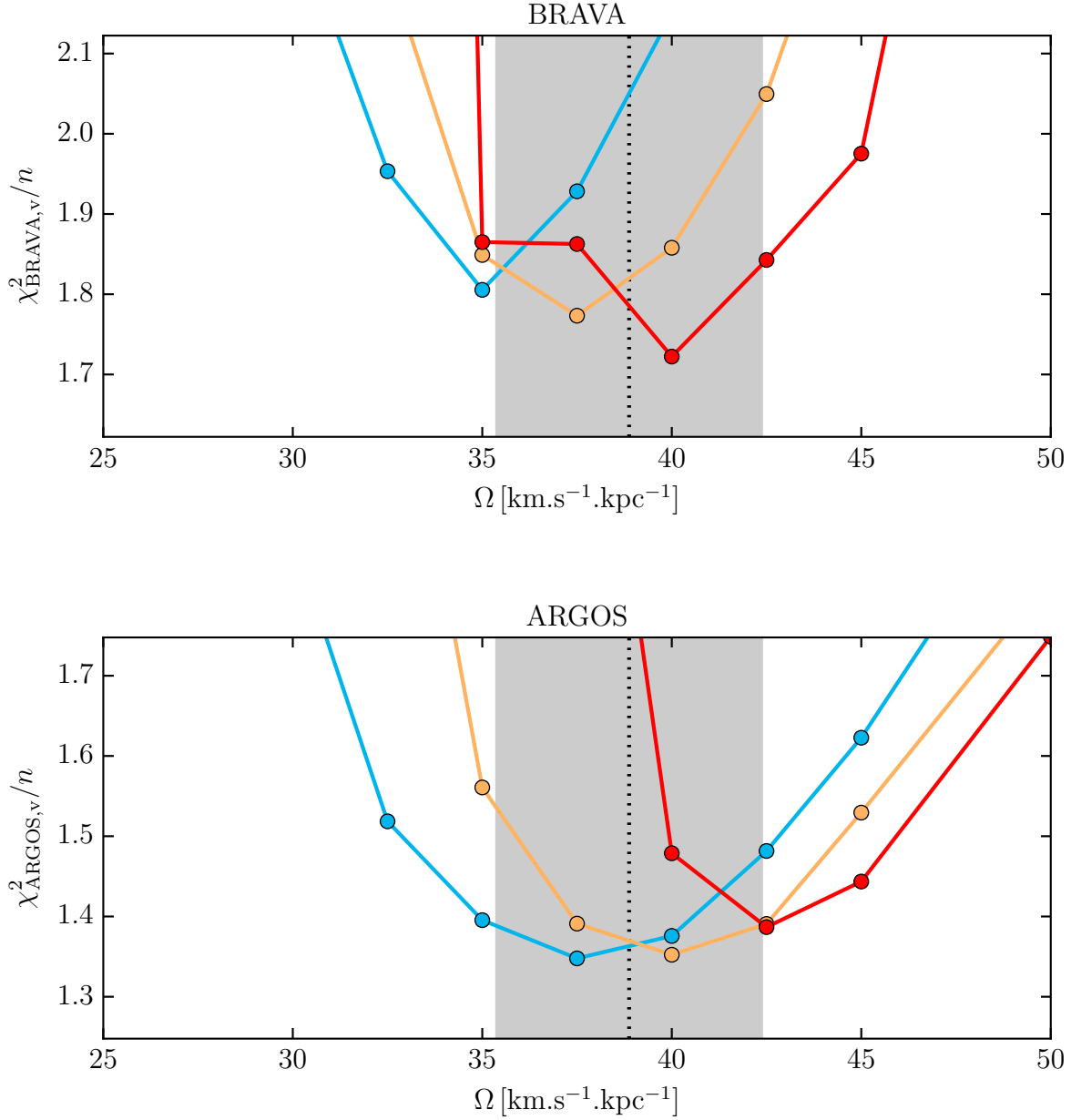


Figure 4.13:  $\chi^2$  per datapoint as a function of the pattern speed  $\Omega_b$  for the BRAVA (top) and ARGOS (bottom) mean velocities, for three slices through our cube of simulations with  $M/n_{\text{RCG}} = 900$  (blue), 1000 (yellow) and 1100 (red), all with  $M_c = 2 \times 10^9 M_\odot$ . The grey area spans the one sigma error range of our pattern speed estimation of  $39 \pm 3.5 \text{ km s}^{-1} \text{ kpc}^{-1}$ .



$\Omega_b$ , from a slice through our cube of simulations at  $M_c = 2 \times 10^9 M_\odot$ . The pattern speed that agrees best with the data is found in the range  $35 - 42.5 \text{ km s}^{-1} \text{ kpc}^{-1}$  depending on the mass-to-clump ratio. An increase in mass-to-clump ratio of 10% requires an increase in  $\Omega_b$  of  $2.5 \text{ km s}^{-1} \text{ kpc}^{-1}$ . We also notice that the ARGOS dataset systematically prefers pattern speeds  $2.5 \text{ km s}^{-1} \text{ kpc}^{-1}$  larger than the BRAVA dataset. Assuming flat priors on the mass-to-clump ratio in the range 900 – 1100, the mean of the best pattern speeds from BRAVA and ARGOS is  $\Omega_b = 39 \text{ km s}^{-1} \text{ kpc}^{-1}$ . As already discussed, the evaluation of statistical errors on measurements and parameters from M2M modelling is usually problematic since the classical  $\Delta\chi^2 = 1$  method tends to underestimate the real error. [Morganti et al. \(2013\)](#) developed a method to better estimate the statistical error using a value of  $\Delta\chi^2$  corresponding to the scatter of the  $\chi^2$  surface from the models around the minimum. Using this method we find statistical errors lower than  $1 \text{ km s}^{-1} \text{ kpc}^{-1}$ , smaller than the systematics arising from both the degeneracy with the mass-to-clump ratio or the systematic offset between the ARGOS and BRAVA datasets. Adding in quadrature an error of  $2.5 \text{ km s}^{-1} \text{ kpc}^{-1}$  from both these sources of systematics, we conclude that the pattern speed of the Milky Way bar is  $\Omega_b = 39 \pm 3.5 \text{ km s}^{-1} \text{ kpc}^{-1}$ . Using the composite rotation curve of [Sofue, Honma & Omodaka \(2009\)](#) rescaled to rescaled  $(R_0, V_0) = (8.2 \text{ kpc}, 238 \text{ km s}^{-1})$ , this place corotation at  $R_{\text{cr}} = 6.1 \pm 0.5 \text{ kpc}$ .

### 4.8.2 Central mass distribution

We showed in [Section 4.7.3](#) the necessity of an additional central mass component  $M_c$  for matching the inner BRAVA dispersions and OGLE proper motions in the  $b$  direction. In [Figure 4.14](#) we show the  $\chi^2$  per datapoint as a function of  $M_c$  for all BRAVA and OGLE fields within  $5^\circ$  from the center. We see that the BRAVA radial velocity prefers an additional mass of  $2 \times 10^9 M_\odot$  with a slight degeneracy with the mass-to-clump ratio where a 10% increase in  $M/n_{\text{RCG}}$  leads to a decrease of  $M_c$  of about  $0.5 \times 10^9 M_\odot$ . The  $\sigma_b$  proper motions appear to have some tension with the BRAVA dispersion, having a best value of  $M_c$  systematically higher by  $0.5 \times 10^9 M_\odot$ . We note however by looking at the  $\chi^2$  of the RCG density as shown in the bottom plot of [Figure 4.14](#) that large values of  $M_c$  go against the peanut shape of the bulge. This is a known effect that the peanut shape is destroyed by large central mass concentrations ([Hasan & Norman 1990](#); [Shen & Sellwood 2004](#); [Athanasoula, Lambert & Dehnen 2005](#)). Since no value of  $M_c$  simultaneously gives a good fit to the OGLE  $\sigma_b$  and the RCG density, there must be systematic effects in at least one of those datasets or in our parametrization. We show in [Figure 4.16](#) that for a central mass of  $2 \times 10^9 M_\odot$  our best model systematically underestimates the proper motion dispersions in both directions but stays on average within 5% of the data, thus providing already a very good fit to the data. Hence we estimate  $M_c$  based on the BRAVA central dispersions to be  $M_c = 2.0 + 0.5 \times (M/n_{\text{RCG}} - 1000)/100 \times 10^9 M_\odot$  and recognize the presence of some tension with both the RCG density and the OGLE proper motions.

Since a 10% increase in mass-to-clump ratio requires a  $2.5 \text{ km s}^{-1} \text{ kpc}^{-1}$  increase in pattern speed and a  $0.5 \times 10^9 M_\odot$  decrease in central mass we define two boundary models around our best model at each end of this three dimensional degeneracy,  $(M/n_{\text{RCG}}, M_c, \Omega_b) =$

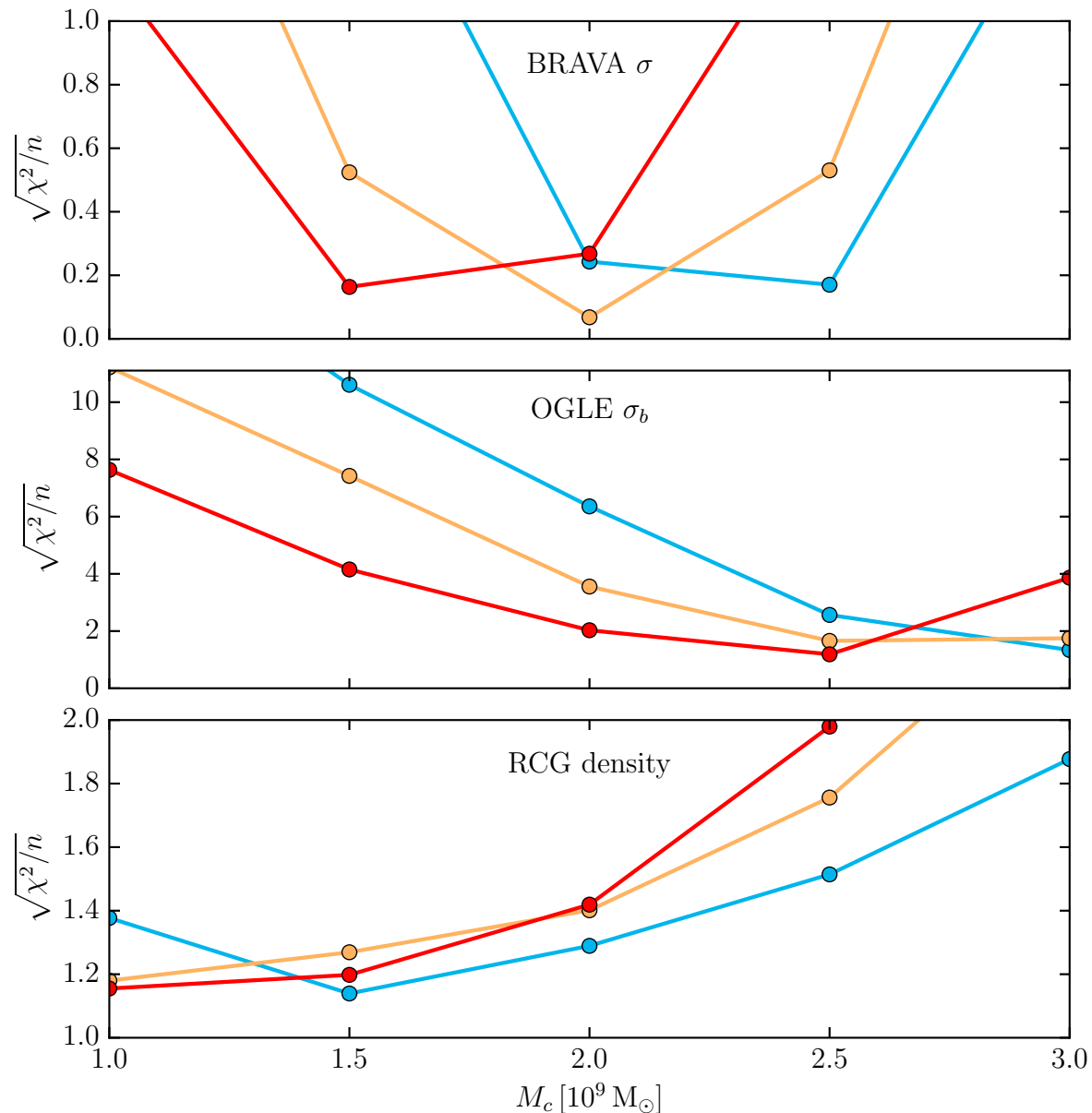


Figure 4.14:  $\chi^2$  per datapoint as a function of the additional central mass  $M_c$  from the central BRAVA dispersions (top) and the OGLE proper motions in the  $b$  direction (middle) and the RCG density (bottom) for three mass-to-clump ratios (900 in blue, 1000 in yellow and 1100 in red) all for  $\Omega_b = 40 \text{ km s}^{-1} \text{ kpc}^{-1}$ . Proper motion and RCG density are slightly inconsistent as proper motions prefer large central masses that tend to destroy the peanut shape.

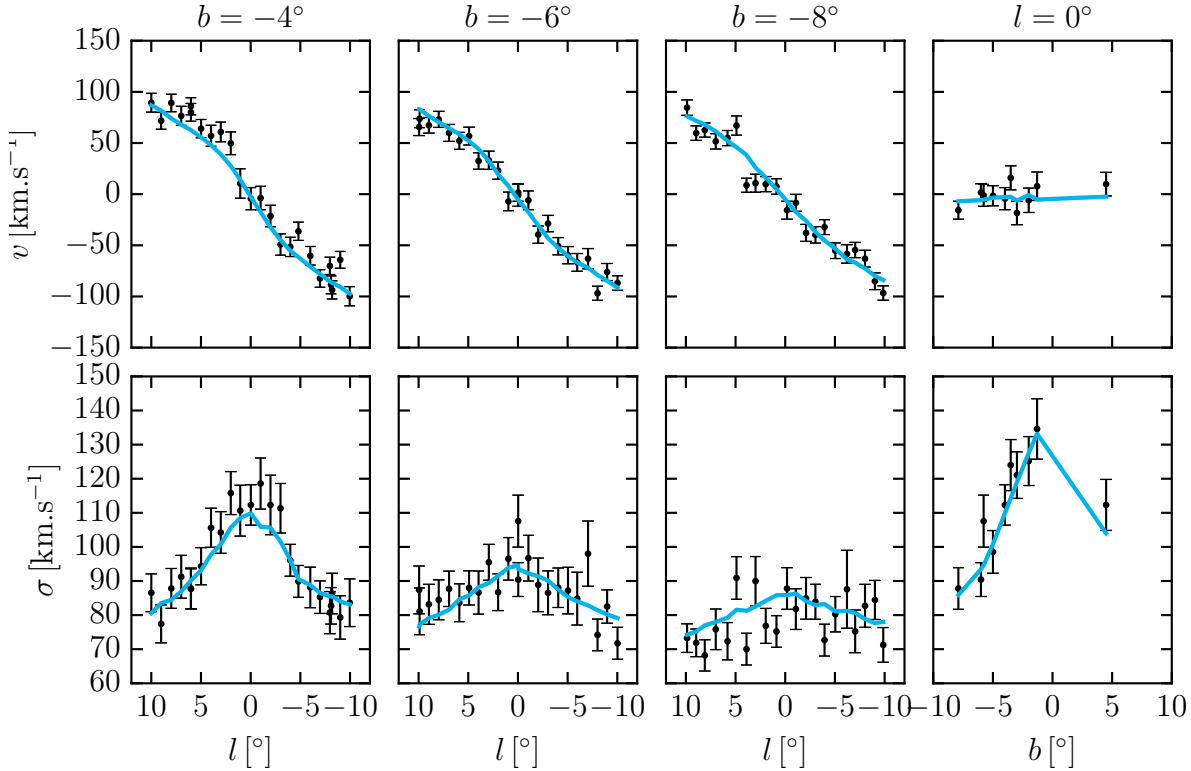


Figure 4.15: Comparison of our best model with the BRAVA mean radial velocities (upper row) and velocity dispersions (lower row) for latitude slices at  $-4^\circ$ ,  $-6^\circ$  and  $-8^\circ$  and along the minor axis.

$(900, 2.5 \times 10^9 M_\odot, 37.5 \text{ km s}^{-1} \text{ kpc}^{-1})$  and  $(M/n_{\text{RCG}}, M_c, \Omega_b) = (1100, 1.5 \times 10^9 M_\odot, 42.5 \text{ km s}^{-1} \text{ kpc}^{-1})$ . Those two models are indicated by the grey squares in Figure 4.12 and are used in Section 4.9 to quantify uncertainties in measuring the stellar and dark matter mass distributions.

### 4.8.3 Best fitting dynamical model of the Galaxy

Starting with the bulge kinematics, Figure 4.15 shows how our best model compares to the BRAVA mean velocities and velocity dispersions. The agreement is overall very good and is an improvement over P15 where the dispersions at  $-6^\circ$  were always underestimated.

The largest improvement over P15 is seen in the proper motion dispersions in the  $l$  and  $b$  directions shown in Figure 4.16. In nearly all fields the model is within 10% of the OGLE proper motions even though the proper motion data were not included in the fitting procedure. We notice however that the model tends to systematically underestimate the data by about 5%. An increase in  $\sigma_b$  can be obtained by increasing the central mass but at the cost of losing the peanut shape; or by lowering the pattern speed at the cost of a worse agreement with the mean radial velocity. In the  $l$  direction an increase in  $\sigma_l$  can be obtained by increasing the bar angle, at the cost of a worse fit to the RCGs histograms in

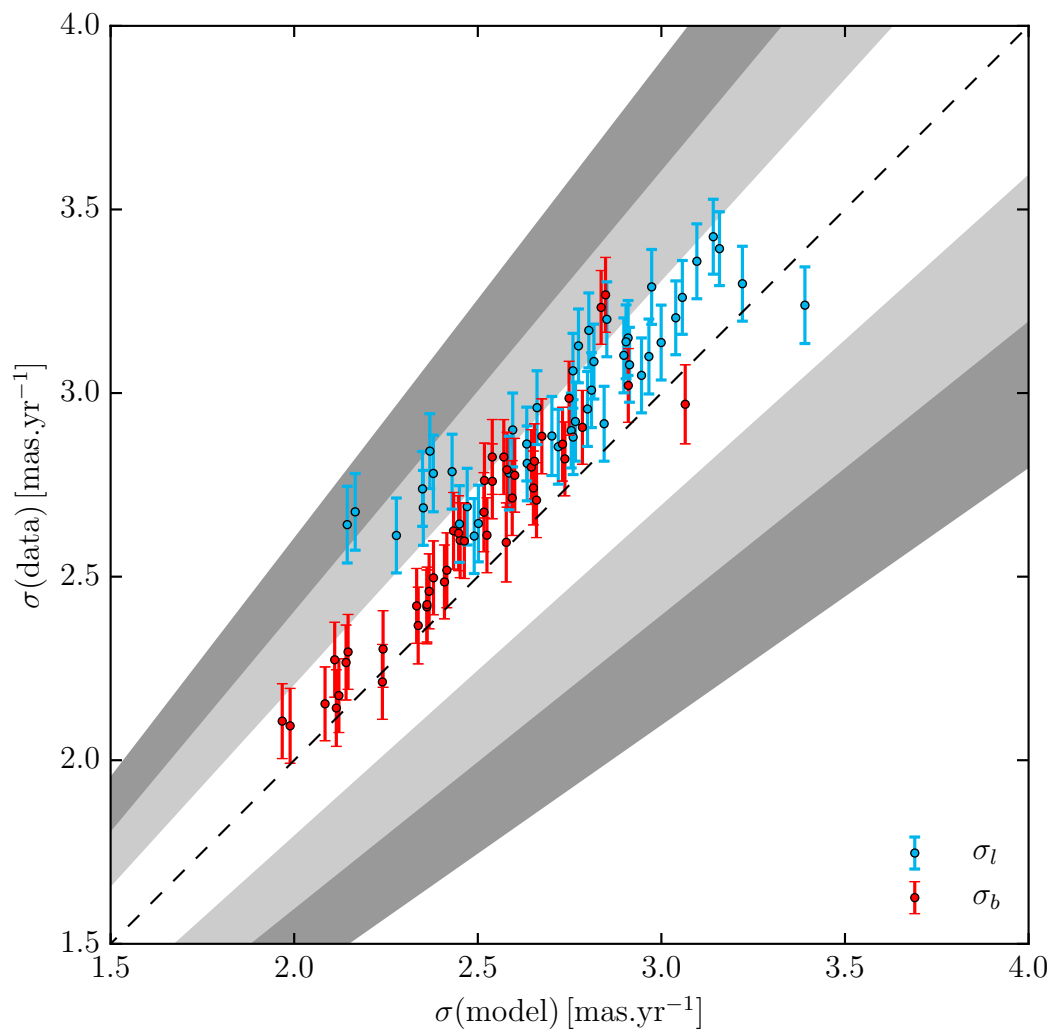


Figure 4.16: Comparison model/data of the OGLE proper motion dispersion in the  $l$  (blue) and  $b$  (red) directions. Shaded areas indicate fractional differences between 10 and 20%, and between 20 and 30%. Nearly all our best model proper motions are within 10% of the data.

the bar. Since 10% is about the size of the systematic errors in the OGLE proper motion we consider our model as already consistent with the data.

Extending to the bar region, [Figure 4.17](#) shows the ARGOS mean velocity as a function of distance. The streaming motion along the bar is very visible at latitude  $b = -5^\circ$  from the twist in the mean velocity as a function of distance. Here again the model performs very well in reproducing the data. The transition between the bulge and the bar, together with the in-plane structure of the bar, is shown in [Figure 4.19](#). The model does a very good job at reproducing the RCG distribution for  $|b| \geq 2^\circ$ . In the plane, and mostly in the region  $12 \leq l \leq 22^\circ$ , the model cannot find a good fit to the very narrow distribution of RCGs along the line of sight. This is probably due to the superthin bar component found by W15. The investigation of the detailed structure of the superthin bar is beyond the scope of this paper but could be addressed in the future using the APOGEE data. The APOGEE survey, as an infrared spectroscopic survey, can penetrate the high extinction in the plane and provides stellar kinematics and chemical abundances in the superthin bar region. By looking at clumps in chemical space [Hogg et al. \(2016\)](#) already found evidence for a very young stellar component that may correspond to the superthin bar of W15. Anticipating the future use of APOGEE to constrain the dynamical models further we show in [Figure 4.18](#) a comparison between our best model and the latest APOGEE kinematics from [Ness et al. \(2016\)](#). Our model is already in very good qualitative agreement with APOGEE even though a more quantitative comparison would require the modelling of the APOGEE selection function which is not included here.

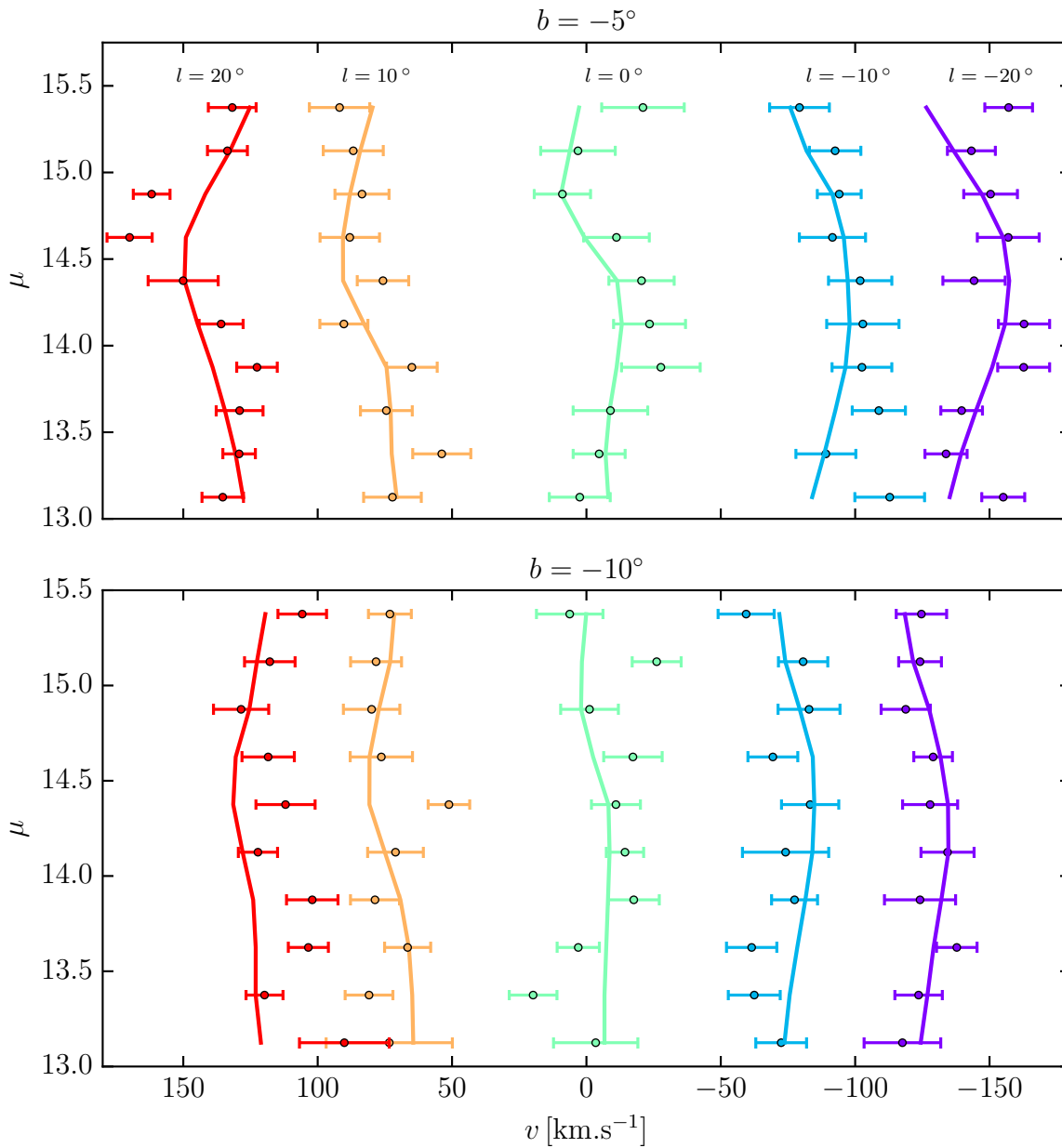


Figure 4.17: ARGOS mean radial velocities as a function of distance modulus compared with our best model, at  $b = -5^\circ$  (upper panel) and  $b = -10^\circ$  (lower panel). Different colors show different longitudes spaced every  $10^\circ$  from  $-20^\circ$  (purple) to  $+20^\circ$  (red). The curvature along the minor axis field (green) is a clear signature of the streaming motions in the bar.

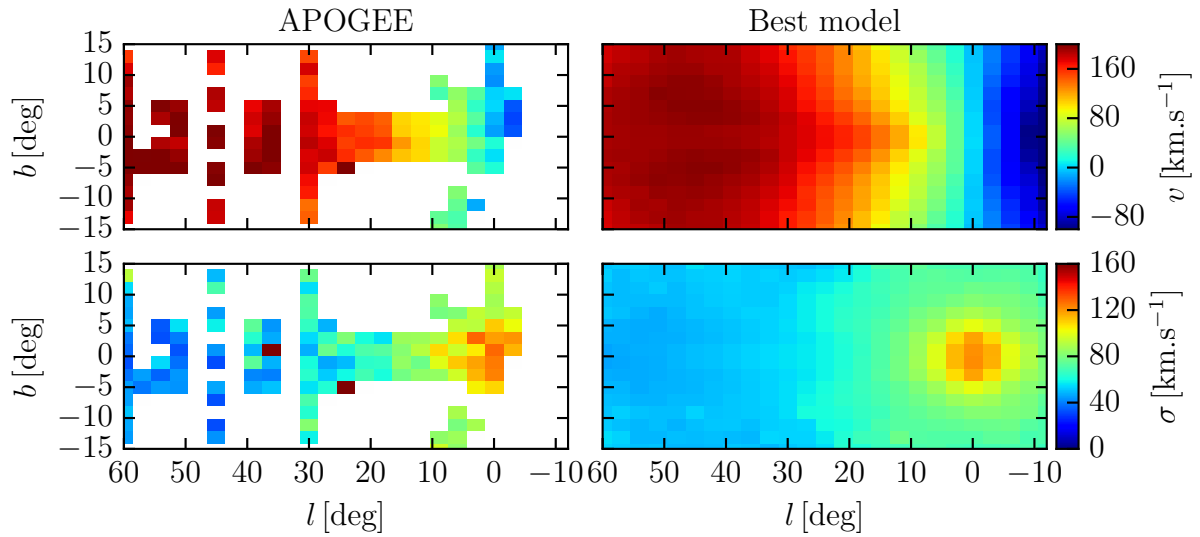


Figure 4.18: Comparison of the mean velocity (top) and velocity dispersion (bottom) between the latest APOGEE kinematics from [Ness et al. \(2016\)](#) (left) and our best model (right). Velocities are expressed in the galactic inertial frame and only stars between 4 kpc and 12 kpc along the line of sight are taken into account. Even though not fitted outside the bar region the model is already in good agreement with the APOGEE kinematics.

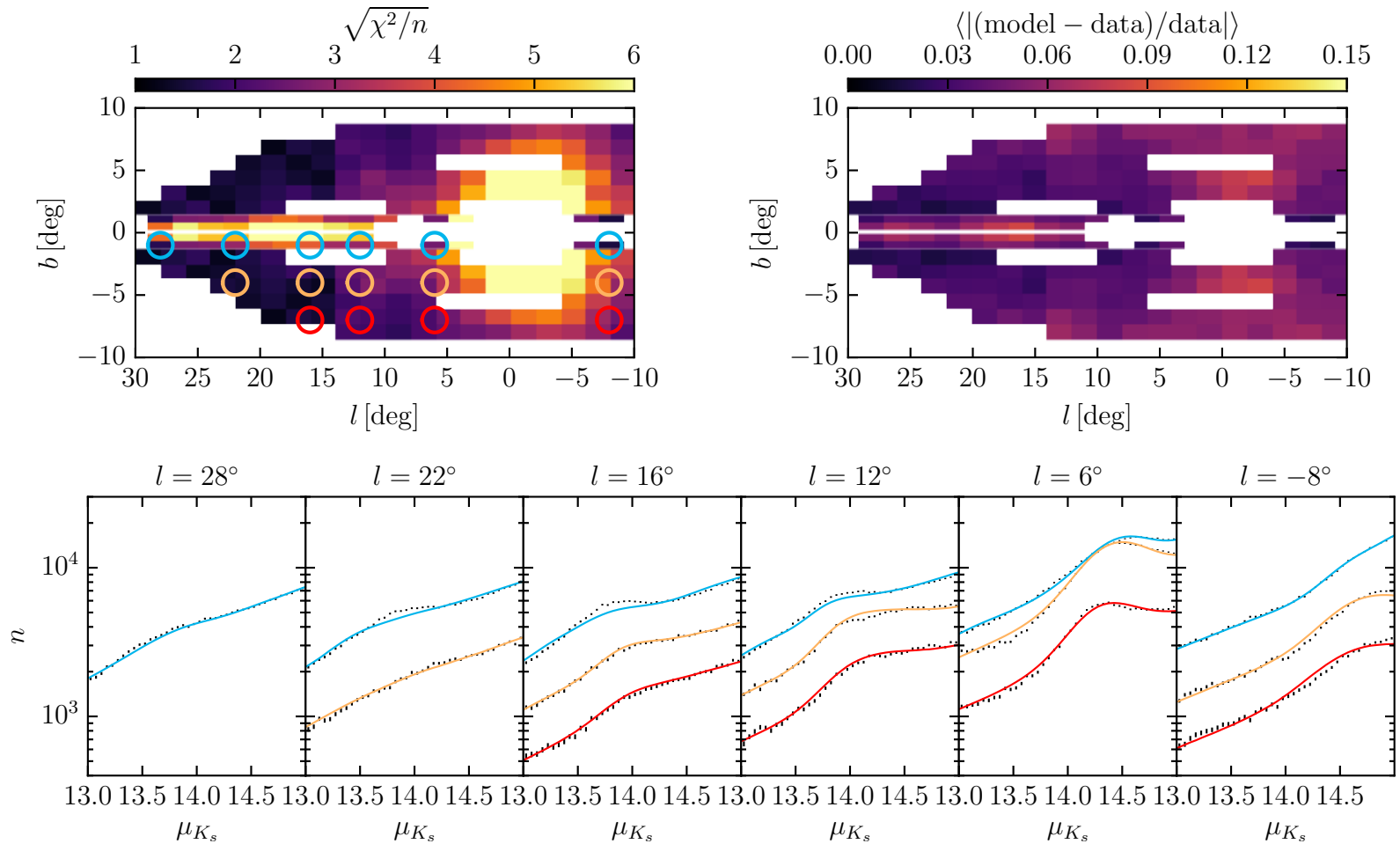


Figure 4.19: Red clump magnitude distribution of our best model across the bulge and long bar region. The upper left panel shows the reduced  $\chi^2$  between the model and the data along all considered lines of sight and the upper right panel the mean fractional errors. The  $\chi^2$  is formally poor in the bulge and close to the plane due to the very low statistical errors arising from the large number of observed stars. The lower six panels show the model line of sight magnitude distributions on top of the data for six different longitudes at three heights below the plane as indicated by the colored circles in the top left panel.



## 4.9 Stellar and dark matter mass distribution in the Milky Way

In this section we study the stellar and dark matter mass distribution of our best model and evaluate the effect of variations in the different modelling assumptions. As a range of reasonable variations around our best model we will consider:

- The two boundary models of [Section 4.8](#) found at each end of the three dimensional degeneracy valley between mass-to-clump ratio, bar pattern speed and additional central mass;
- Varying the bar angle from our fiducial  $28^\circ$  to either  $23^\circ$  or  $33^\circ$ ;
- Varying the dark matter flattening from our fiducial 0.8 to either 0.6 or 0.4;
- Varying the outer disk scale length from our fiducial 2.4 kpc to either 2.15 kpc [Bovy & Rix \(2013\)](#) or 2.6 kpc ([Jurić et al. 2008](#));

These variations will be used to evaluate (systematic) errors on the mass parameters found from our best model.

### 4.9.1 Bulge, bar, inner and outer disk

In [Figure 4.20](#) and [Figure 4.21](#) we show the surface density map and profiles of our best model with the range of the model variations, assuming that the additional mass component is stellar as discussed in [Section 4.10.2](#). The entire Galaxy is to some level non-axisymmetric. This is very clear at the edge of the bulge where the surface density along the minor axis at 2 kpc is a factor of about 4 smaller than along the major axis. Both profiles cross at 6.3 kpc from the center, close to the corotation radius. Beyond corotation the surface density becomes larger along the minor axis than along the major axis, as one would expect based on the linear perturbation of near circular orbit ([Binney & Tremaine 2008](#); [Dehnen 2000b](#)). Along the major axis the density of the bar is close to exponential. This is a characteristic of late-type barred galaxies as revealed by the S<sup>4</sup>G survey ([Elmegreen et al. 2011](#)). Traditionally the complex structure of the stellar density of the Galaxy has been divided into a small number of discrete components, mainly bulge, bar and disk for which we would wish to measure mass and shape. We will focus here on three definitions:

1. Bar, bulge and disk structure from stellar mass “photometric” profiles: From the major and minor axis profiles in [Figure 4.21](#) we see clearly three regimes: (a) the outer disk, nearly axisymmetric and exponential outside  $\sim 5.3$  kpc (b) the inner disk, axisymmetric with a nearly constant surface density inside 5.3 kpc (c) the bar/bulge, i.e. the bar which formed a bulge in its inner part. This photometric definition of the bar and inner disk components has the advantage to be easily applicable to external galaxies. By integrating the surface density associated with the “photometric” bulge

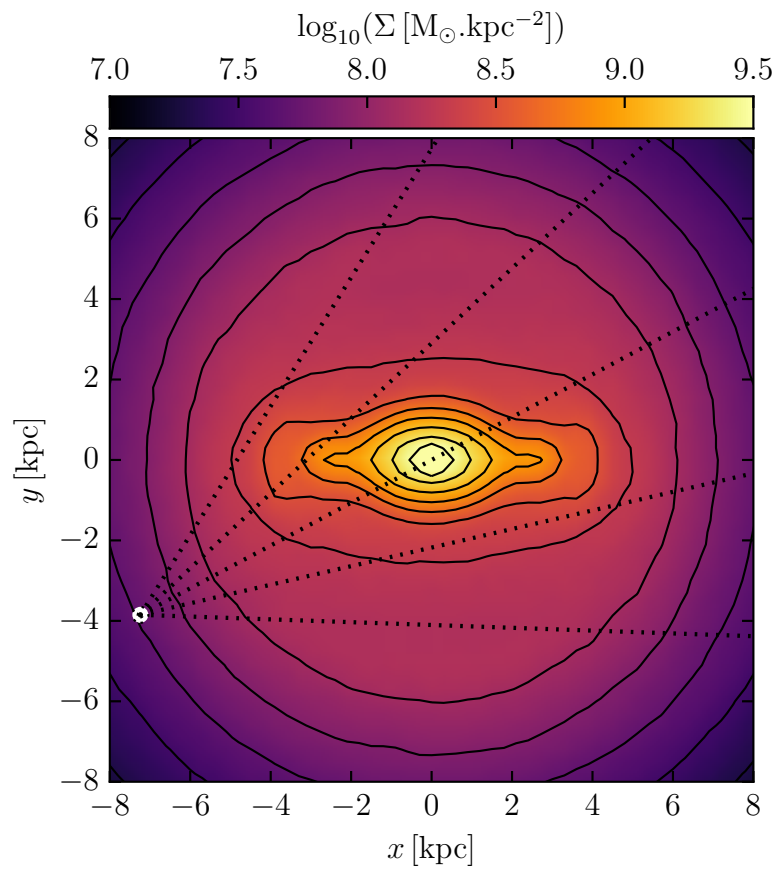


Figure 4.20: Surface density map of our best model. The bar extends to 5.3 kpc from the center and rotates at  $\Omega_b = 40 \text{ km s}^{-1} \text{ kpc}^{-1}$ .

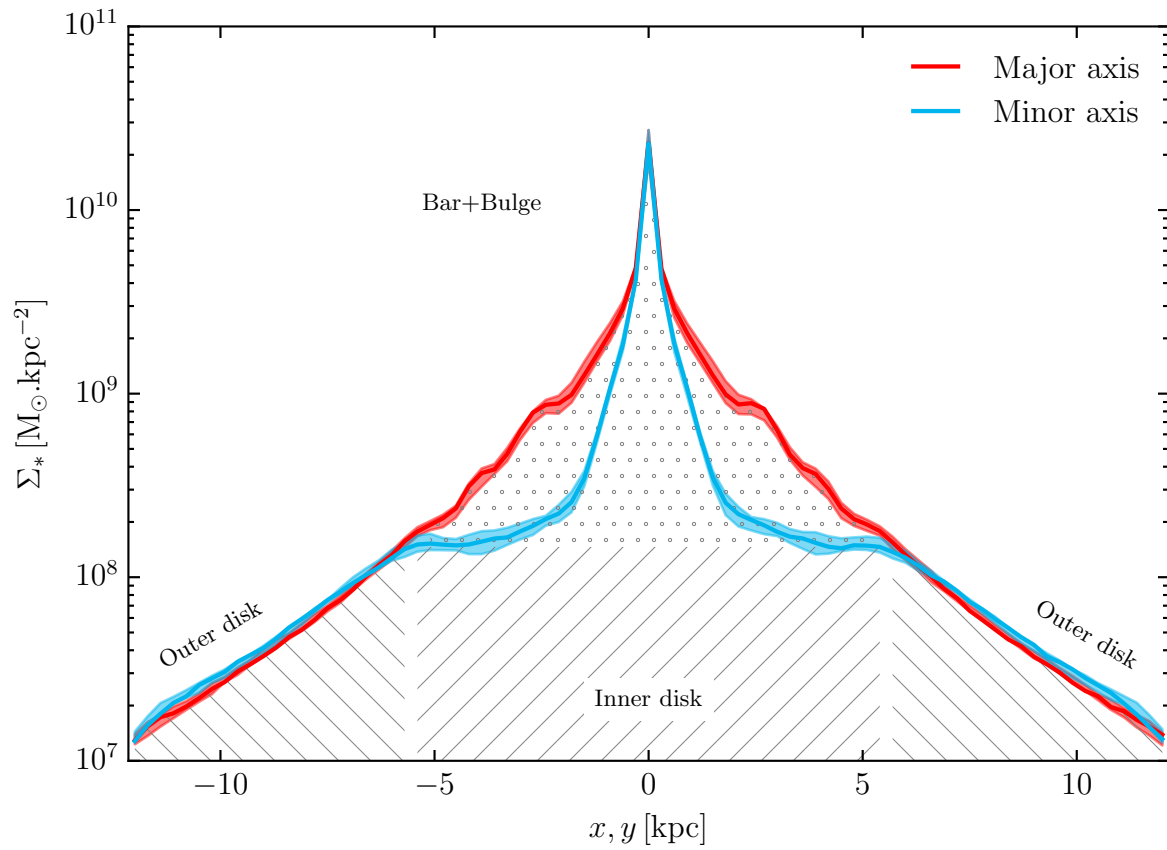


Figure 4.21: Stellar surface density profiles along the bar major axis (red) and bar in-plane minor axis (blue) for our best model (solid line) and the variation models (color span). The hatched region indicates the bar+bulge component (circle) the inner disk (/) and the outer disk (\) according to our photometric definition of the components.

and bar we find a “photometric” bar/bulge stellar mass of  $M_{\text{bar/bulge}} = 1.88 \pm 0.12 \times 10^{10} M_{\odot}$ , among which  $1.34 \pm 0.04 \times 10^{10} M_{\odot}$  is located in the bulge and  $5.4 \pm 0.4 \times 10^9 M_{\odot}$  in the long bar. The “photometric” stellar mass associated to the inner disk within the bar region is found to be  $M_{\text{inner disk}} = 1.29 \pm 0.12 \times 10^{10} M_{\odot}$ , lower than the mass of the bar/bulge structure. The errors in these quantities are systematics derived from the variation models presented previously.

2. Non-axisymmetric long bar from 2D-“photometry”: An alternative way to define the bar component is to search for non axisymmetries in the face-on surface density. We first define a maximum axisymmetric model using the minor axis profile and remove this maximum axisymmetric model from the original surface density map. By integrating the residuals for radii inside 5.3 kpc and outside the bulge we find a non-axisymmetric long bar mass of  $M_{\text{non-axi}} = 4.6 \pm 0.3 \times 10^9 M_{\odot}$ . This measure is similar but slightly lower than the previous “photometric” long bar mass since the inner disk has a similar but slightly lower surface density than our maximum axisymmetric model. From both estimates combined, the bar outside the bulge has slightly less than half the mass of the disk in the same radial range.
3. Bar-following orbits: Unlike some spiral structures, the bar is not a density wave: stars that form the bar stay in the bar and orbit mostly along elongated orbits of the  $x_1$  family and its descendants (Contopoulos & Grosbøl 1989). Since we have access to individual orbits in our dynamical model we can directly identify orbits that compose the bar using the method of Portail, Wegg & Gerhard (2015). We integrate all particles and compute the dominant frequencies of the time variation of the cylindrical radius  $f_r$  and bar major axis position  $f_x$ . Bar-supporting orbits are found in the vicinity of  $f_r/f_x = 2$ , i.e. have two radial oscillations for one period along the bar. In the bar region, particles that do not follow the bar have rosetta-like orbits in the bar frame for which  $f_r/f_x \neq 2$ ; they build the inner disk. This orbit-based definition of the bar is more elegant than the “photometric” definition and is also closer to what makes the bar a separate component but is in general not observable in external galaxies for which individual orbits are usually unknown. We find a stellar mass on bar-supporting orbit of  $10.4 \pm 0.6 \times 10^9 M_{\odot}$ . This estimate misses the non-bar following orbits in the bulge.

W15 determined from a combination of VVV, UKIDSS and 2MASS data the length of the bar and found a half-length of  $5.0 \pm 0.2$  kpc. Since our model is the first non-parametric fit of the galactic bulge and bar it is important to see how it compares to direct determination from the data. We follow W15 and focus on the following three methods to measure the bar half-length:

- $L_{\text{drop}}$ : radius at which the ellipticity of the bar drop the fastest
- $L_{\text{prof}}$ : radius at which the major and minor axis agrees within 30%
- $L_{\text{m=2}}$ : radius at which the relative m=2 component of the Fourier decomposition of the surface density drops to 20% of its maximum value

We measure  $L_{\text{drop}} = 5.77$  kpc,  $L_{\text{prof}} = 5.12$  kpc and  $L_{m=2} = 5.02$  kpc. By taking the mean of those three measurements and the standard deviation of the three measurements applied on all our variation models we find a bar half-length of the galactic bar of  $5.30 \pm 0.36$  kpc, in good agreement with the measurement of  $5.0 \pm 0.2$  kpc found by W15 from the their component fit of the RCG magnitude distributions.

### 4.9.2 The dark matter mass distribution in the Milky Way

In [Section 4.7.2](#) we showed how we recognize and evaluate the need of dark matter in the bulge from the BRAVA kinematics once the stellar density and bar pattern speed are fixed. Since we have a  $\sim 10\%$  accurate measurement of the mass-to-clump ratio in the bulge we have access to the dark matter mass distribution in the bulge. In the volume of the box in which the RCG density was measured, i.e. a box of  $(\pm 2.2 \times \pm 1.4 \times \pm 1.2)$  kpc along the bar principal axes, the mass budget of the bulge is found to be as follows: stars as traced by RCGs account for  $1.32 \pm 0.08 \times 10^{10} M_{\odot}$ , dark matter accounts for  $3.2 \pm 0.5 \times 10^9 M_{\odot}$  and  $2 \times 10^9 M_{\odot}$  of additional mass are required in the center, probably stars in the nuclear disk (see [Section 4.10.2](#)). The resulting total dynamical bulge mass is  $1.85 \pm 0.05 \times 10^{10} M_{\odot}$ , in excellent agreement with our estimation of  $1.84 \pm 0.07 \times 10^{10} M_{\odot}$  found in P15 from modelling the bulge only. Altogether we find a low dark matter fraction in the bulge of only  $17\% \pm 2\%$ . The small error arises because variations in the total mass, stellar mass and central mass of the bulge in our models approximately compensate.

Going away from the bulge, the dark matter halo profile of our best model is shown in [Figure 4.22](#) together with the range of profiles from the variation models. We find a local dark matter density of  $\rho_{\text{DM}}(R_0) = 0.0132 \pm 0.0014 M_{\odot} \cdot \text{pc}^{-3}$ , in very good agreement with the recent measurement of  $\rho_{\text{DM}}(R_0) = 0.0154 \pm 0.0023 M_{\odot} \cdot \text{pc}^{-3}$  from [Piffl et al. \(2014\)](#) for a halo flattening of 0.8 (see [Read \(2014\)](#) for a review). Interestingly our dark matter profile is cored. For the fitted Einasto density profiles, the presence of a core is consequence of accounting simultaneously for a low dark matter mass in the bulge, a significant dark matter mass enclosed within the solar radius, and a gently rising halo rotation curve.

Would an NFW halo profile be allowed by our data? In the Milky Way, an NFW halo density would be expected to have a scale radius of 20 – 40 kpc ([Bland-Hawthorn & Gerhard 2016](#)). Thus in the bar region the density would be well approximated by a simple power-law  $\rho_{\text{DM}}(r) \propto r^{-1}$ . Given the baryonic mass distribution of our best model and scaling  $\rho_{\text{DM}}$  on the total circular velocity at the solar radius, we find a dark matter mass in the bulge that coincidentally is in very good agreement with our best model value. However, such a NFW halo fails to reproduce the nearly flat total rotation curve observed between 6 and 8 kpc, with a halo circular velocity that is about  $17 \text{ km s}^{-1}$  lower than the data at 6 kpc shown in [Figure 4.23](#). The presence of a core in our best model halo density thus appears as a consequence of the constraint on the flat shape of the total circular velocity in the 6 – 8 kpc range, which for our baryonic mass distribution requires the dark matter density to fall-off more steeply than  $\rho_{\text{DM}}(r) \propto r^{-1}$ . In order to then not overpredict the dark matter mass in the bulge, the dark halo density is forced to become shallower further in.

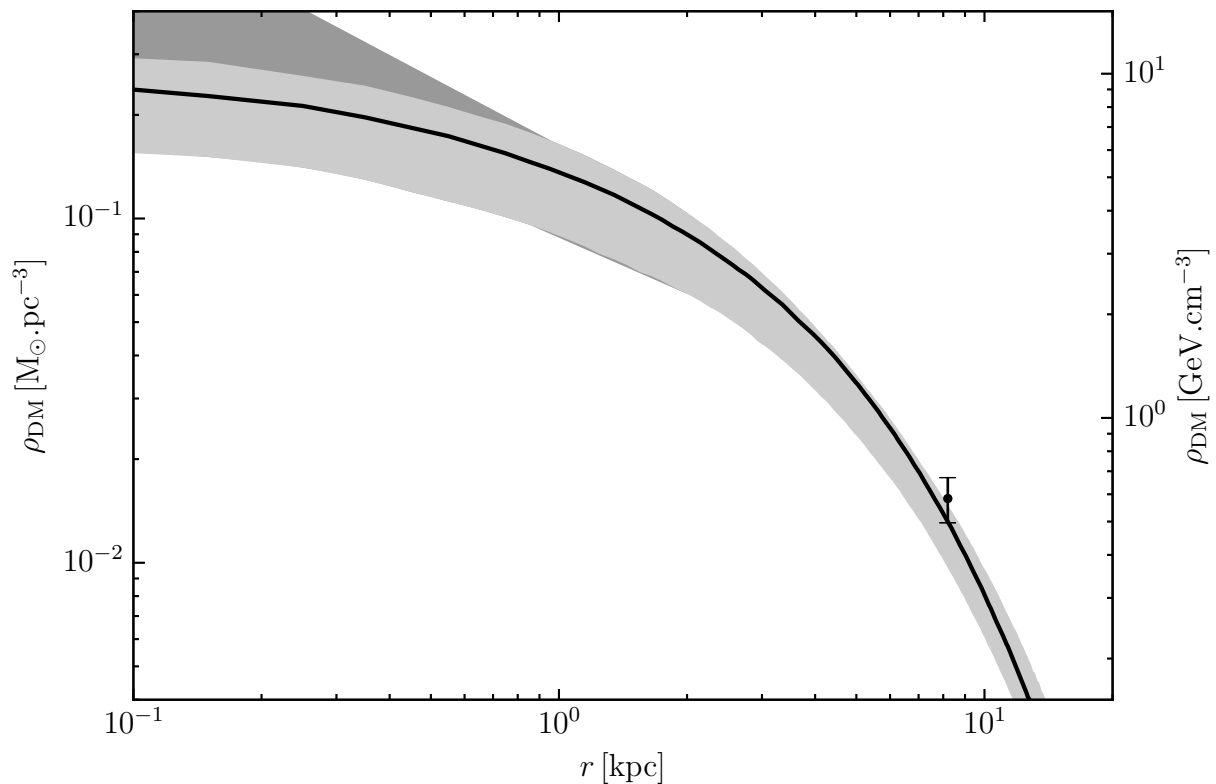


Figure 4.22: Dark matter density profile of our best model (black line), range of profiles from variation models (light grey span) and range of possible inner power-law density variations that would keep constant the dark matter mass enclosed in the bulge (dark grey span). Under the assumption of an Einasto halo, all models require a central core to account simultaneously for a low dark matter fraction in the bulge and the rotation curve at the solar radius. The datapoint at 8.2 kpc is the local measurement of the dark matter density from the analysis of RAVE stars from [Piffl et al. \(2014\)](#), in good agreement with our best model.

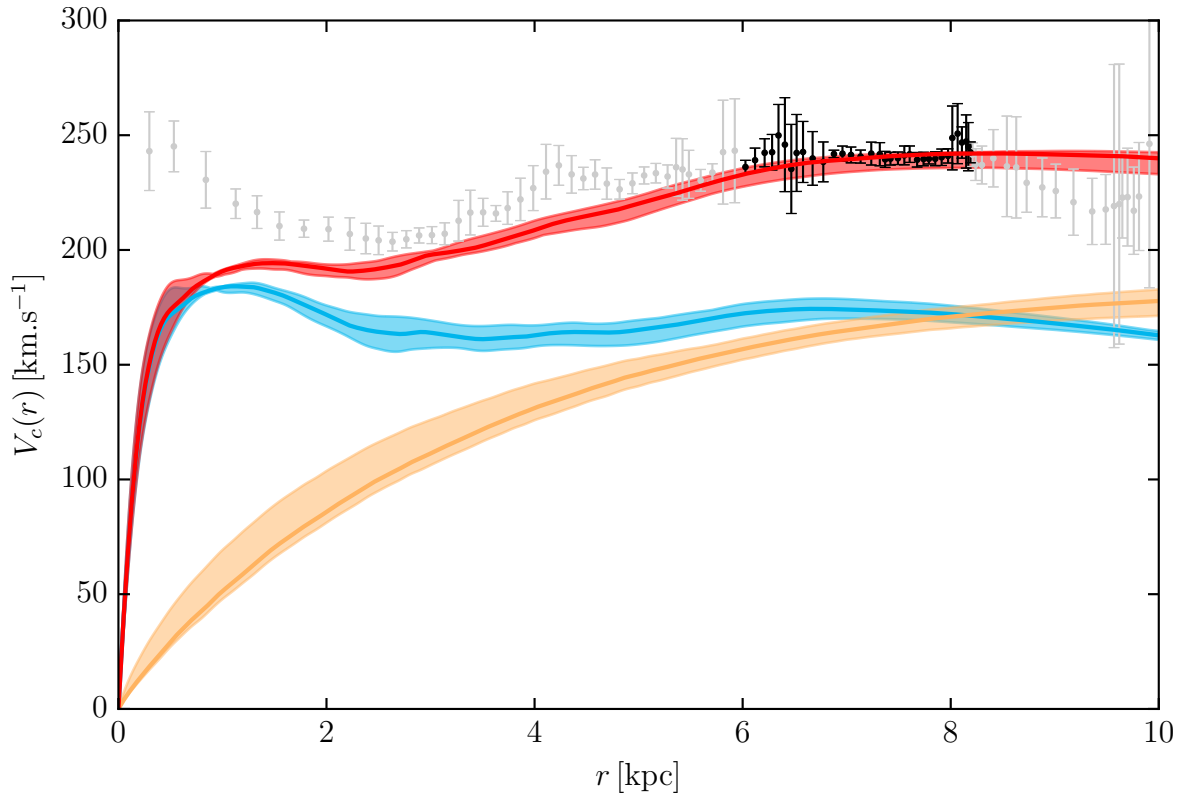


Figure 4.23: Rotation curve of our best model and range of model variations for evaluation of systematics on top of the composite rotation curve measurements from Sofue, Honma & Omodaka (2009). Blue, yellow and red curves represent respectively the baryonic, dark matter and total rotation curve, assuming that the totality of the additional central mass is baryonic

For an Einasto profile this results in a central core. However, we note that our constraint on the dark matter density in the bulge arises from a constraint on the dynamical mass of the bulge. Thus we would also expect good agreement with the data for a steeper halo density profile in the bulge, provided it has the same dark matter mass in the bulge. In order to evaluate the possibility of a steeper density in the inner halo we perform the following experiment. Assuming for the dark matter inside 2 kpc a power-law density  $\rho \propto r^{-\alpha}$ , we determine for each model the power-law index  $\alpha$  that would keep constant the dark matter mass enclosed within 2 kpc, while ensuring continuity of the density profile at 2 kpc. Doing so we find from our models power law slopes of  $\sim -0.6$ , whose range is shown as the dark grey span in Figure 4.22. We thus conclude that a central power-law cusp shallower than  $-\alpha \sim -0.6$  would also provide a good fit to the data.

A different view at the dark matter contribution to the gravitational potential can be seen in Figure 4.23 where we plot the resulting rotation curve of our best model and the range of rotation curves provided by the model variations, again considering the additional central mass as entirely baryonic. The dark matter support to the rotation is often ex-

pressed as the degree of maximality the disk (Sackett 1997), representing the ratio of the stellar rotation velocity to the total rotation velocity at some particular radius. In case of an axisymmetric disk galaxy this radius is traditionally chosen to be 2.2 disk scale length, corresponding to the position of the peak of the disk rotation curve. Since the Milky Way is not axisymmetric and hosts a central bulge, the stellar rotation curve does not peak at 2.2 outer disk scale lengths but instead at only about 1 kpc where a stellar rotation of  $185 \text{ km s}^{-1}$  provides 94% of the rotational support. At 2.2 outer disk scale lengths, the stellar contribution to the rotation curve drops to 75% still within the range of what would be called a maximum disk (Sackett 1997). This result is in agreement with the microlensing analysis of Wegg, Gerhard & Portail (2016).

## 4.10 Discussion

### 4.10.1 An intermediate bar pattern speed

The bar pattern speed is a fundamental quantity that sets the position of resonances in the Milky Way. It has been the focus of many studies in the last two decades but the scatter between different determination methods remains surprisingly large. The new value determined in this paper from the dynamics of the bulge and long bar is  $39 \pm 3.5 \text{ km s}^{-1} \text{ kpc}^{-1}$ , based on several large photometric and kinematic survey data sets.

A number of previous determinations concluded on rather large pattern speeds in the range of  $50 - 65 \text{ km s}^{-1} \text{ kpc}^{-1}$  from gas dynamics (Englmaier & Gerhard 1999; Fux 1999; Bissantz, Englmaier & Gerhard 2003), continuity of a tracer stellar population (Debattista, Gerhard & Sevenster 2002) or interpretation of stellar stream in the solar neighborhood as a resonance effect (Dehnen 2000b; Antoja et al. 2014). Other studies found lower values in the range  $25 - 40 \text{ km s}^{-1} \text{ kpc}^{-1}$  from gas dynamics (Weiner & Sellwood 1999; Rodriguez-Fernandez & Combes 2008; Sormani, Binney & Magorrian 2015; Li et al. 2016) or stellar dynamics (Long et al. 2013; P15).

Our new value for the bar pattern speed agrees very well with the extensive recent analysis of gas-dynamical models by Sormani, Binney & Magorrian (2015), but it is not consistent with the most precise determination so far based on recent analysis of the Hercules stream; this gives  $53 \pm 0.5 \text{ km s}^{-1}$  when rescaled to  $(R_0, V_0) = (8.2 \text{ pc}, 238 \text{ km s}^{-1})$  (Antoja et al. 2014). However, this measurement is model dependent, assuming that the Hercules stream originates from the bar's outer Lindblad resonance. Future work must show whether an alternative interpretation of the Hercules stream can be found.

Lower or intermediate pattern speeds are supported by the recent measurement of the long bar half-length of  $5.0 \pm 0.2 \text{ kpc}$  by W15. Since the bar cannot extend beyond corotation (Contopoulos 1980), the corotation radius has to be greater than  $\sim 5 \text{ kpc}$ , putting an upper limit on the pattern speed of about  $\sim 48 \text{ km s}^{-1} \text{ kpc}^{-1}$ . Bar pattern speeds are often expressed in term of the dimensionless ratio  $\mathcal{R}$  between the corotation radius  $R_{\text{cr}}$  and the bar half-length  $R_{\text{bar}}$ . Typical values for external disk galaxies are  $\mathcal{R} = 1.2 \pm 0.2$  (Elmegreen et al. 1996) with an indication of a correlation with bar strength (Aguerri, Beckman &



Prieto 1998) and morphological type (Rautiainen, Salo & Laurikainen 2008). Using the measured  $R_{\text{bar}} = 5.0 \pm 0.2$  kpc from W15 and our determination of  $R_{\text{cr}} = 6.1 \pm 0.5$  kpc, we find for the Milky Way a ratio of  $\mathcal{R} = 1.22 \pm 0.11$ . This places the Milky Way together with the bulk of external barred spiral galaxies, with a bar that can be classified as a fast rotator ( $\mathcal{R} \leq 1.4$ , Debattista & Sellwood (2000)).

### 4.10.2 The extra central mass

We found in Section 4.7.3 kinematic evidence for an additional central concentration of mass that was not included in our fiducial RCG bulge model. We can find good agreement with the kinematics by including an additional central mass component, mostly located in the plane where the RCG density has not been directly measured. Therefore assuming that the required mass is stellar mass does not violate the 3D density measured from RCGs. In fact there are several evidences for a stellar over-density in the plane and near the Galactic Centre but no consensus yet on the precise shape and mass of such over-density. Launhardt, Zylka & Mezger (2002) found a very concentrated nuclear bulge component in the central 220 pc from decomposition of the IRAS and COBE DIRBE data and estimate its mass to  $1.4 \times 10^9 M_{\odot}$ . From star counts, this component has a near-exponential vertical profile with scale height 45 pc corresponding to a nuclear stellar disk with axis ratio  $\sim 3 - 5 : 1$  (Nishiyama et al. 2013). Schönrich, Aumer & Sale (2015) found in the APOGEE data kinematic evidence of a nuclear disk extending to  $\sim 150$  pc with a vertical height of 50 pc. They measure a rotation velocity of  $120 \text{ km s}^{-1}$  at 150 pc which, assuming an exponential density profile, leads to a nuclear bulge mass in reasonable agreement with the mass estimate from Launhardt, Zylka & Mezger (2002). In addition Debattista et al. (2015) postulated the presence of a kpc scale nuclear disk to explain the high velocity peaks in the line of sight velocity distributions of the APOGEE commissioning data (Nidever et al. 2012). Such a large scale disk would not be concentrated enough to sufficiently increase the central velocity dispersion required by the modelling, but could account for part of the mass in the galactic plane in the bulge region.

Hence the most likely interpretation for our extra central mass component is simply a stellar over density near the center, not included in the large-scale RCG bulge. This could well be a similar component as in the SBb galaxy NGC 4565 where HST and Spitzer photometry revealed an additional diskly pseudobulge hidden inside the B/P bulge (Kormendy & Barentine 2010). More data closer to the center and extending into the plane such as APOGEE (Majewski 2012) or GIBS (Zoccali et al. 2014) would be required to investigate the structure of this extra mass further.

Some contribution to the required central mass could also come from metal poor stars not traced by RCGs such as old RR Lyrae stars (Dékány et al. 2013; Pietrukowicz et al. 2015). In the ARGOS fields metal poor stars with  $[\text{Fe}/\text{H}] \leq -0.9$  are only 7% of the total sample but since they are more concentrated than the RCG bulge stars they could still play a role in the center. However there is still no clear picture about what component these stars belong to and what mass is associated to it. Favorite hypotheses are either an old thick disk (Di Matteo et al. 2015), a small classical bulge (Kunder et al. 2016) or the

inner part of the stellar halo (Pérez-Villegas, Portail & Gerhard 2016).

### 4.10.3 Comparison with the bulge models of P15

In Portail et al. (2015, P15) we made a series of five dynamical models of the galactic bulge with different dark matter fractions called M80 to M90 by combining the 3D density of RCGs in the bulge from Wegg & Gerhard (2013) and the BRAVA kinematics. Our main findings from these models were a measurement of the bulge total mass (stellar + dark matter) of  $1.84 \pm 0.07 \times 10^{10} M_{\odot}$  and a rather low bulge pattern speed in the range  $25 - 30 \text{ km s}^{-1} \text{ kpc}^{-1}$ . In comparison, our new best model presented here has a total bulge mass of  $1.85 \times 10^{10} M_{\odot}$ , in very good agreement with our previous determination. However, from our more advanced modelling we find a higher pattern speed of  $40 \text{ km s}^{-1} \text{ kpc}^{-1}$ . We attribute the difference to the lack of mass surrounding the bulge in the models of P15. As already stated in Section 4.2.2 bars formed in N-body models are generally several disk scale lengths long, which consequently underestimate the impact of inner disk and long bar orbits on the bulge dynamics. Hence, caution must be taken when interpreting the dynamics of N-body B/P bulges, unless the bulge, bar and disk scale lengths are all consistent with each other.

The present best model has a smooth bulge stellar mass of  $1.32 \times 10^{10} M_{\odot}$ , an additional central mass of  $2 \times 10^9 M_{\odot}$  and a dark matter mass in the bulge of  $3.2 \times 10^9 M_{\odot}$ , summing up to the  $1.85 \times 10^{10} M_{\odot}$  stated above. Its closest equivalent in the P15 series of models is the fitted model M82.5 which has a mass-to-clump ratio of 1014, close to the value of 1000 we measured directly<sup>2</sup>. The main differences are the larger bar pattern speed in the new model and the fact that the new model has  $2 \times 10^9 M_{\odot}$  less dark matter in the bulge but instead a similar additional mass close to the center, as required by the central velocity dispersion for a larger pattern speed.

### 4.10.4 Dark matter in the Galaxy

Early N-body dark matter simulations predicted a universal cuspy dark matter density profile (Navarro, Frenk & White 1997). This was later confirmed by new simulations with higher resolution able to resolve halo densities on scales smaller than a percent of  $r_{200}$  (Navarro et al. 2010), i.e about 2 kpc for the Milky Way halo (Bland-Hawthorn & Gerhard 2016). In addition, since the inner part of dark matter halos is actually populated by baryons that collapse through dissipative processes, dark halos should contract, thus exacerbating any pre-existing cusp (Blumenthal et al. 1986; Gnedin et al. 2004; Abadi et al. 2010). However, the degree of contraction of the halo varies greatly between authors (see Wegg, Gerhard & Portail 2016 for a recent comparison).

In disk galaxies, processes related to the dominant role of baryons in the central parts have been found to be able to transform a primordial cusp into a core. Such processes

---

<sup>2</sup>This corrects Fig. 16 of P15 where all model values of the mass-to-clump ratios are underestimated by  $\sim 20\%$  due to an overestimate of the RGBB fraction.

are the resonance effects of a large primordial stellar bar (Weinberg & Katz 2002; but see Dubinski, Berentzen & Shlosman 2009), supernova feedback (Pontzen & Governato 2012) and stellar feedback (Schaller et al. 2015; Chan et al. 2015; but see Marinacci, Pakmor & Springel 2014). How important those processes are is not yet settled, resulting in a cusp/core controversy similar to that in dwarf galaxies (Moore 1994; Burkert 1995; De Blok 2010).

From our modelling we find a low dark matter fraction in the galactic bulge of  $17 \pm 2\%$ . In order to match simultaneously a low dark matter fraction in the bulge with the flat rotation curve close to the solar radius  $R_0$ , the dark matter density of our model has a power law slope that is steeper than  $\propto r^{-1}$  immediately inside  $R_0$  and then flattens to a shallow cusp or a core in the bulge region. This result is consistent with the recent work of Wegg, Gerhard & Portail (2016) who find a high baryonic fraction is required to account for the high optical depths towards the bulge measured in the EROS-II and MOA-II microlensing data. Given the similarity between the best model here and the fiducial model of Wegg, Gerhard & Portail (2016) we expect our best model to be also consistent with microlensing constraints towards the bulge; this will be discussed in a later paper.

## 4.11 Conclusion

We build a large number of dynamical models of the bar region in the Milky Way using the Made-to-Measure method. We first create a set of N-body models of barred disks that broadly matches the bulge, bar and outer disk density by adiabatic adaptation of a initial N-body model. This adiabatic procedure allows us to adapt the dark matter distribution to the rotation curve of the Galaxy inside 10 kpc and also to modify the pattern speed of the galactic bar. We then constrain those models with the stellar density of the bulge and bar as traced by red clump giants from a combination of the VVV, UKIDSS and 2MASS surveys, together with stellar kinematics from the BRAVA, OGLE and ARGOS surveys. We explore a three dimensional parameter space given by the stellar mass fraction in the bulge, the bulge and bar pattern speed and the nuclear disk mass, and provide constraints on the galactic effective potential. Our main conclusions are the following:

1. Modelling the stellar dynamics in the bar region requires a bar pattern speed of  $\Omega_b = 39 \pm 3.5 \text{ km s}^{-1} \text{ kpc}^{-1}$ , placing corotation at  $6.1 \pm 0.5 \text{ kpc}$  from the Galactic Centre. The ratio of corotation radius to bar half-length ( $R_{\text{bar}} = 5.0 \pm 0.2 \text{ kpc}$  from Wegg, Gerhard & Portail 2015) of the Galaxy is found to be  $\mathcal{R} = 1.22 \pm 0.11$ , in good agreement with what is seen in external disk galaxies.
2. We find a total dynamical mass of the bulge of  $1.85 \pm 0.05 \times 10^{10} M_\odot$ , in excellent agreement with the value found in Portail et al. (2015) from modelling the bulge only.
3. We find dynamical evidence for an extra central mass component, not included in our previous bulge models, of about  $2 \times 10^9 M_\odot$  and probably related to a nuclear disk or disky pseudo-bulge.

4. We evaluate from our model the mass of the long bar and bulge structure and find  $M_{\text{bar/bulge}} = 1.88 \pm 0.12 \times 10^{10} M_{\odot}$ , larger than the mass of disk in the bar region,  $M_{\text{inner disk}} = 1.29 \pm 0.12 \times 10^{10} M_{\odot}$ . The mass of the long bar is slightly less than half the disk mass in the same radial range. Our models predict a non-exponential surface density for the disk in the bar region and illustrate the transition between the bar region and the outer disk.
5. We also evaluate the need of dark matter in the inner Milky Way. Using recent measurements of the bulge IMF and more extended data we now better constrain the stellar to dark matter fraction in the bulge and find a preference for a mass-to-clump ratio of 1000 and a low dark matter fraction of  $17 \pm 2\%$  in the bulge. In order to match simultaneously a low dark matter fraction in the bulge with the flat rotation curve close to the Solar radius  $R_0$ , the dark matter density of our model has a power law slope that is steeper than  $\propto r^{-1}$  immediately inside  $R_0$  and then flattens to a shallow cusp or a core in the bulge region.

Our best fitting model is the first non-parametric model of the entire bar region of the Milky Way and can be of significant use for several on-going and future Milky Way studies including gas dynamics in realistic galactic bar potentials and chemodynamics of the different stellar populations. We plan to make the model available upon request once the paper is accepted.

## Acknowledgments

We thank Manuela Zoccali and Elena Valenti for helpful discussions, and are grateful to Jerry Sellwood and Monica Valluri for making their potential solver code available to us. We acknowledge the great work of the VVV, ARGOS, BRAVA, UKIDSS, OGLE and 2MASS survey teams upon which this paper is built.

# Chapter 5

## Chemodynamical Modelling of the Inner Galaxy

**Future publication:** Matthieu Portail, Christopher Wegg, Ortwin Gerhard and Melissa Ness, in preparation

### Abstract

We present the first self-consistent chemodynamical model fitted to reproduce real data for the galactic bar. We present an extension of the Made-to-Measure method to an augmented phase-space including the metallicity of stars, and show its first application on the bar region of the Milky Way. Our model is based on the recent dynamical model of the bulge, bar and inner disk from [Portail et al. \(2016\)](#), that fits the distribution of red clump giants in the bar region from a combination of the VVV, UKIDSS and 2MASS surveys together with stellar kinematics from the BRAVA, OGLE and ARGOS surveys. The metallicity of stars is modeled and adapted to reproduce the fractional density and stellar kinematics of the different metallicity components observed in the ARGOS and APOGEE surveys. Our model reproduces the spatial and kinematic variations of the different metallicity components seen in the data. It thus allows the study of the different metallicity components in great detail, from their 3D density distributions to different features in their kinematics and orbital structures. Our model show that metal-rich stars with  $[\text{Fe}/\text{H}] \geq -0.5$  are strongly barred and have dynamical properties that are consistent with a common disk origin. Metal-poor stars with  $[\text{Fe}/\text{H}] \leq -0.5$  show an evolving trend with metallicity, indicating different contributions from different underlying metal-poor stellar populations. Enlightened by our model, the presence of an old classical spheroid that would represent a significant fraction of bulge stars in Baade's window, as claimed by [Babusiaux et al. \(2010\)](#), appears as extremely unlikely. This paper demonstrates the power of Made-to-Measure chemodynamical models, that once extended to other chemical dimensions, will be very powerful tools to maximize the information obtained from on-going and future spectroscopic surveys in the Galaxy, such as APOGEE, GALAH and

MOONS.

## 5.1 Introduction

In the last two decades, our understanding of the inner Galaxy and in particular its central bulge has dramatically changed, driven by the growing interest of the community and the availability of large scale surveys. The galactic bulge was initially thought to be a classical bulge, a spheroidal remnant of mergers that happened during the hierarchical assembly of the Galaxy. This was supported by its old age (Ortolani et al. 1995) and the presence of a vertical metallicity gradient, which was thought at the time to rule out other formation scenarios (Friedli, Benz & Kennicutt 1994). The picture changed when non-axisymmetries, found consistently in the H $\alpha$  and CO gas flow (Binney et al. 1991; Englmaier & Gerhard 1999; Fux 1999), in the near infrared light distribution (Blitz & Spergel 1991; Weiland et al. 1994; Bissantz & Gerhard 2002) and star counts (Nakada et al. 1991; Stanek et al. 1997; López-Corredoira, Cabrera-Lavers & Gerhard 2005) revealed the presence of a triaxial and rather short boxy bar structure in the bulge (Dwek et al. 1995; Binney, Gerhard & Spergel 1997), extending to 2 – 3 kpc from the center.

Very recently, Nataf et al. (2010) and McWilliam & Zoccali (2010) independently discovered the so-called split red clump, resulting from a double bump in the density distribution of red clump giants (RCGs) in the bulge. Such a double bump feature, similar to the one seen in N-body simulations of boxy/peanut (B/P) bulge, indicated a different formation scenario for the galactic bulge. Indeed, N-body simulations showed that B/P bulges could form from disk stars through the vertical instability of a stellar bar (Combes & Sanders 1981; Raha et al. 1991; Debattista & Sellwood 2000; Athanassoula 2005; Martínez-Valpuesta, Shlosman & Heller 2006). Such a formation scenario for the galactic bulge is now supported by many recent analyses. Using 8 million RCGs stars identified in the VVV catalogue, Wegg & Gerhard (2013) were able to directly reconstruct the 3D density of stars in the galactic bulge by deconvolution the magnitude distribution of RCGs in many fields though the bulge. In addition, several spectroscopic surveys such as the BRAVA survey (Kunder et al. 2012) and the ARGOS survey (Freeman et al. 2013) were carried out in the bulge and revealed its cylindrical rotation, characteristic of a disk origin. The bulge is now believed to be the vertically extended part of a buckled long bar component, qualitatively similar to the bar produced in N-body simulations. Last year, Wegg, Gerhard & Portail (2015) showed by combining the VVV, UKIDSS and 2MASS catalogs that the galactic bulge smoothly segues into the flat long bar, that extends to about 5 kpc from the Galactic Centre. They find that both the bulge and the long bar appear at a consistent angle with respect to the line-of-sight towards the Galactic Centre, resolving the controversy about the possible presence of a double bar system in the Galaxy (Benjamin et al. 2005; López-Corredoira, Cabrera-Lavers & Gerhard 2005; Cabrera-Lavers et al. 2008; Martínez-Valpuesta & Gerhard 2011). The bar region, including the B/p bulge, long bar component and inner disk has been recently modeled by Portail et al. (2016, hereafter P16) in a self-consistent way. Using the Made-to-measure method (M2M), P16 were able to to

find a dynamical equilibrium model that reproduces simultaneously the RCGs density in the bulge and bar region from a combination of the the VVV, UKIDSS and 2MASS surveys together with stellar kinematics from the BRAVA, OGLE and ARGOS surveys.

Based on our new knowledge of the current dynamical state of the inner Milky Way the next stage is to try to understand its formation history. Although individual orbits of stars are scrambled during the bar formation and subsequent buckling instability, [Martinez-Valpuesta & Gerhard \(2013\)](#) showed that Jacobi energy of stars is largely conserved during the process. Thus, by advanced modelling of the current state of the Galaxy we can hope to trace back earlier stages ([Di Matteo et al. 2014](#)). However this is challenging, it requires as much data as possible, including chemical information on stars. Several studies have tried to infer a formation scenario for the bulge based on measurements of the stellar metallicity and its gradient along the bulge minor axis. However, [Martinez-Valpuesta & Gerhard \(2013\)](#) showed that the presence of a vertical metallicity gradient in the bulge was in itself not a strong argument for the presence of a classical bulge component as previously thought. They showed that an initial radial gradient in a disk can, after bar formation and buckling, result in a vertical metallicity gradient similar to that observed in the galactic bulge ([Minniti et al. 1995](#); [Zoccali et al. 2008](#); [Gonzalez et al. 2011b](#)), thus suggesting that the galactic bulge could have a pure disk origin. However, other studies (e.g. [Babusiaux et al. 2010](#); [Hill et al. 2011](#); [Gonzalez et al. 2011a](#); [Uttenthaler et al. 2012](#)) have found evidence for two different stellar populations in the bulge with different kinematics: a metal-rich population centered on  $[\text{Fe}/\text{H}] \sim 0.25$ , rapidly rotating and dynamically cold and a metal-poor population centered on  $[\text{Fe}/\text{H}] \sim -0.3$ , dynamically hotter and more slowly rotating. These authors associated the metal-rich component to a B/P bulge with disk origin and suggested that the metal-poor component is an old classical spheroid, which in Baade's window would account for about half of the stars in the bulge.

This view of a very prominent classical bulge in the Galaxy has been also challenged by the ARGOS survey and its associated series of papers. Using the full ARGOS sample, [Ness et al. \(2013a\)](#) showed that the metallicity distributions of stars in different fields though the inner Galaxy were well represented by five different components whose relative fraction change from field to field, thus explaining the vertical metallicity gradient of the bulge as a change in the relative fractions of the components. For each of these components, labeled from A to E in the order of decreasing metallicity they speculate a different origin as summarized below:

- A ( $[\text{Fe}/\text{H}] \sim 0.1$ ): Metal-rich cold component of the B/P bulge. A is concentrated to the plane and associated to a more recent star formation episode than B.
- B ( $[\text{Fe}/\text{H}] \sim -0.3$ ): Main component of the B/P bulge originating from the thin disk after the bar formation and secular evolution.
- C ( $[\text{Fe}/\text{H}] \sim -0.7$ ): More metal-poor disky population that does not significantly support the B/P shape of the bulge. C is associated to the hot and less dynamically responsive inner thick disk at the time where the bar formed.

- D ( $[\text{Fe}/\text{H}] \sim -1.2$ ): Metal weak thick disk, similar to the thick disk seen in the solar neighborhood.
- E ( $[\text{Fe}/\text{H}] \sim -1.7$ ): Very metal-poor stars, associated to either a small classical bulge component or the inner part of the stellar halo.

The interpretation of the ARGOS components and their kinematics has been discussed by [Di Matteo et al. \(2014\)](#) and [Di Matteo et al. \(2015\)](#) who conclude that:

- A&B have both a disk origin, with B formed on average at larger radii than A. Since the bar formation keeps record of the birth origin, an initial metallicity gradient in the disk creates a correlation between birth radius and metallicity. A is associated to the inner thin disk and B to the more extended parts of the thin disk ([Di Matteo et al. 2015](#)), or to the young thick disk ( $\leq 8$  Gyr, [Haywood et al. 2013](#)).
- C cannot be formed from thin disk stars. In a scenario where the bulge originates from a pure thin disk with an initial metallicity gradient, [Di Matteo et al. \(2014\)](#) show that the metal-poor stars would be dynamically hotter and would rotate faster than the more metal-rich stars after bar formation. In the ARGOS data, C is found to be rotating more slowly than B and thus cannot originate from the thin disk. The fact that C does not show the split red clump is another piece of evidence that it does not originate from the thin disk.
- C can hardly be associated to a classical bulge component and is therefore likely to have a disk origin as well, probably the old thick disk (8 – 10 Gyr, [Haywood et al. 2013](#)).

Stars with  $[\text{Fe}/\text{H}] \leq -1$ , such as stars traced by the RR Lyrae stars in the bulge, have also a controversial origin. RR Lyrae in the bulge have been found by [Pietrukowicz et al. \(2015\)](#) to be bar-shaped and centrally concentrated. From spectroscopic measurements, [Kunder et al. \(2016\)](#) found that they formed a hot population, with a velocity dispersion of  $\sim 130 \text{ km s}^{-1}$  and were only slowly rotating or not rotating at all. They conclude that bulge RR Lyrae stars are consistent with forming a small classical bulge component. Instead [Pérez-Villegas, Portail & Gerhard \(2016\)](#) showed that both their density and kinematics are consistent with what is expected from the inner part of the stellar halo that co-evolved with the galactic bar.

In this context of controversies, the goal of this paper is two-fold. First, we aim at presenting an extension of the M2M method for constructing chemodynamical models fitted to galaxies by attaching chemical quantities to N-body orbits in a self-consistent dynamical model. Such M2M chemodynamical models have the power to extract maximum information from the data and could be a valuable tool in the near future for modelling the data provided by the currently running and future large spectroscopic surveys in the Galaxy. We focus here on the metallicity distribution but future applications extend the modelling to other chemical quantities, such as  $[\alpha/\text{Fe}]$  for example. This is described in [Section 5.2](#). Second, we aim at clarifying what available data can tell us about the



present state of the inner Galaxy in the 7-dimensional extended phase-space of position, velocity and metallicity by applying our chemodynamical M2M method in the galactic bar region. We base the underlying dynamical model on P16. This model is a very good representation of the inner Galaxy and provides us with a library of N-body orbits which we use to fit the spatial and kinematic variations of the metallicity of stars as seen in the ARGOS and APOGEE data. We describe this fitting procedure in [Section 5.3](#) and show in [Section 5.4](#) and [Section 5.5](#) the spatial distribution and kinematics of the different metallicity components in the inner Galaxy. We finally discuss possible formation scenarios for the different metallicity components in the light of other works and conclude in [Section 5.6](#).

## 5.2 Made-to-measure chemodynamical modelling

### 5.2.1 The Made-to-Measure method

The Made-to-Measure method (M2M) is a particle-based modelling technique that allows the creation of constrained equilibrium models ([Syer & Tremaine 1996](#)). Initially developed to tailor N-body initial conditions ([Syer & Tremaine 1996](#); [Dehnen 2009](#)), the M2M method was adapted by [De Lorenzi et al. \(2007\)](#) to create dynamical models of real galaxies by fitting observational data. The idea behind the M2M method is to slowly adapt the particle weights of a N-body model in order to reproduce a given set of data. The N-body weights, representing mass elements in phase-space in the classical N-body approach are simultaneously seen as weighting factors of the N-body orbits on which the particles are. The M2M method has the advantage to be applicable in complex systems like barred galaxies where other modelling techniques such as moment-based methods ([Binney, Davies & Illingworth 1990](#); [Cappellari et al. 2009](#)), classical distribution function-based methods ([Dejonghe 1984](#); [Qian et al. 1995](#)), actions-based methods ([Binney 2010](#); [Sanders & Binney 2013](#)) or orbit-based methods ([Schwarzschild 1979](#); [Thomas et al. 2009](#)) would be either not applicable or very expensive.

Formally, we represent the equilibrium state of the Galaxy by its distribution function  $f(\mathbf{x}, \mathbf{v})$  and write any observable  $y$  as

$$y = \int K(\mathbf{x}, \mathbf{v}) f(\mathbf{x}, \mathbf{v}) d^3\mathbf{x} d^3\mathbf{v} \quad (5.1)$$

where  $\mathbf{x}, \mathbf{v}$  is the phase space vector and  $K$  is called the kernel of the observable. In the M2M method,  $f(\mathbf{x}, \mathbf{v})$  is approximated by a discrete sample of  $N$  particles with particle weights  $w_i(t)$ . [Equation 5.1](#) is then evaluated by

$$y(t) = \sum_{i=1}^N w_i(t) \times K(\mathbf{x}_i(t), \mathbf{v}_i(t)) \quad (5.2)$$

where  $(\mathbf{x}_i(t), \mathbf{v}_i(t))$  is the phase-space coordinates of particle  $i$  at time  $t$ . In practice  $y(t)$  is often noisy due to the limited number of particles in the model. A convenient way to

significantly reduce the particle noise is to replace the observable  $y(t)$  by the temporally smoothed observable  $\tilde{y}(t)$ , defined as

$$\tilde{y}(t) = \int_{\tau} y(t - \tau) \times e^{-\alpha\tau} d\tau \quad (5.3)$$

where  $\alpha$  sets the temporal smoothing timescale.

The M2M method consist of adjusting the particle weights  $w_i$  in order to maximize a given profit function  $F$ . This is done through a simple gradient descent method where the particle weights evolve with time according to

$$\frac{dw_i}{dt} = \varepsilon w_i \frac{\partial F}{\partial w_i} \quad (5.4)$$

with  $\varepsilon$  a numerical factor that sets the typical timescale of the weight evolution. The profit function  $F$  usually consists of a  $\chi^2$  term that drives the model towards some data plus possibly a regularization term for minimizing the broadening of the weight distribution. After one decades of refinement this modelling technique is now mature and has been used in both extragalactic (e.g. De Lorenzi et al. 2008, 2009; Das et al. 2011; Morganti et al. 2013; Zhu et al. 2014) and Galactic context (e.g. Bissantz, Debattista & Gerhard 2004; Long et al. 2013; Hunt & Kawata 2014; Portail et al. 2015; P16).

### 5.2.2 Modelling the metallicity of stars

In regular M2M modelling  $f$  is simply a function of phase-space. The method can be extended to chemodynamical models by introducing the metallicity dimension  $[\text{Fe}/\text{H}]$  into the phase-space, changing Equation 5.2 into

$$y = \int_{[\text{Fe}/\text{H}]} \int_{\mathbf{x}, \mathbf{v}} K(\mathbf{x}, \mathbf{v}, [\text{Fe}/\text{H}]) f(\mathbf{x}, \mathbf{v}, [\text{Fe}/\text{H}]) d^3\mathbf{x} d^3\mathbf{v} d[\text{Fe}/\text{H}]. \quad (5.5)$$

Several choices can be made in constructing a particle-based representation of  $f(\mathbf{x}, \mathbf{v}, [\text{Fe}/\text{H}])$ . One possibility is to affect a single metallicity value  $[\text{Fe}/\text{H}]_i$  for each particle, and approximate  $f$  as the sum of delta functions  $f(\mathbf{x}, \mathbf{v}, [\text{Fe}/\text{H}]) = \sum_i w_i \times \delta(\mathbf{x} - \mathbf{x}_i) \delta(\mathbf{v} - \mathbf{v}_i) \delta([\text{Fe}/\text{H}] - [\text{Fe}/\text{H}]_i)$ . It is however not straightforward to derive a method for adjusting the single metallicity value of each particle in order to drive the model towards the data. Instead we adopt for each particle a Metallicity Distribution Function (MDF), denoted  $f_{[\text{Fe}/\text{H}],i}$ , and write the distribution function as

$$f(\mathbf{x}, \mathbf{v}, [\text{Fe}/\text{H}]) = \sum_i w_i \times \delta(\mathbf{x} - \mathbf{x}_i) \delta(\mathbf{v} - \mathbf{v}_i) f_{[\text{Fe}/\text{H}],i}([\text{Fe}/\text{H}]). \quad (5.6)$$

We then model  $f_{[\text{Fe}/\text{H}],i}([\text{Fe}/\text{H}])$  as an expansion on some mathematical set of elementary MDFs, common for all particles and thus represent  $f_{[\text{Fe}/\text{H}],i}([\text{Fe}/\text{H}])$  by a discrete set of numbers. The choice of the number and form of the elementary MDFs is limited by both

Table 5.1: Parameters of the four components of the particles MDF used to introduce the metallicity in the M2M modelling, computed from Table 3 of [Ness et al. \(2013a\)](#).

	$\alpha$	$\beta$	$\gamma$	$\delta$
$[\text{Fe}/\text{H}]_X^0$	0.11	-0.28	-0.69	-1.18
$\sigma_X$	0.12	0.13	0.15	0.14

physical and technical constraints. First, as discussed later in [Section 5.3.2](#), stars with different metallicities have different luminosity functions and thus usually have a different probability to be detected by a given survey depending on its selection criteria. The set of elementary MDFs should allow a faithful representation of the full MDF of stars in the Galaxy, and not for example only in a limited metallicity range. Second, the number of parameters used to represent the particles MDFs should be large enough to capture all relevant variations as a function of metallicity shown by the fitted data, but also be as small as possible to avoid degeneracies and computational overhead.

From the ARGOS data, [Ness et al. \(2013a\)](#) showed that the metallicity distribution and its field-to-field variations across the bar region could be well represented by only 5 numbers, representing the varying amplitude of 5 Gaussians with approximately fixed means and dispersions. Hence those Gaussians, denoted  $\alpha$ ,  $\beta$ ,  $\gamma$ ,  $\delta$  and  $\epsilon$  in the order of decreasing metallicity form a suitable set of elementary MDFs for modelling the metallicity distribution of any particle. For efficiency we neglect the Gaussian  $\epsilon$  since it represents only about half a percent of all stars in the ARGOS survey and is thus very poorly constrained by the data. Note that Gaussian components  $\alpha$ - $\delta$  were originally named components A-D in [Ness et al. \(2013a\)](#). We chose here a different naming convention to highlight the difference between the Gaussian components  $\alpha$ - $\delta$ , and the metallicity bins A-D introduced by [Ness et al. \(2013b\)](#) and used later in [Section 5.3](#).

The MDF of each particle is then modeled as

$$f_{[\text{Fe}/\text{H}],i} = \sum_{c \in \alpha-\delta} w_{i,c} \mathcal{G}_{[[\text{Fe}/\text{H}]_c^0, \sigma_c]} \quad (5.7)$$

where  $w_{i,c}$  is the weights of the Gaussian component  $c$  in the MDF of particle  $i$ ,  $[\text{Fe}/\text{H}]_c^0$  and  $\sigma_c$  are the mean and standard deviation of the components and  $\mathcal{G}_{[\mu,\sigma]}$  is the Gaussian distribution of mean  $\mu$  and standard deviation  $\sigma$ . Adopted values for  $[\text{Fe}/\text{H}]_c^0$  and  $\sigma_c$  are quoted in [Table 5.1](#) and correspond to the mean of the values determined by [Ness et al. \(2013a\)](#) (see their Table 3). Note that we do not need to assume that the Gaussian components  $\alpha$  -  $\delta$  are actual physical components of the Galaxy with different origin and history. Their use is purely restricted to a mathematical set of elementary MDFs that allow modelling reasonable particle MDFs with only four numbers per particle.

From the MDF of every particle we can evaluate any metallicity dependent observable  $y$  on the model by

$$y = \sum_i w_i \times \sum_{c \in \alpha-\delta} K_{i,c} w_{i,c} \quad (5.8)$$

where

$$K_{i,c} = \int_{[\text{Fe}/\text{H}]} K(\mathbf{x}_i, \mathbf{v}_i, [\text{Fe}/\text{H}]) \times \mathcal{G}_{[[\text{Fe}/\text{H}]_c^0, \sigma_c]}([\text{Fe}/\text{H}]) d[\text{Fe}/\text{H}]. \quad (5.9)$$

The purpose of the kernel function  $K(\mathbf{x}_i, \mathbf{v}_i, [\text{Fe}/\text{H}])$  is to limit the observable to a given volume in phase-space and apply on the model any observational bias that can exist on the real data the model is compared to. We describe in detail how we model these observational bias for the ARGOS and APOGEE surveys in [Section 5.3](#).

### 5.2.3 M2M fit of the MDF

The M2M adaptation of the particle MDF weights  $w_{i,c}$  is done in a similar fashion as the M2M evolution of the physical weights of the particles. The components weights  $w_{i,c}$  are evolved in the direction of the gradient of the profit function  $F$  according to

$$\frac{dw_{i,c}}{dt} = \varepsilon_c \frac{\partial F}{\partial w_{i,c}} \quad (5.10)$$

where  $\varepsilon_c$  set the strength of the MDF fitting.

As a profit function we adopt a simple chi-square given by

$$F = -\frac{1}{2} \sum_j \left( \frac{y_j - Y_j}{\sigma(Y_j)} \right)^2 \quad (5.11)$$

where the  $y_j$ ,  $Y_j$  and  $\sigma(Y_j)$  are respectively the model observables, the data and its associated errors. The  $w_{i,c}$  are additionally constrained to  $\sum_c w_{i,c} = 1$  for each particle. Note that the weight adaptation described in [Equation 5.10](#) requires some initial values for the particle weights  $w_{i,c}$  to start with, as discussed in more detail in [Section 5.3.1](#). For simplicity, we keep the particle masses  $w_i$  constant throughout the M2M fit and only adapt the particle weights  $w_{i,c}$ . This is justified since our initial model is already a good dynamical model of the entire galactic bar region, as described in the next section.

The M2M fit is performed in three successive phases. First the model observable are initialized by evolving the N-body model for a time  $T_{\text{smooth}}$  and computing the temporally smoothed model observables. Then the model is evolved while adapting the weights  $w_{i,c}$  for a time  $T_{\text{M2M}}$ . Finally the model is relaxed for a time  $T_{\text{relax}}$ , to test the stability of the M2M fit. By using an internal time unit (iu) in which a circular orbit at 4 kpc has an orbital period of unity, we adopt for  $T_{\text{smooth}}$ ,  $T_{\text{M2M}}$  and  $T_{\text{relax}}$  the respective values of 4, 40 and 16 iu. The temporal smoothing timescale is set to  $\alpha = 1 \text{ iu}^{-1}$  and the strength of the MDF fitting to  $\varepsilon_c = 10 \text{ iu}^{-1}$ .

The weight evolution described by [Equation 5.10](#) is performed iteratively by a first-order integration with small time step  $\delta t = 10^{-3} \text{ iu}$ . Between two iterations of the weight adaptation procedure, the N-body model is integrated forward using an adaptive drift-kick-drift leap-frog algorithm. The gravitational potential is computed directly from the particle distribution (stellar and dark matter particles) using the hybrid grid method of

Sellwood & Valluri (1997), modified in P16 for allowing better vertical resolution in the bar region. We assume that the gravitational potential rotates at a constant pattern speed of  $40 \text{ km s}^{-1} \text{ kpc}^{-1}$  corresponding to the pattern speed of the bar in the model of P16 that matches both the BRAVA data in the bulge and the ARGOS data in the bar region.

## 5.3 Dynamical model and data constraints on the MDF

In this section we describe in detail the initial dynamical model used to provide the N-body orbits onto which we fit the particle MDFs in Section 5.3.1 together with the two spectroscopic datasets, the ARGOS survey in Section 5.3.2 and APOGEE surveys in Section 5.3.3. We then describe and compare our fiducial model to the data, and present variational models used to quantify systematic uncertainties.

### 5.3.1 Dynamical model of the galactic bar region

In P16 we presented the first non-parametric dynamical model of the entire bar region. This model reproduces the 3D density of RCGs in the bulge from Wegg & Gerhard (2013), the magnitude distributions of RCGs across the bar region from combination of the VVV, UKIDSS and 2MASS surveys (Wegg, Gerhard & Portail 2015), together with stellar kinematics from the BRAVA, OGLE and ARGOS surveys. Including the kinematics as a function of distance from the ARGOS survey we were able to recover the bar pattern speed and the mass distribution of both stars and dark matter in the inner 5 kpc of the Galaxy, hence constraining the full effective potential in the galactic bar region. We base our work on this model that provides a gravitational potential and a self-consistent library of N-body orbits. note that throughout the chemodynamical M2M fit the particles masses and the gravitational potential in the bar frame are both kept fixed. Figure 4.20 shows the face-on surface density of this model. The bar rotates at  $\Omega = 40 \text{ km s}^{-1} \text{ kpc}^{-1}$ , as required to fit both the BRAVA kinematics in the bulge and the ARGOS radial velocity field in the bar region, and has in the model a half-length of  $5.30 \pm 0.36 \text{ kpc}$ , in good agreement with the determination of bar the half-length in the Milky Way of  $5.0 \pm 0.2 \text{ kpc}$  by Wegg, Gerhard & Portail (2015).

We introduce the metallicity of stars in the dynamical model by specifying for each particle an initial value for the four weights  $w_{i,c}$ . We call these initial weights the “prior” MDF although they do not correspond to a formal Bayesian prior. It is a priori unclear how much the final result of a chemodynamical M2M fitting depends on the assumed prior MDF, as the weights  $w_{i,c}$  are only allowed to change when traveling through a portion of space constrained by the data. Since we focus on the bar region that is well covered by the ARGOS survey, our fiducial choice for the prior MDF is  $w_{i,\alpha} = 0.23$ ,  $w_{i,\beta} = 0.43$ ,  $w_{i,\gamma} = 0.29$  and  $w_{i,\delta} = 0.05$ , fractions that correspond to overall MDF of all the ARGOS stars. We consider alternative priors and quantify their effects on the final results in Section 5.3.4.

The bar is oriented at an angle of  $28^\circ$  to the line of sight towards the Galactic Centre (Wegg, Gerhard & Portail 2015). Following the recommendations of Bland-Hawthorn &

Gerhard (2016) we place the Sun at  $R_0 = 8.2$  kpc and assume that the Local Standard at Rest (LSR) is on a circular orbit at  $V(R_0) = 238$  km s<sup>-1</sup>. We adopt for the peculiar motion of the Sun in the LSR the values of  $(U, V, W) = (11.1, 12.24, 7.25)$  km s<sup>-1</sup> as measured by Schönrich, Binney & Dehnen (2010). Altogether these assumptions lead to a proper motion of the Galactic Centre of  $30.5$  km s<sup>-1</sup> kpc<sup>-1</sup> consistent with the proper motion of SgrA\* of  $30.57 \pm 0.43$  km s<sup>-1</sup> kpc<sup>-1</sup> measured by Reid et al. (2014). All radial velocities quoted in this work are expressed in the Galactocentric inertial frame. We re-transformed the radial velocity measurements of the ARGOS and APOGEE surveys using our set of assumptions since it differ from the traditional transformation used by many spectroscopic surveys. In order to predict the selection function of the surveys and apply them when observing the model we use the PARSEC isochrones (Bressan et al. 2012; Chen et al. 2014; Tang et al. 2014) and assume a 10 Gyr old population for a Kroupa IMF.

### 5.3.2 ARGOS as a function of distance and metallicity

The Abundance and Radial velocity Galactic Origin Survey (ARGOS) is a large spectroscopic survey of about 28000 stars of the galactic bulge and inner disk, designed to sample RCGs all the way from the nearby disk ( $\sim 4.5$  kpc from the Sun) to the far side of the Galactic Centre ( $\sim 13$  kpc from the Sun). The surveys covers lines of sight at longitudes between  $l = -20^\circ$  and  $l = 20^\circ$  and latitudes between  $b = -5^\circ$  and  $-10^\circ$ , as shown in Figure 5.2. The ARGOS stars are selected from the 2MASS catalog according to a procedure fully described in Freeman et al. (2013) for which we modeled the selection function in P16. In brief, the ARGOS selection function consist of (i) a weight for each star and (ii) a function of the extinction corrected magnitude  $C(K_{s0})$  for each field. The set of weights comes from the fact that for each field an equal number of stars were selected in three magnitude bins in order to sample the full range of distance from the nearby disk to the far side of the bulge. The selection function as a function of magnitude represents the probability for a star to pass the various selection criteria of the survey, thus taking into account the magnitudes and color cuts, high-quality imaging criteria and incompleteness of the input catalog that altogether bias the survey towards nearby stars. Details about the modelling of the ARGOS selection function can be found in P16.

From the medium resolution spectra of the ARGOS stars, Ness et al. (2013a) estimated various stellar parameters including the radial velocity and the metallicity with a typical error of  $1$  km s<sup>-1</sup> and  $0.1$  dex respectively. Since the ARGOS stars are primarily RCGs which are approximate standard candles, we can infer accurate stellar distances from their photometry. We adopt an absolute magnitude of  $M_{K_s, \text{RCG}} = -1.72$  as found by Wegg & Gerhard (2013) in the bulge, and bin stars as a function of distance. In P16 we constructed the ARGOS radial velocity field by computing for each survey field the mean velocity and velocity dispersion of the stars in several distance modulus bins of  $0.25$  mag along the line of sight. We adopt here the same distance bins as P16 and since the number of stars per distance bin is typically  $\sim 80 - 100$  in each field, we can bin further in the metallicity space.

Following Ness et al. (2013b) we define four metallicity bins of  $\Delta[\text{Fe}/\text{H}] = 0.5$  dex called

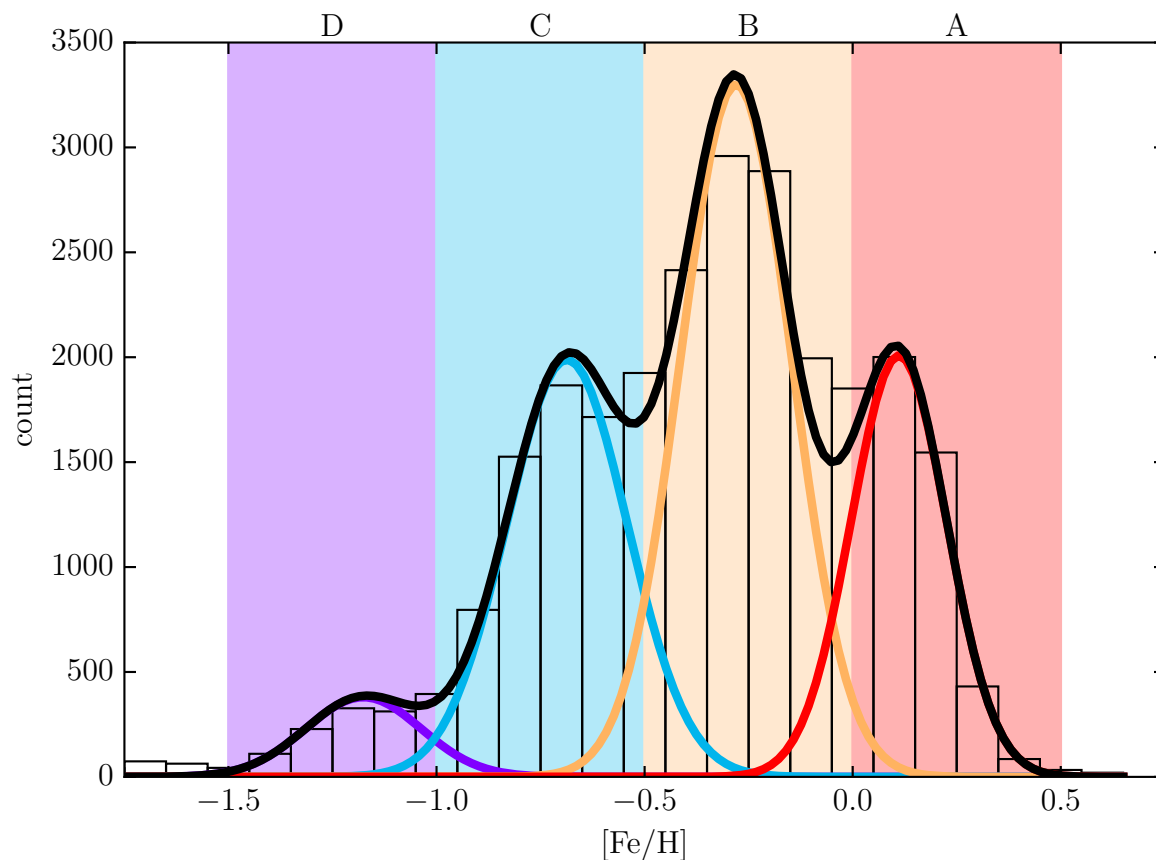


Figure 5.1: Gaussian components  $\alpha - \delta$  vs metallicity bins A-D. The observed example MDF (histogram) is binned in four bins A-D shown by the color bands. From the number count in each band we can compute the four components weights  $w_c$  of the Gaussians  $\alpha - \delta$  (see Table 5.1) that gives the same counts in the same bands (colored solid lines). The resulting MDF (black line) is a very good representation of the underlying histograms and justify our use of the Gaussians as a set of elementary MDFs to model the particle MDFs.

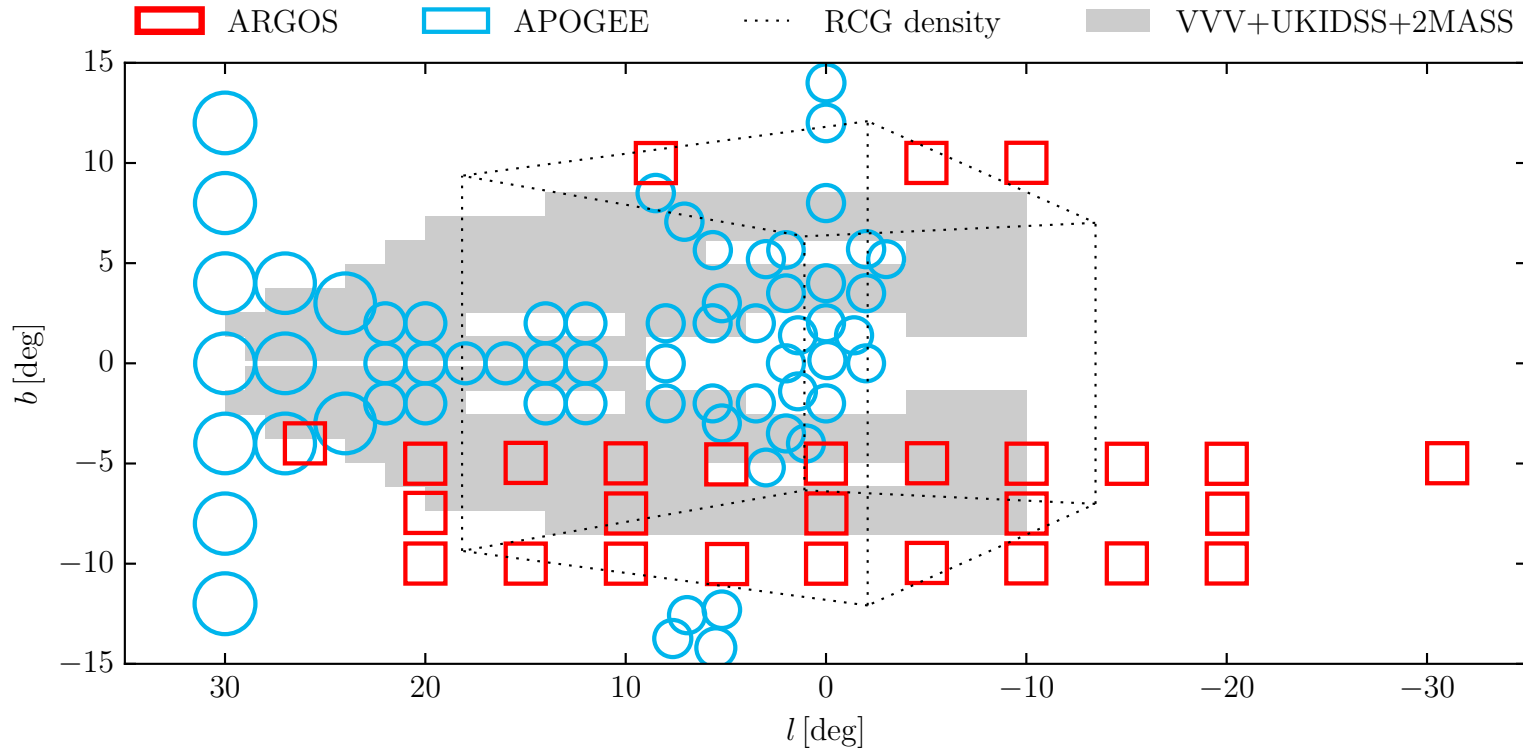


Figure 5.2: Spatial coverage in galactic coordinates of the datasets used to constrain the MDF in the model. Red squares show the ARGOS fields, constraining the three-dimensional spatial and kinematic variations of metallicity (i.e. on the sky and also as a function of line of sight distance, see [Section 5.3.2](#)). Blue circles show the APOGEE fields, constraining the spatial and kinematic variations of metallicity integrated along the line of sight ([Section 5.3.3](#)). The dashed box and grey regions show the coverage of the 3D density of RCGs in the bulge and the magnitude distributions of RCGs from VVV + UKIDSS + 2MASS used in P16 to constrain the dynamical model.



A-D ranging from  $0.5 \geq [\text{Fe}/\text{H}] > 0$  (A),  $0 \geq [\text{Fe}/\text{H}] > -0.5$  (B),  $-0.5 \geq [\text{Fe}/\text{H}] > -1$  (C) and  $-1 \geq [\text{Fe}/\text{H}] > -1.5$  (D). Binning the stars has the advantage of avoiding correlations between data points and is therefore better suited to the  $\chi^2$  minimization of the M2M method. Figure 5.1 highlights the difference between the metallicity components  $\alpha - \delta$  introduced in Section 5.2.2 and the metallicity bins introduced here. The histogram shows a typical MDF observed in a field towards the bulge. By binning the stars in the four bins A-D we obtain a low resolution version of the MDF. However, this low resolution MDF is not a faithful representation of the real underlying MDF, which for example has many more stars close to the lower end of the bin than close to the higher end in bin A. A more faithful representation of the MDF is obtained using the set of elementary MDFs  $\alpha - \delta$ . From the counts in the four bins A-D we search for the four weights  $w_c$  of the Gaussian components  $\alpha - \delta$  that have the same counts in the same bins. Summing up the Gaussian components we obtain a MDF, constructed from 4 numbers only, that is a very good representation of the underlying histogram. The relation between the count in bins A-D and the components weights is given by a  $4 \times 4$  matrix that is mostly diagonal.

For a field indexed by  $j$ , distance bin indexed by  $d$  and metallicity bin  $m$  we compute the following three quantities

1. The fraction  $f_{j,d,m}$ , of the observed stars in distance bin  $d$  of field  $j$  that have metallicities within bin  $m$
2. Mean velocity  $v_{j,d,m}$  of the stars considered above
3. Velocity dispersion  $\sigma_{j,d,m}$  of the stars considered above

Errors of  $f_{j,d,m}$ ,  $v_{j,d,m}$  and  $\sigma_{j,d,m}$  are computed from 1000 bootstrap resampling, and bins with less than 10 stars are excluded from further consideration, to avoid underestimate of the dispersion potentially arising from low number statistics. In some fields and metallicity bins there are not enough stars in the ARGOS sample to also bin in distance. Hence for each field  $j$  and metallicity bin  $m$  we also compute the three similar quantities noted  $f_{j,m}$ ,  $v_{j,m}$  and  $\sigma_{j,m}$  corresponding to the fraction, mean velocity and velocity dispersion of stars integrated along the line of sight.  $f_{j,d,m}$ ,  $v_{j,d,m}$  and  $\sigma_{j,d,m}$  are shown respectively in Figures 5.4, 5.5 and 5.6 together with our fiducial chemodynamical model described in Section 5.3.4.

In order to compare the model to the data we need to form model observables that are the model equivalent quantities of  $f_{j,d,m}$ ,  $v_{j,d,m}$  and  $\sigma_{j,d,m}$ . We do so we first turn the model particles into mock stars, then apply the ARGOS selection function and finally reproduce the procedure of estimating the distance of an observed star assuming it is a RCG. This procedure is described in detail in P16 and will only be outlined here. For a given particle, we simulate a mock stellar population and use the isochrones in combination with the selection function to predict the magnitude distribution of ARGOS mock stars, i.e. RCGs on top of a background of giant stars. We then apply the distance estimation based on the RCG magnitude as we do for the ARGOS stars and simulate an inferred distribution of distance of the particle. This distribution called  $f_i(\mu)$  in P16 encloses

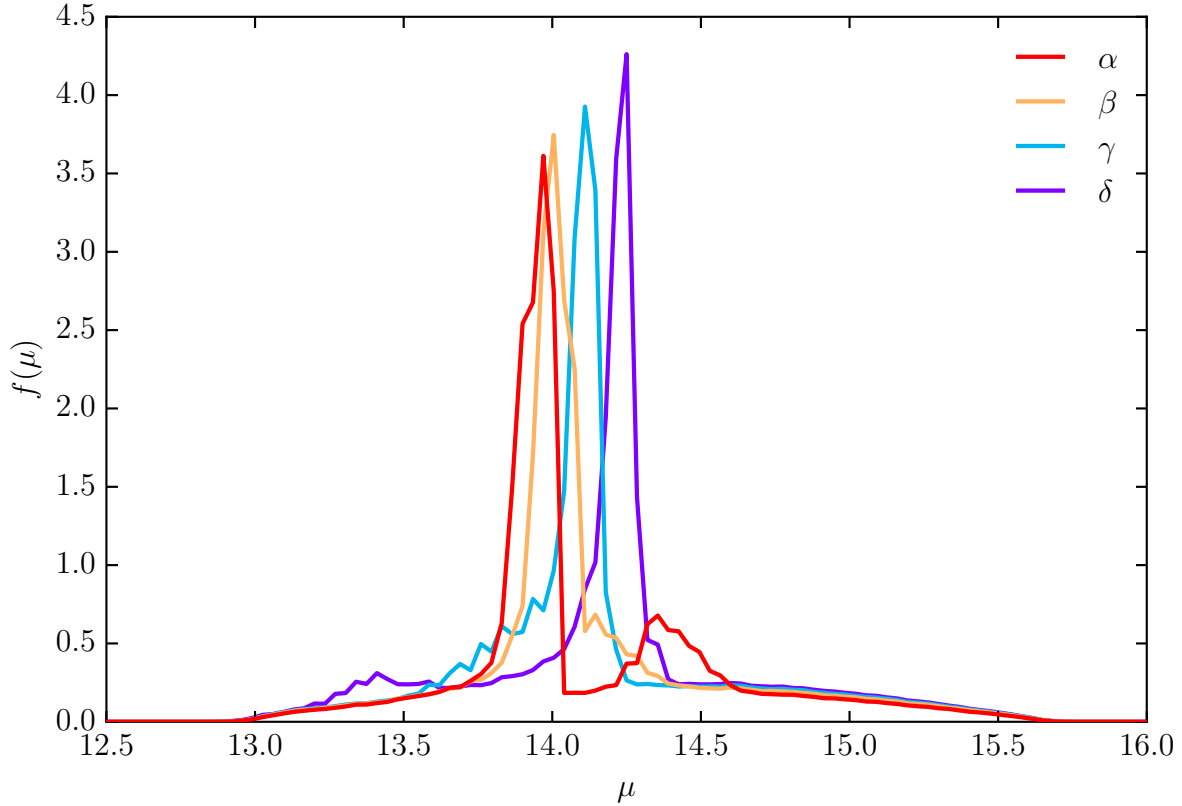


Figure 5.3: Distribution of observed distances for mocks stars drawn a particle at distance modulus  $\mu = 14.0$  for the metallicity distributions of the Gaussian components  $\alpha - \delta$ . Metal-rich RCGs are typically brighter than more metal-poor stars RCGs and appear therefore closer.

all selection and stellar population effects but do not depend on metallicity. Here we extend  $f_i(\mu)$  to  $f_i(\mu, [\text{Fe}/\text{H}])$  taking into account the fact that the luminosity function of different metallicities is slightly different: more metal-rich RCGs are brighter than more metal-poor RCGs. The effect of metallicity is illustrated in Figure 5.3 where we show the inferred distance distributions of a particle at  $\mu = 14.0$  for different metallicity distributions corresponding to the four elementary MDF components  $\alpha - \delta$ . More metal-rich stars appear at closer distances than more metal-poor stars.

We finally define our NMAGIC kernel observables to be used in Equation 5.9 as the number count and first and second mass weighted velocity moments given by the following equations for a field  $j$ , a distance bin  $d$  and a metallicity bin  $m$ .

$$K_{j,d,m}^{\text{ARGOS},0}(\mathbf{z}_i) = \delta_{j,d,m}^{\text{ARGOS}}(\mathbf{z}_i) \quad (5.12)$$

$$K_{j,d,m}^{\text{ARGOS},1}(\mathbf{z}_i) = \frac{\delta_{j,d,m}^{\text{ARGOS}}(\mathbf{z}_i)}{W_{j,d,m}^{\text{ARGOS}}} \times v_i \quad (5.13)$$

and

$$K_{j,d,m}^{\text{ARGOS},2}(\mathbf{z}_i) = \frac{\delta_{j,d,m}^{\text{ARGOS}}(\mathbf{z}_i)}{W_{j,d,m}^{\text{ARGOS}}} \times v_i^2 \quad (5.14)$$

where  $\mathbf{z}_i$  is the extended phase-space vector of particle  $i$  and  $v_i$  its radial velocity.  $W_{j,d,m}^{\text{ARGOS}}$  is given by

$$W_{j,d,m}^{\text{ARGOS}} = \sum_i w_i \delta_{j,d,m}^{\text{ARGOS}}(\mathbf{z}_i) \quad (5.15)$$

and  $\delta_{j,d,m}^{\text{ARGOS}}(\mathbf{z}_i)$  by

$$\delta_{j,d,m}^{\text{ARGOS}} = \begin{cases} \int_{\mu^{(d)}}^{\mu^{(d+1)}} f_i(\mu, [\text{Fe}/\text{H}]) d\mu & \text{if } i \in \text{field } j \\ & \text{and } [\text{Fe}/\text{H}] \text{ in bin } m, \\ 0 & \text{otherwise} \end{cases} \quad (5.16)$$

with  $\mu^{(d)}$  and  $\mu^{(d+1)}$  the boundaries of the distance modulus bin  $d$ . NMAGIC kernels for data integrated along the line of sight are defined in a similar way.

### 5.3.3 APOGEE as a function of metallicity

The Apache Point Observatory Galactic Evolution Experiment (APOGEE) is a high resolution spectroscopic survey designed to sample a large number of stars ( $\sim 1.5 \times 10^5$ ) in all possible galactic environments, from the stellar halo to the disk and the bulge (Eisenstein et al. 2011; Majewski 2012). APOGEE operates in the near-infrared and is therefore able to pierce through highly dust obscured regions. Among the  $\sim 1.5 \times 10^5$  stars about  $10^4$  are located in fields towards the bulge and long bar, some of which are directly in the galactic plane. We thus use APOGEE to complement ARGOS in the galactic plane, in the fields shown in Figure 5.2. We use the stellar parameters and spectroscopic distances of stars in the APOGEE bulge and bar fields determined by Ness et al. (2016) from the publicly available spectra of DR12 using the machine learning method *The Cannon* (Ness et al. 2015). The APOGEE bar and bulge fields do not contain enough stars for binning both in distance and metallicity. We thus consider for each field only a single distance bin ranging from 4 kpc to 12 kpc from the Sun and bin the stars in the four metallicity bins A-D. As in Section 5.3.2 we construct for each APOGEE field the quantities  $f_{j,m}$ ,  $v_{j,m}$  and  $\sigma_{j,m}$  corresponding to the fraction, mean velocity and dispersion of the observed stars of field  $j$  that have metallicities within bin  $m$ .

The APOGEE survey is targeted at bright red giants selected from the 2MASS catalogue according to a complex procedure fully described in Zasowski et al. (2013). To fairly compare the model to the APOGEE data we need to model the distance and metallicity biases introduced by the APOGEE selection criteria. Luckily Bovy (2016) and Bovy et al. (2016a) computed and made available the APOGEE selection function for any kind of tracer stellar population. Assuming a 10 Gyr old population and a Kroupa IMF we compute for each field the fraction of stars selected in the APOGEE survey as a function of distance and metallicity. This provides us directly with the function  $f_i(\mu, [\text{Fe}/\text{H}])$  already

used to define the ARGOS kernels in Equation 5.16. Hence our APOGEE kernels are basically the same as Equation 5.16 with the exception that we have only one large bin in distance covering all the way from 4 kpc to 12 kpc along the line of sight.  $f_{j,m}$ ,  $v_{j,m}$  and  $\sigma_{j,m}$  are shown respectively in Figures 5.7, 5.8 and 5.9 together with our fiducial M2M chemodynamical model described in the next subsection.

### 5.3.4 Fiducial and variation models

Our fiducial model is obtained by fitting the best fitting dynamical model of P16 to the ARGOS and APOGEE data using the M2M chemodynamical method described in Section 5.2.

Figures 5.4, 5.5 and 5.6 show respectively the comparison between our fiducial model and the ARGOS data for the fraction of stars in each metallicity and distance bin  $f_{j,d,m}$ , their mean radial velocity  $v_{j,d,m}$  and radial velocity dispersion  $\sigma_{j,d,m}$ . The distance distribution of the metallicity bins B and C are remarkably well fitted. Our model slightly overpredicts A in the central field along the minor axis at  $b = -5^\circ$ , which is also the field most affected by selection effects. The kinematics is also well fitted and reproduces the main trends as a function of metallicity already described by Ness et al. (2013b): B is a hotter and slightly faster replica of A while C and D are hotter and slower than both B and A at  $|b| = 5^\circ$ . We note however that the model systematically overpredicts the dispersion of the very cold metallicity bin A by about  $10 \text{ km s}^{-1}$ .

Similarly, Figures 5.7, 5.8 and 5.9 show respectively the comparison of our model with the fraction  $f_{j,m}$ , mean radial velocity  $v_{j,m}$  and radial velocity dispersion  $\sigma_{j,m}$  as computed from the APOGEE data. In all metallicity bins the model performs reasonably well at reproducing the data. We note however in metallicity bin A that the model tends to systematically underpredict the fraction of stars, opposite trend to the one found in the ARGOS data. This disagreement here is probably due to a slight inconsistency between the two datasets, possibly originating from systematic effects in the selection function or from a difference in the upper end of the metallicity scales in ARGOS and APOGEE.

Our fiducial model is based on modelling assumptions whose effects need to be quantified before analyzing the spatial and kinematic distribution of the different metallicity components in the inner Galaxy. To this end we repeated the modelling for five alternative models with different assumptions as described below:

- (i) and (ii) As already mentioned in Section 5.3.1, part of the Galaxy is not constrained by our datasets and therefore the model partly depends on the prior MDF distribution assumed. We thus consider two variations of the prior distribution, the first corresponding to “flat-priors” where we initialize all  $w_{i,c}$  to 0.25 and a second more complex corresponding for each particle to the values determined from the MDF at the position of the particle in the Besançon Galaxy Model (Robin et al. 2003).
- (iii) The APOGEE sample is subject to a severe metallicity bias in the inner Galaxy, as discussed in the appendix of Hayden et al. (2015) and shown very clearly in Fig.

2 of [Ness et al. \(2016\)](#). Only few stars in the APOGEE fields towards the bulge are actually in the bulge, and those are preferentially metal-poor stars. This bias against metal-rich stars is already modeled by the APOGEE selection function but is also somewhat uncertain since it relies on stellar population models and assumptions about the IMF and age of the stellar population in the inner part of the Galaxy. [Hayden et al. \(2015\)](#) showed that this bias could be reduced by removing from the sample all stars with  $\log g \leq 1$  dex. We thus repeat the fitting using this cut in surface gravity and modify the selection function accordingly.

**(iv) and (v)** When using APOGEE in combination with ARGOS we might expect a systematic difference in the metallicity scales of the two surveys. Such differences in scale are always present between different spectroscopic surveys and [Smiljanic et al. \(2014\)](#) showed that even when analyzing the exact same spectra, different working groups would measure  $[\text{Fe}/\text{H}]$  with systematic variations of  $\sim 0.1$  dex. There are not enough stars in common between ARGOS and APOGEE to empirically derive a relation between the two metallicity scales. Thus we limit ourself to the first order and consider two alternative APOGEE datasets where values for  $[\text{Fe}/\text{H}]$  are offsets by  $\pm 0.1$  dex.

In all the following we will use the standard deviation of the results provided by the fiducial model plus its five variations as a measure of the systematic uncertainty affecting our results.

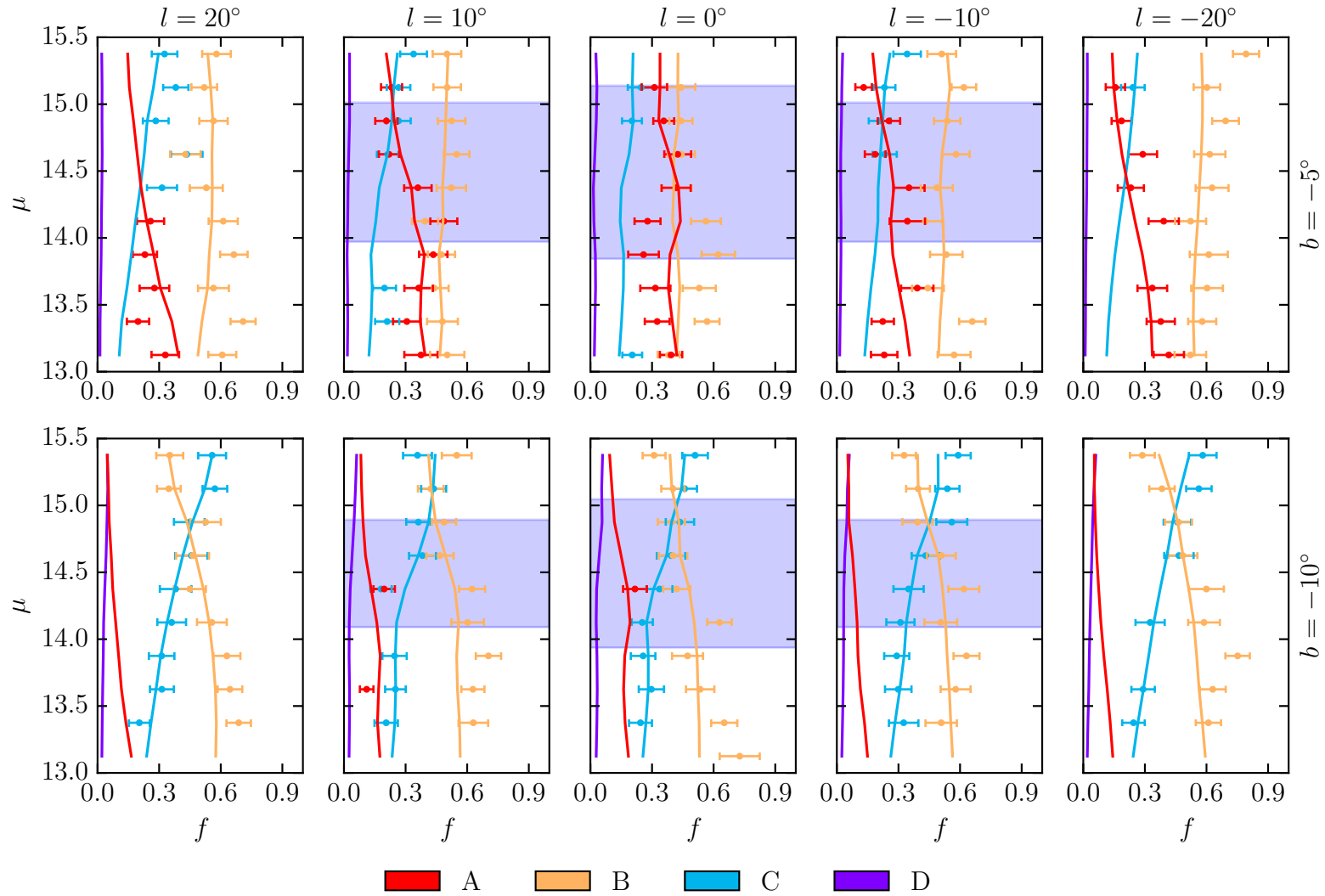


Figure 5.4: Fraction of each metallicity bin as a function of distance modulus for our fiducial model, compared to the ARGOS data. The first (second) row shows fields at  $b = -5^\circ$  ( $b = -10^\circ$ ) for  $l$  between  $20^\circ$  and  $-20^\circ$ , thus covering the bar region. The shaded area indicates the boundary of the volume within 2.5 kpc from the Galactic Centre.

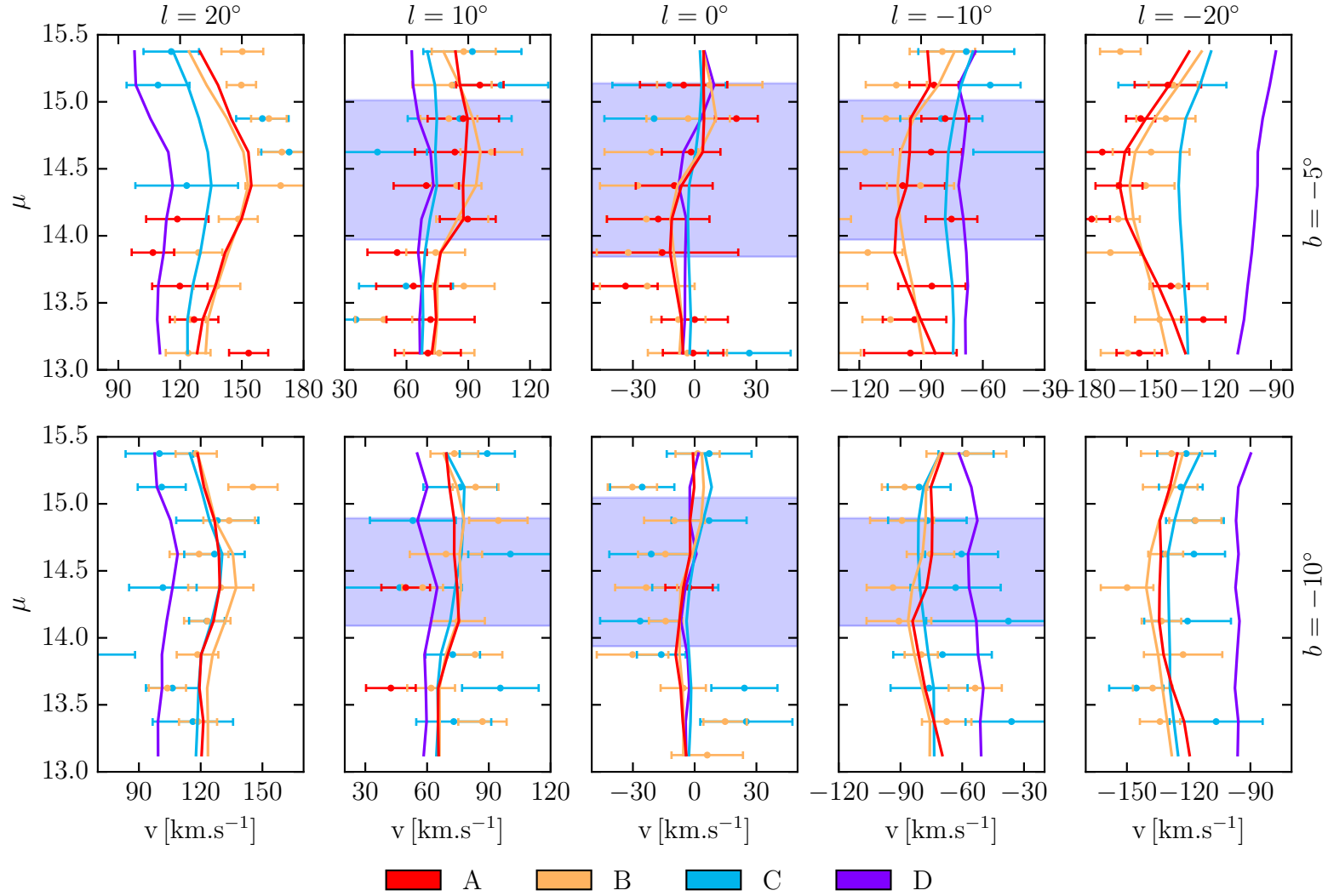


Figure 5.5: Mean radial velocity as a function of distance modulus for the four metallicity bins, compared to the ARGOS data. The first (second) row shows fields at  $b = -5^\circ$  ( $b = -10^\circ$ ) for  $l$  between  $20^\circ$  and  $-20^\circ$ , thus covering the bar region. The shaded area indicates the boundary of the volume within 2.5 kpc from the Galactic Centre.

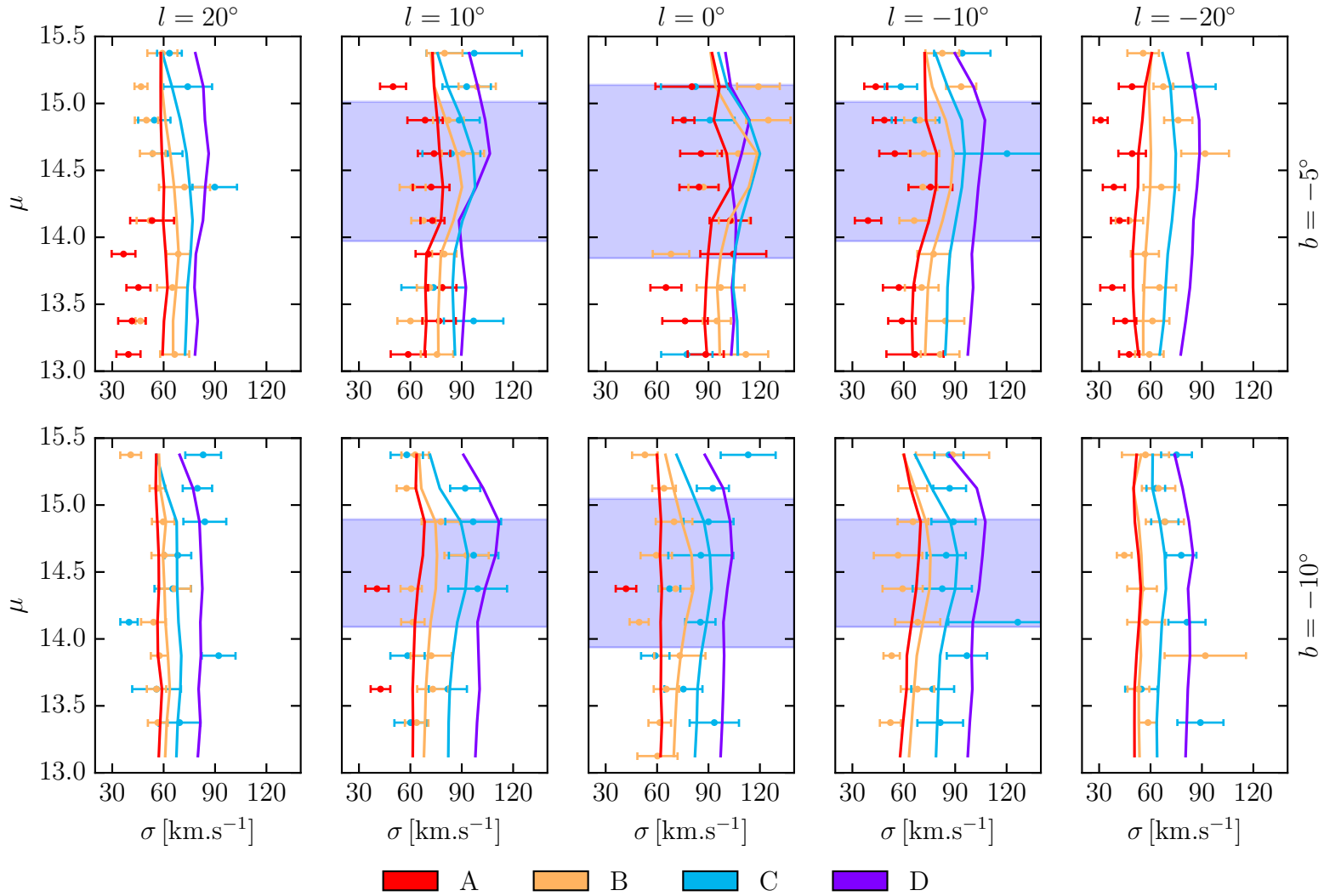


Figure 5.6: Radial velocity dispersion as a function of distance modulus for the four metallicity bins, compared to the ARGOS data. The first (second) row shows fields at  $b = -5^\circ$  ( $b = -10^\circ$ ) for  $l$  between  $20^\circ$  and  $-20^\circ$ , thus covering the bar region. The shaded area indicates the boundary of the volume within 2.5 kpc from the Galactic Centre.



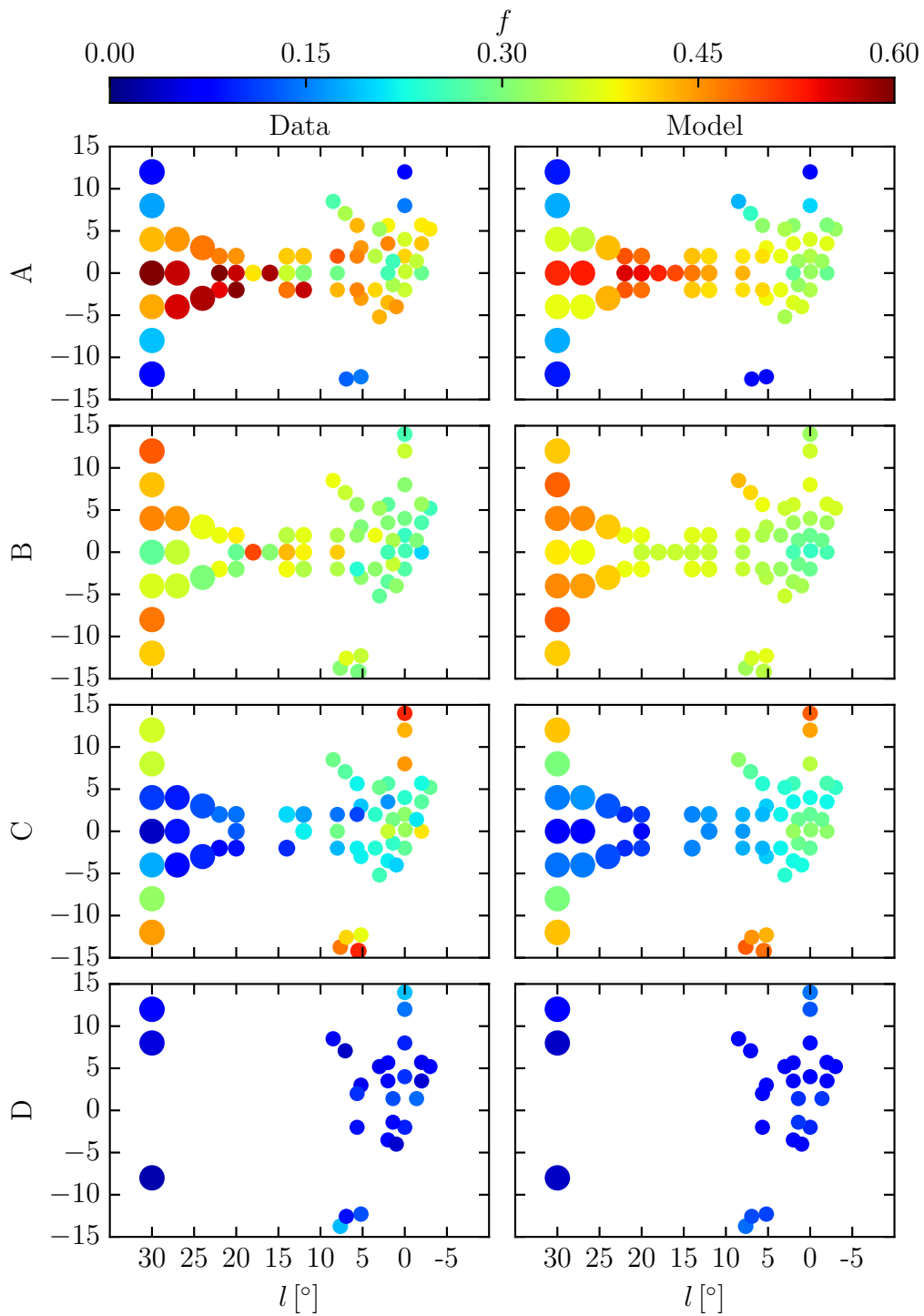


Figure 5.7: Comparison in galactic coordinates between the fraction of stars in the four metallicity bins (rows) in the APOGEE data (left column) and in the model (right column).

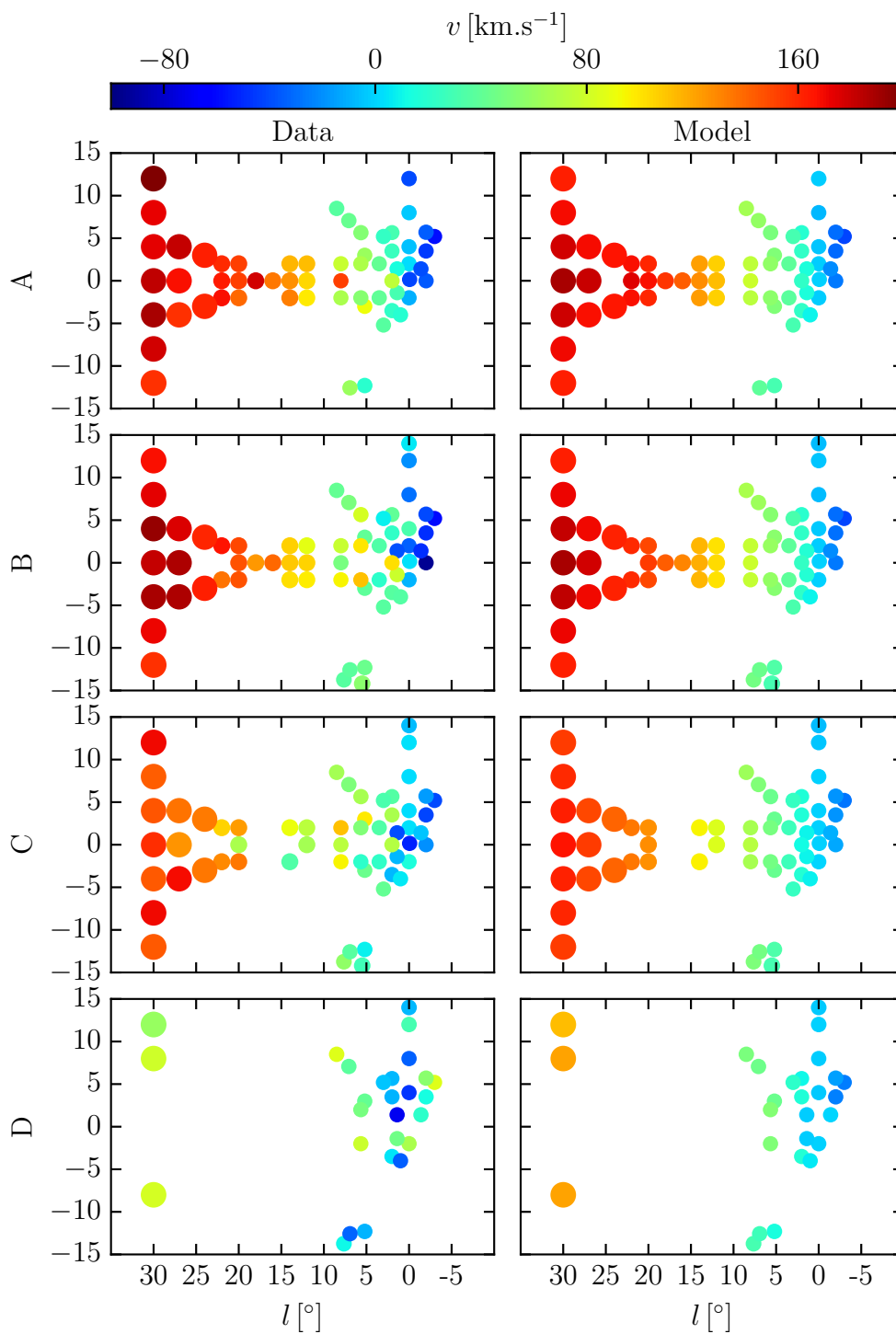


Figure 5.8: Comparison in galactic coordinates between the mean radial velocity of stars in the four metallicity bins (rows) in the APOGEE data (left column) and in the model (right column).

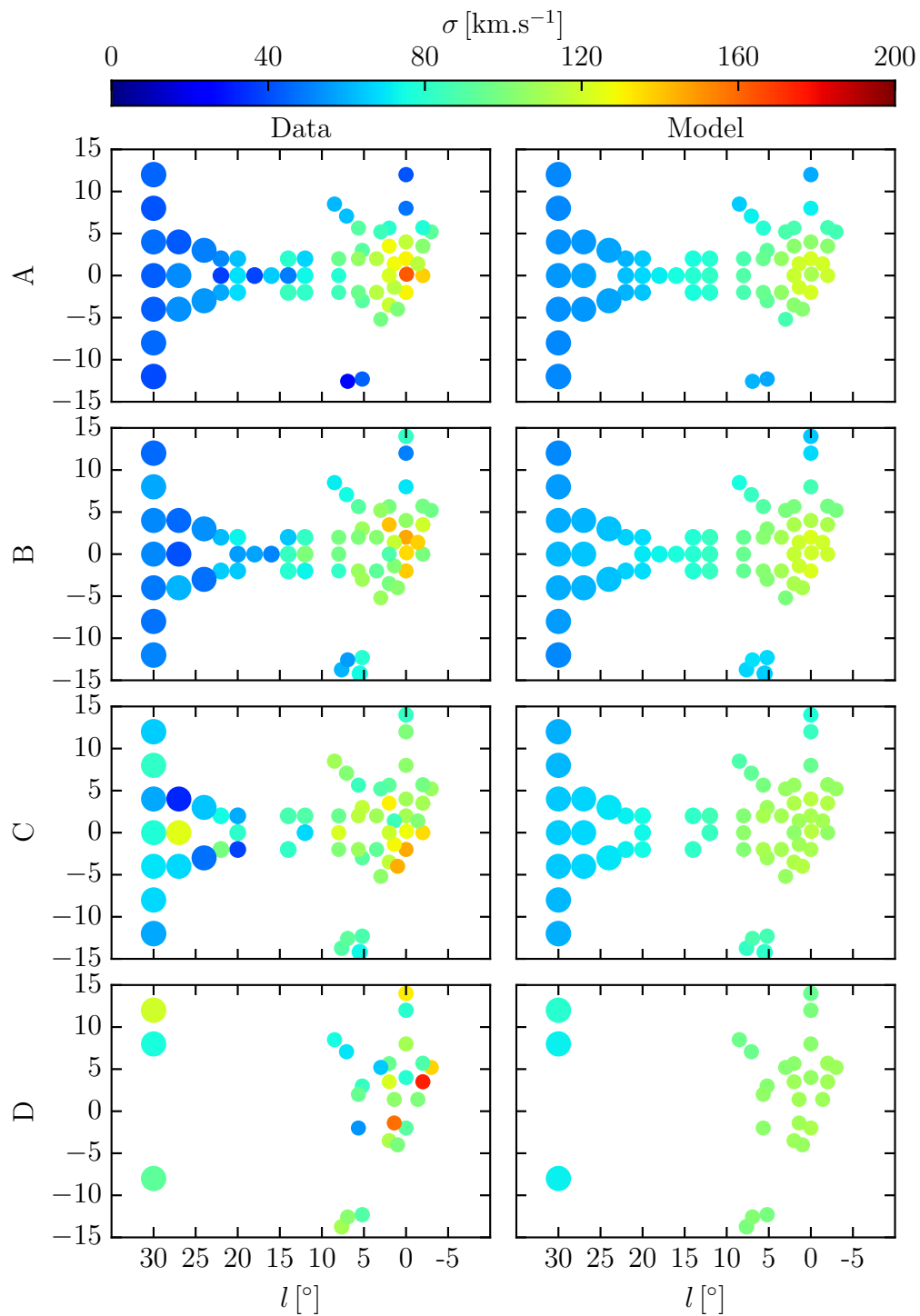


Figure 5.9: Comparison in galactic coordinates between the radial velocity dispersion of stars in the four metallicity bins (rows) in the APOGEE data (left column) and in the model (right column).

## 5.4 Spatial distribution of the metallicity in the inner Galaxy

In this section we show how stars in the four ARGOS metallicity bins are spatially distributed in the Galaxy. To recall, the metallicity bins A, B, C and D correspond respectively to  $0.5 \geq [\text{Fe}/\text{H}] > 0$  (A),  $0 \geq [\text{Fe}/\text{H}] > -0.5$  (B),  $-0.5 \geq [\text{Fe}/\text{H}] > -1$  (C) and  $-1 \geq [\text{Fe}/\text{H}] > -1.5$  (D).

### 5.4.1 The 3D distribution of metallicity

The surface density in face-on and side-on projections of our fiducial model in the four metallicity bins A-D are shown in [Figure 5.10](#). White regions indicate parts of the Galaxy where the systematic uncertainties are larger than 10%. The component A appears to be concentrated to the plane and is strongly bar shaped. The hammer-like shape of the bar ends is similar to the shape of the superthin bar component, discovered in the VVV + UKIDSS + 2MASS data by [Wegg, Gerhard & Portail \(2015\)](#). This hammer-shape is confined to the plane and although being very clear in the midplane density, it is usually absent in the total surface density because of the mass distribution above and below the plane (see [Figure 4.20](#) for example). We thus speculate that the superthin component is significantly metal-rich. The component B is also strongly bar shaped but is less concentrated to the plane and does not contain a significant fraction of the superthin bar component. In addition, A and B both have a B/P shape in the bulge, as already claimed by [Ness et al. \(2012\)](#).

C and D are much more extended vertically, are both slightly bar shaped, but do not show any significant B/P shape in the bulge. They represent only a small fraction of stars in the plane and are therefore more uncertain there. From its side-on projection in [Figure 5.10](#), C is found to have a vertical flattening of  $\sim 0.3$ , making it more likely to be associated to a thick disk rather than an old classical spheroid. D is quite poorly constrained by our data ( $\sim 5\%$  of the ARGOS stars) and appears only at heights  $\geq 1$  kpc.

Another perspective at the spatial distribution of the different metallicities in the Galaxy is given in the galactic coordinates projections of [Figure 5.11](#). C and D have only slightly asymmetric projections in galactic coordinates, indicating that they do not significantly support the B/P shape. B is found to be very similar to a thicker replica of A. Finally, we provide in [Figure 5.12](#) an axisymmetric average of the 3D density of each component, shown in the meridional plane. This figure better highlights the internal vertical structure and clearly shows the gradual thickening of the components with decreasing metallicities. Note that in this figure, the peanut-like contours seen in components C and D are not associated with the peanut shape of the bulge but instead arise from the axisymmetric average of slightly barred densities.

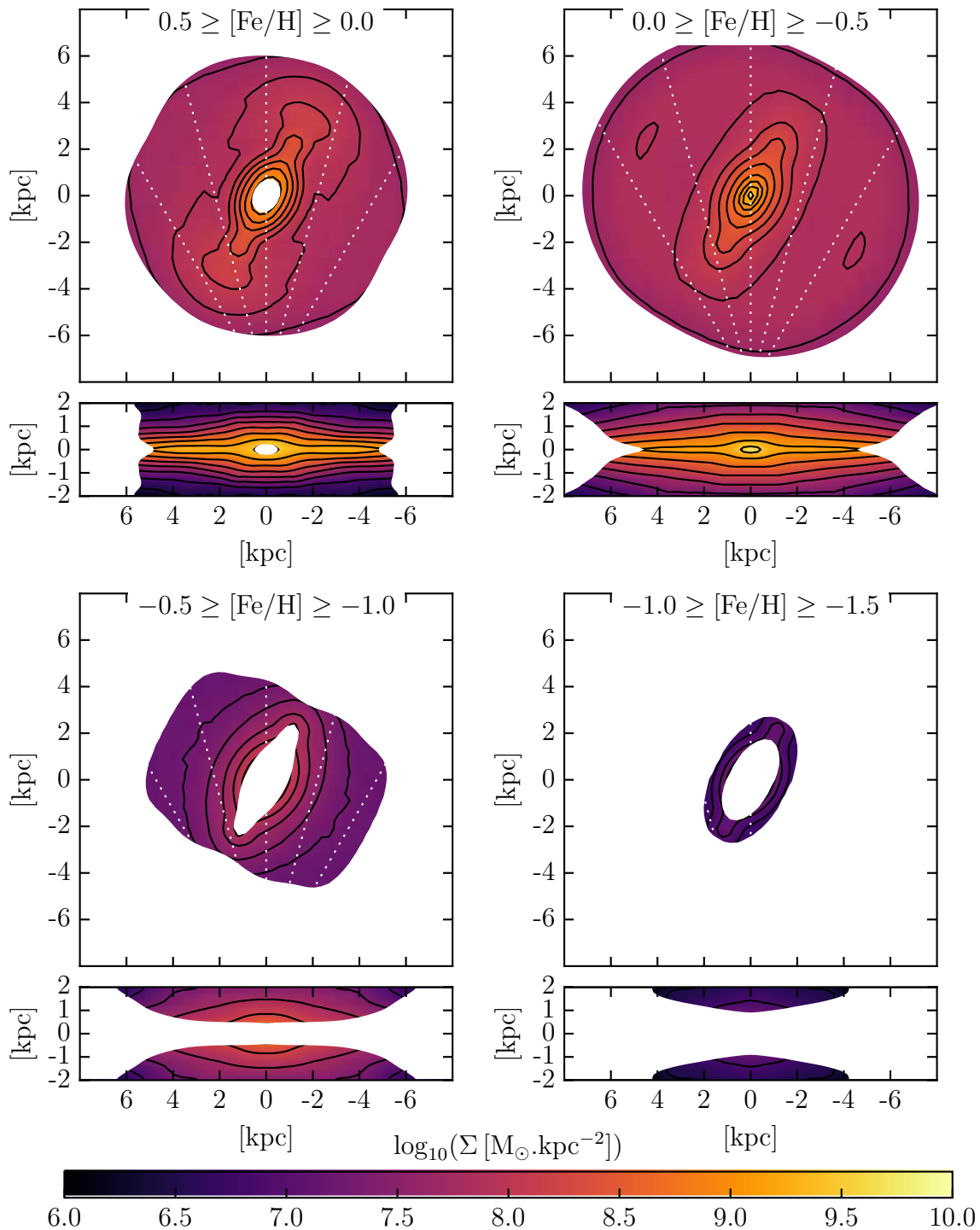


Figure 5.10: Face-on and side-on surface densities of the fiducial model in the four metallicity bins obtained after fitting the ARGOS and APOGEE metallicity data. Regions where systematic uncertainties are larger than 10% are masked.

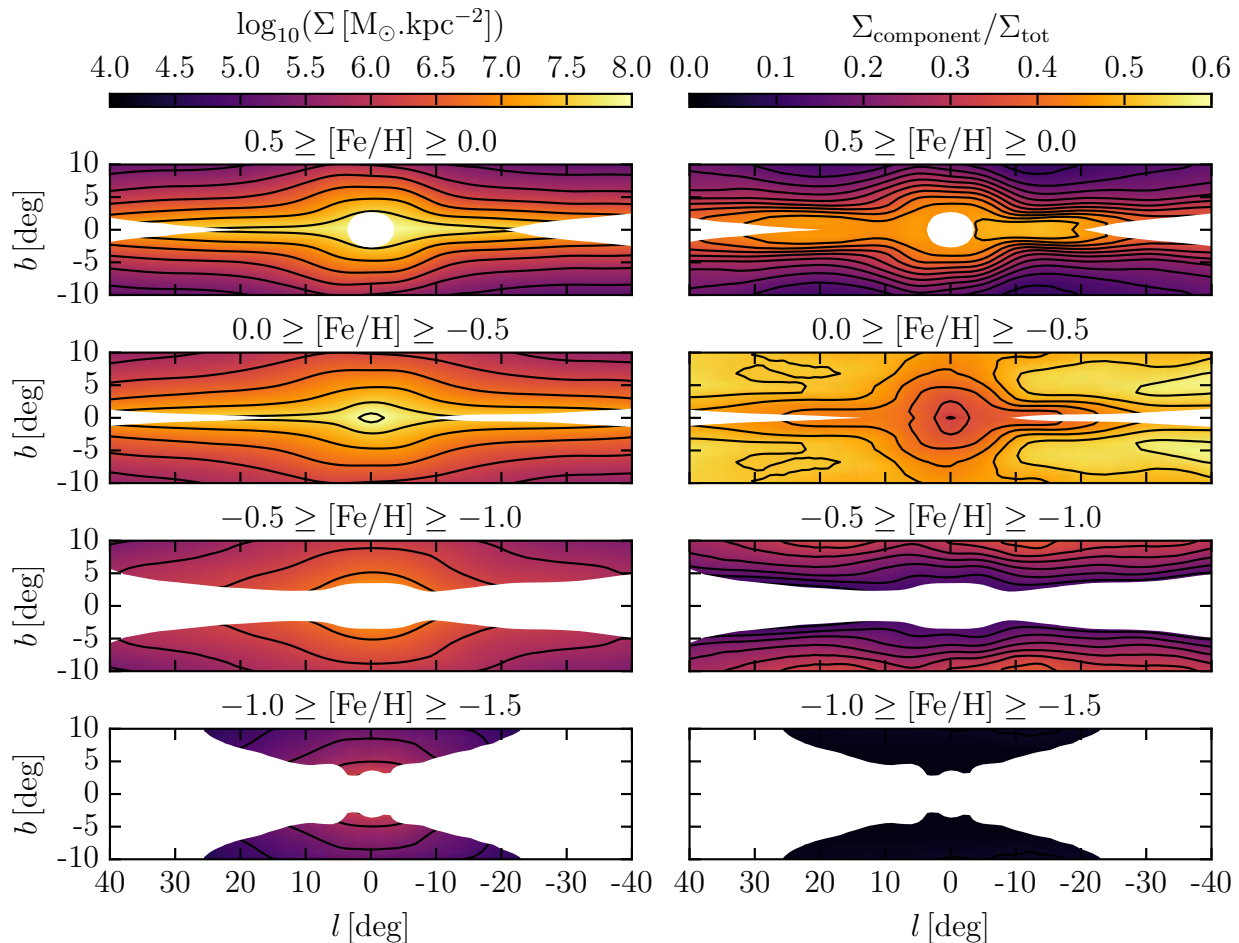


Figure 5.11: Left column: projections in galactic coordinates of the surface density of the fiducial model in the four metallicity bins obtained after fitting the ARGOS and APOGEE metallicity data. Right column: fractional surface density of each metallicity bin. Regions where systematic uncertainties are larger than 10% are masked.

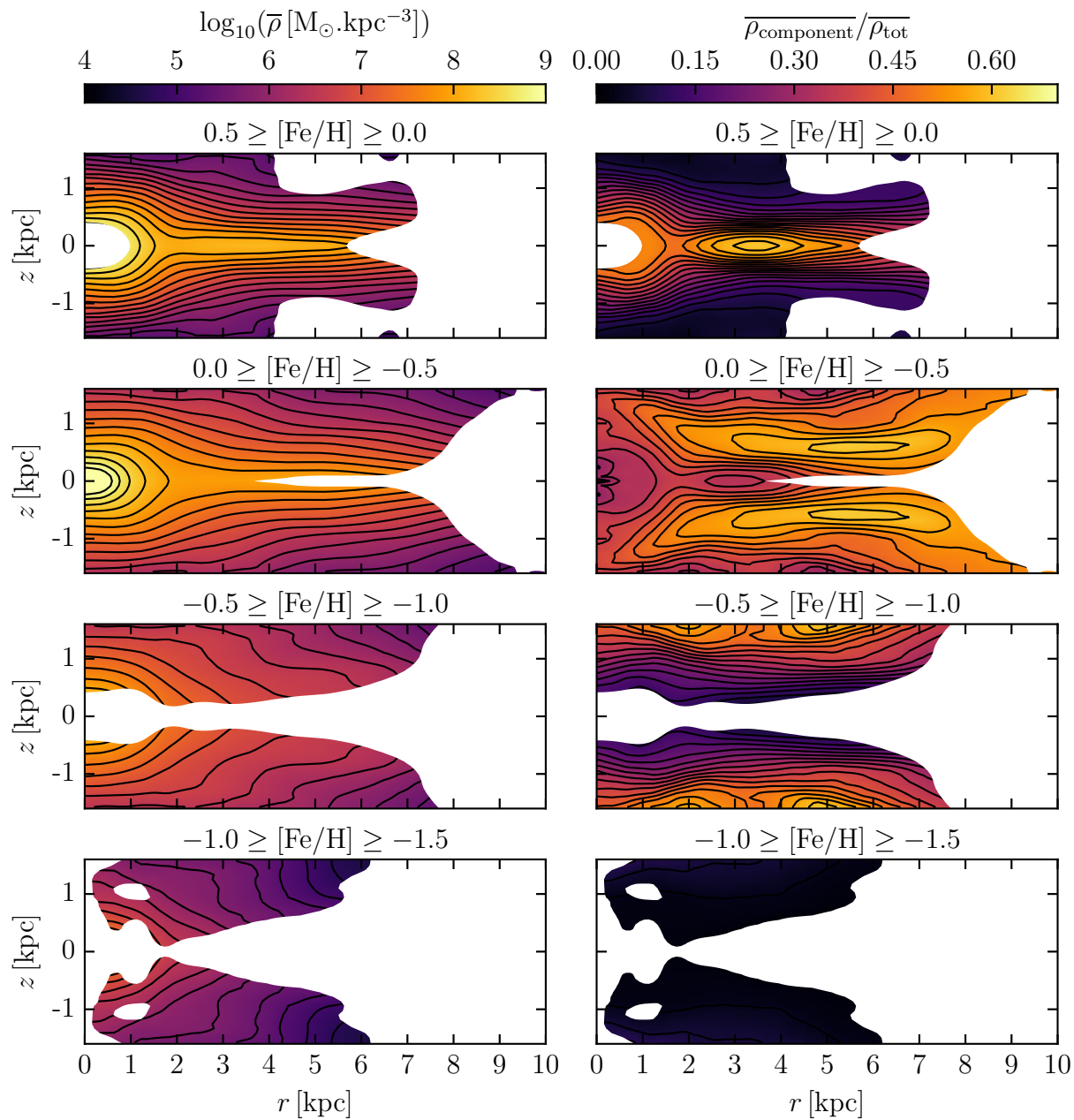


Figure 5.12: Left column: azimuthally averaged density of the fiducial model in the four metallicity bins obtained after fitting the ARGOS and APOGEE metallicity data. Right column: fractional azimuthally averaged density of each metallicity bin. Regions where systematic uncertainties are larger than 10% are masked.

### 5.4.2 Metallicity gradients in the bar region

The presence of a vertical metallicity gradient along the minor axis of the galactic bulge was first reported by [Minniti et al. \(1995\)](#). They derived the metallicity of many K giants at 1.5 – 1.7 kpc from the galactic plane and, by comparing to previous metallicity measurements in Baade’s window, concluded the presence of a vertical gradient estimated to  $-0.35 \text{ dex. kpc}^{-1}$ . Later studies confirmed the presence of a gradient although its magnitude has a large scatter in the literature. [Zoccali et al. \(2008\)](#) observed a gradient of  $-0.6 \text{ dex. kpc}^{-1}$  from bulge K giants between  $b = -4^\circ$  and  $b = -6^\circ$ , while [Ness et al. \(2013a\)](#) finds a gradient of  $-0.45 \text{ dex. kpc}^{-1}$  from 2000 ARGOS stars between  $b = -5^\circ$  and  $b = -10^\circ$ . In addition [Rich et al. \(2007\)](#) found evidence for a flattening of the metallicity gradient between  $b = -1^\circ$  and  $b = -4^\circ$ . This flattening is also well recovered by the first continuous metallicity maps of the bulge by [Gonzalez et al. \(2011b\)](#) and [Gonzalez et al. \(2013\)](#) who derived photometric metallicities of red giants across the entire bulge from 2MASS and VVV, finding an overall gradient of  $-0.28 \text{ dex. kpc}^{-1}$  for latitudes between  $b = -2^\circ$  and  $b = -10^\circ$ .

In [Figure 5.13](#) we show maps the mean metallicity and metallicity dispersion of our fiducial model in both galactic projection and azimuthal averaged on the meridional plane. In the plane for  $|b| < 5^\circ$ , the mean metallicity of the model is quite uncertain since in addition of having a broad MDF with a dispersion of  $\sim 0.35 \text{ dex}$ , it is only constrained by the APOGEE data which struggles to reach the bulge. Above or below  $5^\circ$  the presence of a vertical gradient in the central region is very clear. Along the minor axis of the bulge, including only stars between 6 kpc and 10 kpc along the line of sight, we find a vertical gradient of the mean metallicity in the bulge between  $|b| = 5^\circ$  and  $|b| = 10^\circ$  of  $-0.42 \pm 0.03 \text{ dex. kpc}^{-1}$ , in good agreement with values from [Ness et al. \(2013a\)](#). This gradient is however slightly larger than the photometric gradient measured by [Gonzalez et al. \(2013\)](#) although the latitude range in the latter study includes part of the strip at  $|b| \leq 4^\circ$  where the metallicity gradient flattens. Note that the gradient of the median metallicity differs from that of the mean, being for our fiducial model only  $-0.30 \pm 0.02 \text{ dex. kpc}^{-1}$  in the bulge.

The shape of the B/P bulge is also visible at all heights in [Figure 5.13](#), supporting the idea that the vertical metallicity gradient in the bulge is actually produced by a change in the relative amplitude between the two main metal-rich components A and B forming the B/P bulge, rather than a gradual change in the relative amplitude of a unique metal-rich bulge (A & B together) to a more metal-poor surrounding (C & D together). Outside the bulge, the mean metallicity only slowly changes with radius, with slight signs of flaring for galactocentric distances larger than 3 – 4 kpc, as also found by [Bovy \(2016\)](#) who showed from APOGEE RCGs that the scale height of more metal-poor stars increases with increasing radius.



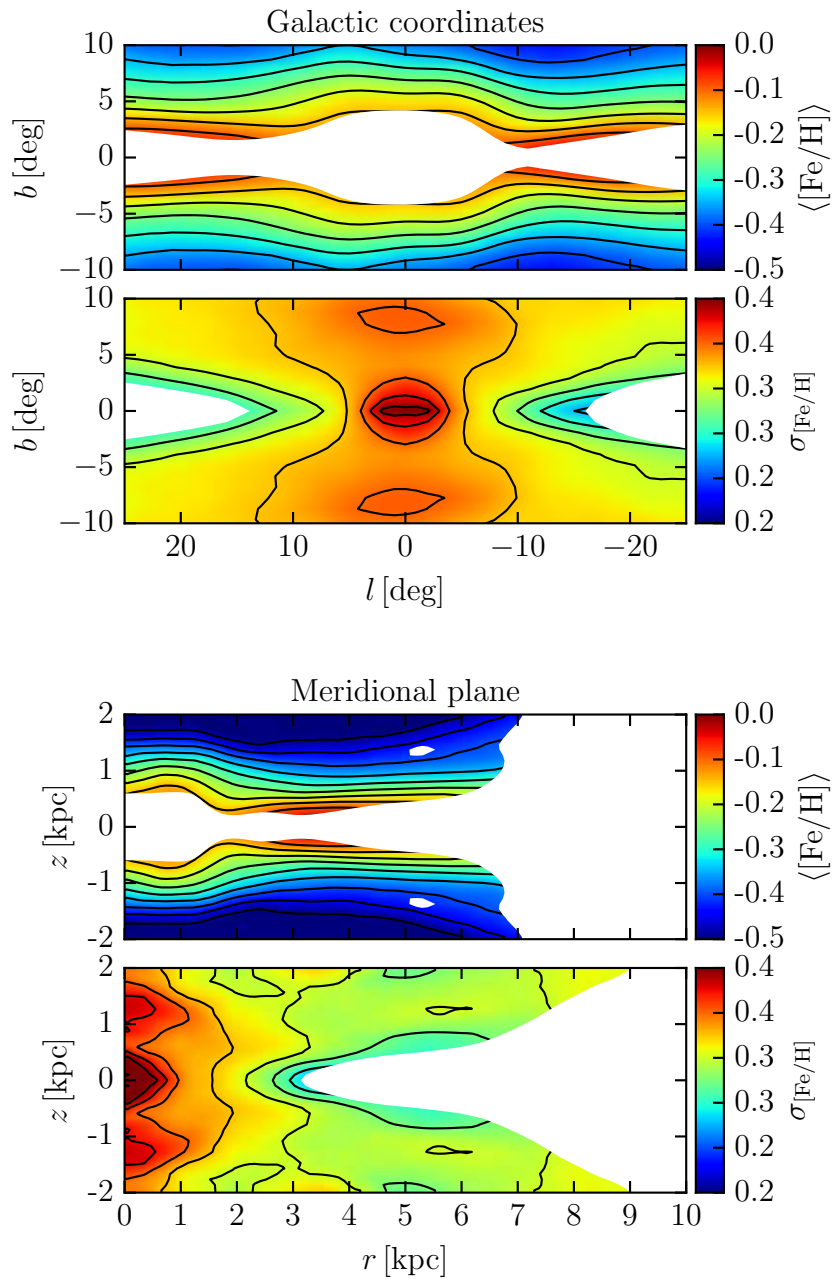


Figure 5.13: Mean metallicity (top) and its standard deviation (bottom) in galactic projection (left) and azimuthal average (right). Regions where systematic uncertainties are larger than 0.02 dex are masked.

## 5.5 Kinematic distribution of the metallicity in the Galaxy

In this section we show how stars in the different metallicity bins differ by their kinematics and orbital properties. As already pointed by Babusiaux et al. (2010) and Ness et al. (2013b), metal-rich stars with  $[\text{Fe}/\text{H}] \geq -0.5$  (i.e A and B) have very different kinematics than more metal-poor stars with  $[\text{Fe}/\text{H}] \leq -0.5$  (i.e C and D). We now analyze in detail these two main groups separately using our fiducial chemodynamical model of Section 5.3.4.

### 5.5.1 Bar-like kinematics of metal-rich stars

A and B are found in the ARGOS data to be similar to each other, as shown by Ness et al. (2013b). They are both rapidly and cylindrically rotating, i.e with only weak variations as a function of latitude. They have similar dispersion profiles, both steeply rising towards the center. B is found in the ARGOS data to rotate slightly faster than A, with a central dispersion about  $20 \text{ km s}^{-1}$  higher at the center. Their kinematic similarities have been interpreted as an indication of a common thin disk origin. The simulations of Di Matteo et al. (2014) showed that starting from an initial disk with a radial metallicity gradient, stars that formed on average at larger radii would be mapped after bar formation and buckling into a more metal-poor stellar population that would exhibit faster rotation and higher dispersion. Thus B and A are believed to originate from the same disk, with B composed of stars that formed on average at larger radii than the stars that compose A.

This simple picture however does not entirely capture the trend we see in our fiducial chemodynamical model. We show in Figure 5.14 maps in galactic coordinates of the mean radial velocity and velocity dispersion of components A and B, integrating along the line of sight between 3 and 12 kpc from the Sun. We see that B is indeed faster than A for  $b \geq 5^\circ$  where the ARGOS fields are located, but not in the plane for  $b \leq 5^\circ$  where we find the inverse trend, with A being about  $10 \text{ km s}^{-1}$  faster than B at  $l = 20^\circ$ . This result is likely to be originating from the complex orbital structure of the in-plane bar, mostly populated by component A. Although the study of the orbital structure of the bulge and bar in the dynamical model of P16 is beyond the scope of this paper, we can investigate the origin of this separate relative behavior of A and B in the plane by experimenting with various cuts in the model. Doing so we find that the particles that are responsible for A being faster than B in the plane are located less than 2 kpc away from the bar major axis, and predominantly along the rear-side of the bar. These particles produce a high-velocity tail in the line of sight distributions, thus shifting the mean velocity of component A to higher values. We thus speculate that the faster rotation of A in the plane is likely to be caused by the complex orbital structure of the bar, in possible relation with the orbits found by Aumer & Schönrich (2015) to be at the origin of the high velocity peak observed in the APOGEE data for  $l = 4^\circ - 14^\circ$  and  $|b| \leq 2^\circ$ . Note however that the model only shows a high velocity tail, with no sign for a separate high-velocity peak. A detailed orbit analysis would be required to investigate the cause of the fast rotation of A further.

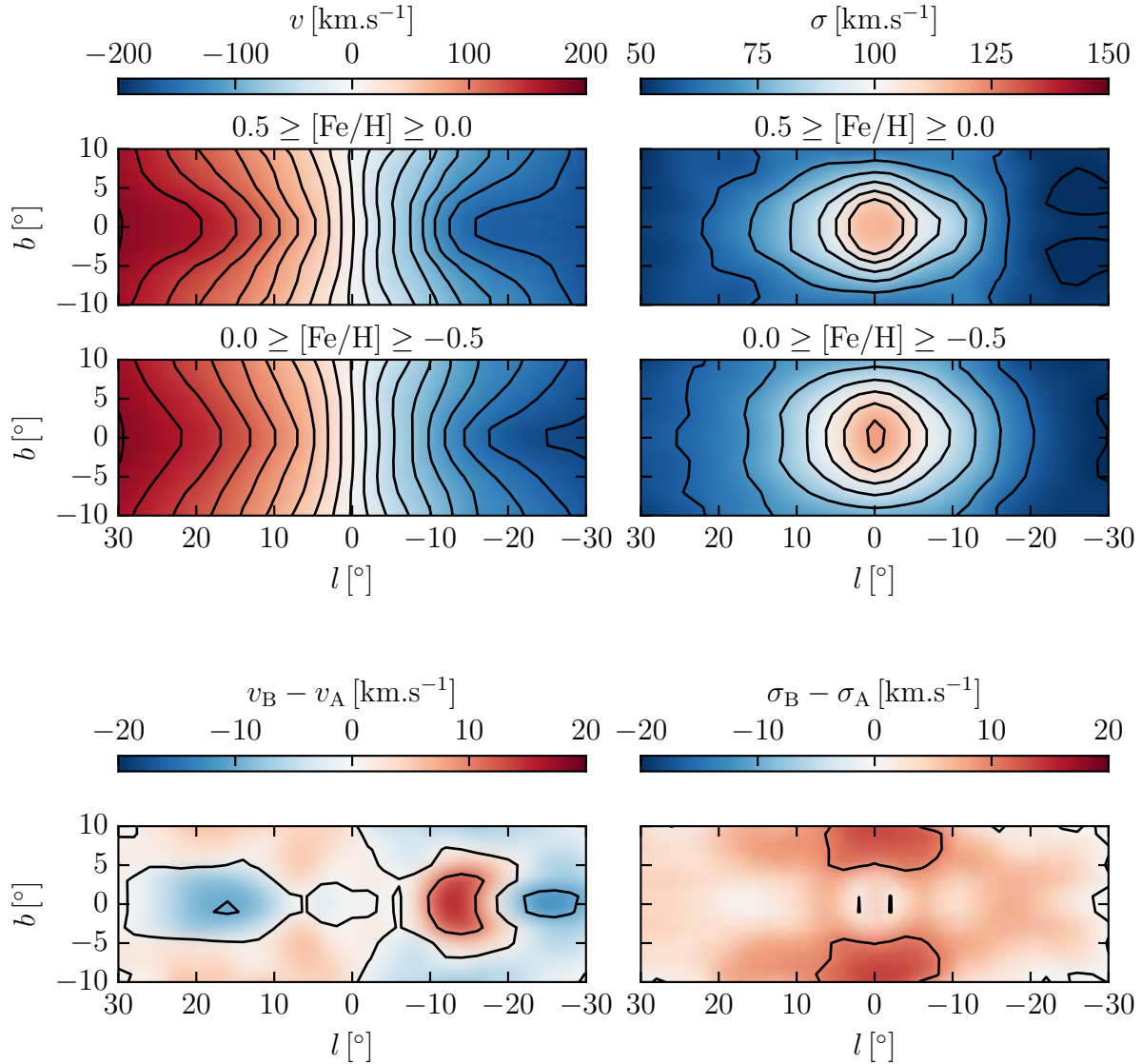


Figure 5.14: Upper four panels: Maps of the mean radial velocity (left) and velocity dispersion (right) for component A (top) and B (bottom). Since A and B have similar kinematics, we show in the bottom two panels the difference maps between B and A. B is hotter and rotates faster than A for  $|b| \geq 5^\circ$ , as reported in [Ness et al. \(2013b\)](#). We find however that B appears to rotate slower than A for  $|b| \leq 5^\circ$ . Regions where systematic uncertainties are larger than  $2 \text{ km s}^{-1}$  are masked.

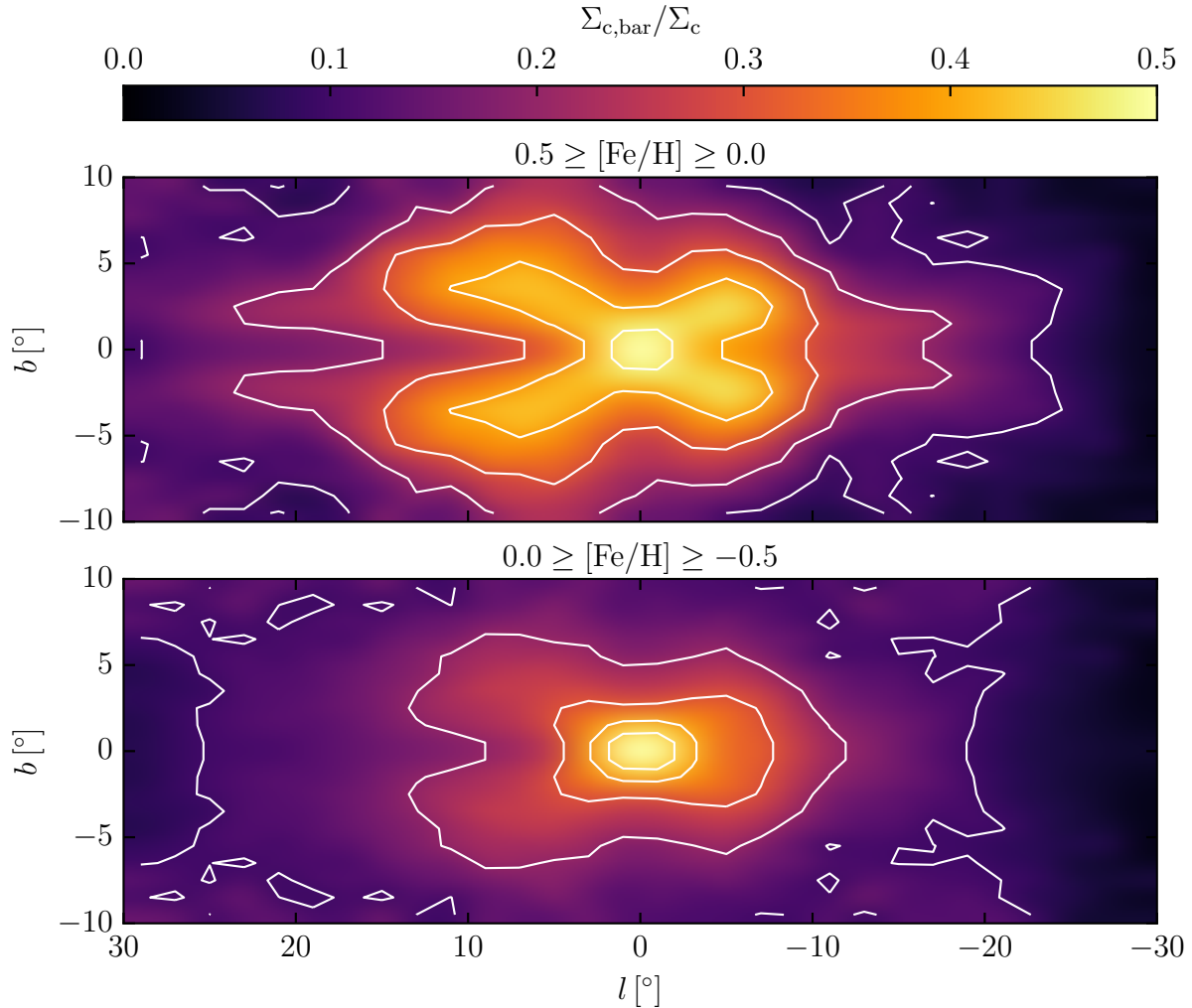


Figure 5.15: Fraction of the surface density of components A (top) and B (bottom) in galactic coordinates that originates from bar-supporting orbits. The support of component A to the B/P shape of the bulge is beautifully striking.

In the face-on views of [Figure 5.10](#) it is clear that neither A nor B form the bar by itself. Instead both metallicity components have a fraction of stars that follow the bar and a fraction of stars that do not, instead forming the inner disk in the bar region. To isolate the bar from the inner disk we first classify the N-body orbits of the model of P16 into two classes, the bar-supporting orbits and the not bar-supporting orbits. Following the method of [Portail, Wegg & Gerhard \(2015\)](#), we identify the bar-supporting orbits as the orbits for which  $f_r/f_x = 2 \pm 0.1$ , where  $f_r$  and  $f_x$  are respectively the dominant frequency of the oscillations of the cylindrical radius and bar major axis coordinate along the orbits. In [Figure 5.15](#) we show for components A and B the fraction of the surface density in galactic coordinates that originates from bar supporting orbits. Both components exhibit an increase of bar supporting orbits towards the corners of the bulge, as expected from

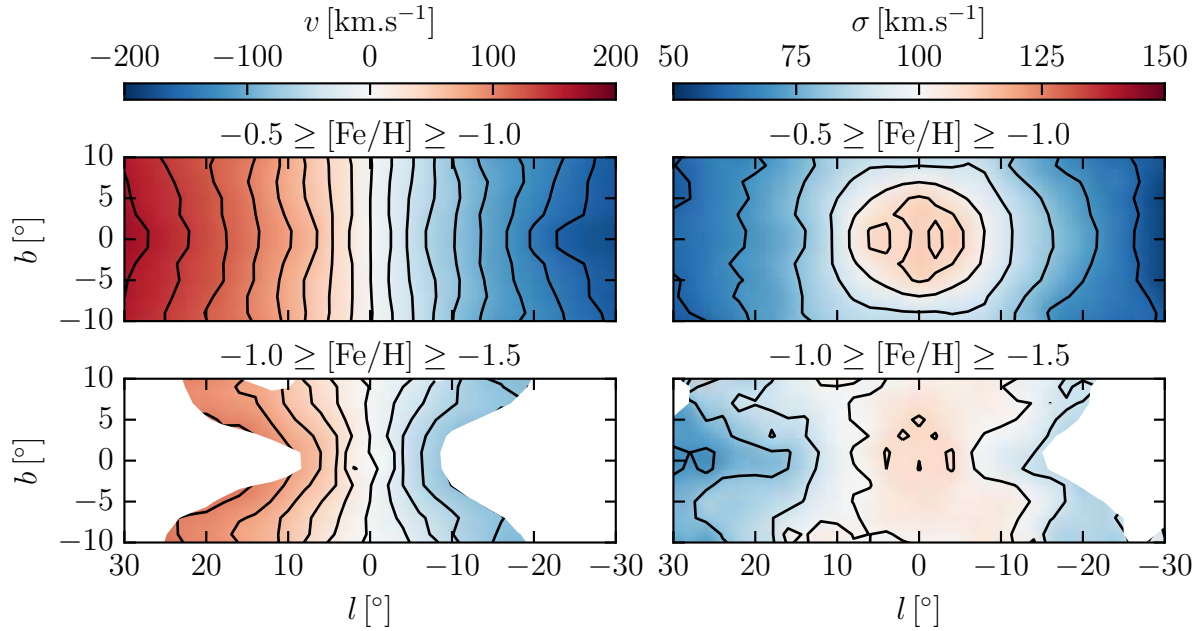


Figure 5.16: Mean radial velocity (left) and velocity dispersion (right) of metallicity bins C (top) and D (bottom). Regions where systematic uncertainties are larger than  $3 \text{ km s}^{-1}$  are masked.

orbits supporting the B/P shape of the bulge. Note that for component A about half the stars in this “orbital X-shape” are supporting the bar.

How are the bar and inner disk orbits populated by the different metallicity bins? Using our orbit classification we find that the galactic bar is composed at  $50\% \pm 5\%$  of stars with metallicities within bin A,  $33\% \pm 3\%$  of stars with metallicities within bin B, and only  $14\% \pm 2\%$  and  $3\% \pm 1\%$  of stars with metallicities within bin C and D respectively. For the inner disk, the fractions of stars in A, B C and D are respectively  $40\% \pm 3\%$ ,  $44\% \pm 2\%$ ,  $14\% \pm 1\%$  and  $2\% \pm 1\%$ . Note that although B is found in [Ness et al. \(2013b\)](#) to be the main component of the MDF in ARGOS survey, A is found to be the main mass component of the bar and has a similar role as B in building the inner disk.

### 5.5.2 Kinematics of the metal-poor stars

The metal-poor stars, often defined by  $[\text{Fe}/\text{H}] \leq -0.5$ , have been shown to be kinematically distinct from their metal-rich counterpart. They are generally rotating more slowly and have a higher dispersion. This kinematic separation between metal-rich and metal-poor stars indicates the presence of at least two separate populations in the inner Galaxy, where metal-poor stars cannot be seen as just the metal-poor tail of a single population with a broad MDF. This is illustrated in more detail in [Figure 5.16](#) where we show maps of the mean radial velocity and velocity dispersion of components C and D from our fiducial model. By comparing with [Figure 5.14](#), both C and D appear to have a higher dispersion

than their surrounding, except in the central few degrees where the metal-rich components have larger dispersions, caused by their bar supporting orbits. Because of their hot kinematics, C and D are less responsive to the barred potential than A and B and thus do not significantly support the bar. We note however that metal-poor stars with  $[\text{Fe}/\text{H}] \leq -0.5$  do not share a unique kinematic behavior but rather show smoothly evolving trends with metallicity. In the ARGOS data, component C at  $b = -5^\circ$  reaches a mean velocity of  $\sim 120 \text{ km s}^{-1}$  at  $l = 20^\circ$  while component D reaches only  $\sim 70 \text{ km s}^{-1}$ .

Smooth kinematic transitions are expected since the underlying physical components present in the inner Galaxy are likely to overlap in metallicity space. Several of such metal-poor components are expected or suspected to be present in the inner Galaxy. The thick disk is found to be metal-poor in the solar neighborhood with  $[\text{Fe}/\text{H}] \sim -0.7$  (Bensby et al. 2007) and since Cheng et al. (2012) observed from SEGUE stars that the radial metallicity gradient in the disk flattens above 1 kpc from the plane, the thick disk is likely to compose a fraction of the metal-poor stars in the inner Galaxy. The stellar halo is also a candidate for a metal-poor stellar population in the inner Galaxy. Between 7 and 25 kpc from the Galactic Centre the stellar halo is found to have a mean metallicity of  $[\text{Fe}/\text{H}] \sim -1.4$  (Torrealba et al. 2014) and a steep radial profile  $\rho(r) \propto r^{-3}$  (Wetterer & McGraw 1996; Jurić et al. 2008). The inner stellar halo would therefore also be part of the components C and D. Finally, we might also expect the presence of a classical bulge component, remaining of early mergers which would also be metal-poor. The RR Lyrae stars in the bulge, observed by Pietrukowicz et al. (2015), and claimed from their kinematics to be candidate for classical bulge stars by Kunder et al. (2016), have a narrow MDF centered on  $[\text{Fe}/\text{H}] = -1$  and would thus also contribute to both C and D. Note however that Pérez-Villegas, Portail & Gerhard (2016) showed that both the density and kinematics of RR Lyrae stars in the bulge are also consistent with what would be expected for the inner part of the stellar halo.

This smooth evolution of kinematics as a function of metallicity is illustrated in Figure 5.17 where we show the vertex deviation in Baade’s window  $\theta_{r,l}$  of our model compared to the data from Soto, Rich & Kuijken (2007) and Babusiaux et al. (2010). The vertex deviation  $\theta_{r,l}$  is defined by

$$\tan(2\theta_{r,l}) = \frac{2\sigma_{r,l}^2}{|\sigma_r^2 - \sigma_l^2|} \quad (5.17)$$

where  $\sigma_{r,l}^2$ ,  $\sigma_r^2$  and  $\sigma_l^2$  are respectively the covariances of the radial velocity and proper motion dispersion in the longitudinal direction, with their two associated variances. The vertex deviation represents the angle of the principal axis of the velocity ellipsoid in non-isotropic cases. It is clear in Figure 5.17 that  $\theta_{r,l}$  is significantly non-zero for stars with  $[\text{Fe}/\text{H}] \geq -0.5$  while gradually transition to zero for more metal-poor stars. Our fiducial model reproduces the observed evolution of  $\theta_{r,l}$  with metallicity well, providing a good fit to the data although not directly fitted to it.

The absence of a significant vertex deviation for  $-1 \leq [\text{Fe}/\text{H}] \leq -0.5$  (C) has been interpreted by Soto, Rich & Kuijken (2007) and Babusiaux et al. (2010) as a signature of the presence of an old metal-poor spheroid. This interpretation can be questioned by our model for which component C is found to have no significant vertex deviation  $\theta_{r,l}$  but

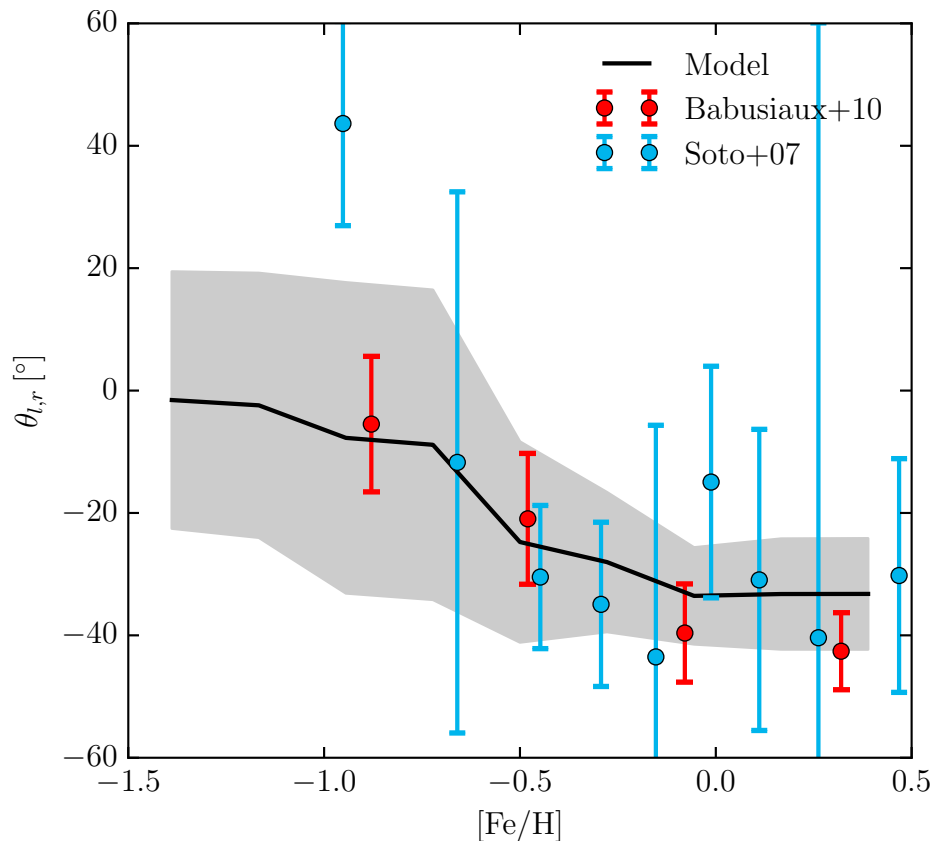


Figure 5.17: Vertex deviation  $\theta_{l,r}$  in Baade’s window as a function of metallicity for our fiducial model compared to the data of Babusiaux et al. (2010) and Soto, Rich & Kuijken (2007). In computing the model predictions we include only stellar particles between 6 kpc and 10 kpc away along the line of sight. The shaded area indicates the one sigma statistical error on the model vertex deviation. The large errors in the model predictions at low metallicity arise from the fact that  $\sigma_r^2$  and  $\sigma_l^2$  are increasingly closer to each other with decreasing  $[\text{Fe}/\text{H}]$ .

has a spatial distribution and kinematics similar to that of a disk rather than that of a spheroid. Indeed, C was found in Section 5.4.1 to have a vertical flattening of  $\sim 0.3$ , quite extreme for a classical bulge according to external galaxies (Kormendy & Kennicutt 2004) or simulations (Saha, Martinez-Valpuesta & Gerhard 2012). In addition, C is shown in Figure 5.16 to be cylindrically rotating, with a rotation only slightly slower than that of the metal-rich components. Nevertheless, the contribution of a classical bulge to component C cannot be completely ruled out. N-body simulations by Saha, Martinez-Valpuesta & Gerhard (2012) showed that an initially non-rotating classical bulge could gain a significant amount of angular momentum transfer through resonances with the bar and thus develop fast and cylindrical rotation. Predictions for the signature of a classical bulge in the inner Galaxy will be shown in a later paper (Wegg et al. 2016, in preparation). We conclude from our model that C is likely to host the contribution of several metal-poor components overlapping: a thick disk, the inner part of the stellar halo and a possible contribution from a classical bulge. Its disk-like spatial distribution and kinematics however suggests that it is highly dominated by thick disk stars.

Little can be reliably said from our model about component D since it is only poorly constrained by the data. D is found in the model to be cylindrically rotating, but at a slower rate than C and has a dispersion that varies only slightly in the inner  $10^\circ$  of the Galaxy. Differences between C and D are likely to highlight different contributions of the underlying metal-poor stellar population described above. More data would be required to investigate the metal-poor stars further.

## 5.6 Discussion and conclusion

We presented an extension of the Made-to-Measure (M2M) method for modelling self-consistent equilibrium chemodynamical models of galaxies. Its application in the inner Milky Way results in the first chemodynamical particle model fitted to chemo-kinematic data in the bulge and bar. Such chemodynamical models will be invaluable in the near-future for interpreting chemical abundances and stellar parameters provided by the many on-going and future large-scale spectroscopic surveys of the Galaxy. Indeed, M2M chemodynamical models allow to maximize the information extracted from spectroscopic data by containing at once the spatial distribution and kinematics of stars with the orbital distribution of a self-consistent dynamical model. Since it is built upon the standard M2M method, it is flexible enough to be applicable to complex systems such as the inner barred galactic disk, where other modelling technique would be either not applicable or too complex.

We applied the method based on the dynamical model of the bar region recently made by Portail et al. (2016), and successfully reproduced the spatial and kinematic variations of the metallicities of stars seen in the ARGOS and APOGEE surveys. Our chemodynamical model allows us to the study of the different metallicity components in great detail, from the 3D density distributions of the components to distinct features in their kinematics and to their origins in term of orbital structure. Summarizing the properties of the different metallicity components in the inner 5 kpc of the Galaxy, as found in our model, but also



in the light of the work of [Ness et al. \(2013a,b\)](#) and [Di Matteo et al. \(2014, 2015\)](#), we conclude the following:

- A** ( $0.5 \geq [\text{Fe}/\text{H}] > 0$ ): We find that A is the main metallicity component of the galactic bar and bulge structure in its current state. A is strongly barred and hosts  $50\% \pm 5\%$  of the bar supporting orbits. It is generally thin, dominates the other components in the plane and provides a very strong support to the B/P shape in the bulge. Its hammer-like shape at the outer part of the bar indicates that component A probably contains a significant fraction of the superthin bar. A has a very low dispersion of only about  $\sigma \approx 60 - 80 \text{ km s}^{-1}$  that steeply rises in the central  $5^\circ$ , caused by the bar supporting orbits. A is found to be more quickly rotating than other components for longitudes between  $10$  and  $30^\circ$  at  $|b| \leq 5^\circ$  and shows a high velocity tail in the line of sight velocity distribution there. We speculate that this tail, shifting the mean velocity to a higher value, is caused by the complex orbital structure of the bar in the plane. A also contributes in our model  $40\% \pm 3\%$  of the inner disk. In good agreement with [Ness et al. \(2013b\)](#) and [Di Matteo et al. \(2015\)](#), A is thus mostly consistent with an early thin disk origin. However, since the superthin bar is probably associated to a more recent star formation episode ([Wegg, Gerhard & Portail 2015](#)), A is probably a composite population, hosting old but metal-rich stars formed in the early disk and later mapped into the bar, together with stars formed more recently in the superthin bar or trapped by the bar.
- B** ( $0 \geq [\text{Fe}/\text{H}] > -0.5$ ): We find that B is the second main component of the galactic bulge and bar structure, but dominates A at  $|b| \geq 5^\circ$ . B is also strongly barred, with  $33\% \pm 3\%$  of the bar supporting orbits and also contributes to the B/P shape in the bulge. B is found to be more extended vertically than A, in good agreement with [Ness et al. \(2013a\)](#). It is generally hotter than A and also shows a steep rise in the dispersion towards the centre, a signature of its barred nature. B rotates generally faster than A at  $|b| \geq 5^\circ$ , except in the plane where it does not share the complex orbital structure of A. It accounts for  $44\% \pm 2\%$  of the inner disk, a similar share than that of component A. B thus appears to be also consistent with a disk origin, being formed from stars initially located at larger radii than stars forming A, as found by [Di Matteo et al. \(2014\)](#) to explain the faster rotation and larger dispersion.
- C** ( $-0.5 \geq [\text{Fe}/\text{H}] > -1$ ): C shows significant differences from A and B. It is thicker, rotates more slowly and has a larger velocity dispersion than the more metal-rich stars. Being dynamically less responsive to the influence of the bar, C is found to offer only a weak support to the bar, hosting  $14\% \pm 2\%$  of the bar supporting orbits and a similar fraction of the inner disk. From our models, we find that C is strongly vertically flattened ( $\sim 0.3$ ), in addition to its fast and cylindrical rotation. It thus appears to have both the spatial distribution and kinematics of a disk rather than that of an old classical spheroid. Several metal-poor components are expected to be present in the inner Galaxy, thick disk, stellar halo and possibly a classical bulge, which would all be expected to contribute to component C at some level. However its

disk-like behavior indicates that it is dominated by thick disk stars, as suggested by [Di Matteo et al. \(2015\)](#). The contribution of a large classical bulge component that would have been significantly flattened and spun-up by the bar cannot be directly ruled out but seems very unlikely; from both the mass-metallicity relation of bulges in external galaxies (as discussed in [Di Matteo et al. 2014](#)) and also the strong flattening of component C, stronger than expected even from low mass and very responsive classical bulge (flattening  $\sim 0.5$ , see [Saha, Martinez-Valpuesta & Gerhard 2012](#)). As a consequence, the thick disk appears as the favorite candidate for the origin of the dominant population of component C, as proposed by [Di Matteo et al. \(2015\)](#).

**D** ( $-1 \geq [\text{Fe}/\text{H}] > -1.5$ ): D is only weakly constrained by the ARGOS data and even less by the APOGEE data since the fraction of metal-poor stars increases with height above the plane. In our models, D is found to be a very thick, high dispersion and slowly rotating stellar population. It is however different from a metal-poor tail of C and this supports the idea that at the metal-poor end of the metallicity distribution, several components are present and overlap significantly in metallicity.

To conclude, most of the metal-rich stars (B & most of A) appear to have a common and relatively simple origin, the early thin disk, which after bar formation and buckling became mapped into different spatial distributions and a rather complex orbital structure. Part of A could also be associated to a more recent star formation episode, as indicated by the similarities between the superthin bar and the shape of the bar end in component A. On the contrary, metal-poor stars (C & D) appear to presently have a relatively simple structure, only weakly bar-following but they are probably composed of a complex superposition of components: thick disk, inner halo and possible classical bulge, for which very little is known.

Our M2M chemodynamical model of the bar region, although the first of its kind, represents a first step towards more complete models, that by including additional chemical dimensions will be able to better constrain the formation history of the Galaxy. On-going and future spectroscopic surveys such as APOGEE, GAIA-ESO, GALAH and MOONS will provide stellar abundances of 10-20 elements for more than  $10^5$  stars each. This profusion of data allows extending the dimensionality of the chemical phase-space in M2M chemodynamical models to other elements that better constrain the origin of stars. The abundance in  $\alpha$ -elements is of primary importance, since it is a natural chemical “clock” giving the timescale of stars formation of a given stellar population. We plan in the near future to first extend the modelling of the bar region to a two dimensional chemical space, including  $[\text{Fe}/\text{H}]$  and  $[\alpha/\text{Fe}]$ , and later to other elements.

## Acknowledgments

We are grateful to Jo Bovy for publicly releasing his tools dealing with APOGEE data, and particularly its selection function. We acknowledge the use of the p3lib potential solver,

made available to us by Jerry Sellwood and Monica Valluri.



# Chapter 6

## Outlook & Further Work

### 6.1 Outlook

The study of the formation history of our home Galaxy, is currently a very active field in astronomy. Although the Milky Way is a single Galaxy, it can be used as a benchmark to test our theories of how disk galaxies form in a cosmological context. Since the Milky Way can be observed on a star-by-star basis we can hope to reconstruct its formation history in much greater detail than any other external galaxy. However, a necessary first step before understanding how the Galaxy formed is to understand how the Galaxy actually is. The many photometric and spectroscopic surveys of the Galaxy performed over the last two decades, as described in detail in [Section 1.2.3](#), provide a large collection of data to analyze and understand. This motivated the present work in which a self-gravitating dynamical model of our home Galaxy that reproduces as many datasets as possible was constructed. Modelling the dynamics is a key element of this work as it relates the density of stars and dark matter to the stellar kinematics. Since the mass distribution in the inner part of the Galaxy exercises its gravitational force everywhere outwards, we adopted an inside-out approach starting from the galactic bulge, moving out to the bar region and up to the Solar circle.

#### 6.1.1 The galactic bulge

We started by focusing on the galactic bulge, taking advantage of the new direct measurement of the 3D density of the bulge as traced by RCGs from [Wegg & Gerhard \(2013\)](#). Early studies of the bulge were limited to parametric fits of either the integrated light (e.g. [Dwek et al. 1995](#) from the COBE/DIRBE light) or star counts (e.g. [Rattenbury et al. 2007a](#) from OGLE-II data). With the arrival of more accurate data [McWilliam & Zoccali \(2010\)](#) and [Nataf et al. \(2010\)](#) independently discovered the presence of dip in the magnitude distribution of RCGs towards the bulge minor axis from respectively 2MASS and OGLE-III data. It was quickly realized that such a dip could be reproduced by a boxy/peanut shape in the bulge density. Such a boxy/peanut shape was not reproduced by the assumed parametric forms of previous bulge models. Using data from the deeper VVV survey, [Wegg & Gerhard](#)

(2013) made a major step forward, producing the first non-parametric 3D density model of the bulge, shown in projection in [Figure 2.3](#). It was then natural to try understanding the dynamical properties of such a strong peanut bulge and this motivated the construction of the dynamical models of the galactic bulge presented in [Chapter 2](#).

By combining the bulge density as traced by RCGs together with stellar radial kinematics from the BRAVA survey, we built a family of five Made-to-Measure models of the bulge with different dark matter fractions called M80, M82.5, M85, M87.5 and M90. Our main finding is the most accurate measurement of the dynamical mass of the bulge up to date of  $1.84 \pm 0.07 \times 10^{10} M_{\odot}$ . In addition to being very precise, our dynamical mass measurement refers to the total mass inside a well define volume, a box of  $\pm 2.2 \times \pm 1.4 \times \pm 1.2$  kpc along the bar axis. Measuring the bulge mass in term of the mass enclosed in a given volume is a significant improvement over other bulge masses found in the literature, which all use different definitions of the bulge, usually based on their measurement methods. For instance, a recent mass measurement of the bulge by [Valenti et al. \(2015\)](#) uses giants and RCGs stars identified in the VVV bulge fields and convert the total count within some magnitude range into stellar mass, using as standard the mass in the NICMOS field from [Zoccali et al. \(2000\)](#). They find a bulge stellar mass of  $2.0 \pm 0.3 \times 10^{10} M_{\odot}$  apparently inconsistent with our dynamical mass determination. However, their definition of “bulge” corresponds to the mass in a non-trivial volume, not provided by the authors but likely to be larger than the volume of our RCG box. Our dynamical models of the bulge have been used up to now in four different studies.

The first application was the study of the orbital structure of the peanut shape, described in detail in [Chapter 3](#). We find that boxy/peanut bulges in general are not necessarily made of vertically resonant *banana orbits*, contrary to the classical picture well-spread in the literature. We find instead in our models that the peanut shape can be seen as the superposition of several peanut shapes, all embedded into another and made by different orbital families as shown in [Figure 3.2](#). The main orbital family in our dynamical models of the bulge only is supported by a novel orbit we called *brezel* orbits, probably associated with a vertical bifurcation of the  $x_1\text{mul}_2$  family. Since then, the brezel orbit has been seen in other simulations including the controlled N-body+smoothed particle hydrodynamics simulation of a growing disk galaxy by [Aumer & Schönrich \(2015\)](#). In this work the authors show that complex orbits, including brezel-like orbits contribute to a significant fraction of the high velocity peak stars found in the commissioning APOGEE data ([Nidever et al. 2012](#)).

Our second application of our dynamical models of the bulge is the study by [Li et al. \(2016\)](#) of the gas flow in a low bar pattern speed model. As shown in [Section 2.4.3](#) our dynamical models of the bulge only require a rather low bar pattern speed of  $25 - 30 \text{ km s}^{-1} \text{ kpc}^{-1}$  in order to match the stellar kinematics from the BRAVA survey. This result is in apparent contradiction with the larger values of  $50 - 65 \text{ km s}^{-1} \text{ kpc}^{-1}$  obtained from earlier gas dynamics studies, trying to reproduce the observed position-velocity diagram of  $\text{H}_I$  and CO gas ([Englmaier & Gerhard 1999](#); [Fux 1999](#); [Bissantz, Englmaier & Gerhard 2003](#)). However, none of the previous gas models were able to reproduce all the features of the position-velocity diagram at once, leaving the possibility for a low bar pat-

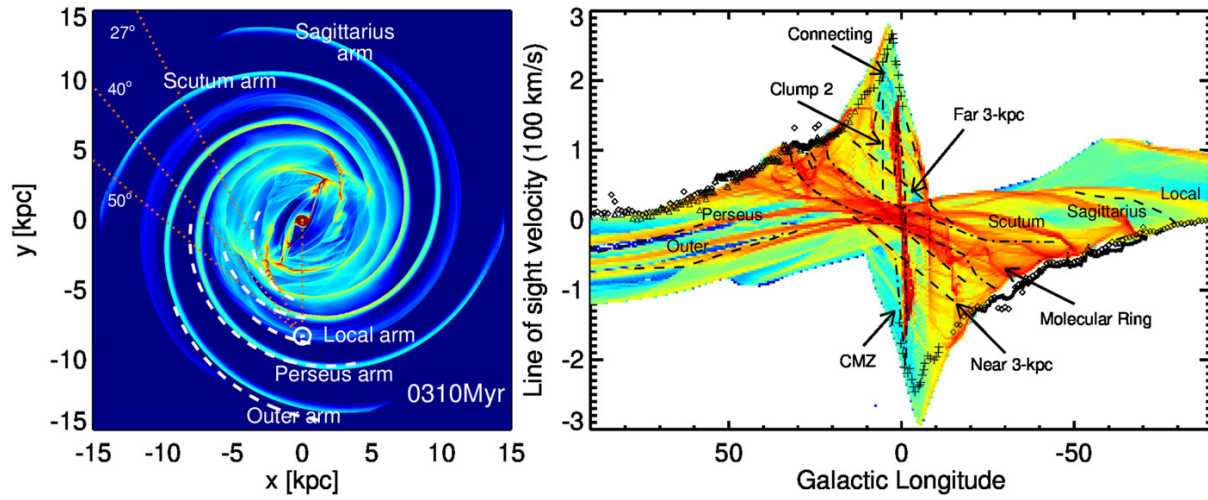


Figure 6.1: The gas flow in a low bar pattern speed model, taken from [Li et al. \(2016\)](#), with permission. Left: Gas surface density of the best fitting model in a potential based on the bulge model of [Chapter 2](#), rotating at a low pattern speed of  $33 \text{ km s}^{-1} \text{ kpc}^{-1}$ . Right: corresponding longitude-velocity diagram of the model, compared to  $\text{H I}$  and CO terminal velocity data (black symbols). The dotted lines illustrate various features identified in the observed data by [Rodríguez-Fernández & Combes \(2008\)](#) and are generally well reproduced by the model.

tern speed model to also produce a reasonable agreement with the observation. [Li et al. \(2016\)](#) computed the gas-flow in a gravitational potential based on the fitted bulge model M80 and were able to reproduce the nuclear ring, Baniyas Clump 2, the connecting arm, the near and far 3-kpc arms, the Molecular Ring, and the spiral arm tangent points. Having a fit of similar quality than earlier studies but with a lower bar pattern speed, [Li et al. \(2016\)](#) conclude that a low bar pattern speed in the Milky Way is not ruled out by gas dynamics. The best fitting model of [Li et al. \(2016\)](#) is illustrated and compared to the data in [Figure 6.1](#).

The third application aimed at breaking the degeneracy between stellar and dark matter mass using microlensing data. As described in detail in [Section 2.5.1](#) our five models M80-M90 with different dark matter fractions all provided similar fits to the data, leading to a very accurate measurement of the total mass but a degeneracy between the stellar and dark matter components. Only stellar mass objects are able to microlense. [Wyrzykowski et al. \(2011\)](#) showed, by measuring the microlensing optical depth towards the towards the Large Magellanic Cloud, that it was too small to allow more than a small fraction of the galactic dark halo to be formed from the so-called MACHOs (Massive Astrophysical Compact Halo Objects). Hence the microlensing optical depth is a unique way to measure directly the mass distributed into compact objects, i.e mostly stars, and thus break the degeneracy between stellar and dark matter mass in our bulge models. This motivated the work of [Wegg, Gerhard & Portail \(2016\)](#) who compared predictions of optical depth and

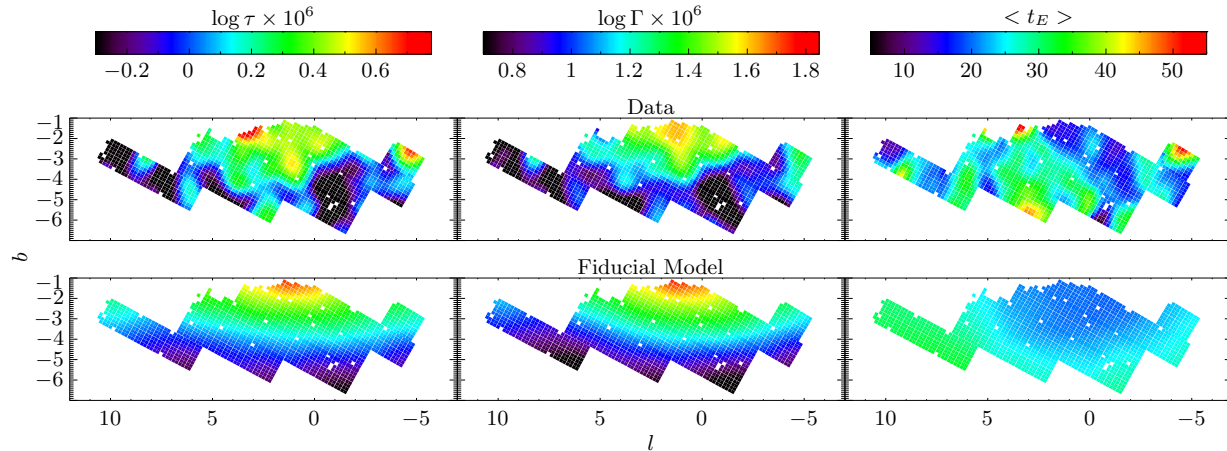


Figure 6.2: Maps of microlensing properties towards the bulge, taken from Wegg, Gerhard & Portail (2016) with permission. From left to right, the optical depth, the event rate per star, and mean microlensing timescale are shown for the MOA-II revised data from Sumi & Penny (2016) (top) and the fiducial model of Wegg, Gerhard & Portail (2016) (bottom). The optical depth and event rate maps show good qualitative agreement, while the mean timescale map has large observational error due to the large statistical variance of timescale caused by the rare very long timescale events.

microlensing event rate for models with different dark matter fractions and outer stellar disks to the revised MOA-II (Sumi & Penny 2016) and EROS-II (Hamadache et al. 2006) microlensing data. In this work, we find that in order to match the data a low dark matter fraction is required in the bulge. Additional constraints on the rotation curve also require a near maximum stellar disk, providing at one sigma  $88\% \pm 7\%$  of the stellar rotation curve at the position of its peak. A comparison between the fiducial model of Wegg, Gerhard & Portail (2016) and the revised MOA-II data is shown in Figure 6.2.

Finally the last application of our bulge models is the study of the inner galactic stellar halo by Pérez-Villegas, Portail & Gerhard (2016). There has been much recent interest in the scientific community about the metal-poor RR Lyrae stars in the bulge. RR Lyrae stars are variable stars, for which the pulsation period is related to their intrinsic brightness, hence allowing accurate distance estimates. In the bulge, RR Lyrae have been shown to form a triaxial structure with steeply decreasing density profile, decreasing proportionally to the inverse third power of the major axis distance (Pietrukowicz et al. 2015). Pérez-Villegas, Portail & Gerhard (2016) find that the stellar density profile of the RR Lyrae in the bulge naturally agrees with the inward extrapolation of the density profile of the stellar halo observed at larger radius, as shown in Figure 6.3. This coincidence motivated the study of the evolution of the inner part of a stellar halo when co-evolving with a bar forming disk. Using the N-body model M85, Pérez-Villegas, Portail & Gerhard (2016) show that an initially oblate stellar halo would become slightly triaxial in its central part, in good qualitative agreement with the shape of RR Lyrae in the bulge determined by Pietrukowicz et al. (2015). In addition, the kinematic properties of such an evolved stellar



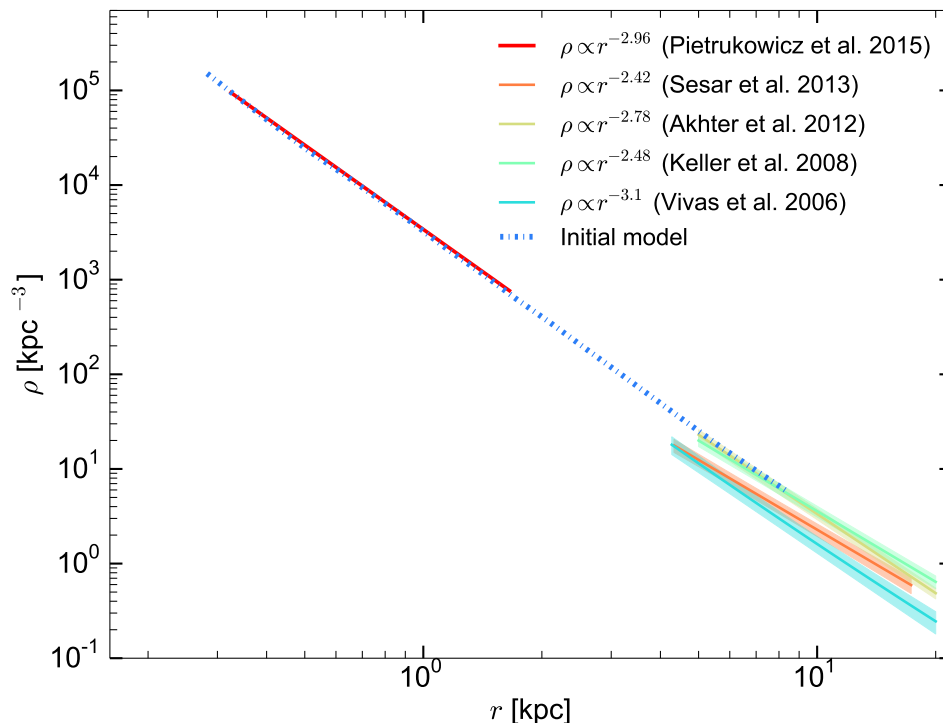


Figure 6.3: Spatial density profiles of RR Lyrae as a function of spherical radius, for stars in the bulge as measured by Pietrukowicz et al. (2015) in red, compared to stars in the halo further out as measured from various studies indicated in the legend. The density of bulge RR Lyrae naturally lines up with the outer halo, motivating the idea that bulge RR Lyrae stars could just be the inner part of the stellar halo. Taken from Pérez-Villegas, Portail & Gerhard (2016), with permission.

halo in the bulge region are shown to be very similar to the recent kinematic measurements of RR Lyrae stars in the bulge from Kunder et al. (2016), who find a very slow rotation and a large velocity dispersion. Pérez-Villegas, Portail & Gerhard (2016) conclude that the metal poor stars in the bulge are consistent with being simply the inward extension of the stellar halo, with no need for an extra classical bulge component as first suggested by Kunder et al. (2016).

### 6.1.2 The galactic bar

Moving out of the bulge, the next challenge was the twenty year long controversy about the nature of the long bar, flat extension of the bar outside the bulge. Initially discovered in 1994 from NIR star counts by Hammersley et al. (1994) the long bar was suggested to be oriented at an angle of about  $45^\circ$  from the line of sight to the Galactic Centre, i.e about  $15^\circ - 20^\circ$  leading the bulge. This misalignment has also been found by later studies focusing on the position of the red clump peak in magnitude distributions from

2MASS (Cabrera-Lavers et al. 2007) and UKIDSS data (Cabrera-Lavers et al. 2008), and also from star counts from the GLIMPSE survey (Benjamin et al. 2005). However, a misalignment between the bulge and the long bar would be dynamically surprising since the mutual torque should be strong. Wegg, Gerhard & Portail (2015) combined the VVV, UKIDSS, 2MASS and GLIMPSE data to analyze the structure of the bar in the galactic plane and found that the long bar lies at an angle in the range  $28^\circ - 33^\circ$ , consistent with the bulge orientation. In addition, the bulge is seen to smoothly transition into the long bar. As a consequence the bulge and long bar are now considered to be two facets of a single bar structure, similar to those formed in N-body models where a long flat bar formed in the stellar disk vertically buckles in its inner part and produces a boxy/peanut bulge. A remarkable conclusion of this later work is that long bar is found to extend to  $5.0 \pm 0.2$  kpc from the Galactic Centre. How does a long bar, only  $\sim 4.5$  kpc away from the Sun, influence the galactic disk? How do the bulge and long bar relate dynamically? How massive is the long bar? All these questions motivated the dynamical modelling effort of the entire bar region, described in Chapter 4.

We learned a lot about the Milky Way in modelling the entire bar region. The first result is that the surrounds of the bulge matters dynamically. The absence of a significant long bar and inner disk component in our models of the bulge biased the bulge dynamics towards a lower bar pattern speed of only  $25 - 30 \text{ km s}^{-1} \text{ kpc}^{-1}$  instead of the  $40 \text{ km s}^{-1} \text{ kpc}^{-1}$  found in the more complete models of the entire bar structure. We find also for the bulge and bar a stellar mass of  $M_{\text{bar/bulge}} = 1.88 \pm 0.12 \times 10^{10} M_\odot$ , larger than the mass of the underlying inner disk in the bar region of only  $M_{\text{inner disk}} = 1.29 \pm 0.12 \times 10^{10} M_\odot$ . The long bar is found to account for slightly less than half the disk mass in the same radial range and is hence expected to have a significant influence on its surrounding. More detailed studies of the influence of the bar are now possible in our new galactic potential, which is accurate inside corotation.

### 6.1.3 The dark matter halo

If it is clear that dark matter is required in general to explain the flattening of the 21cm-rotation curves of external disk galaxies, this is however at large radii and little is known about the dark matter density in the inner part of disk galaxies. Indeed, the decomposition of observed rotation curve into stellar and dark matter components is subject to a large degeneracy, where comparable fits to the data can be obtained for different mass-to-light ratio varying up to a factor of 20 (e.g van Albada et al. 1985). Hence the precise determination of the stellar mass-to-light ratio becomes a crucial element in the determination of the dark matter density. The mass-to-light ratio and its potential spatial variations can be in theory determined by comparing the observed color of a galaxy with predictions from stellar population models. However, advanced models by Portinari, Sommer-Larsen & Tantalo (2004) show that the end result is affected by many unknown or poorly constrained parameters, such as the star formation and chemical enrichment history, the IMF or the life-time of the TP-AGB stars. An alternative is to use dynamics. Bershadsky et al. (2010) undertook the Disk Mass Survey, an integral field spectroscopic survey of nearly face-on

disk galaxies. By measuring the vertical velocity dispersion in the disk and assuming a vertical scale height from a statistical scale height/scale length relation, they can measure the dynamical disk surface density and use this measurement as an additional constraint on the rotation curve fitting. Their conclusion is that external disk galaxies are submaximal, with the disk component contributing to only 15% – 30% of the dynamical mass within 2.2 disk scale lengths (Bershady et al. 2011). This result for external disk galaxies is in tension with our findings in the Milky Way. Indeed, using constraints on the IMF from recent HST measurements we find in the Galaxy a low central dark matter fraction and a nearly maximum disk, consistently from both dynamical modelling of the entire bar region (see Figure 4.23) and microlensing towards the bulge (Wegg, Gerhard & Portail 2016). However, Aniyán et al. (2015) show that the method of the Disk Mass Survey is likely to be biased because the two key elements, vertical velocity dispersion of the disk and vertical disk scale length are measured from different tracer populations. The disk scale height is determined from near-IR photometry, dominated by old giants stars, while the vertical velocity dispersion is determined from absorption lines close to the V-band, including contribution from giants of all ages. Estimating the importance of this bias from data in the solar vicinity, Aniyán et al. (2015) find that the disk surface densities in the Disk Mass Survey is likely to be underestimated by a factor of  $\sim 2$ , making disks appear submaximal. Future work is thus required to attest how our results on the Milky Way’s dark halo fit in the context of external disk Galaxies.

## 6.2 Further work

### 6.2.1 Spin-off projects on the new galactic potential

Our best dynamical model of the bar region presented in Chapter 4 can be used for several future projects in the same way as our bulge models of Chapter 2. The first spin-off project is the extension of the M2M modelling to chemodynamical modelling, described in Chapter 5. A metallicity distribution function was added to each particle and fitted to reproduce the variations of the fractional density and stellar kinematics of different metallicity components seen in the ARGOS and APOGEE data. The resulting model, the first M2M chemodynamical model, allows the study of the different metallicity components in great detail, from their 3D structures to their orbital compositions. The model supports the idea that metal-rich stars with  $[\text{Fe}/\text{H}] \geq -0.5$  have a common disk origin, although a fraction of the stars with  $[\text{Fe}/\text{H}] \geq 0$  is found to form the superthin bar and thus probably corresponds to a more recent star formation episode. Metal-poor stars with  $[\text{Fe}/\text{H}] \leq -0.5$  show an evolving trend with metallicity, indicating different contributions from different underlying metal-poor stellar populations, but it is likely to be dominated by thick disk stars rather than forming an old classical spheroid.

A second spin-off project is make the dynamical model publicly available in the Galaxia code (Sharma et al. 2011) and will be part of a future publication (Wegg et al., in preparation). Galaxia is a code for generating synthetic survey data by turning an N-body model

or a static mass distribution into stars using stellar population models. The ability to easily generate mock data from a model has been shown to be very useful for the scientific community in planning new surveys, evaluating selection biases and making predictions that can be confronted to observations. In particular, the dynamical self-consistency of our model would be a significant improvement over the present day state-of-the-art and widely used Besançon model (Robin et al. 2003).

A third project is the study of the dynamical influence of the bar on the stellar disk and the Solar neighborhood kinematics. The first data release of the *Gaia* mission, planned for mid-September 2016 will provide accurate distances and proper motions of many disk stars whose motion is likely to be affected by the presence of the galactic bar. Our model could thus be a key tool for understanding the effect of the bar on the disk. A second and related point is the dynamics of moving groups in the Solar neighborhood. As already discussed in Section 4.10.1, our finding of a bar pattern speed of  $\sim 40 \text{ km s}^{-1} \text{ kpc}^{-1}$  from bar stellar kinematics is inconsistent with the interpretation of the Hercules stream as a stream of stars scattered by the Outer Lindblad resonance of the bar. Is there an alternative explanation for the Hercules stream? This will be the focus of a future publication by Pérez-Villegas et al., in preparation.

A fourth future project would be the study of the gas dynamics in our new bar model. Li et al. (2016) already studied the gas dynamics of one of our bulge models of Chapter 2 but since only the bulge was fitted to data, we had to complement the potential with an additional nuclear bulge and a long bar. Our new model has already those two components included, fitted to real data and is therefore much more realistic. How does the gas flow in our new potential look like, and can it reproduce all the features of the observed position-velocity diagram at once? In addition, being very concentrated in the plane, the gas could be a good tracer for studying the influence of the superthin bar component.

Finally, a fifth spin-off project would be to use the microlensing event rate data to constrain the IMF in the inner Galaxy. The microlensing event rate is a quantity that depends not only on the density distribution along the line of sight but also on the IMF and the stellar kinematics of both sources and lenses. Hence, using the mass distribution and kinematics of our best model we can directly constrain the IMF by matching the observed microlensing event rates. This was not possible in the work of Wegg, Gerhard & Portail (2016) because it was based on a model from Chapter 2 where the mass distribution outside the bulge was not constrained by data.

### 6.2.2 Towards a more complete model

Our galactic model could be improved by including more data from the many recent, currently running and future surveys. In the bulge, data from the GIBS survey (Zoccali et al. 2014) could be used to better constrain the shape and mass of the nuclear bulge. GIBS is a spectroscopic survey of RCGs identified from VVV and approaching close to the plane at  $b = -2^\circ$ . The data shows a peak in velocity dispersion along the minor axis for  $|b| < 2^\circ$ , indicating a high density in the central 250 pc that corresponds to the expected signature of the nuclear bulge.

The modelling of the bulge could also be improved by the upcoming proper motions from the VVV and VVV-X surveys. These two surveys combined are expected to provide *absolute* proper motions for about 200 million objects, reaching an accuracy of  $\Delta\mu = 200 \mu\text{as.yr}^{-1}$ , corresponding to a tangential velocity of  $\sim 10 \text{ km s}^{-1}$  at 12 kpc. Absolute proper motions would constrain strongly the bulge dynamics since from the Sun perspective most of the streaming velocity in the bulge is along the  $l$  direction.

In the outer disk and the solar neighborhood we could in the near future introduce data from the *Gaia* survey. *Gaia* will revolutionize our understanding of the local disk, streams and spiral arms structure by providing accurate parallax distances and proper motions for more than a billion objects, allowing a direct deprojection of the outer parts of the Galaxy. However *Gaia* is not expected to perform very well towards the Galactic Centre and in the galactic plane because of the large extinction in the visual wavelength range.

Finally, to better constrain from present data the formation history of our Galaxy, an important task would be to extend the chemodynamical modelling to higher dimensions. We carried out a first step towards this goal in [Chapter 5](#) by extending the M2M modelling to metallicity space. More information can be obtained by modelling stellar abundances of other elements that constrain better the formation history. This is for example the case of the  $\alpha$ -elements that are predominantly formed by TypeII supernovas over a shorter timescale compared to iron. Thus the abundance ratio  $[\alpha/\text{Fe}]$  is known as a chemical clock that sets the star formation timescale. We now have the chance to live in an era of large spectroscopic surveys when ongoing and future surveys such as GALAH, APOGEE and GES will provide stellar parameters and abundances for several hundreds of thousands of stars, thus making possible chemodynamical modelling in extended phase-space with several chemical dimensions.

To conclude, the research field of galactic archeology, which aims at understanding the formation history of our Galaxy, promises a very bright future thanks to the many high quality surveys covering the entire Galaxy. Modelling this huge amount of data will be particularly challenging but is expected to provide a clear picture of how the Galaxy formed. To this end, a necessary first step is to build a consensus on how the Galaxy currently is. The work presented in this thesis is the result of an effort of synthesis for establishing a clear picture of the present dynamical state of the Galaxy, focusing on the bar region where 70% of the stars are located. The main result is the construction of the dynamical model of the galactic bar region, that can be iteratively refined and extended in the future to either further spatial extent or higher chemical dimensions.



# Bibliography

- Abadi M. G., Navarro J. F., Fardal M., Babul A., Steinmetz M., 2010, MNRAS, 407, 435, [↗](#) *cited on pages 142*
- Aguerri J. A. L., Beckman J. E., Prieto M., 1998, AJ, 116, 2136, [↗](#) *cited on pages 73 and 140*
- Allende Prieto C. et al., 2008, Astron. Nachrichten, 329, 1018, [↗](#) *cited on pages 6 and 18*
- Alves D. R., 2000, ApJ, 539, 732, [↗](#) *cited on pages 16*
- Aniyan S., Freeman K. C., Gerhard O. E., Arnaboldi M., Flynn C., 2015, MNRAS, 456, 1484, [↗](#) *cited on pages 191*
- Antoja T. et al., 2014, A&A, 563, A60, [↗](#) *cited on pages 18, 74, and 140*
- Athanassoula E., 2002, ApJ, 569, L83, [↗](#) *cited on pages 92*
- Athanassoula E., 2003, MNRAS, 341, 1179, [↗](#) *cited on pages 7 and 30*
- Athanassoula E., 2005, MNRAS, 358, 1477, [↗](#) *cited on pages 146*
- Athanassoula E., 2007, MNRAS, 377, 1569, [↗](#) *cited on pages 92*
- Athanassoula E., Lambert J. C., Dehnen W., 2005, MNRAS, 363, 496, [↗](#) *cited on pages 121 and 125*
- Aumer M., Schönrich R., 2015, MNRAS, 454, 3166, [↗](#) *cited on pages 174 and 186*
- Babusiaux C. et al., 2010, A&A, 519, A77+, [↗](#) *cited on pages 145, 147, 174, 178, and 179*
- Beaulieu S. F., Freeman K. C., Kalnajs A. J., Saha P., Zhao H., 2000, AJ, 120, 855, [↗](#) *cited on pages 30*
- Becklin E. E., Neugebauer G., 1968, ApJ, 151, 145, [↗](#) *cited on pages 4*
- Bell E. F. et al., 2008, ApJ, 680, 295, [↗](#) *cited on pages 12*
- Benjamin R. A. et al., 2005, ApJ, 630, L149, [↗](#) *cited on pages 7, 17, 30, 32, 90, 146, and 190*



















- Bensby T., 2014, Proc. Int. Astron. Union, 9, 17, ☞ *cited on pages 10*
- Bensby T. et al., 2011, A&A, 533, ☞ *cited on pages 95*
- Bensby T. et al., 2013, A&A, 549, A147, ☞ *cited on pages 95*
- Bensby T., Zenn A., Oey M., Feltzing S., 2007, ApJ, 663, L13, ☞ *cited on pages 178*
- Bershadsky M. A., Martinsson T. P. K., Verheijen M. A. W., Westfall K. B., Andersen D. R., Swaters R. A., 2011, ApJ, 739, L47, ☞ *cited on pages 191*
- Bershadsky M. A., Verheijen M. A. W., Swaters R. A., Andersen D. R., Westfall K. B., Martinsson T., 2010, ApJ, 716, 72, ☞ *cited on pages 190*
- Binney J., 2010, MNRAS, 401, 2318, ☞ *cited on pages 22, 36, 91, and 149*
- Binney J., Gerhard O., Spergel D., 1997, MNRAS, 288, 365, ☞ *cited on pages 6, 30, and 146*
- Binney J., Gerhard O. E., Stark A. A., Bally J., Uchida K. I., 1991, MNRAS, 252, 210, ☞ *cited on pages 6, 30, 90, and 146*
- Binney J., Mamon G. A., 1982, MNRAS, 200, 361, ☞ *cited on pages 23*
- Binney J., Tremaine S., 2008, Galact. Dyn. Second Ed., ☞ *cited on pages 19, 21, 22, 23, and 133*
- Binney J. J., Davies R. L., Illingworth G. D., 1990, ApJ, 361, 78, ☞ *cited on pages 23, 36, 91, and 149*
- Bissantz N., Debattista V. P., Gerhard O., 2004, ApJ, 601, L155, ☞ *cited on pages 26, 31, 36, 91, and 150*
- Bissantz N., Englmaier P., Gerhard O., 2003, MNRAS, 340, 949, ☞ *cited on pages 72, 74, 140, and 186*
- Bissantz N., Gerhard O., 2002, MNRAS, 330, 591, ☞ *cited on pages 59, 72, and 146*
- Bland-Hawthorn J., Gerhard O., 2016, ARA&A, 69, ☞ *cited on pages 9, 10, 12, 18, 92, 94, 96, 102, 137, 142, and 153*
- Blitz L., Spergel D. N., 1991, ApJ, 379, 631, ☞ *cited on pages 6, 30, 90, and 146*
- Blum R. D., 1995, ApJ, 444, L89, ☞ *cited on pages 72*
- Blumenthal G. R., Faber S. M., Flores R., Primack J. R., 1986, ApJ, 301, 27, ☞ *cited on pages 142*













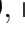


- Boily C. M., Kroupa P., Peñarrubia-Garrido J., 2001, *New Astron.*, 6, 27, [↗](#)  
*cited on pages 31*
- Bovy J., 2016, *ApJ*, 817, 49, [↗](#) *cited on pages 159 and 172*
- Bovy J. et al., 2012, *ApJ*, 759, 131, [↗](#) *cited on pages 42 and 94*
- Bovy J., Rix H.-W., 2013, *ApJ*, 779, 115, [↗](#) *cited on pages 10, 18, 99, 102, and 133*
- Bovy J., Rix H.-W., Green G. M., Schlafly E. F., Finkbeiner D. P., 2016a, *ApJ*, 818, 130, [↗](#)  
*cited on pages 159*
- Bovy J., Rix H.-W., Schlafly E. F., Nidever D. L., Holtzman J. A., Shetrone M., Beers T. C., 2016b, *ApJ*, 823, 30, [↗](#) *cited on pages 10 and 11*
- Bovy J., Tremaine S., 2012, *ApJ*, 756, 89, [↗](#) *cited on pages 23*
- Bressan A., Marigo P., Girardi L., Salasnich B., Dal Cero C., Rubele S., Nanni A., 2012, *MNRAS*, 427, 127, [↗](#) *cited on pages 16, 110, and 154*
- Bullock J. S., Johnston K. V., 2004, *ASP Conf.Ser.*, Vol. 327, *Satell. Tidal Streams. Astron. Soc. Pac.*, San Fr. p. 80, 327, 1, [↗](#) *cited on pages 12*
- Bureau M., Aronica G., Athanassoula E., Dettmar R.-J., Bosma A., Freeman K. C., 2006, *MNRAS*, 370, 753, [↗](#) *cited on pages 68, 69, 75, 82, and 86*
- Burkert A., 1995, *ApJ*, 447, [↗](#) *cited on pages 143*
- Cabrera-Lavers A., González-Fernández C., Garzón F., Hammersley P. L., López-Corredoira M., 2008, *A&A*, 491, 781, [↗](#)  
*cited on pages 7, 32, 74, 90, 146, and 190*
- Cabrera-Lavers A., Hammersley P. L., González-Fernández C., López-Corredoira M., Garzón F., Mahoney T. J., 2007, *A&A*, 465, 825, [↗](#) *cited on pages 7, 30, 32, 79, and 190*
- Calamida A. et al., 2015, *ApJ*, 810, 8, [↗](#) *cited on pages 95 and 96*
- Cappellari M., 2008, *MNRAS*, 390, 71, [↗](#) *cited on pages 22 and 23*
- Cappellari M. et al., 2009, *ApJ*, 704, L34, [↗](#) *cited on pages 36, 91, and 149*
- Cappellari M. et al., 2013, *MNRAS*, 432, 1709, [↗](#) *cited on pages 23*
- Carollo C. M., Stiavelli M., de Zeeuw P. T., Mack J., 1997, *AJ*, 114, 2366, [↗](#)  
*cited on pages 4*
- Catelan M., Pritzl B. J., Smith H. A., 2004, *Astrophys. J. Suppl. Ser.*, 154, 633, [↗](#)  
*cited on pages 16*

- Chabrier G., 2003, ApJ, 586, L133, [↗](#) *cited on pages 61 and 62*
- Chan T. K., Kereš D., Oñorbe J., Hopkins P. F., Muratov A. L., Faucher-Giguère C.-A., Quataert E., 2015, MNRAS, 454, 2981, [↗](#) *cited on pages 143*
- Chandrasekhar S., 1960, Principles of stellar dynamics. New York: Dover  
*cited on pages 19*
- Chatzopoulos S., Fritz T. K., Gerhard O., Gillessen S., Wegg C., Genzel R., Pfuhl O., 2015, MNRAS, 447, 948, [↗](#) *cited on pages 4, 22, 32, and 79*
- Chemin L., Renaud F., Soubiran C., 2015, A&A, 578, A14, [↗](#) *cited on pages 101*
- Chen Y., Girardi L., Bressan A., Marigo P., Barbieri M., Kong X., 2014, MNRAS, 444, 2525, [↗](#) *cited on pages 110 and 154*
- Cheng J. Y. et al., 2012, ApJ, 746, 149, [↗](#) *cited on pages 178*
- Churchwell E. et al., 2009, PASP, 121, 213, [↗](#) *cited on pages 17*
- Clarkson W. et al., 2008, ApJ, 684, 1110, [↗](#) *cited on pages 95*
- Combes F., Debbasch F., Friedli D., Pfenniger D., 1990, A&A, 233, 82, [↗](#)  
*cited on pages 82, 90, and 92*
- Combes F., Sanders R. H., 1981, A&A, 96, 164, [↗](#) *cited on pages 7, 30, 31, 78, and 146*
- Contopoulos G., 1980, A&A, 81, 198, [↗](#) *cited on pages 34, 74, and 140*
- Contopoulos G., Barbanis B., 1994, Celest. Mech. Dyn. Astron., 59, 279, [↗](#)  
*cited on pages 82*
- Contopoulos G., Grosbøl P., 1989, A&ARv, 1, 261, [↗](#) *cited on pages 78 and 136*
- Das P., Gerhard O., Mendez R. H., Teodorescu A. M., de Lorenzi F., 2011, MNRAS, 415, 1244, [↗](#) *cited on pages 26, 31, 36, 91, and 150*
- De Blok W. J. G., 2010, Adv. Astron., 2010, [↗](#) *cited on pages 143*
- De Lorenzi F., Debattista V. P., Gerhard O., Sambhus N., 2007, MNRAS, 376, 71, [↗](#)  
*cited on pages 25, 26, 31, 36, 84, 91, 104, 116, 117, 119, and 149*
- De Lorenzi F. et al., 2009, MNRAS, 395, 76, [↗](#) *cited on pages 26, 31, 36, 91, and 150*
- De Lorenzi F., Gerhard O., Saglia R. P., Sambhus N., Debattista V. P., Pannella M., Méndez R. H., 2008, MNRAS, 385, 1729, [↗](#) *cited on pages 42, 91, and 150*
- Deason A. J., Belokurov V., Evans N. W., 2011, MNRAS, 416, 2903, [↗](#) *cited on pages 12*

- Debattista V. P., Gerhard O., Sevenster M. N., 2002, MNRAS, 334, 355, ☞  
*cited on pages 45, 73, and 140*
- Debattista V. P., Ness M., Earp S. W. F., Cole D. R., 2015, ApJ, 812, L16, ☞  
*cited on pages 6 and 141*
- Debattista V. P., Sellwood J. A., 1998, ApJ, 493, L5, ☞ *cited on pages 25*
- Debattista V. P., Sellwood J. A., 2000, ApJ, 543, 704, ☞  
*cited on pages 7, 30, 34, 78, 92, 141, and 146*
- Dehnen W., 2000a, ApJ, 536, L39, ☞ *cited on pages 26, 31, and 74*
- Dehnen W., 2000b, AJ, 119, 800, ☞ *cited on pages 133 and 140*
- Dehnen W., 2009, MNRAS, 395, 1079, ☞ *cited on pages 104 and 149*
- Dehnen W., Gerhard O. E., 1993, MNRAS, 261, 311, ☞ *cited on pages 22*
- Dejonghe H., 1984, A&A, 133, 225, ☞ *cited on pages 22, 36, 91, and 149*
- Dékány I., Minniti D., Catelan M., Zoccali M., Saito R. K., Hempel M., Gonzalez O. A.,  
2013, ApJ, 776, L19, ☞ *cited on pages 16 and 141*
- Di Matteo P. et al., 2015, A&A, 577, A1, ☞ *cited on pages 141, 148, 181, and 182*
- Di Matteo P. et al., 2014, A&A, 567, A122, ☞ *cited on pages 147, 148, 174, 181, and 182*
- Drimmel R., Spergel D. N., 2001, ApJ, 556, 181, ☞ *cited on pages 63*
- Dubinski J., Berentzen I., Shlosman I., 2009, ApJ, 697, 293 *cited on pages 143*
- Dwek E. et al., 1995, ApJ, 445, 716, ☞ *cited on pages 6, 72, 146, and 185*
- Eggen O. J., Lynden-Bell D., Sandage A. R., 1962, ApJ, 136, 748, ☞  
*cited on pages 12 and 15*
- Einasto J., 1965, Tr. Astrofiz. Instituta Alma-Ata, 5, 87, ☞ *cited on pages 99*
- Eisenstein D. J. et al., 2011, AJ, 142, 72, ☞ *cited on pages 159*
- Elmegreen B., 1996, in Astronomical Society of the Pacific Conference Series, Vol. 91, IAU  
Colloq. 157 Barred Galaxies, Buta R., Crocker D., Elmegreen B., eds., p. 197  
*cited on pages 34 and 79*
- Elmegreen B. G., Elmegreen D. M., Chromey F. R., Hasselbacher D. A., Bissell B. A.,  
1996, AJ, 111, 2233, ☞ *cited on pages 140*
- Elmegreen D. M. et al., 2011, ApJ, 737, 32, ☞ *cited on pages 133*

- Emsellem E. et al., 2004, MNRAS, 352, 721,  *cited on pages 22*
- Englmaier P., Gerhard O., 1999, MNRAS, 304, 512,   
*cited on pages 6, 30, 74, 101, 140, 146, and 186*
- ESA, 1997, The HIPPARCOS and TYCHO catalogues. Astrometric and photometric star catalogues derived from the ESA HIPPARCOS Space Astrometry Mission, Vol. 1200  
*cited on pages 16*
- Eskridge P. B. et al., 2000, AJ, 119, 536,  *cited on pages 30*
- Fabrizius M. H., Saglia R. P., Fisher D. B., Drory N., Bender R., Hopp U., 2012, ApJ, 754, 67,  *cited on pages 78*
- Freeman K. et al., 2013, MNRAS, 428, 3660,  *cited on pages 18, 30, 90, 106, 146, and 154*
- Friedli D., Benz W., Kennicutt R., 1994, ApJ, 430, L105,  *cited on pages 6 and 146*
- Fritz T. K. et al., 2016, ApJ, 821, 44,  *cited on pages 4*
- Fritz T. K. et al., 2011, ApJ, 737, 73,  *cited on pages 17*
- Fux R., 1999, A&A, 345, 787,  *cited on pages 6, 30, 74, 140, 146, and 186*
- Galilei G., 1610, Sidereus nuncius magna,  *cited on pages 1*
- Gebhardt K. et al., 2003, ApJ, 583, 92,  *cited on pages 4*
- Gerhard O., 2002, in Astronomical Society of the Pacific Conference Series, Vol. 273, The Dynamics, Structure & History of Galaxies: A Workshop in Honour of Professor Ken Freeman, Da Costa G., Sadler E., Jerjen H., eds., p. 73  
*cited on pages 30*
- Gerhard O., 2011, Mem. della Soc. Astron. Ital. Suppl., 18, 185,  *cited on pages 73*
- Gerhard O. E., 1994, [Elliptical galaxies](#) *cited on pages 21*
- Gillessen S., Eisenhauer F., Trippe S., Alexander T., Genzel R., Martins F., Ott T., 2009, ApJ, 692, 1075,  *cited on pages 4*
- Gilmore G. et al., 2012, The Messenger, 147, 25,  *cited on pages 18*
- Gilmore G., Reid N., 1983, MNRAS, 202, 1025,  *cited on pages 10*
- Gnedin O. Y., Kravtsov A. V., Klypin A. A., Nagai D., 2004, ApJ, 616, 16,  *cited on pages 142*
- Gonzalez O. A. et al., 2011a, A&A, 530, A54,  *cited on pages 147*
- Gonzalez O. A., Rejkuba M., Zoccali M., Valent E., Minniti D., Tobar R., 2013, A&A, 110, A110,  *cited on pages 172*

- Gonzalez O. A. et al., 2012, *A&A*, 543, A13, [↗](#) *cited on pages 17*
- Gonzalez O. A., Rejkuba M., Zoccali M., Valenti E., Minniti D., 2011b, *A&A*, 534, A3, [↗](#)  
*cited on pages 108, 147, and 172*
- Gott III J. R., Jurić M., Schlegel D., Hoyle F., Vogeley M., Tegmark M., Bahcall N.,  
Brinkmann J., 2005, *ApJ*, 624, 463, [↗](#) *cited on pages 4*
- Haefner R. M., Dehnen W., Evans N. W., Binney J., 2000, *MNRAS*, 314, 433, [↗](#)  
*cited on pages 24*
- Hamadache C. et al., 2006, *A&A*, 454, 185, [↗](#) *cited on pages 188*
- Hammersley P. L., Garzon F., Mahoney T., Calbet X., 1994, *MNRAS*, 269, [↗](#)  
*cited on pages 7, 90, and 189*
- Hammersley P. L., Garzon F., Mahoney T. J., Lopez-Corredoira M., Torres M. A. P., 2000,  
*MNRAS*, 317, L45, [↗](#) *cited on pages 30, 32, 74, and 79*
- Han C., Gould A., 1995, *ApJ*, 449, 521, [↗](#) *cited on pages 72*
- Harsoula M., Kalapotharakos C., 2009, *MNRAS*, 394, 1605, [↗](#) *cited on pages 79*
- Hasan H., Norman C., 1990, *ApJ*, 361, 69, [↗](#) *cited on pages 125*
- Hayden M. R. et al., 2015, *ApJ*, 808, 132, [↗](#) *cited on pages 160 and 161*
- Haywood M., Di Matteo P., Lehnert M. D., Katz D., Gómez A., 2013, *A&A*, 560, A109,  
[↗](#) *cited on pages 148*
- Hernquist L., 1993, *Astrophys. J. Suppl. Ser.*, 86, 389, [↗](#) *cited on pages 25*
- Herschel ., 1785, *Philos. Trans. R. Soc. London*, 75, 213, [↗](#) *cited on pages 3*
- Hill V. et al., 2011, *Astron Astrophys*, 534, A80, [↗](#) *cited on pages 147*
- Hogg D. W., Casey A. R., Ness M., Rix H.-W., Foreman-Mackey D., 2016, eprint  
arXiv:1601.05413, [↗](#) *cited on pages 129*
- Howard C. D., Rich R. M., Reitzel D. B., Koch A., De Propriis R., Zhao H., 2008, *ApJ*,  
688, 1060, [↗](#) *cited on pages 31, 39, and 114*
- Hubble E. P., 1929, *ApJ*, 69, 103, [↗](#) *cited on pages 3*
- Hunt J. A. S., Kawata D., 2014, *MNRAS*, 443, 2112, [↗](#)  
*cited on pages 26, 31, 36, 91, and 150*
- Hunt J. A. S., Kawata D., Martel H., 2013, *MNRAS*, 432, 3062, [↗](#) *cited on pages 26*

- Ibata R. A., Wyse R. F. G., Gilmore G., Irwin M. J., Suntzeff N. B., 1997, *AJ*, 113, 634,  *cited on pages 12*
- Jurić M. et al., 2008, *ApJ*, 673, 864,  *cited on pages 10, 99, 102, 133, and 178*
- Kelsall T. et al., 1998, *ApJ*, 508, 44,  *cited on pages 63*
- Kent S. M., 1992, *ApJ*, 387, 181,  *cited on pages 72*
- Kormendy J., Barentine J. C., 2010, *ApJ*, 715, L176,  *cited on pages 141*
- Kormendy J., Kennicutt R. C., 2004, *ARA&A*, 42, 603,  *cited on pages 6 and 180*
- Kroupa P., 2001, *MNRAS*, 322, 231,  *cited on pages 61, 62, and 96*
- Kuijken K., Gilmore G., 1989, *MNRAS*, 239, 651,  *cited on pages 23*
- Kunder A. et al., 2012, *AJ*, 143, 57,  *cited on pages 30, 31, 39, 75, 84, 87, 90, 114, and 146*
- Kunder A. et al., 2016, *ApJ*, 821, L25,  *cited on pages 141, 148, 178, and 189*
- Launhardt R., Zylka R., Mezger P. G., 2002, *A&A*, 384, 112,  *cited on pages 6, 121, and 141*
- Li Z., Gerhard O., Shen J., Portail M., Wegg C., 2016, *ApJ*, 824, 11,  *cited on pages 140, 186, 187, and 192*
- Li Z.-Y., Shen J., 2012, *ApJ*, 757, L7,  *cited on pages 68, 75, and 82*
- Long R. J., Mao S., 2010, *MNRAS*, 405, 301,  *cited on pages 37, 44, 116, and 117*
- Long R. J., Mao S., Shen J., Wang Y., 2013, *MNRAS*, 428, 3478,  *cited on pages 26, 31, 36, 51, 53, 74, 91, 140, and 150*
- López-Corredoira M., Cabrera-Lavers A., Gerhard O. E., 2005, *A&A*, 439, 107,  *cited on pages 6, 7, 30, 90, and 146*
- Lucas P. W. et al., 2008, *MNRAS*, 391, 136,  *cited on pages 17*
- Lütticke R., Dettmar R.-J., Pohlen M., 2000, *A&AS*, 145, 405,  *cited on pages 7 and 78*
- Lynden-Bell D., Lynden-Bell R. M., 1995, *MNRAS*, 275, 429,  *cited on pages 13*
- Majewski S., Zasowski G., Nidever D., 2011, *ApJ*, 739, 25,  *cited on pages 108*
- Majewski S. R., 2012, *Am. Astron. Soc.*,  *cited on pages 141 and 159*
- Majewski S. R., Skrutskie M. F., Weinberg M. D., Ostheimer J. C., 2003, *ApJ*, 599, 1082,  *cited on pages 10 and 13*

- Mamon G., Lokas E., Dekel A., Stoehr F., Cox T., 2006, EAS Publ. Ser., 20, 139, [↗](#)  
*cited on pages 23*
- Maraston C., 1998, MNRAS, 300, 872, [↗](#) *cited on pages 61 and 63*
- Marinacci F., Pakmor R., Springel V., 2014, MNRAS, 437, 1750, [↗](#) *cited on pages 143*
- Marsh T. R., 1995, MNRAS, 275, L1, [↗](#) *cited on pages 66*
- Martinez-Valpuesta I., 2012, in Dyn. Meets Kinematic Tracers, Ringberg Conference  
*cited on pages 31, 36, and 74*
- Martinez-Valpuesta I., Gerhard O., 2011, ApJ, 734, L20, [↗](#)  
*cited on pages 7, 30, 90, and 146*
- Martinez-Valpuesta I., Gerhard O., 2013, ApJ, 766, L3, [↗](#) *cited on pages 147*
- Martinez-Valpuesta I., Shlosman I., 2004, ApJ, 613, L29, [↗](#) *cited on pages 7 and 30*
- Martinez-Valpuesta I., Shlosman I., Heller C., 2006, ApJ, 637, 214, [↗](#)  
*cited on pages 30, 78, 82, 90, 92, and 146*
- McWilliam A., Zoccali M., 2010, ApJ, 724, 1491, [↗](#)  
*cited on pages 6, 30, 77, 90, 146, and 185*
- Merritt D., Fridman T., 1996, ApJ, 460, 136, [↗](#) *cited on pages 86*
- Minniti D. et al., 2010, New Astron., 15, 433, [↗](#) *cited on pages 17*
- Minniti D., Olszewski E. W., Liebert J., White S. D. M., Hill J. M., Irwin M. J., 1995,  
Mon Not R Astron Soc, 277, 1293, [↗](#) *cited on pages 147 and 172*
- Miralda-Escude J., Schwarzschild M., 1989, ApJ, 339, 752, [↗](#) *cited on pages 86*
- Moni Bidin C., Smith R., Carraro G., Méndez R. A., Moyano M., 2014, A&A, 573, A91,  
[↗](#) *cited on pages 23*
- Moore B., 1994, Nature, 370, 629, [↗](#) *cited on pages 143*
- Morganti L., Gerhard O., 2012, MNRAS, 422, 1571, [↗](#) *cited on pages 26 and 116*
- Morganti L., Gerhard O., Coccato L., Martinez-Valpuesta I., Arnaboldi M., 2013, MNRAS,  
431, 3570, [↗](#) *cited on pages 26, 31, 36, 51, 56, 91, 122, 125, and 150*
- Nakada Y., Onaka T., Yamamura I., Deguchi S., Hashimoto O., Izumiura H., Sekiguchi  
K., 1991, Nature, 353, 140, [↗](#) *cited on pages 6, 30, 90, and 146*
- Nataf D. M. et al., 2013, ApJ, 769, 88, [↗](#) *cited on pages 59*

- Nataf D. M., Udalski A., Gould A., Fouqué P., Stanek K. Z., 2010, ApJ, 721, L28, [☞](#)  
*cited on pages 6, 30, 77, 90, 146, and 185*
- Navarro J. F., Frenk C. S., White S. D. M., 1997, ApJ, 490, 493, [☞](#) *cited on pages 142*
- Navarro J. F. et al., 2010, MNRAS, 402, 21, [☞](#) *cited on pages 15, 99, and 142*
- Ness M. et al., 2013a, MNRAS, 430, 836, [☞](#)  
*cited on pages 30, 39, 41, 74, 90, 95, 106, 110, 147, 151, 154, 172, and 181*
- Ness M. et al., 2013b, MNRAS, 432, 2092, [☞](#)  
*cited on pages 151, 154, 160, 174, 175, 177, and 181*
- Ness M. et al., 2012, ApJ, 756, 22, [☞](#) *cited on pages 30, 77, and 168*
- Ness M., Hogg D. W., Rix H.-W., Ho A. Y. Q., Zasowski G., 2015, ApJ, 808, 16, [☞](#)  
*cited on pages 159*
- Ness M. et al., 2016, ApJ, 819, 2, [☞](#) *cited on pages 129, 131, 159, and 161*
- Newberg H. J. et al., 2002, ApJ, 569, 245, [☞](#) *cited on pages 13*
- Nidever D. L. et al., 2012, ApJ, 755, L25, [☞](#) *cited on pages 6, 141, and 186*
- Nishiyama S. et al., 2006, ApJ, 638, 839, [☞](#) *cited on pages 108*
- Nishiyama S., Nagata T., Tamura M., Kandori R., Hatano H., Sato S., Sugitani K., 2008,  
ApJ, 680, 1174 *cited on pages 17*
- Nishiyama S. et al., 2013, ApJ, 769, L28, [☞](#) *cited on pages 6 and 141*
- Nordström B. et al., 2004, A&A, 418, 989, [☞](#) *cited on pages 17*
- Oort J. H., Rougoor G. W., 1960, MNRAS, 121, 171, [☞](#) *cited on pages 4*
- Ortolani S., Renzini A., Gilmozzi R., Marconi G., Barbuy B., Bica E., Rich R., Michael,  
1995, Nature, 377, 701, [☞](#) *cited on pages 6 and 146*
- Patsis P. A., Athanassoula E., Grosbol P., Skokos C., 2002, MNRAS, 335, 1049, [☞](#)  
*cited on pages 78*
- Patsis P. A., Katsanikas M., 2014, MNRAS, 445, 3546, [☞](#) *cited on pages 87*
- Patsis P. A., Skokos C., Athanassoula E., 2002, MNRAS, 337, 578, [☞](#) *cited on pages 82*
- Percival S. M., Salaris M., Cassisi S., Pietrinferni A., 2009, ApJ, 690, 427, [☞](#)  
*cited on pages 63*
- Pérez-Villegas A., Portail M., Gerhard O., 2016, eprint arXiv:1608.08354, [☞](#)  
*cited on pages 12, 142, 148, 178, 188, and 189*



- Peters, III W., 1975, ApJ, 195, 617, [↗](#) *cited on pages 6, 30, and 90*
- Pfenniger D., Friedli D., 1991, A&A, 252, 75, [↗](#) *cited on pages 78, 79, 81, and 82*
- Pietrinferni A., Cassisi S., Salaris M., Castelli F., 2004, ApJ, 612, 168, [↗](#) *cited on pages 61*
- Pietrukowicz P. et al., 2015, ApJ, 811, 113, [↗](#)  
*cited on pages 16, 141, 148, 178, 188, and 189*
- Piffil T. et al., 2014, MNRAS, 445, 3133, [↗](#) *cited on pages 18, 22, 101, 102, 137, and 138*
- Pontzen A., Governato F., 2012, MNRAS, 421, 3464, [↗](#) *cited on pages 143*
- Portail M., Gerhard O., Wegg C., Ness M., 2016, eprint arXiv:1608.07954, [↗](#)  
*cited on pages 145, 146, and 180*
- Portail M., Wegg C., Gerhard O., 2015, MNRASL, 450, L66, [↗](#) *cited on pages 136 and 176*
- Portail M., Wegg C., Gerhard O., Martinez-Valpuesta I., 2015, MNRAS, 448, 713, [↗](#)  
*cited on pages 78, 84, 86, 87, 90, 93, 142, 143, and 150*
- Portinari L., Sommer-Larsen J., Tantaló R., 2004, MNRAS, 347, 691, [↗](#)  
*cited on pages 190*
- Qian E., De Zeeuw P., van der Marel R., Hunter C., 1995, MNRAS, 274, 602, [↗](#)  
*cited on pages 91 and 149*
- Quillen A. C., Minchev I., Sharma S., Qin Y.-J., Di Matteo P., 2013, MNRAS, 437, 1284,  
[↗](#) *cited on pages 82*
- Raha N., Sellwood J. A., James R. A., Kahn F. D., 1991, Nature, 352, 411, [↗](#)  
*cited on pages 7, 30, 31, 78, and 146*
- Rattenbury N. J., Mao S., Debattista V. P., Sumi T., Gerhard O., De Lorenzi F., 2007a,  
MNRAS, 378, 1165, [↗](#) *cited on pages 42, 54, 55, 114, 116, and 185*
- Rattenbury N. J., Mao S., Sumi T., Smith M. C., 2007b, MNRAS, 378, 1064, [↗](#)  
*cited on pages 59*
- Rautiainen P., Salo H., Laurikainen E., 2008, MNRAS, 388, 1803, [↗](#)  
*cited on pages 34, 73, and 141*
- Read J. I., 2014, J. Phys. G Nucl. Part. Phys., 41, 063101, [↗](#)  
*cited on pages 12, 90, and 137*
- Reid M. J. et al., 2014, ApJ, 783, 130, [↗](#) *cited on pages 32, 79, 94, 102, and 154*
- Rich R. M., Reitzel D. B., Howard C. D., Zhao H., 2007, ApJ, 658, L29, [↗](#)  
*cited on pages 18, 30, 39, 90, 114, and 172*

- Richstone D. O., 1980, ApJ, 238, 103, [↗](#) *cited on pages 24*
- Richstone D. O., Tremaine S., 1984, ApJ, 286, 27, [↗](#) *cited on pages 24*
- Rix .-W., deZeeuw ., Cretton ., vanderMarel ., Carollo ., 1997, ApJ, 488, 702, [↗](#)  
*cited on pages 24*
- Robin A. C., Reylé C., Derrière S., Picaud S., 2003, A&A, 409, 523, [↗](#)  
*cited on pages 160 and 192*
- Rodionov S. A., Athanassoula E., Sotnikova N. Y., 2009, MNRAS, 392, 904, [↗](#)  
*cited on pages 25*
- Rodriguez-Fernandez N. J., Combes F., 2008, A&A, 489, 115, [↗](#)  
*cited on pages 74, 140, and 187*
- Sackett P. D., 1997, ApJ, 483, 103, [↗](#) *cited on pages 32 and 140*
- Saha K., Martinez-Valpuesta I., Gerhard O., 2012, MNRAS, 421, 333, [↗](#)  
*cited on pages 180 and 182*
- Saito R. K. et al., 2012, A&A, 537, A107, [↗](#) *cited on pages 30, 84, and 108*
- Salaris M., Girardi L., 2002, MNRAS, 337, 332, [↗](#) *cited on pages 16, 38, and 95*
- Salpeter E. E., 1955, ApJ, 121, 161, [↗](#) *cited on pages 61, 62, and 75*
- Sanders J. L., Binney J., 2013, MNRAS, 433, 1813, [↗](#) *cited on pages 91 and 149*
- Schaller M. et al., 2015, MNRAS, 451, 1247, [↗](#) *cited on pages 143*
- Schlaufman K. C. et al., 2009, ApJ, 703, 2177, [↗](#) *cited on pages 12*
- Schönrich R., 2012, MNRAS, 427, 274, [↗](#) *cited on pages 94 and 102*
- Schönrich R., Aumer M., Sale S. E., 2015, ApJ, 812, L21, [↗](#) *cited on pages 6 and 141*
- Schönrich R., Binney J., Dehnen W., 2010, MNRAS, 403, 1829, [↗](#)  
*cited on pages 94, 102, and 154*
- Schwarzschild M., 1979, ApJ, 232, 236, [↗](#) *cited on pages 23, 36, 91, and 149*
- Searle L., Zinn R., 1978, ApJ, 225, 357, [↗](#) *cited on pages 12 and 15*
- Seidel M. K. et al., 2015, MNRAS, 446, 2837, [↗](#) *cited on pages 78*
- Sellwood J. A., 2003, ApJ, 587, 638, [↗](#) *cited on pages 104*
- Sellwood J. A., Debattista V. P., 2009, MNRAS, 398, 1279, [↗](#) *cited on pages 25 and 92*

- Sellwood J. A., Valluri M., 1997, MNRAS, 287, 124, [☞](#) *cited on pages 43, 104, and 153*
- Shapley ., Curtis ., 1921, Bull. Natl. Res. Counc., 2, 171, [☞](#) *cited on pages 3*
- Sharma S. et al., 2014, ApJ, 793, 51, [☞](#) *cited on pages 17 and 94*
- Sharma S., Bland-Hawthorn J., Johnston K. V., Binney J., 2011, ApJ, 730, 3, [☞](#) *cited on pages 39 and 191*
- Shen J., Rich R. M., Kormendy J., Howard C. D., De Propris R., Kunder A., 2010, ApJ, 720, L72, [☞](#) *cited on pages 30, 68, and 92*
- Shen J., Sellwood J. A., 2004, ApJ, 604, 614, [☞](#) *cited on pages 125*
- Skokos C., Patsis P. A., Athanassoula E., 2002, MNRAS, 333, 847, [☞](#) *cited on pages 79, 82, and 86*
- Skrutskie M. F. et al., 2006, AJ, 131, 1163, [☞](#) *cited on pages 30 and 106*
- Smiljanic R. et al., 2014, A&A, 570, A122, [☞](#) *cited on pages 161*
- Sofue Y., Honma M., Omodaka T., 2009, PASJ, 61, 227, [☞](#) *cited on pages 54, 73, 74, 99, 100, 101, 102, 125, and 139*
- Sohn S. T., Anderson J., van der Marel R. P., 2012, ApJ, 753, 7, [☞](#) *cited on pages 13*
- Sormani M. C., Binney J., Magorrian J., 2015, MNRAS, 454, 1818, [☞](#) *cited on pages 140*
- Soto M., Rich R. M., Kuijken K., 2007, ApJ, 665, L31, [☞](#) *cited on pages 178 and 179*
- Stanek K. Z., Udalski A., Szymanski M., Kaluzny J., Kubiak Z. M., Mateo M., Krzeminski W., 1997, ApJ, 477, 163, [☞](#) *cited on pages 6, 30, 59, 90, and 146*
- Steinmetz M. et al., 2006, AJ, 132, 1645, [☞](#) *cited on pages 17*
- Sumi T., Penny M. T., 2016, eprint arXiv:1603.05797, 37, [☞](#) *cited on pages 188*
- Sumi T. et al., 2004, MNRAS, 348, 1439, [☞](#) *cited on pages 18, 30, and 114*
- Syer D., Tremaine S., 1996, MNRAS, 282, 223, [☞](#) *cited on pages 25, 31, 36, 37, 84, 91, 117, and 149*
- Tang J., Bressan A., Rosenfield P., Slemmer A., Marigo P., Girardi L., Bianchi L., 2014, MNRAS, 445, 4287, [☞](#) *cited on pages 110 and 154*
- Teuben P., 1995, in Astronomical Society of the Pacific Conference Series, Vol. 77, Astron. Data Anal. Softw. Syst. IV, Shaw R., Payne H., Hayes J., eds., p. 398 *cited on pages 24 and 31*

- Thomas J. et al., 2009, MNRAS, 393, 641, [✉](#) *cited on pages 24, 36, 91, and 149*
- Thomas J., Saglia R. P., Bender R., Thomas D., Gebhardt K., Magorrian J., Corsini E. M., Wegner G., 2005, MNRAS, 360, 1355, [✉](#) *cited on pages 24*
- Torrealba G. et al., 2014, MNRAS, 446, 2251, [✉](#) *cited on pages 178*
- Tremaine S., Weinberg M. D., 1984, ApJ, 282, L5, [✉](#) *cited on pages 73*
- Tully R. B., Courtois H., Hoffman Y., Pomarède D., 2014, Nature, 513, 71, [✉](#) *cited on pages 13 and 14*
- Udalski A., Szymanski M., Kaluzny J., Kubiak M., Mateo M., 1992, Acta Astron., 42, 253, [✉](#) *cited on pages 18*
- Uttenhaler S., Schultheis M., Nataf D. M., Robin A. C., Lebzelter T., Chen B., 2012, A&A, 546, A57, [✉](#) *cited on pages 147*
- Valenti E. et al., 2015, A&A, 4, [✉](#) *cited on pages 96 and 186*
- van Albada T. S., Bahcall J. N., Begeman K., Sancisi R., 1985, ApJ, 295, 305, [✉](#) *cited on pages 190*
- van den Bosch R. C. E., van de Ven G., Verolme E. K., Cappellari M., de Zeeuw P. T., 2008, MNRAS, 385, 647, [✉](#) *cited on pages 24*
- van der Marel R. P., Besla G., Cox T. J., Sohn S. T., Anderson J., 2012a, ApJ, 753, 9, [✉](#) *cited on pages 13*
- van der Marel R. P., Fardal M., Besla G., Beaton R. L., Sohn S. T., Anderson J., Brown T., Guhathakurta P., 2012b, ApJ, 753, 8, [✉](#) *cited on pages 13*
- Vasiliev E., 2013, MNRAS, 434, 3174, [✉](#) *cited on pages 24*
- Walcher C. J. et al., 2005, ApJ, 618, 237, [✉](#) *cited on pages 4*
- Walcher C. J. et al., 2014, A&A, 569, A1, [✉](#) *cited on pages 78*
- Wang Y., Mao S., Long R. J., Shen J., 2013, MNRAS, 435, 3437, [✉](#) *cited on pages 24*
- Wang Y., Zhao H., Mao S., Rich R. M., 2012, MNRAS, 427, 1429, [✉](#) *cited on pages 24*
- Wegg C., Gerhard O., 2013, MNRAS, 435, 1874, [✉](#) *cited on pages 16, 17, 26, 30, 31, 35, 40, 49, 58, 71, 72, 73, 75, 77, 79, 84, 85, 87, 90, 94, 95, 96, 102, 108, 110, 113, 142, 146, 153, 154, and 185*
- Wegg C., Gerhard O., Portail M., 2015, MNRAS, 450, 4050, [✉](#) *cited on pages 4, 7, 9, 26, 90, 97, 113, 143, 146, 153, 168, 181, and 190*

- Wegg C., Gerhard O., Portail M., 2016, eprint arXiv:1607.06462, [↗](#)  
*cited on pages 10, 96, 140, 142, 143, 187, 188, 191, and 192*
- Weiland J. L. et al., 1994, ApJ, 425, L81, [↗](#) *cited on pages 6, 30, 90, and 146*
- Weinberg M. D., Katz N., 2002, ApJ, 580, 627, [↗](#) *cited on pages 143*
- Weiner B. J., Sellwood J. A., 1999, ApJ, 524, 112, [↗](#) *cited on pages 74 and 140*
- Wetterer C. J., McGraw J. T., 1996, AJ, 112, 1046, [↗](#) *cited on pages 178*
- Williams M. J., Zamojski M. A., Bureau M., Kuntschner H., Merrifield M. R., Tim de Zeeuw P., Kuijken K., 2011, MNRAS, 414, 2163, [↗](#) *cited on pages 78*
- Wyrzykowski et al., 2011, MNRAS, 413, 493, [↗](#) *cited on pages 187*
- Yanny B. et al., 2009, Astron J, 137, 4377, [↗](#) *cited on pages 18*
- York D. G. et al., 2000, AJ, 120, 1579, [↗](#) *cited on pages 10*
- Yurin D., Springel V., 2014, MNRAS, 444, 62, [↗](#) *cited on pages 25*
- Zasowski G. et al., 2013, AJ, 146, 81, [↗](#) *cited on pages 159*
- Zhao H., 1994, PhD thesis, Columbia Univ., New York *cited on pages 72*
- Zhao H., 1996, MNRAS, 283, 149, [↗](#) *cited on pages 24*
- Zhu L. et al., 2014, ApJ, 792, 59, [↗](#) *cited on pages 91 and 150*
- Zoccali M., Cassisi S., Frogel J. A., Gould A., Ortolani S., Renzini A., Rich R. M., Stephens A. W., 2000, ApJ, 530, 418, [↗](#) *cited on pages 61, 62, 73, 75, 96, 113, and 186*
- Zoccali M. et al., 2014, A&A, 562, A66, [↗](#) *cited on pages 18, 141, and 192*
- Zoccali M., Hill V., Lecureur A., Barbuy B., Renzini A., Minniti D., Gómez A., Ortolani S., 2008, A&A, 486, 177, [↗](#) *cited on pages 147 and 172*
- Zoccali M. et al., 2003, A&A, 399, 931, [↗](#) *cited on pages 38 and 95*



# Acknowledgements

Before this thesis reaches its end, I would like to thank all the people that made its completion possible and enjoyable.

First of all I would like to express my sincere gratitude to my advisor Prof. Dr. Ortwin Gerhard for his trust and guidance throughout this adventure. Despite my prior lack of astronomical education, Ortwin offered me the opportunity to complete this PhD in a world-class institution, keeping his optimism and faith in me even when I had lost mine. His impressive level of scientific expertise and rigour are a model that changed my way to think, and I am very grateful to him for that.

I am greatly indebted to my office-mate, collaborator and above all good friend Dr. Christopher Wegg for his support, nearly on a daily basis. His quick understanding and limitless competences, including his ability to talk to machines, have been of enormous help during these years.

Special thanks goes to my wife Léonie for her continuous encouragements, psychological support and infinite patience. We went through this adventure as a team, like we always do. She taught me how to become such a calm and relax person, although she may think there is still some room for further progresses.

I would also like to thank my fellow group members and students and friends, who made all these years both scientifically inspiring and delightful. By alphabetical order, my warmest thank go to Anna, Angeles, Alessia, Claudia, Fabrizio, Florian, Isabella, Jethro, Johanna, Karla, Laura, Magda, Matías, Matteo and Sotiris.

I am grateful for the financial support of the Max-Planck-Institut für Extraterrestrische Physik, the computational support of the Max-Planck Computing and Data Facility and the scientific support of the International Max Planck Research School on Astrophysics.

I wish in addition to thank all the members of my thesis and examination committees, Dr. Richard Davies, Prof. Dr. Andreas Burkert, Prof. Dr. Georg Raffelt, Prof. Dr. Jan Lipfert, Prof. Dr. Torsten Enßlin and Prof. Dr. Jörg Schreiber as well my collaborators Dr. Inma Martinez-Valpuesta and Dr. Melissa Ness.

Finally want to acknowledge the assistance of my entire family, parents, sisters and grand-parents who always encouraged me to go further and strive to higher purposes.